

Observations of Whistler-Mode Signals in the OGO Satellites From VLF Ground Station Transmitters

by

Robert L. Heyborne

November 1966

N67-30831
(ACCESSION NUMBER)
713.003
(PAGES)
CR-84869
(NASA CR OR TMX OR AD NUMBER)

(THRU)
1
(CODE)
13
(CATEGORY)

Technical Report No. 3415/3418-1

Prepared under
National Aeronautics and Space Administration
Contracts NAS 5-2131 and NAS 5-3093
National Science Foundation, Section on
Atmosphere Sciences
Grant NSF GP-2247

RADIOSCIENCE LABORATORY
STANFORD ELECTRONICS LABORATORIES
STANFORD UNIVERSITY • STANFORD, CALIFORNIA



OBSERVATIONS OF WHISTLER-MODE SIGNALS IN THE OGO
SATELLITES FROM VLF GROUND STATION TRANSMITTERS

by

Robert L. Heyborne

November 1966

Technical Report No. 3415/3418-1

Prepared under

National Aeronautics and Space Administration

Contracts NAS 5-2131 and NAS 5-3093

National Science Foundation, Section on Atmospheric Sciences
Grant NSF GP-2247

Radioscience Laboratory

Stanford University

Stanford, California

ABSTRACT

In the ionospheric plasma, electromagnetic propagation is possible at frequencies below the plasma frequency and the electron gyrofrequency. This mode of propagation is commonly known as the whistler mode.

Amplitude calibrated receivers aboard two satellites (OGO-I and OGO-II) are used to receive signals propagating in the whistler mode from U. S. Navy vlf stations on the ground. Existing theory is utilized to calculate the expected intensities of these signals. Measured and calculated intensities are then compared.

The two satellites effectively sub-divide the whistler mode path into two main parts: (1) the earth-ionosphere waveguide loss, the boundary and excitation loss, and the absorption loss through the ionosphere to the altitudes of OGO-II and (2) losses due to divergence of the signal between OGO-II and the higher altitudes of OGO-I plus any additional absorption above OGO-II. These data are utilized to determine more precisely the major features and loss characteristics of whistler-mode paths inferred from previous experiments, and to determine the accuracy of attenuation rates predicted earlier by theoretical means.

It is concluded that the average intensity of vlf whistler-mode signals in the magnetosphere may usually be predicted to an accuracy of ± 10 db by the use of available models and existing theory. This study strongly supports present understanding of the major features of whistler-mode propagation which until now has been based largely on theoretical developments and experimental observations of naturally occurring phenomena.

Several new observations have been made. These include:

(1) A Northern hemisphere latitudinal cutoff of vlf signals. Signal intensities have been observed to decrease as much as 40 db as OGO-II moves from approximately 59° to 60° Northern geomagnetic latitude. Signals are seldom observed at latitudes above the cutoff region. There is evidence that the cutoff is more pronounced during the daytime and when the geomagnetic planetary K_p index is high. It is hypothesized that the $N\sqrt{\nu}$ product in the D and E regions of the ionosphere increases rapidly with latitude near the cutoff region. The evidence suggests that the observed cutoff is

consistent with an absorption explanation.

(2) Strong enhancements of vlf signals near the antipodes of vlf transmitters. Enhancement factors as high as 25 db have been observed when the satellite flies within 200 km of the antipode. Enhancements have also been observed near the magnetic conjugate of the antipode.

(3) A pronounced dip in the intensity of vlf signals over the geomagnetic equator. Seen at all longitudes, both daytime and nighttime, the magnitude of the equatorial dip is typically 12 to 20 db during the daytime and 5 to 10 db during the nighttime. The observation is explained on the basis of absorption.

(4) A band of intense noise at 18 kHz around both polar regions. The intense noise is observed in a band 3 to 11 degrees wide centered near 75 degrees geomagnetic latitude. Occurrence of the noise exhibits seasonal dependence with local summer rates higher than winter. Although there is evidence that the intense noise is more likely to be observed during magnetically disturbed periods, fluctuations in the noise magnitude can not be explained by fluctuations in the K_p index.

CONTENTS

	<u>Page</u>
I. INTRODUCTION	1
A. Objective	1
B. Organization of Material	1
C. Whistler-Mode Characteristics	2
D. Whistler-Mode Propagation	3
E. The Problem and a Solution	11
F. Contributions of the Present Work	13
II. THE OGO-I EXPERIMENT	14
A. The Satellite	14
B. The Orbit	14
C. The Equipment	16
D. Obtaining the Data	18
E. Source of Errors	41
F. Data Reduction	45
G. Presentation of the Data	51
III. FIELD STRENGTH CALCULATIONS	53
A. Introduction	53
B. Earth-Ionosphere Waveguide	53
C. Absorption	59
D. Divergence	62
E. Impedance Transformation Effects	71
F. Total Path Calculations	75
IV. THE OGO-I DATA	80
A. Introduction	80

CONTENTS (cont.)

	<u>Page</u>
B. OGO-I Field Intensities Versus Universal Time	80
V. THE OGO-II EXPERIMENT	92
A. The Satellite	92
B. The Orbit	93
C. Equipment	95
D. Obtaining the Data	96
E. Source of Errors	99
F. Presentation of the Data	101
VI. THE OGO-II DATA	111
A. Introduction	111
B. OGO-II Field Intensities Versus Dipole Latitude	111
VII. REFINEMENT OF THE MODEL	146
A. The Earth-Ionosphere Waveguide Loss	146
B. Absorption Loss	156
C. Divergence Loss	159
1. Ray Tracing	160
2. Measured Divergence	167
VIII. NEW OBSERVATIONS	169
A. Latitudinal Cutoff of Whistler-Mode Signals	169
B. Observation of Intense Noise	171
C. Antipodal Enhancements	175
D. Equatorial Dip	177
E. Terminal Region Bursts	178
F. Fading of Whistler-Mode Signals	179

CONTENTS (cont.)

	<u>Page</u>
G. Cyclotron Absorption	180
IX. INTERPRETATIONS AND CONCLUSIONS	181
A. The Earth Ionosphere Waveguide Loss	181
B. Divergence Loss	183
C. Latitudinal Cutoff of Whistler-Mode Signals	184
D. Antipodal Enhancements	187
E. Intense Noise	188
F. Cyclotron Absorption	189
G. Fading	190
H. Terminal Region Bursts	192
I. The Equatorial Dip	193
J. Measurements versus Calculations	196
K. Discussion and Conclusions	200
L. Suggestions for Further Work	201
REFERENCES	202

LIST OF TABLES

<u>Table</u>		<u>Page</u>
1	OGO-I definitive orbital parameters	17
2	Locations of pertinent stations	42
3	Parameters used in field-strength calculations	57
4	OGO-II definitive orbital parameters	94
5	A summary, by revolution, of the ACS modes and the available control for OGO-II during the period of time covered by this study	97
6	Attenuation rates in the earth-ionosphere waveguide as indicated by normalizing the OGO data	153
7	Launch point characteristics for a variety of wave normal directions at the satellite (OGO-I) for 1100 UT 17 February 1965	162
8	Divergence loss as indicated by tracing pairs of rays to the OGO-I satellite location on 17 February 1965 . . .	165
9	Divergence loss as indicated by several different methods for OGO-I on 17 February 1965	168
10	Major features of the northern hemisphere latitudinal cutoff of NPG and NAA signals observed by OGO-II	170
11	Major features of the southern hemisphere cutoff of NPG and NAA signals observed by OGO-II	172
12	Major features of the intense 18 kHz noise observed by OGO-II	176

ILLUSTRATIONS

<u>Figure</u>		<u>Page</u>
1	A typical whistler-mode path when both the source and the receiver are ground-based and located in opposite hemispheres	3
2	Wave coordinates in relation to the earth's magnetic field as used in the investigation of whistler-mode propagation .	7
3	The general configuration of the OGO-I satellite showing the position of the vlf loop antenna and the coordinate system	15
4	Data from the PCM telemetry, showing the simultaneous outputs of the band 1, band 2, and band 3 receivers	20
5	A continuation of the data shown in figure 4	21
6	A continuation of the data shown in figures 4 and 5	22
7	A continuation of the data shown in figures 4, 5 and 6 . .	23
8	Data from the PCM telemetry showing the output of the band 3 receiver	24
9	A continuation of the data shown in figure 8	25
10	Data from the PCM telemetry showing the band 3 output . . .	26
11	A continuation of the data shown in figure 10	27
12	A continuation of the data shown in figures 10 and 11 showing a total absence of signals from NPG, although NPG was transmitting during this time	28
13	A continuation of the data shown in figures 10, 11 and 12	29
14	Data from the PCM telemetry showing the output of band 3 .	30
15	A continuation of the data shown in figure 14	31
16	A 16mm frame of data from the OGO-I PCM telemetry as prepared by Stanford Research Institute	32
17	A typical display of data from the satellite VCO via the special purpose telemetry as prepared by the Stanford Radioscience Laboratory	33

ILLUSTRATIONS (cont.)

<u>Figure</u>		<u>Page</u>
18	A long period of CW (FM) transmission from NPG as indicated by the OGO-I satellite VCO via the special purpose telemetry	34
19	A continuation of the data shown in figure 18	35
20	A continuation of the data shown in figures 18 and 19 . . .	36
21	A continuation of the data shown in figures 18, 19 and 20 .	37
22	A continuation of the data shown in figures 18, 19, 20 and 21	38
23	A flow diagram of the routine OGO system operations	46
24	Ratio of peak to median values (in db) as scaled from key-down periods of data from OGO-I	50
25	Ratio of peak to median values (in db) as scaled from key-down periods of data from OGO-II	50
26	Ray path geometry for propagation in the earth-ionosphere waveguide	54
27	Field intensity of transmitted ionosphere wave versus distance from a short vertical antenna at the ground radiating 1 kw at 15.5 kHz	56
28	Derived models of the lower ionosphere	63
29	Absorption of a vertically incident wave integrated through the lower and upper ionosphere as a function of latitude .	64
30	Relation between the ray and the refractive index surface in a uniaxial medium	66
31	Ray direction versus wave-normal direction, parametric in normalized frequency	67
32	Maximum ray angle versus normalized frequency	67
33	To illustrate divergence of a field-aligned whistler-mode wave	70
34	OGO-I magnetic field strength versus time for NAA on 24 November 1964	81

ILLUSTRATIONS (cont.)

<u>Figure</u>		<u>Page</u>
35	OGO-I magnetic field strength versus time for NPG on 17 February 1965	82
36	OGO-I magnetic field strength versus time for NPG on 29 March 1965	83
37	OGO-I magnetic field strength versus time for NAA on 1 April 1965	84
38	OGO-I magnetic field strength versus time for NPG on 6 April 1965	85
39	OGO-I magnetic field strength versus time for NAA on 17 August 1965	86
40	OGO-I magnetic field strength versus time for NAA on 18 September 1965	87
41	OGO-I magnetic field strength versus time for NAA on 21 September 1965	88
42	OGO-I magnetic field strength versus time for NPG on 26 September 1965	89
43	OGO-I magnetic field strength versus time for NPG on 4 October 1965	90
44	OGO-I magnetic field strength versus time for NPG on 2 November 1964	91
45	OGO-II spacecraft and vlf loop antenna orientation in stabilized flight mode 3	93
46	OGO-II spacecraft and vlf loop antenna orientation in flight mode 2C	98
47	To illustrate a sharp latitudinal cut off of whistler-mode signals observed in OGO-II	102
48	A continuation of the data shown in figure 47	103
49	To illustrate a signal enhancement of approximately 25 db near the NPG antipode	104
50	To illustrate high intensity NPG signals (second trace from the top) over an earth-ionosphere waveguide distance of almost 9 kkm	105

ILLUSTRATIONS (cont.)

<u>Figure</u>		<u>Page</u>
51	A continuation of the data shown in figure 50, demonstrating one of the few instances where the latitudinal cut off is not observed, the intense noise (which began in FR 68 of figure 50) does not persist, and vlf signals are observed at high latitudes (up to 81° in FR 73)	106
52	Fairly rapid fading patterns during periods of CW transmission from NPG as indicated by the OGO-II satellite VCO via the special purpose telemetry	107
53	To illustrate some of the deepest and most rapid fading patterns observed by OGO-II	108
54	To illustrate fading patterns observed by OGO-II which resemble the fading observed by OGO-I	109
55	A rayspan record of the latitudinal cutoff phenomena shown in figures 47 and 48	110
56	OGO-II orbital subsatellite plot where vlf data were obtained during rev. 74	112
57	OGO-II magnetic field strength versus dipole latitude for NAA on 19 October 1965	113
58	OGO-II orbital subsatellite plot where vlf data were obtained during rev. 75	114
59	OGO-II magnetic field strength versus dipole latitude for NAA and NPG on 19 October 1965	115
60	OGO-II orbital subsatellite plot where vlf data were obtained during rev. 76	116
61	OGO-II magnetic field strength versus dipole latitude for NPG on 20 October 1965	117
62	OGO-II orbital subsatellite plot where vlf data were obtained during rev. 103 and 104	118
63	OGO-II magnetic field strength versus dipole latitude for NPG on 21 October 1965	119
64	OGO-II orbital subsatellite plot where vlf data were obtained during rev. 105	120
65	OGO-II magnetic field strength versus dipole latitude for NPG on 22 October 1965	121

ILLUSTRATIONS (cont.)

<u>Figure</u>	<u>Page</u>
66	OGO-II orbital subsatellite plot where vlf data were obtained during rev. 106 122
67	OGO-II magnetic field strength versus dipole latitude for NPG on 22 October 1965 123
68	OGO-II orbital subsatellite plot where vlf data were obtained during rev. 107 124
69	OGO-II magnetic field strength versus dipole latitude for NPG on 22 October 1965 125
70	OGO-II orbital subsatellite plot where vlf data were obtained during rev. 109 126
71	OGO-II magnetic field strength versus dipole latitude for NAA on 22 October 1965 127
72	OGO-II orbital subsatellite plot where vlf data were obtained during rev. 122 and 123 128
73	OGO-II magnetic field strength versus dipole latitude for NPG on 23 October 1965 129
74	OGO-II orbital subsatellite plot where vlf data were obtained during rev. 124 130
75	OGO-II magnetic field strength versus dipole latitude for NPG on 23 October 1965 131
76	OGO-II orbital subsatellite plot where vlf data were obtained during rev. 125 132
77	OGO-II magnetic field strength versus dipole latitude for NAA on 23 October 1965 133
78	OGO-II orbital subsatellite plot where vlf data were obtained during rev. 126 134
79	OGO-II magnetic field strength versus dipole latitude for NAA on 23 October 1965 135
80	OGO-II orbital subsatellite plot where vlf data were obtained during rev. 127 136
81	OGO-II magnetic field strength versus dipole latitude for NAA on 23 October 1965 137

ILLUSTRATIONS (cont.)

<u>Figure</u>		<u>Page</u>
82	OGO-II orbital subsatellite plot where vlf data were obtained during rev. 128	138
83	OGO-II magnetic field strength versus dipole latitude for NAA on 23 October 1965	139
84	OGO-II orbital subsatellite plot where vlf data were obtained during rev. 130	140
85	OGO-II magnetic field strength versus universal time for NPG on 23 October 1965	141
86	OGO-II orbital subsatellite plot where vlf data were obtained during rev. 131 and 132	142
87	OGO-II magnetic field strength versus dipole latitude for NPG on 24 October 1965	143
88	OGO-II orbital subsatellite plot where vlf data were obtained during rev. 134	144
89	OGO-II magnetic field strength versus dipole latitude for NAA on 24 October 1965	146
90	Field intensity of daytime transmitted wave (just above the boundary) versus distance from short vertical antenna at ground radiating 1 kw	154
91	Field intensity of nighttime transmitted wave (just above the boundary) versus distance from short vertical antenna at ground radiating 1 kw	155
92	Absorption of a vertically incident wave integrated through the lower and upper ionosphere as a function of latitude showing the effects of a reduction in f_oF2	157
93	Total absorption as a function of height for a vertically incident wave integrated through the lower and upper ionosphere	158
94	Divergence in the magnetic meridian as obtained by tracing pairs of rays from a height of 250 km to the OGO-I satellite location on 17 February 1965	161
95	Geometrical relationships of the incident and transmitted waves, the earth's magnetic field (H_o) and the radius vector (R_o) at the launch point	163

ILLUSTRATIONS (cont.)

<u>Figure</u>		<u>Page</u>
96	To illustrate the manner in which ray tracing and Eq. (7.13) are utilized to determine divergence loss	166
97	Geometrical relationship between incident and transmitted wave and the earth's magnetic field at a dipole latitude of 27°	195

ACKNOWLEDGMENT

The author wishes to acknowledge his sincere appreciation to his co-workers in the Radioscience Laboratory of Stanford University for their helpfulness during the course of this work; in particular to Professors Robert A. Helliwell and Hugh H. Skilling and Dr. R. L. Smith for their patience, guidance, and encouragement. The assistance of John Katsufakis, Nicholas Duncel, Bruce Edgar, Drs. T. F. Bell, D. L. Carpenter, and Jacyntho Angerami is gratefully acknowledged. Only through their assistance was it possible to obtain and interpret the data for this study.

The author is also indebted to B. Ficklin, L. Rorden, N. Schlosser, G. Carpenter and W. Blair of the Stanford Research Institute. They were all very helpful in supplying details concerning the reduction of digital data.

Special thanks go to the U. S. Navy Radio Communication Center at Stockton, California, specifically to Mr. R. Jones who kindly provided key-down periods of transmission from NPG. Special thanks also to Commander J. J. Forrester, Commanding Officer of the U. S. Navy Radio Station NAA in Cutler, Maine, who kindly supplied information concerning NAA transmission schedules.

This research was supported by the National Aeronautics and Space Administration through Goddard Space Flight Center under contracts NAS 5-2131 and NAS 5-3093. The ground data for this study were acquired at Stanford University under grant GP-2247 from the Atmospheric Sciences Section of the National Science Foundation. Computer time for the ray tracing computations was funded by the Office of Computer Sciences in the Mathematical Division of the National Science Foundation under grant NSF GP-948.

I. INTRODUCTION

A. OBJECTIVE

The objective of this research is to utilize data from the OGO satellites to provide new insights to the subject of whistler-mode propagation. Specifically, it is planned experimentally to determine total-path transmission loss, so as to (1) define more precisely the major features and loss characteristics of paths inferred from previous experiments, and (2) determine the accuracy of attenuation rates predicted earlier by theoretical means.

It is believed that this research will be helpful in evaluating the possible usefulness of this mode of propagation as a means of communication by determining the intensity of whistler-mode signals produced in the magnetosphere by a very low frequency (vlf) transmitter on the ground.

This work should also be of interest to those who are involved with vlf navigation systems, since it provides new information concerning such characteristics as the depth and frequency of occurrence of whistler-mode fading, which might affect these systems.

The OGO satellites are unique in providing: (1) accurate amplitude measurements of whistler-mode signals at high altitudes (OGO-I) and (2) accurate amplitude measurements of whistler-mode signals at high latitudes (OGO-II).

B. ORGANIZATION OF MATERIAL

Since the data presented here were obtained from two satellites (OGO-I which is in a high altitude equatorial orbit and OGO-II which is in a low altitude polar orbit) separate chapters are devoted to each.

The OGO-I experiment is discussed in Chapter II. Data from OGO-I are presented in Chapter IV. The OGO-II experiment is discussed in Chapter V; its data are presented in Chapter VI.

In the process of analyzing these data in the study of whistler-mode propagation per se (which was the initial objective of this work) several new phenomena have been observed. Since these constitute in essence new topics they are all gathered in one chapter (Chapter VIII).

The locations of the satellite tracking stations and the U. S. Navy vlf stations from which data were used throughout this study are listed in Table 2 for easy identification of the code abbreviations used in many of the illustrations.

C. WHISTLER-MODE CHARACTERISTICS

Whistlers are generated by lightning discharges which radiate impulses of electromagnetic energy. As this energy spreads out beneath the ionosphere in the earth-ionosphere waveguide, continual leakage into the ionosphere occurs and whistler-mode waves will be excited wherever the polarization of the waves is appropriate. These waves then propagate approximately along the lines of force of the earth's magnetic field from one hemisphere to the other. The energy is dispersed as it travels through the magnetosphere, causing the original signal, which can be considered an impulse, to be dispersed into a gliding tone typically lasting about a second. This gliding tone is called a whistler. The dispersion is a measure of the electron content along the path.

Studies of dispersion characteristics of whistlers have provided new data on electron concentration in the magnetosphere and on the paths of whistlers. Smith [1960a] showed that from the "nose" frequency of a whistler the latitude of the propagation path could be determined, and that the group delay at this frequency gives a measure of the electron concentration in the outer ionosphere along the path of propagation. Carpenter [1962a, 1962b] found that during magnetic storms, measurements of whistlers gave normal electron concentrations for the lower latitude paths, but that along higher latitude paths the electron concentrations were typically much less than in magnetically quiet periods. He called this transition region the "knee."

It should be noted that the actual path of a whistler has never been observed experimentally, but has only been inferred from experimental results. This path is believed to involve the earth-ionosphere waveguide possibly at both ends of the path depending on the location of the source and the receiver [Allcock, 1966; Allcock and McNeill, 1966], plus an outer ionospheric or magnetospheric path along the earth's field between

the two hemispheres, such as shown in Fig. 1.

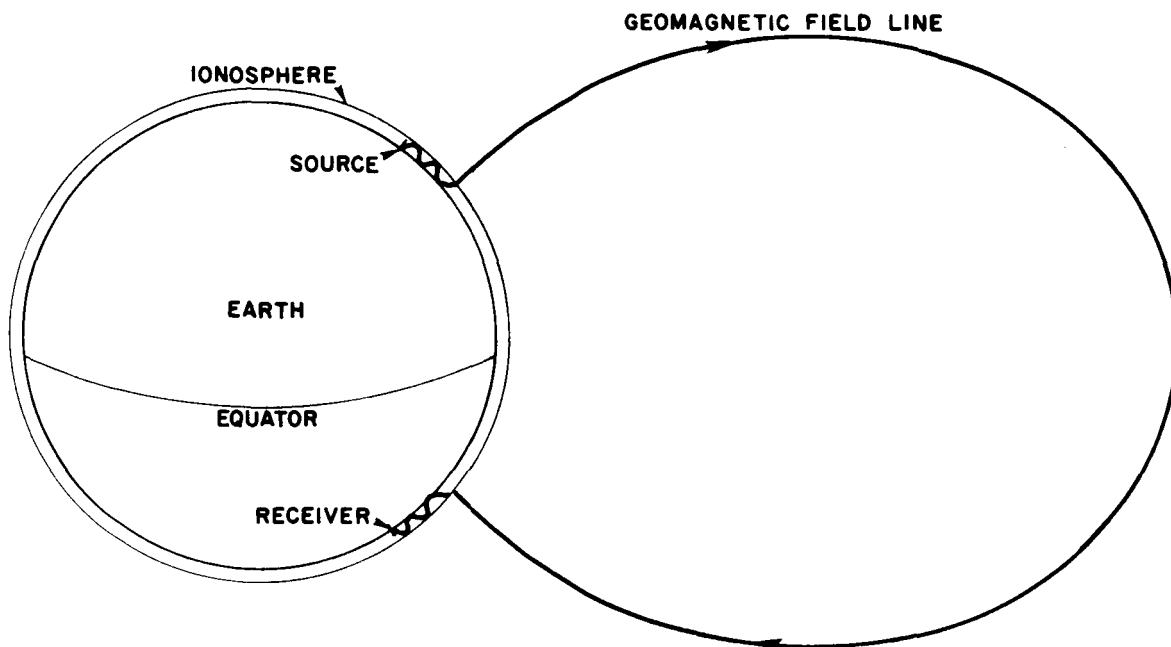


FIG. 1. A TYPICAL WHISTLER-MODE PATH WHERE BOTH THE SOURCE AND THE RECEIVER ARE GROUND-BASED AND LOCATED IN OPPOSITE HEMISPHERES.

Delloue [1957], Crary [1961] and others have conducted experiments utilizing direction-finding techniques to determine the direction of arrival and the polarization of whistlers observed on the ground. These studies have been useful in postulating the exit point of a whistler from the magnetosphere into the earth-ionosphere waveguide.

Helliwell [1965] presents a comprehensive treatment of whistlers and related ionospheric phenomena. He points out that the rapid growth of this aspect of radio science is illustrated by the number of publications, which was no more than 15 before 1951 and now exceeds 500.

D. WHISTLER-MODE PROPAGATION

As a direct result of extensive research prior to the advent of vlf

satellite experiments, whistlers were well understood and much appreciation has been gained for their usefulness as a research tool with which to study the earth's environment.

Much of the theory of whistlers centers around the Appleton-Hartree equations which describe the refractive index and polarization of electromagnetic waves propagating in a homogeneous gaseous medium permeated by a static magnetic field. In the ionospheric plasma, electromagnetic propagation is possible at frequencies below the plasma and the electron gyrofrequency...a mode of propagation commonly known as the whistler mode.

Pre-satellite whistler observations gave ample evidence that the dispersion properties of whistlers agreed well with the quasi-longitudinal (QL) cold-plasma electrons-only magnetoionic theory described in detail by Storey [1953], Ratcliffe [1959], Helliwell [1965], and others. These observations also supported the hypothesis that whistlers observed on the ground are ducted by enhanced columns of ionization [Smith, 1960a]. The ground observations are now well understood, and their agreement with the QL case for whistler-mode propagation is good.

While satellite measurements of whistlers have not conflicted with ground measurements, they have provided an abundant variety of whistler-mode forms which have never been observed on the ground. These new phenomena include ion-cyclotron whistlers [Gurnett, et al, 1965], the SP whistlers (occasionally also observed on the ground) [Carpenter, 1964; and Smith, 1964], the transverse whistlers, [Carpenter and Dunckel, 1965; Kimura, et al, 1965] and the psuedo-nose whistlers [Smith, 1966].

The satellite measurements have uncovered an entirely new area of whistler-mode propagation in the ionosphere which involves transverse propagation, large wave normal angles, and various other new modes which apparently owe their existence to the effects of ions [Smith and Brice, 1964].

It can be shown [Hines, 1957] that for frequencies well above the lower hybrid resonance [Smith, et al, 1966] the effects of ions may be neglected, and then the properties of whistler-mode propagation are explained approximately by the classical magnetoionic theory utilizing the customary QL approximation assuming only electrons. Since the

frequencies in this study are limited to approximately 18 kHz, the effects of ions are therefore ignored and the cold plasma QL theory is applied.

Since the publications mentioned above give detailed treatment of the magnetoionic theory, only a very brief outline including the more important results which are vital to this study will be presented here. References to the complete theory are included in the bibliography.

The static magnetic field of the earth causes the ionosphere to be anisotropic. Hence, there are in general two values for the refractive index, corresponding to the two characteristic waves that can propagate. The complete expressions for refractive index and polarization (see Helliwell [1965], Ratcliffe [1959]) are difficult to use because of their complexity. For many applications these expressions may be simplified by using the quasi-longitudinal (QL) approximation discussed below. With this approximation the complete expressions may be reduced to

$$n^2 = 1 - \frac{X}{1 - iZ \pm |Y_L|} \quad (1.1)$$

and

$$R = - \frac{H_y}{H_x} = \frac{E_x}{E_y} = \pm i \frac{|Y_L|}{Y_L} . \quad (1.2)$$

where R is the polarization,

n = complex refractive index = $\mu - i\chi$,

μ = refractive index (real part of n) ,

χ = $\alpha c/\omega$ = absorption index (negative imaginary part of n) ,

α = absorption coefficient (nepers/meter) ,

c = velocity of light ,

H_x, H_y = components of magnetic field of the wave ,

E_x, E_y, E_z = components of electric field of the wave ,

x, y, z = coordinate axes as shown in Fig. 2 ,

$i = \sqrt{-1}$,

$Y_L = f_L/f$,

$\omega = 2\pi f$,

$Z = v/\omega$,

f = wave frequency,

$$\omega_o = 2\pi f_o = \sqrt{Ne^2/(\epsilon_o m)} ,$$

$$X = \frac{f_o^2}{f^2} ,$$

$$\omega_L = 2\pi f_L = \omega_H \cos \theta ,$$

$$Y = \frac{f_H}{f} = \sqrt{Y_L^2 + Y_T^2} ,$$

$$\omega_H = 2\pi f_H = \frac{\mu_o |H_o| e}{m} ,$$

$$Y_T = \frac{f_T}{f} ,$$

f_o = plasma frequency,

f_H = electron gyrofrequency,

ν = frequency of collision of electrons with heavy particles,

N = number density of electrons,

e = charge on an electron,

ϵ_o = dielectric constant of free space (rationalized units),

m = mass of electron,

μ_o = permeability of free space,

H_o = imposed magnetic field,

θ = angle between H_o and Oz (Fig. 2).

The correct sign for the whistler mode is easily determined by considering Eq. (1.1) at levels well above the F2 layer where Z is negligibly small and $X > 1 + Y_L$. It is then clear that propagation can take place only for the minus sign in Eq. (1.1). The polarization of the propagating wave is described by Eq. (1.2) with the corresponding choice of the minus sign.

The QL approximation by which Eq. (1.1) and Eq. (1.2) are obtained is valid when the direction of propagation is sufficiently close to the direction of the earth's magnetic field to permit dropping terms containing Y_T in the general expression. The necessary condition for the QL approximation to hold is given by

$$\frac{Y_T^4}{4Y_L^2} \ll |(1-X-iZ)^2|, \quad (1.3)$$

which can be written

$$\frac{Y^2 \sin^4 \theta}{4 \cos^2 \theta} \ll |(1-X-iZ)^2|. \quad (1.4)$$

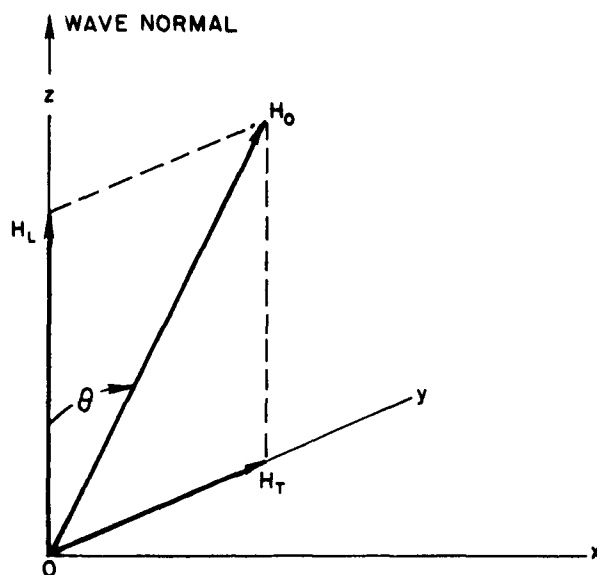


FIG. 2. WAVE COORDINATES IN RELATION TO THE EARTH'S MAGNETIC FIELD AS USED IN THE INVESTIGATION OF WHISTLER-MODE PROPAGATION.

Helliwell [1965] discusses the QL approximation in detail. He calculates the range of wave-normal angles θ over which the QL approximation is valid for the case of no collisions and for $X \gg 1$, and shows that the approximation is usually good up to angles of at least forty-five degrees or more. He also calculates the QL criterion as a function of wave frequency for the region between 60 and 120 km using appropriate ionospheric models for both daytime and nighttime. These results show

that a vertically incident 18 kHz wave will meet the QL condition during daytime for values of θ less than approximately 50° . At night the QL condition is satisfied for values of θ less than approximately 30° . Based on the above arguments, and the discussion in section D of Chapter III, the QL approximation has been used for all calculations in this study. Inaccuracies incurred through the use of this approximation are probably less than those produced by uncertainties in the ionospheric models employed.

In the lower regions of the ionosphere where the collisional term (Z) of Eq. (1.1) is important $|Y_L| \gg 1$, therefore the term 1 in the denominator can be neglected. This term may also be neglected in higher regions where collisions are no longer important, providing $|Y_L|$ remains much greater than 1. For the OGO-I orbit and a frequency of approximately 18 kHz (the frequencies used in this study), this condition is satisfied out to a distance of approximately 3 earth radii. Beyond this region the term must be retained.

In Eq. (1.1), the first term (the quantity 1) may be neglected whenever $X \gg 1$. For a frequency of 18 kHz this condition is satisfied for virtually all regions from which data for this study were obtained.

It should be noted at this point that the general behavior of the refractive index is given by Eq. (1.1). Helliwell [1965] presents several figures showing the variation of n^2 with X and with Y for conditions of interest in whistler propagation. For the case of no losses, coupling to the whistler mode from free space appears difficult because the refractive index of the ordinary branch does not remain real in the lower ionosphere transition region near $X = 1$, except for the purely longitudinal case. However, as Helliwell notes, if the effect of collisions is included, coupling can occur over a finite range of θ [Ratcliffe, 1959]. Another factor that promotes coupling is a steep gradient of refractive index near $X = 1$. The combined effects of collisions and a steep gradient account for the excitation of the whistler mode at the lower boundary of the ionosphere. Helliwell [1965] calculates the absorption rate and refractive index as functions of height for a vertically incident wave in the normal daytime ionosphere. His calculations show that the refractive index of the whistler-mode (minus sign

in Eq. (1.1)) does indeed remain real and greater than unity for all heights between 60 and 1400 km.

The important dispersive effects in whistler-mode propagation take place in regions of very low collisional frequency. From the arguments above and Eq. (1.1), the refractive index of this region is

$$n^2 = \mu^2 \cong \frac{X}{|Y_L| - 1} \quad (1.5)$$

where n is the refractive index of the propagating whistler-mode wave. Replacing X and Y with the appropriate expressions given above, Eq. (1.5) becomes

$$\mu^2 \cong \frac{f_o^2}{f(f_H \cos \theta - f)} \quad (1.6)$$

$$= \frac{B^2}{\Lambda(\cos \theta - \Lambda)} \quad (1.7)$$

where $\Lambda = \frac{f}{f_H}$, and $B = \frac{f_o}{f_H}$.

Whistler data consist primarily of measurements of group delay versus frequency, therefore it is necessary to obtain an expression for the group velocity v_g from Eq. (1.7). The dispersive characteristics of a homogeneous medium are usually described in terms of the group refractive index $\mu' = c/v_g$, which is related to the refractive index by the equation

$$\mu' = \frac{d(\mu f)}{df} = \mu + f \frac{d\mu}{df} \quad (1.8)$$

From Eq. (1.7) and Eq. (1.8) the group velocity is given by

$$v_g = \frac{c}{\mu'} = 2c \frac{\Lambda^{1/2}(\cos \theta - \Lambda)^{3/2}}{B \cos \theta} = 2c \frac{f^{1/2}(f_H \cos \theta - f)^{3/2}}{f_o f_H \cos \theta} \quad (1.9)$$

Equation (1.9) defines the speed of travel of a beat between two infinite plane waves of slightly different frequency whose wave-normal directions are the same. Helliwell [1965] shows that for frequencies below $\Lambda/2$, the group velocity exceeds the phase velocity, and at higher frequencies it is lower than the phase velocity.

For purely longitudinal propagation the group delay of a whistler-mode signal traveling over a given path is

$$T = \int_{\text{path}} \frac{ds}{v_g} . \quad (1.10)$$

For longitudinal propagation ($\theta = 0^\circ$) in a homogeneous medium, and over a path of length c/B substitution of Eq. (1.9) into Eq. (1.10) gives

$$T = \frac{1}{2\Lambda^{1/2}(1 - \Lambda)^{3/2}} \text{ sec} . \quad (1.11)$$

Helliwell [1965] refers to this normalized form of the time-delay integral as the high-density approximation. He also develops the low-frequency, or Eckersley-Storey approximation, and compares the two results. The latter is only useful for very low values of normalized frequency Λ , and can not be used to describe nose whistlers whose frequency-time curve exhibits both rising and falling branches. By plotting a curve of normalized frequency versus time from Eq. (1.11) one obtains the frequency versus time profile as actually observed in naturally occurring whistlers.

One is sometimes asked if the signals from the vlf stations which propagate in the whistler-mode between the ground transmitters and the satellite make a whistling sound. The answer of course is "no." Since all of the energy from a vlf transmitter is essentially at a single frequency, only one frequency is received and therefore no whistling sound is heard.

Other parts of the magnetoionic theory which are important to this study but not presented above will be developed as needed in later sections.

These include absorption and divergence of the whistler-mode wave and impedance transformation effects. All are discussed in Chapter III. In each case the development begins with the ideas outlined above.

E. THE PROBLEM AND A SOLUTION

When one wishes to study transmission loss and attenuation rates of whistler-mode propagation using whistlers, two major problems arise. First, the exact location of the causative lightning flash is difficult to pinpoint, and secondly, the magnitude of the radiated power is not known. To cope with these and other problems Helliwell and Gehrels [1958] and Helliwell, et al [1962] devised a new type of experiment designed for the study of whistler-mode propagation. The program was based on the use of special pulse signals provided by vlf transmitters of the U. S. Navy operating on frequencies between 15.5 and 22.3 kHz. Tuned narrowband receivers located at Stanford, California; Greenbank, West Virginia; Santiago, Chile; Ushuaia, Argentina; Wellington, New Zealand; and Byrd Station, Antarctica consistently received the direct signal from the transmitters, plus whistler-mode "echo" signals with delays of the order of one second. These experiments provided, for the first time, a reliable source of signals of known characteristics with which to study whistler-mode propagation. Much valuable information was obtained concerning whistler-mode activity such as diurnal and seasonal variations, day-to-day activity, fading characteristics, and group delay distributions. However, the nature of the analysis equipment did not allow quantitative amplitude information to be obtained. Hence, attenuation rates in the whistler-mode remained unspecified.

With the advent of scientific rocket probes and low-altitude satellites, another dimension was added to the study of whistler-mode propagation. Using vlf stations as the source, and with calibrated receivers aboard, these experiments began providing detailed information concerning absorption of vlf signals as they penetrated the ionosphere. The results of such studies are reported by several researchers including Lomax [1961], Leiphart, et al [1962], Maeda, et al [1965], Cartwright [1964], Rorden, et al [1964], Mlodnosky, et al [1965] and Orsak, et al [1965].

While the above studies contributed significant new information concerning absorption, they all were limited to altitudes of approximately 1000 km or less. The launching of the first Orbiting Geophysical Observatory (OGO-I) from Cape Kennedy at 0123 UT on September 5, 1964, removed this restriction and for the first time a controlled experiment in whistler-mode propagation involving attenuation along a magnetospheric path was underway. The OGO-I data provided new information on whistler-mode transmission loss by supplying accurate amplitude measurements over major portions of the path. Now for the first time a vlf receiver was at a known location in the magnetosphere receiving whistler-mode signals from a known source on the ground. By utilizing the existing magnetoionic theory and the theoretical results of earlier researchers, it is possible to calculate the intensity of vlf signals one would expect to find at the satellite. These calculations may then be compared to the intensities measured by OGO-I, thus allowing an experimental test of the theory.

The launching of OGO-II into a low altitude polar orbit provided another valuable input to the solution. The two satellites effectively subdivide the total path into two main parts: (1) the earth-ionosphere waveguide loss, the boundary and excitation loss, and the absorption loss through the ionosphere to the altitudes of OGO-II, and (2) losses due to divergence of the signal between OGO-II and the higher altitudes of OGO-I plus any additional absorption above OGO-II.

With this major subdivision of the total loss, and with accurate amplitude information available from both satellites the total-path whistler-mode transmission loss problem may be approached more confidently than was before possible. To treat this problem utilizing these new data is the objective of this research.

Predicted signal power at the satellite has been computed on the basis of a model path having three major sources of loss: (1) excitation of the whistler-mode at the foot of the field line passing through the satellite, (2) absorption of the signal in passing through the lower and upper ionosphere, (3) divergence within the magnetosphere. These calculated values are then compared to the measured values, and refinements to improve the model are suggested. It should be noted that item (1) includes the earth-ionosphere waveguide loss between the vlf transmitter and the foot of the

field line as well as the losses due to reflection at the boundary. The reasons for this are discussed in Chapter III.

F. CONTRIBUTIONS OF THE PRESENT WORK

Perhaps the most important contribution of this work is the demonstration by a controlled experiment that in general the intensity of vlf whistler-mode signals in the magnetosphere may be predicted with a surprising degree of accuracy by existing theory. This is to say that our present understanding of the major features of whistler-mode propagation, which has been based largely on theoretical developments and experimental observations of naturally occurring phenomena, is apparently correct. Figure 35 is probably the best demonstration of how closely the predictions (calculations) fit the measurements over an extensive magnetospheric path. While all of the measurements do not agree this well with the calculations, the agreement is in general surprisingly good. Most of the discrepancies may be explained by reasonable arguments based on related phenomena already reported in the literature.

Other important contributions have arisen in the course of this study. These are listed as new observations in Chapter VIII and include:

1. A northern hemisphere latitudinal cutoff of vlf signals which originate in the northern hemisphere.
2. Strong enhancements of vlf signals near the antipodes of vlf transmitters at altitudes of approximately 1,000 km.
3. A pronounced dip in the intensity of vlf signals over the geomagnetic equator.
4. A band, or ring, of intense noise at 18 kHz around both polar regions.

II. THE OGO-I EXPERIMENT

A. THE SATELLITE

The first Orbiting Geophysical Observatory (OGO-I) was launched from Cape Kennedy at 0123 UT on 5 September 1964, and at that time, was probably the most sophisticated multipurpose satellite ever launched. Weighing approximately 1,000 pounds, the basic spacecraft is a rectangular box about three by three by six feet. Protruding from it are various booms, antennas, attitude control jets and solar panels. With the booms fully extended the satellite is approximately 59 feet long, and 50 feet wide. The general configuration of the spacecraft is shown in Fig. 3.

OGO-I was the first in a series of six orbiting geophysical observatories planned by the National Aeronautics and Space Administration (NASA). OGO-I, OGO-II, and OGO-III are now in orbit, and in so far as the vlf experiment is concerned, they all carry essentially the same equipment. OGO-II was launched into a low-altitude polar orbit at 1312 UT on 14 October 1965, and OGO-III was launched at 0248 UT on 7 June 1966 into a high altitude equatorial orbit similar to the orbit of OGO-I.

All of the data for this report came from OGO-I and OGO-II. The OGO-I data are presented in Chapter IV, and the OGO-II data in Chapter VI. Data from both satellites are then combined and utilized to study the total-path whistler-mode transmission loss problem in Chapter VII.

B. THE ORBIT

The OGO-I orbit is highly elliptical, with an apogee altitude of more than one-third of the distance to the moon's orbit. Initial perigee altitude, which has been steadily increasing at a rate of approximately 5,000 km per year, was 280 km. The inclination of the orbit at launch was 31 degrees. This parameter is also steadily increasing, at a rate of approximately 18 degrees per year. The period of the orbit is very close to 64 hours (63 hours, 59 minutes); therefore the earth rotates an even eight times for every three OGO-I revolutions which bring the satellite to an almost identical position with respect to the earth and its magnetic field every eight days.

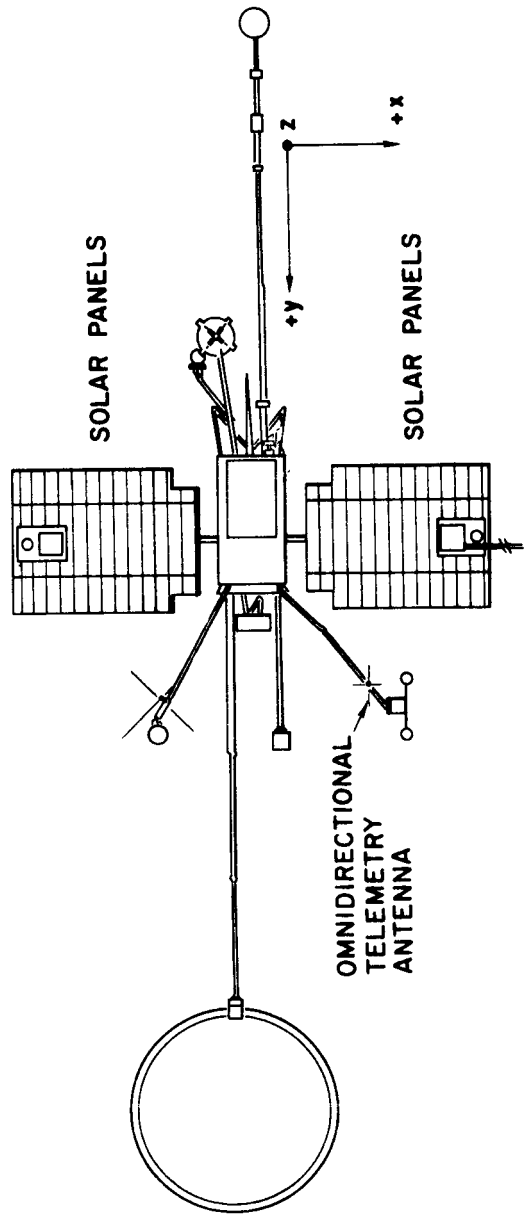
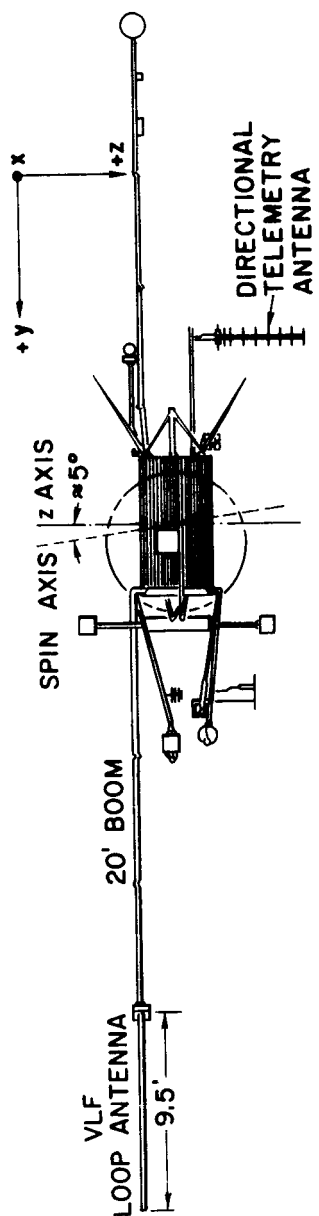


FIG. 3. THE GENERAL CONFIGURATION OF THE OGO-I SATELLITE SHOWING THE POSITION OF THE VLF LOOP ANTENNA AND THE COORDINATE SYSTEM.

Table 1 shows all of the pertinent OGO-I definitive orbital parameters which were kindly supplied by Dr. George H. Ludwig, EGO Project Scientist at Goddard Space Flight Center.

C. EQUIPMENT

OGO-I carries, among a total of 20 experiments, four vlf receivers covering the frequency range 0.2 to 100 kHz [Rorden, et al, 1966b]. All of the vlf receivers are driven by one 9.5 foot inflatable toroidal loop antenna and a broadband pre-amplifier mounted at the end of a 20 foot boom. Three of the receivers are step-frequency superheterodynes whose local oscillator frequencies are derived from a common source which operates on any one of 256 discrete frequencies between 112 and 200 kHz. The Band 1 receiver covers 0.131 to 1.59 kHz with 50 Hz bandwidth, the Band 2 receiver covers 1.048 to 12.718 kHz with 160 Hz bandwidth, and the Band 3 receiver covers 8.387 to 101.742 kHz with 500 Hz bandwidth [L. H. Rorden, private communication]. The fourth receiver is broadband, covering 0.3 to 12.5 kHz.

Two modes of operation are possible for the Band 1, 2, and 3 receivers: (1) the "sweeping" mode, where each receiver scans its entire frequency range in a time period determined by the data rate (every 2.3 seconds in the high bit rate); and (2) the fixed-frequency or "narrowband" mode in which the sweeping is stopped and the receivers are tuned to any desired fixed frequency by the proper sequence of commands from the ground.

All of the data for this research have been obtained in the latter mode with the Band 3 receiver tuned to either NPG (18.6 kHz) or NAA (17.8 kHz).

The output of each receiver is a voltage representing the log-compressed amplitude of the received signal which provides a full 90 db dynamic range.

On every 16th sweep, a spectrum of all 1 kHz harmonics is injected into the antenna to provide accurate amplitude and frequency calibration.

The level of calibration and the method of insertion is alternated according to a fixed pattern: high voltage, high current, low voltage, low current, etc. Comparative amplitude calibration measurements have

TABLE 1
OGO I DEFINITIVE ORBITAL PARAMETERS

EPOCH	9/5/64	10/14/64	11/13/64	12/12/64	2/6/65	3/13/65	4/17/65	5/27/65	6/22/65	7/27/65	8/25/65	9/26/65	10/31/65	12/12/65	12/26/65	1/24/66	2/23/66
DAY	0657.00	2351.20	1009.22	1559.13	1823.00	1059.00	0244.00	0244.00	1840.00	1057.00	1916.00	1930.00	1143.50	1100.00	1200.00	1955.00	0428.00
SEMI-MAJOR AXIS KILOMETERS	081222.90 050469.47 0.91802	081225.69 050471.20 0.90779	081250.04 050489.33 0.90261	081249.23 050485.83 0.89970	081256.47 050490.33 0.89965	081256.35 050490.25 0.87931	081255.25 050491.57 0.86883	081254.17 050488.90 0.86813	081250.82 050493.03 0.85723	081259.86 050492.44 0.85069	081224.62 050470.54 0.84007	081261.31 050493.34 0.82679	081244.22 050482.72 0.81775	081243.53 050482.29 0.81049	081256.53 050490.37 0.80723	081234.68 050476.79 0.79757	081234.07 050476.41 0.78495
ECCENTRICITY	031.116	032.131	032.947	034.375	038.188	039.466	039.596	040.717	042.124	044.110	045.125	045.231	045.285	046.169	047.302	048.536	049.058
INCLINATION DEGREES	015.060	015.583	015.993	016.172	016.033	016.045	016.052	016.058	016.067	016.075	016.082	016.086	016.089	016.091	016.092	016.093	016.094
MEAN ANOMALY DEGREES	313.173	317.201	319.727	322.759	328.673	330.696	331.591	332.886	334.150	335.810	336.866	337.449	337.676	338.095	338.708	339.567	340.180
ARGUMENT OF PERIGEE DEGREES	00.0728	00.0565	00.0496	00.0447	00.0398	00.0358	00.0320	00.0288	00.0268	00.0259	00.0251	00.0244	00.0238	00.0232	00.0227	00.0222	00.0218
DEG. PER DAY	168.411	164.719	162.159	158.965	152.862	150.829	149.860	148.072	146.509	144.638	143.624	143.061	142.479	141.611	140.752	139.863	139.347
R. A. OF ASCEND. NODE DEGREES	-00.0468	-00.0370	-00.0330	-00.0307	-00.0264	-00.0202	-00.0172	-00.0153	-00.0142	-00.0127	-00.0110	-00.0095	-00.0086	-00.0079	-00.0075	-00.0067	-00.0060
ANOMALISTIC PERIOD MINUTES	3839.39718	3839.59498	3841.38534	3841.26626	3841.77784	3841.76948	3841.61513	3841.69172	3842.08620	3842.01853	3839.51940	3842.12153	3840.90918	3840.86016	3841.76247	3840.23285	3840.18968
MIN. PER DAY	0.00000	0.00000	-0.00584	-0.00250	0.00000	-0.00258	0.00000	0.00000	-0.00239	-0.00005	-0.00262	-0.00091	-0.00227	0.00000	0.00000	-0.00122	-0.00003
HEIGHT OF PERIGEE KILOMETERS	000280.53	001111.55	001534.60	001771.31	002588.45	003428.12	004336.79	004929.92	005223.17	005754.55	006612.02	007696.89	008428.50	009018.39	009285.57	010065.79	011091.26
MILES	000174.31	000690.68	000936.00	001100.64	001608.38	002130.13	002694.75	003063.30	003245.52	003576.70	004108.51	004782.61	005237.22	005603.76	005769.77	006254.58	006891.78
HEIGHT OF APOGEE KILOMETERS	149408.48	148583.05	148210.50	147970.36	147167.72	146327.80	145414.79	144823.81	144541.69	144008.40	143080.44	142068.97	141303.16	140711.89	140470.73	139646.80	138620.11
MILES	092837.94	092325.04	092088.00	091944.34	091445.60	090923.70	090556.38	089989.17	089813.86	089482.49	088905.89	088277.39	087801.54	087434.14	087284.29	086772.33	086134.37
VELOCITY AT PERIGEE KM. PER HOUR	038575	036275	035244	034702	032996	031465	030012	029157	028758	028072	027051	025894	025184	024414	023764	022975	022168
MI. PER HOUR	023970	022540	021900	021563	020503	019551	018648	018117	017869	017445	016809	016090	015648	015315	014766	014276	013720
VELOCITY AT APOGEE KM. PER HOUR	001649	001753	001804	01832	001927	002021	002119	002181	002211	002265	002351	002455	002525	002580	002604	002676	002768
MI. PER HOUR	001025	001089	001121	001139	001197	001256	001316	001355	001374	001407	001461	001526	001569	001603	001618	001663	001720
GEOC. LAT. OF PERIGEE DEGREES	-22.1400	-21.183	-20.583	-19.979	-18.750	-18.125	-17.692	-17.296	-17.005	-16.571	-16.165	-15.797	-15.688	-15.612	-15.479	-15.166	-14.840

been made periodically from pre-launch to the present time and it is well established that the calibration level has not changed appreciably.

It is believed that the OGO-I equipment capability allows one to determine amplitudes of vlf signals to an accuracy of ± 1 db. However, in the final analysis a more realistic figure is probably ± 2 or 3 db due to the difficulty of accurately scaling the data from records produced from the telemetry signals.

Methods of data reduction and further comments on accuracy are presented in sections D and E.

D. OBTAINING THE DATA

It was planned to have OGO-I earth-stabilized with the z-axis (see Fig. 3) always pointing towards the earth and the solar arrays always pointing towards the sun, but difficulties that appeared immediately after launch prevented this. As a result the satellite became spin stabilized, spinning at a rate of approximately 5 rpm. Although the spin axis orientation is not known precisely, independent measurements show it to be less than 5 degrees from the z-axis. Values of 42.5 degrees in right ascension and -9 degrees in declination have been adopted as the most probable spin axis orientation. The spin axis is sufficiently parallel to the null axis of the loop antenna that the spin causes no observable effect in the vlf data used in the present study.

The unplanned spinning and mis-orientation did however create two problems for the vlf experiment which need explanation. First, the spacecraft orientation prevented the solar arrays from always pointing towards the sun. This reduced the amount of power available for equipment operation. However, periodic slewing of the solar arrays by command from the ground made at least some power available at all times, except for two "seasons" each year of about two months duration each, and approximately centered on 1 February and 1 August. This handicap resulted in the loss of data for these periods of time.

The second problem involves the spacecraft's two telemetry antennas; one a directional and the other a non-directional antenna. Improper orientation decreased the telemetry signal levels from the satellite far

below that expected.

Because the omni-directional antenna is eclipsed by the observatory once every 12 seconds the directional antenna is normally used even though it is pointed away from the earth during most of the orbit and therefore provides much lower signal levels than the omni-directional antenna.

The major effect of this condition is to require the use of more sensitive and elaborate ground receiving equipment than would normally have been necessary. For instance, at the Stanford University field site instead of being able to utilize modest gain equipment with a simple antenna it was necessary to use the 150-foot diameter parabolic dish antenna and associated equipment to provide adequate signal-to-noise ratio.

Two separate telemetry systems are used on OGO-I. The first transmits digital data to the ground using pulse code modulation. This is referred to as the PCM telemetry. The second system transmits ac voltages in the frequency range 0.3 to 100 kHz by using them to phase-modulate a second transmitter. This system is referred to as the "special purpose" (SP) telemetry. Vlf data is returned to satellite monitoring stations via either telemetry system. Data from the PCM telemetry system appear on a strip-chart recording such as shown in Figs. 4 through 15, or on a 16mm film record as shown in Fig. 16. Typical vlf data from the SP telemetry are shown in Figs. 17 through 22.

Both telemetry transmitters operate near 400 MHz and may be switched separately to either the directional or the omni-directional antenna.

The satellite is capable of recognizing more than 150 commands from the ground. This allows the observatory to be configured in a variety of modes, and to operate usefully even though some systems fail.

Two tape recorders are aboard and available for data storage which permits delayed transmission from another part of the orbit.

It is not proposed at this point to discuss in detail the data shown in Figs. 4 through 22, although these data have been carefully chosen to illustrate important analysis points in later chapters.

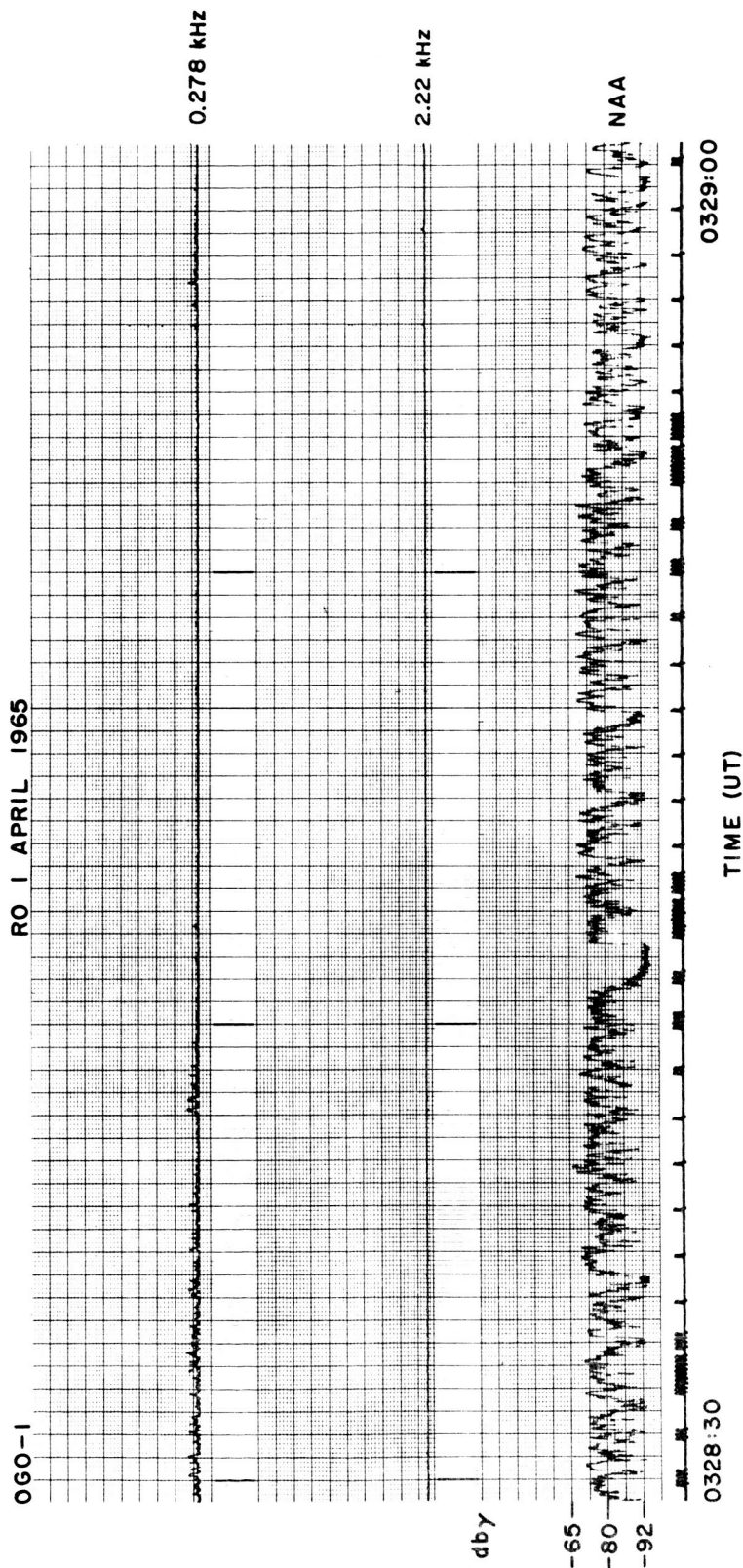


FIG. 4. DATA FROM THE PCM TELEMETRY, SHOWING THE SIMULTANEOUS OUTPUTS OF THE BAND 1, BAND 2, AND BAND 3 RECEIVERS. The bottom trace is serial decimal time. OGO-I positional parameters are approximately: $R = 18.396$ kkm, $\phi = 4.27^\circ$, $\lambda = 41.6^\circ$, $d_e = 1.871$ kkm, $d_f = 12.377$ kkm, $L = 5.22$, $f_H = 53.2$ kHz.

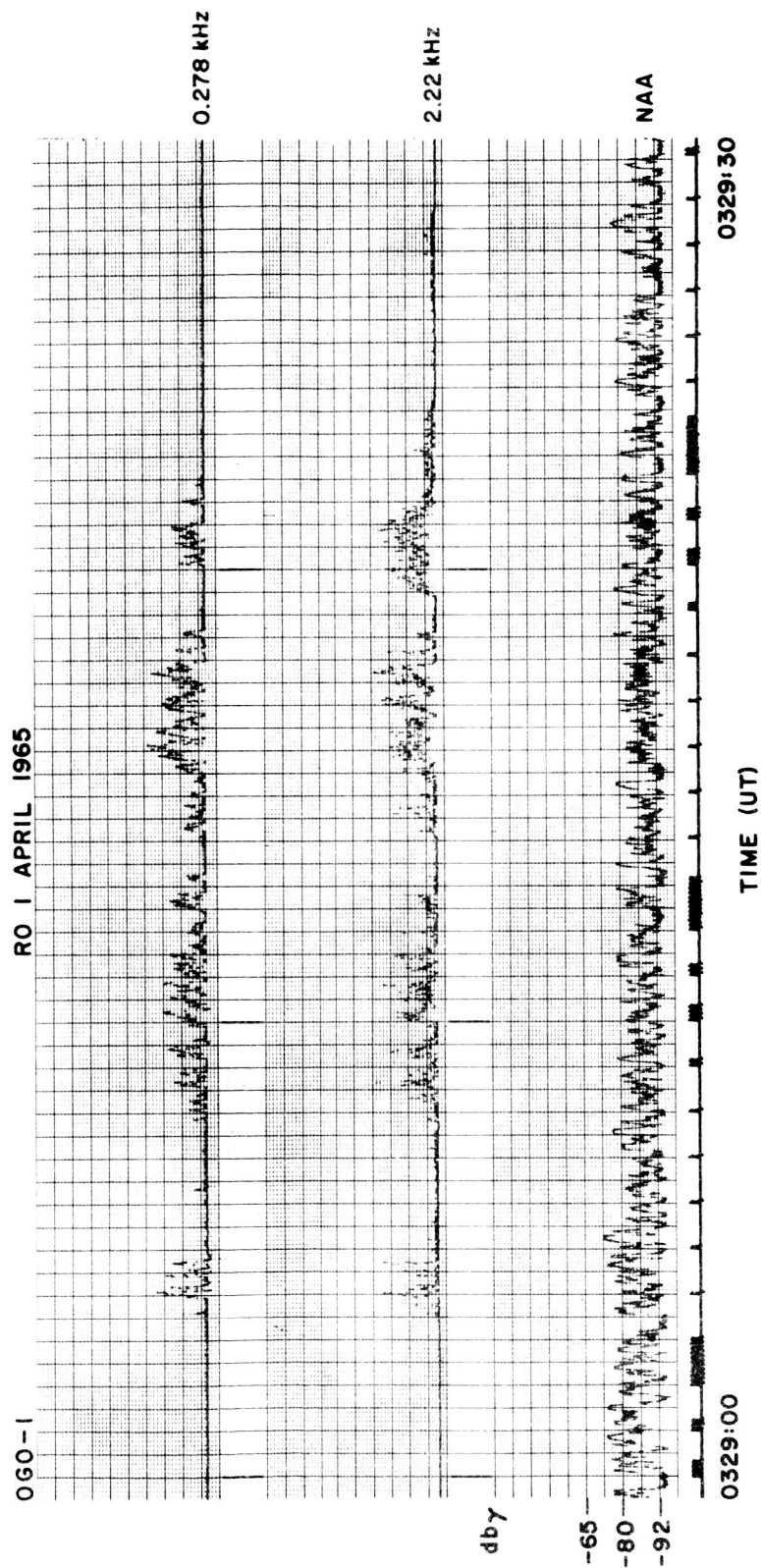


FIG. 5. A CONTINUATION OF THE DATA SHOWN IN FIG. 4. Note the noise bursts in Bands 1 and 2 that are less evident in Band 3.

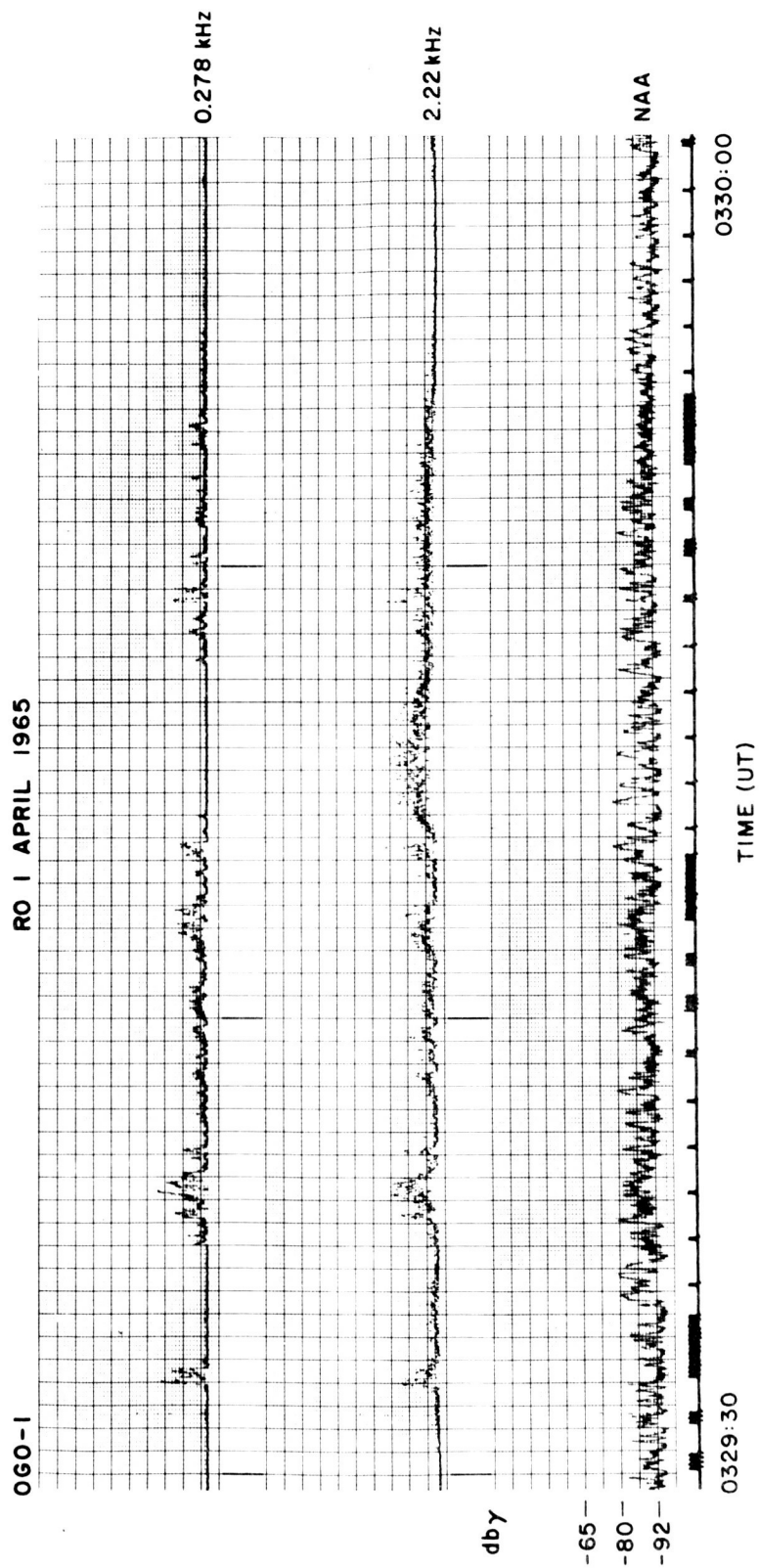


FIG. 6. A CONTINUATION OF THE DATA SHOWN IN FIGS. 4 AND 5. Note the 3 second noise burst in Band 2 which is not seen in Band 1, and only questionably in Band 3.

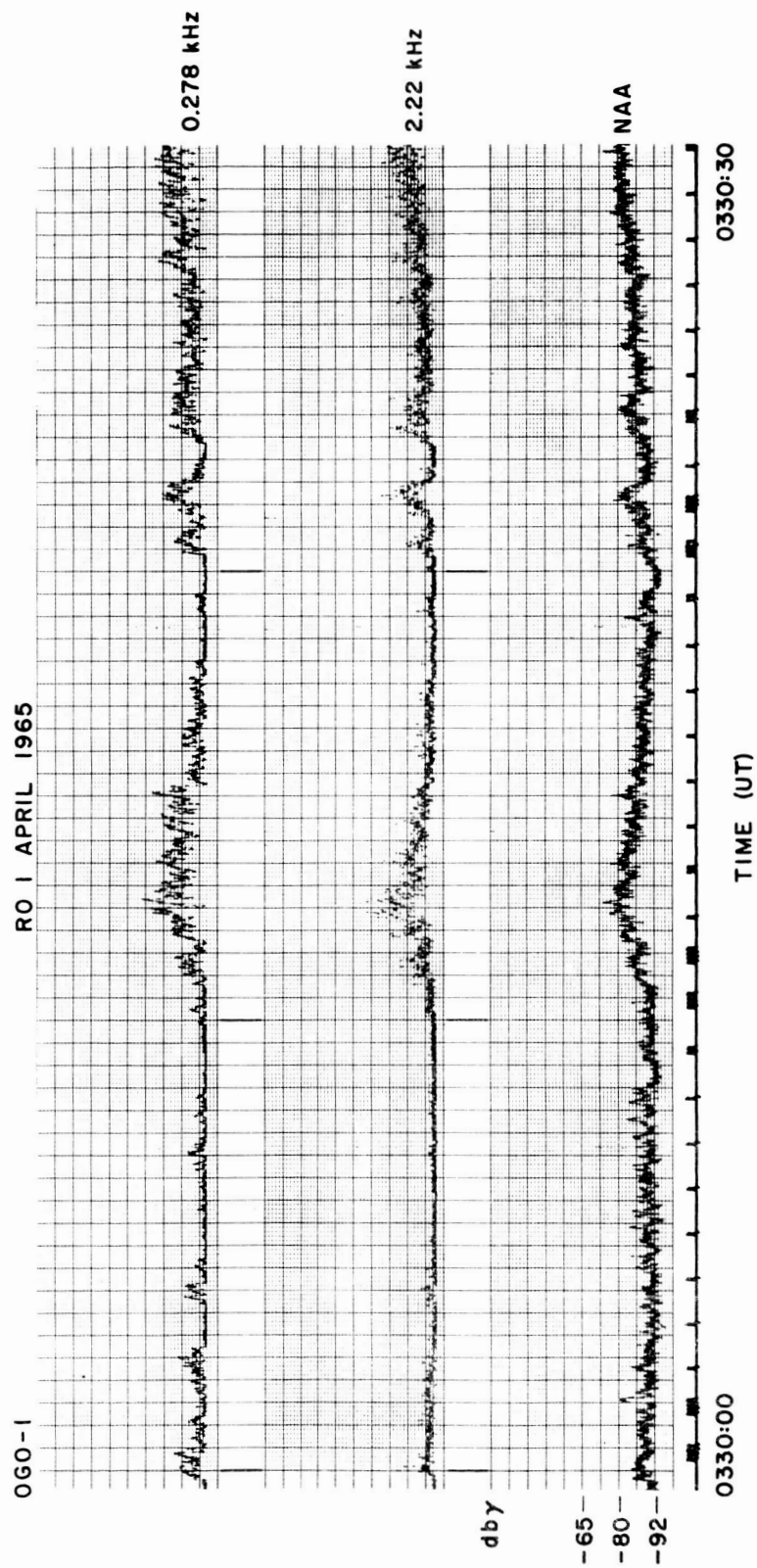


FIG. 7. A CONTINUATION OF THE DATA SHOWN IN FIGS. 4, 5 AND 6. Here all three bands show synchronous noise.

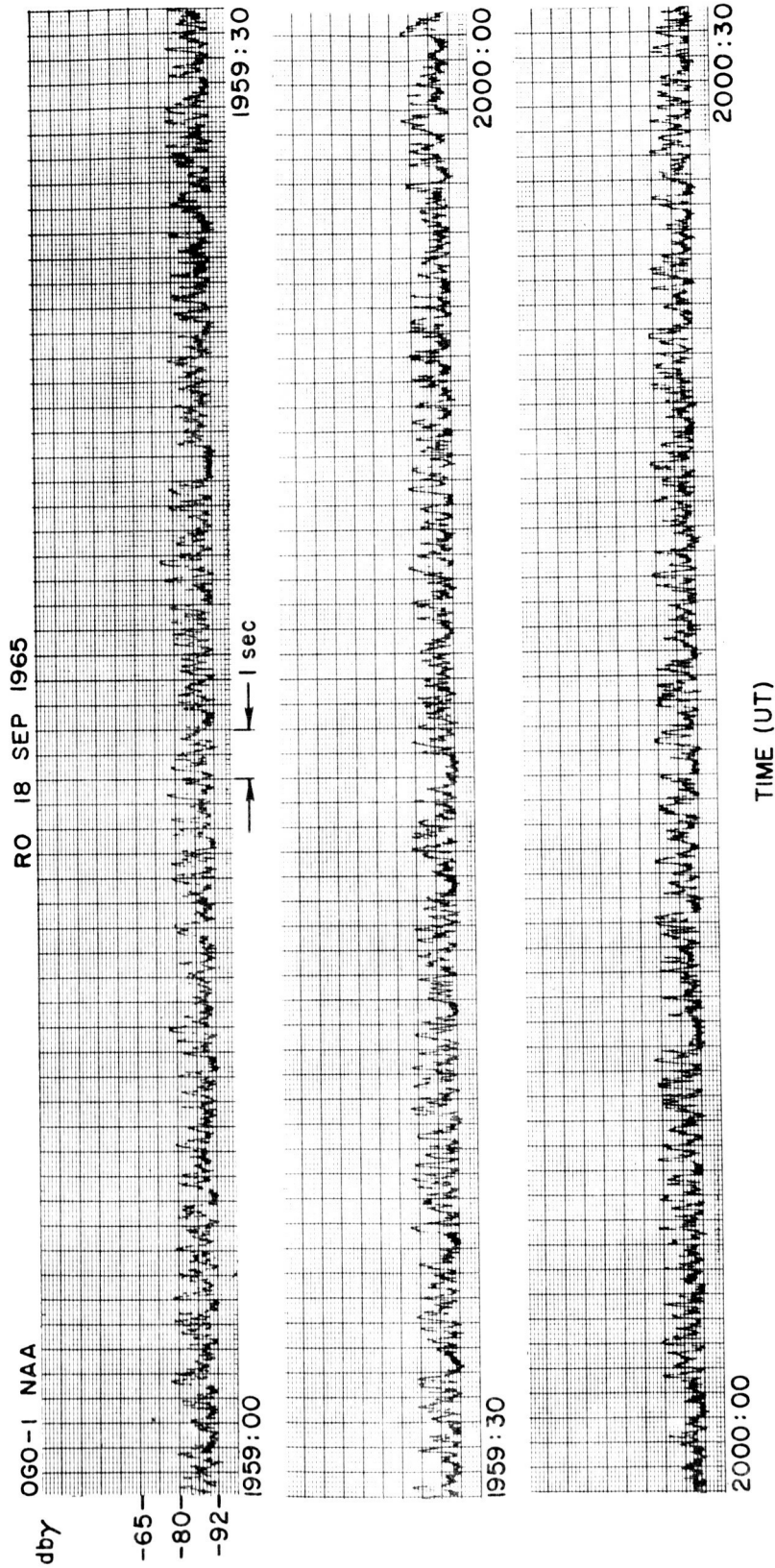


FIG. 8. DATA FROM THE PCM TELEMETRY SHOWING THE OUTPUT OF THE BAND 3 RECEIVER. OGO-I positional parameters are approximately: $R = 17.021$ kkm, $\phi = 27.2^\circ$, $\lambda = -130.6^\circ$, $d_e = 4.011$ kkm, $d_f = 12.02$ kkm, $L = 3.32$, $f_H = 59.6$ kHz.

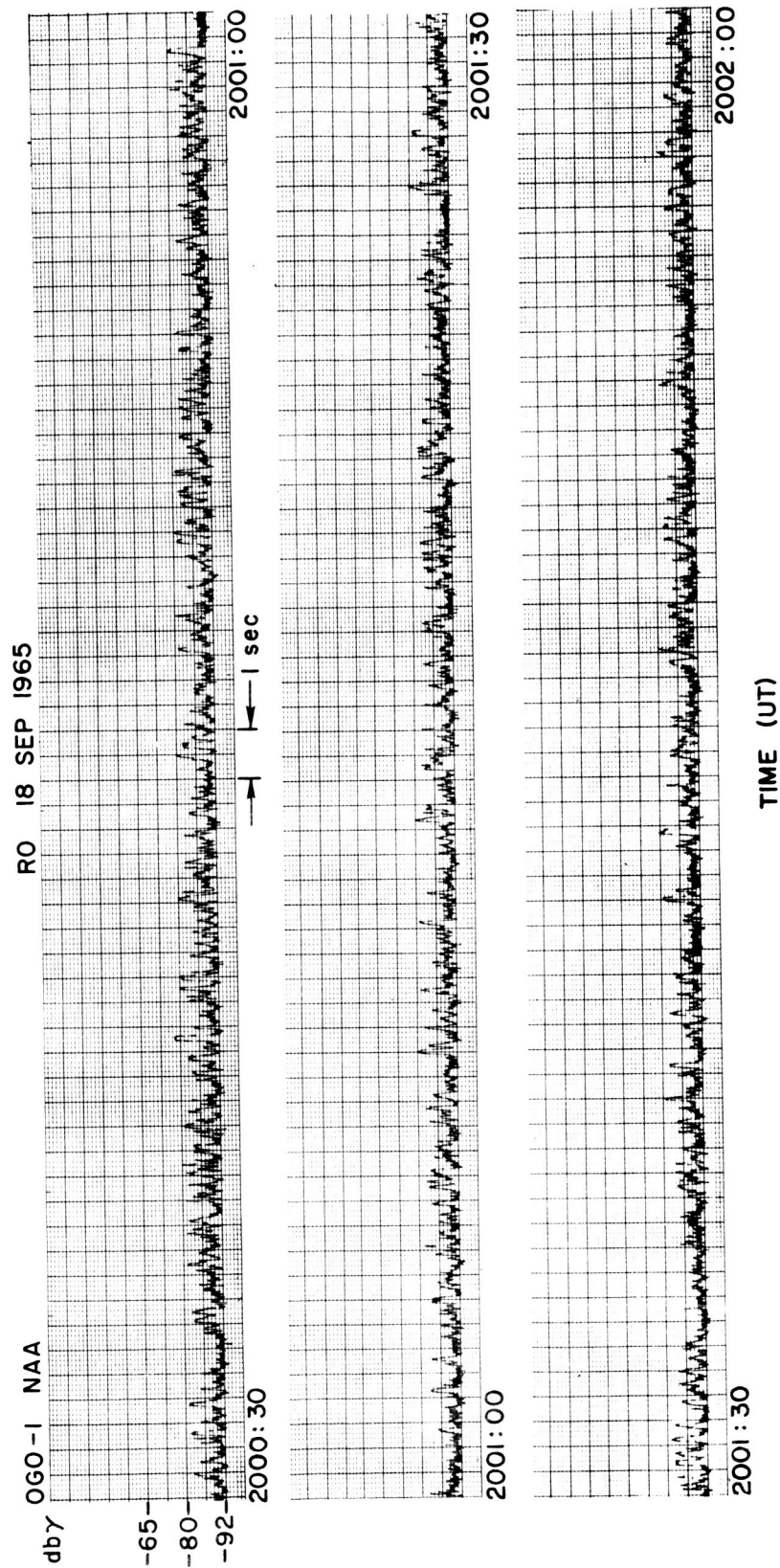


FIG. 9. A CONTINUATION OF THE DATA SHOWN IN FIG. 8. Note that the NAA signals gradually fade out.

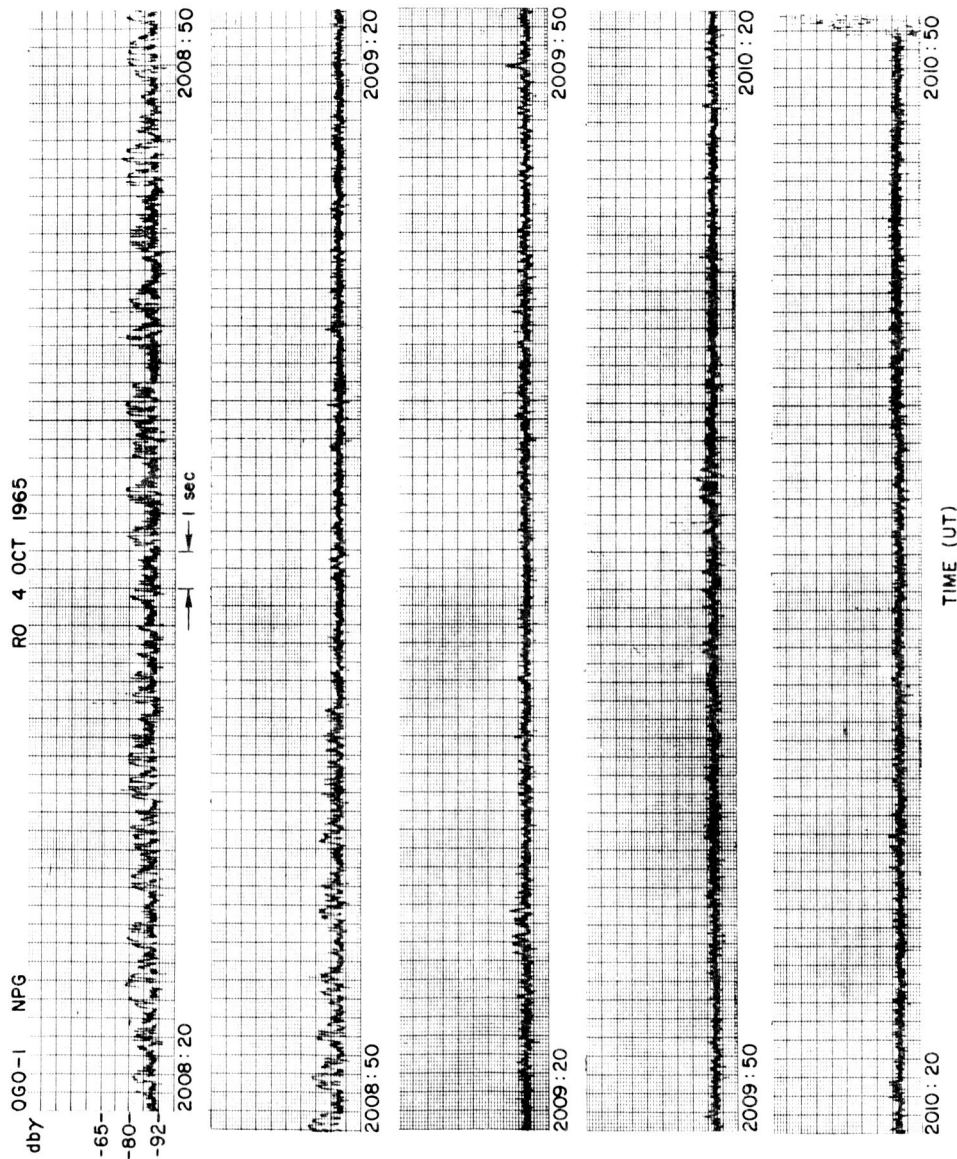


FIG. 10. DATA FROM THE PCM TELEMETRY SHOWING THE BAND 3 OUTPUT. OGO-I positional parameters are approximately: $R = 18.879$ kkm, $\phi = 30.1^\circ$, $\lambda = -143.1^\circ$, $d_e = 1.148$ kkm, $d_f = 13.885$ kkm, $L = 3.88$, $f_H = 44.9$ kHz.

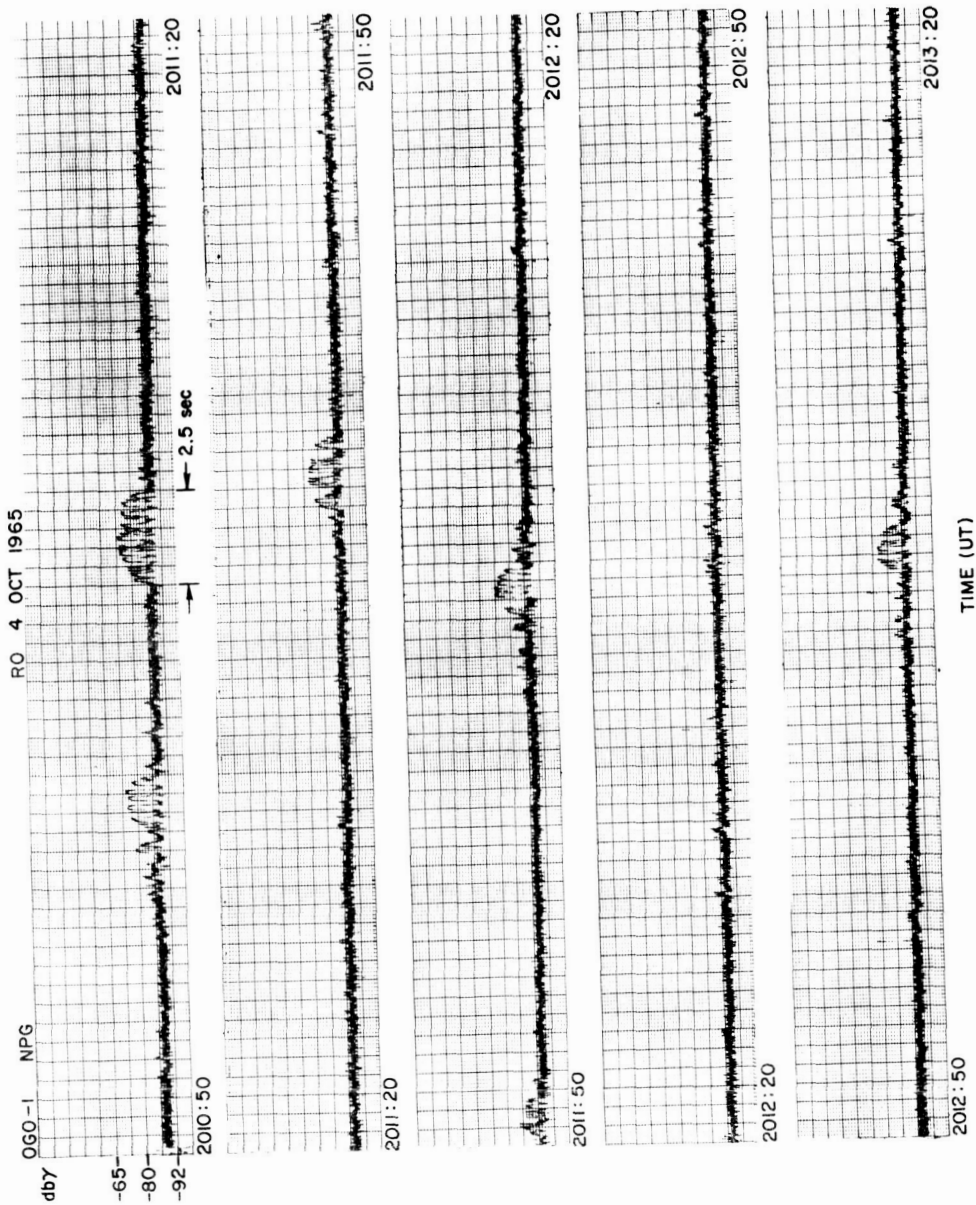


FIG. 11. A CONTINUATION OF THE DATA SHOWN IN FIG. 10. Note the beginning of the discrete bursts of signal from NPG.

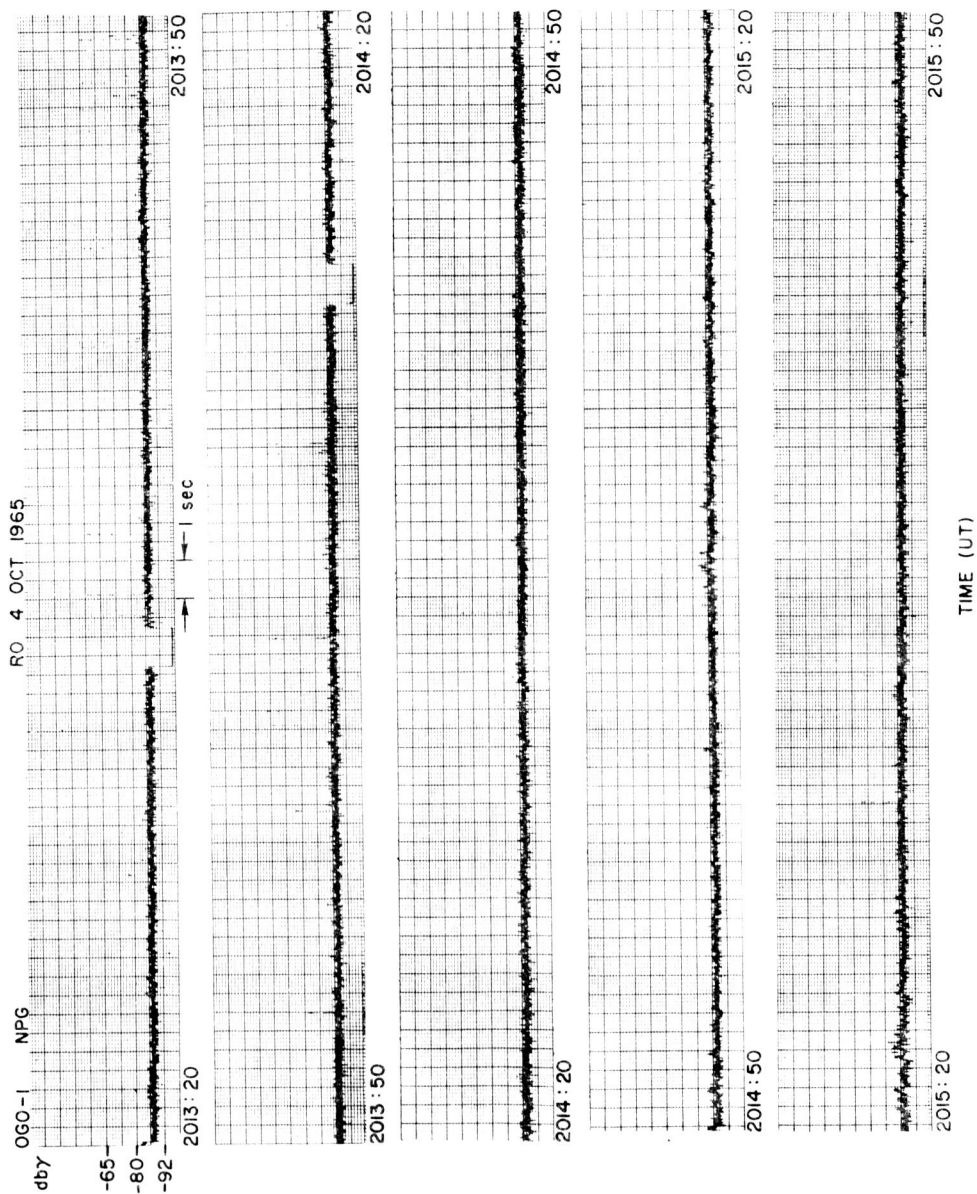


FIG. 12. A CONTINUATION OF THE DATA SHOWN IN FIGS. 10 AND 11 SHOWING A TOTAL ABSENCE OF SIGNALS FROM NPG, ALTHOUGH NPG WAS TRANSMITTING DURING THIS TIME.

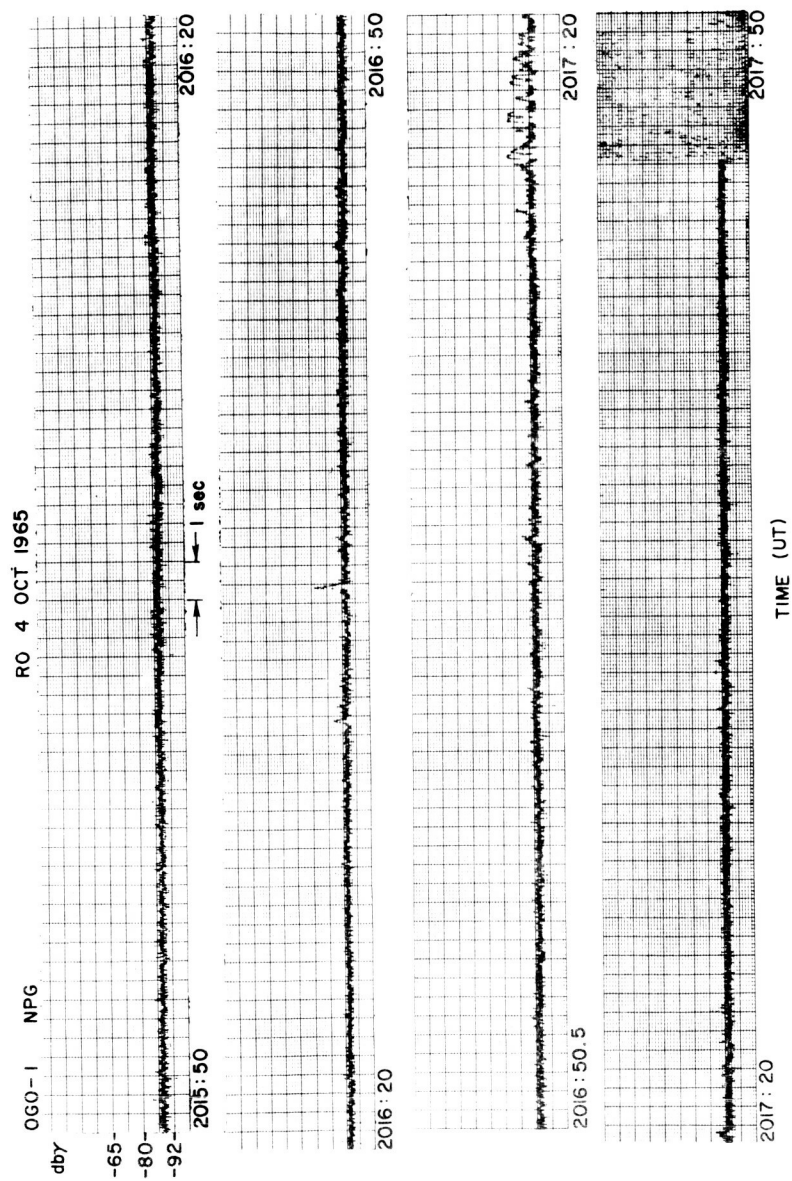


FIG. 13. A CONTINUATION OF THE DATA SHOWN IN FIGS. 10, 11 AND 12. Note the single discrete burst of signal from NPG beginning at 2017:16 UT.

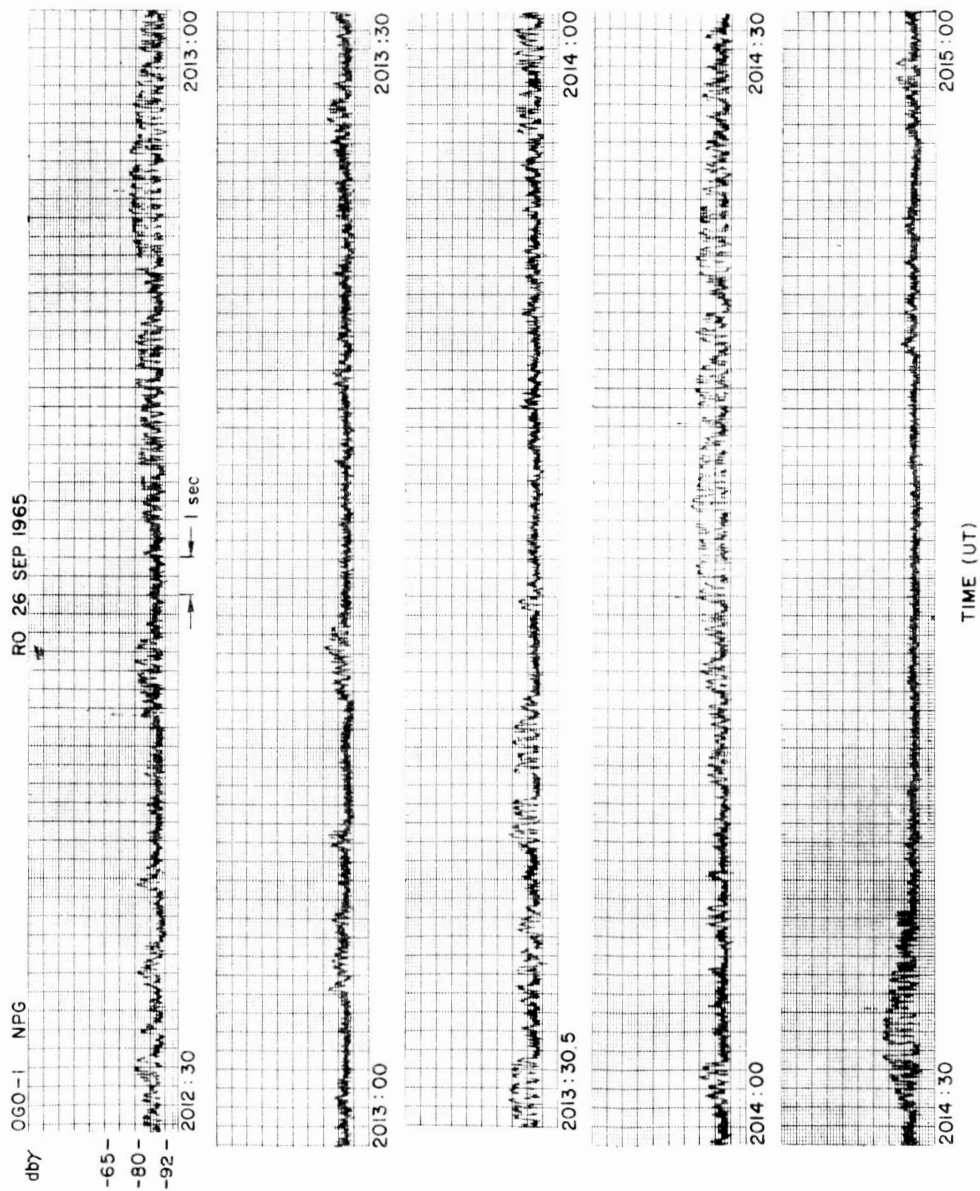


FIG. 14. DATA FROM THE PCM TELEMETRY SHOWING THE OUTPUT OF BAND 3. OGO-I positional parameters are approximately: $R = 18.5$ kkm, $\phi = 30^\circ$, $\lambda = 135^\circ$, $d_e = 0.85$ kkm, $d_f = 13.5$ kkm, $L = 4.2$, $f_H = 45$ kHz.

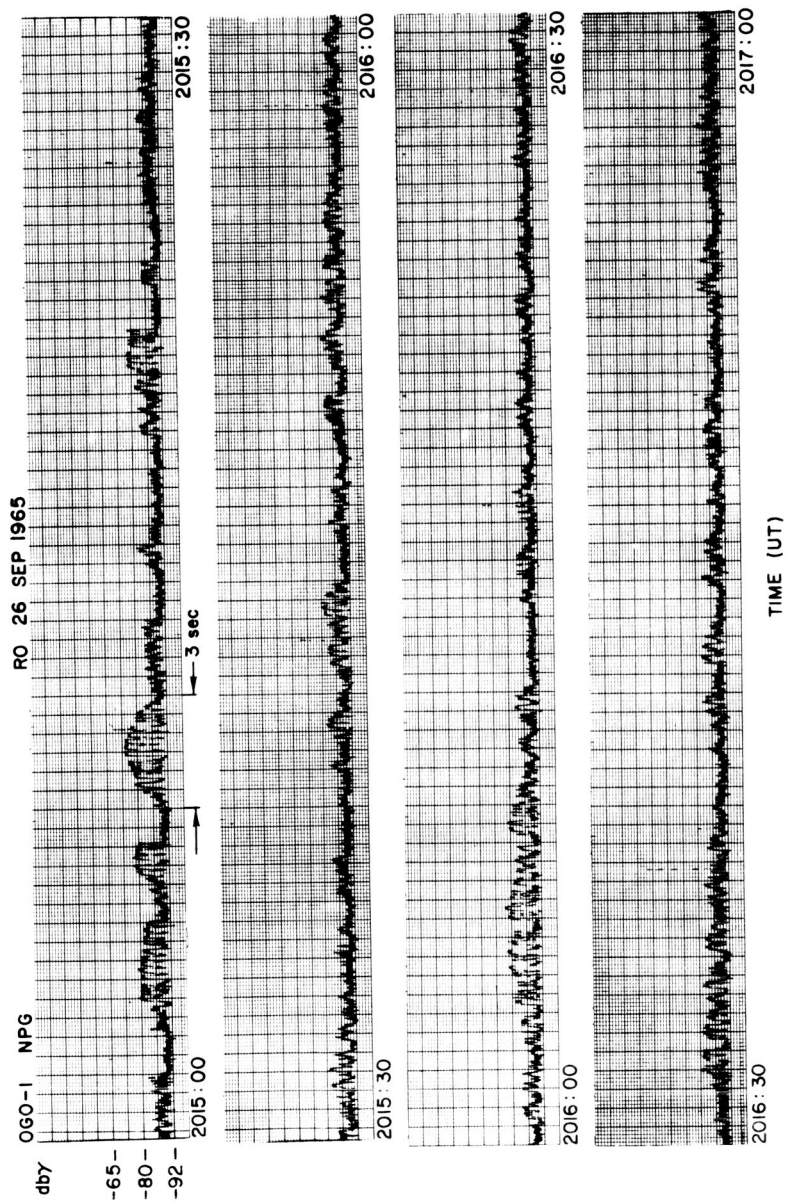


FIG. 15. A CONTINUATION OF THE DATA SHOWN IN FIG. 14. Note the signal bursts followed by gradual fade out.

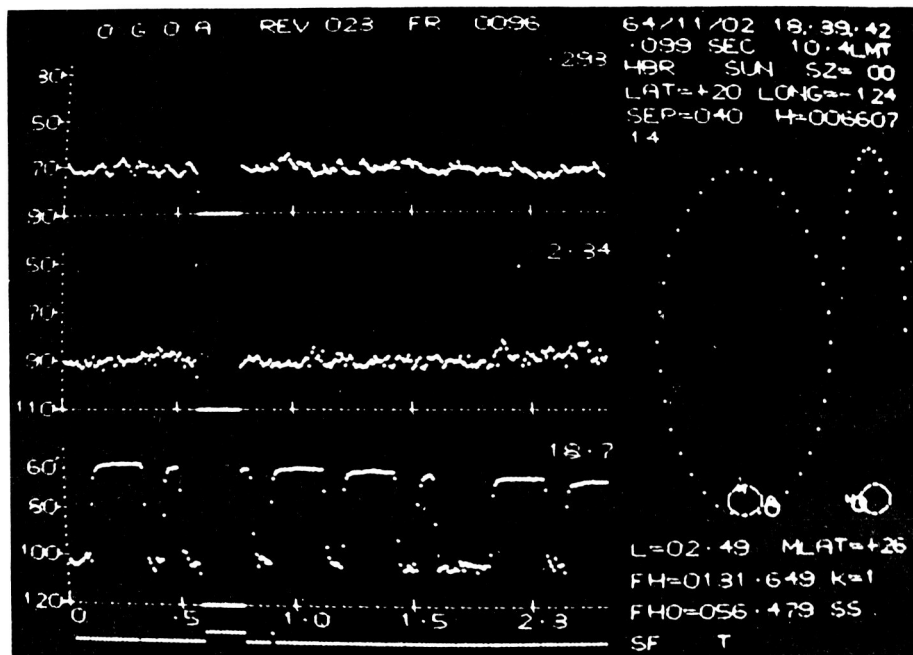


FIG. 16. A 16mm FRAME OF DATA FROM THE OGO-I PCM TELEMETRY AS PREPARED BY STANFORD RESEARCH INSTITUTE. The data are displayed on a cathode ray tube and then photographed. Each frame covers 2.3 seconds of real time. Note the satellite positional parameters contained on each frame, and also the base-line interruptions which serve as "bad data" indicators.

Group delays of vlf signals propagating in the whistler mode are obtained from records such as shown in Figs. 17 and 18, however there is only a limited amount of such data available. A striking feature of the group delay data is the large range of delays observed. For instance, between 1842 UT and 1852 UT on 2 Nov. 1964 group delays varied between 74 ms and 154 ms. The ray tracing results in Chapter VII indicate that delays of this magnitude are reasonable for this satellite location.

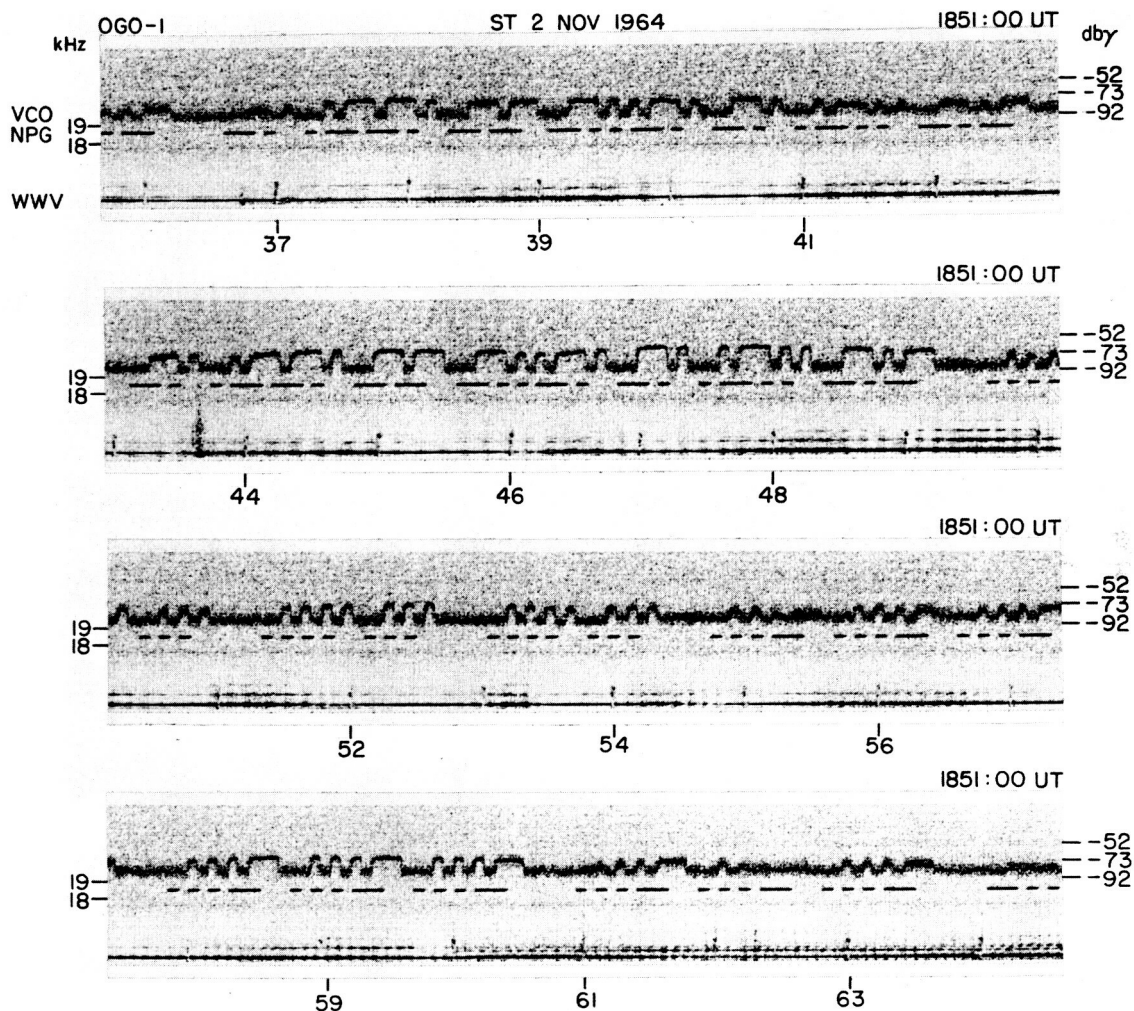


FIG. 17. A TYPICAL DISPLAY OF DATA FROM THE SATELLITE VCO VIA THE SPECIAL PURPOSE TELEMETRY AS PREPARED BY THE STANFORD RADIOSCIENCE LABORATORY. The NPG and WWV signals are obtained from receivers at Stanford and are inserted simultaneously as the VCO signal is being received from the satellite telemetry. Note the obvious time delay between the NPG ground signal received at Stanford and the same NPG signal received at the satellite via the whistler-mode.

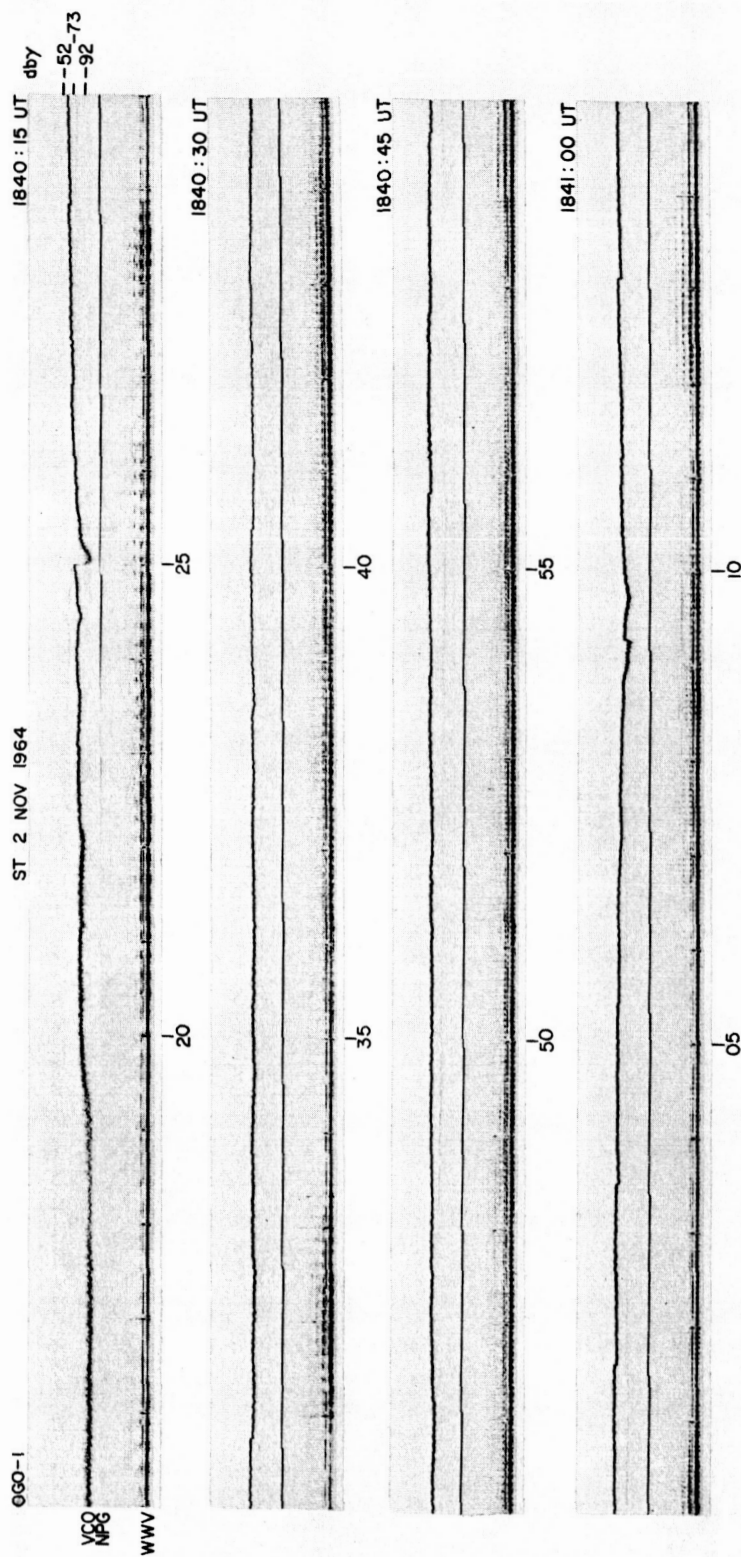


FIG. 18. A LONG PERIOD OF CW (FM) TRANSMISSION FROM NPG AS INDICATED BY THE OGO-I SATELLITE VCO VIA THE SPECIAL PURPOSE TELEMETRY. The NPG and WWV signals are obtained from receivers at Stanford and are inserted simultaneously as the VCO signal is being received from the satellite telemetry. The satellite positional parameters for Figs. 18 through 22 are shown in Fig. 44.

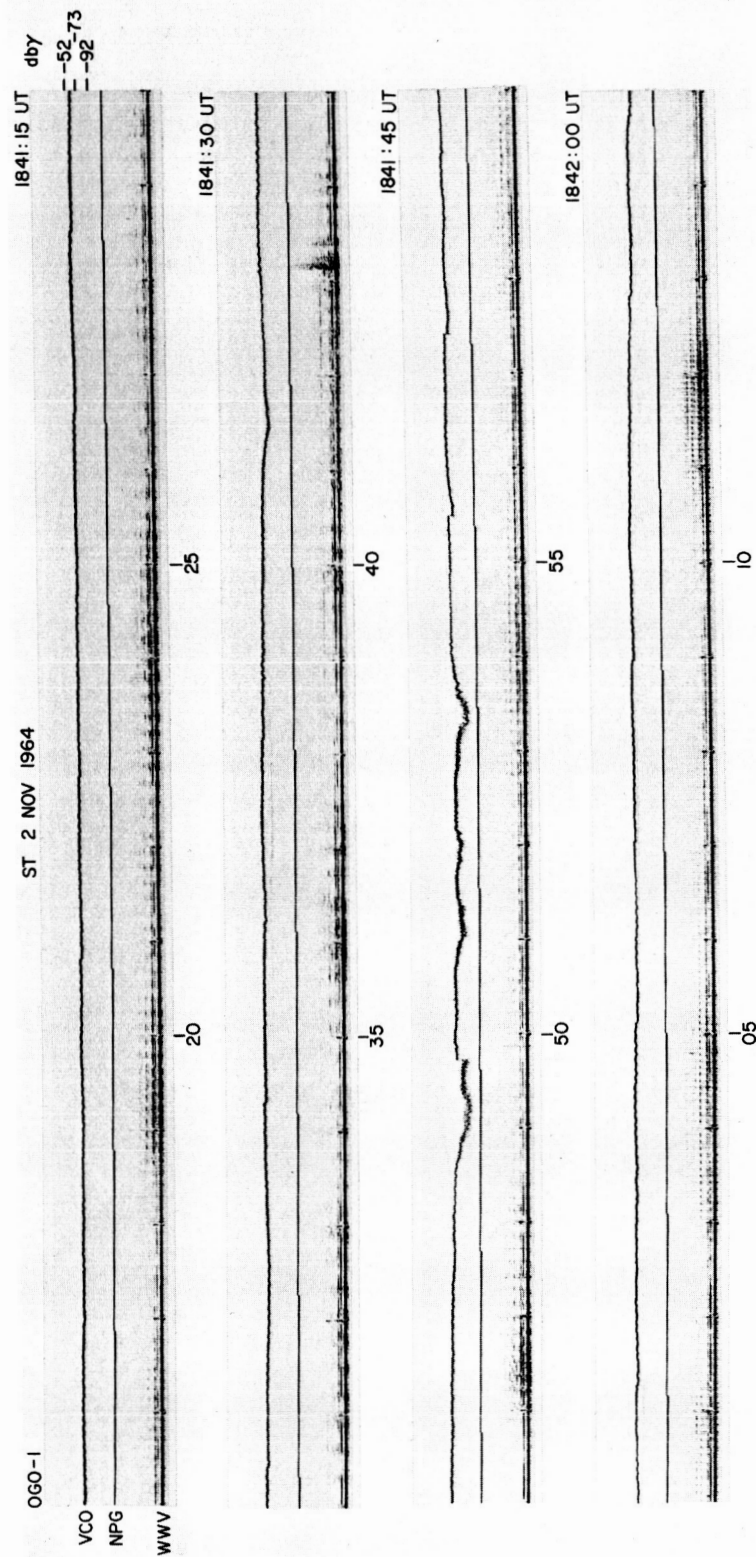


FIG. 19. A CONTINUATION OF THE DATA SHOWN IN FIG. 18. Since the bandwidth of the satellite Band 3 receiver is 500 Hz, and the center frequency of the NPG carrier is shifted by only ± 50 Hz in the "FM" keying schedule, the NPG signal may be considered as CW (key-down) for amplitude study purposes.

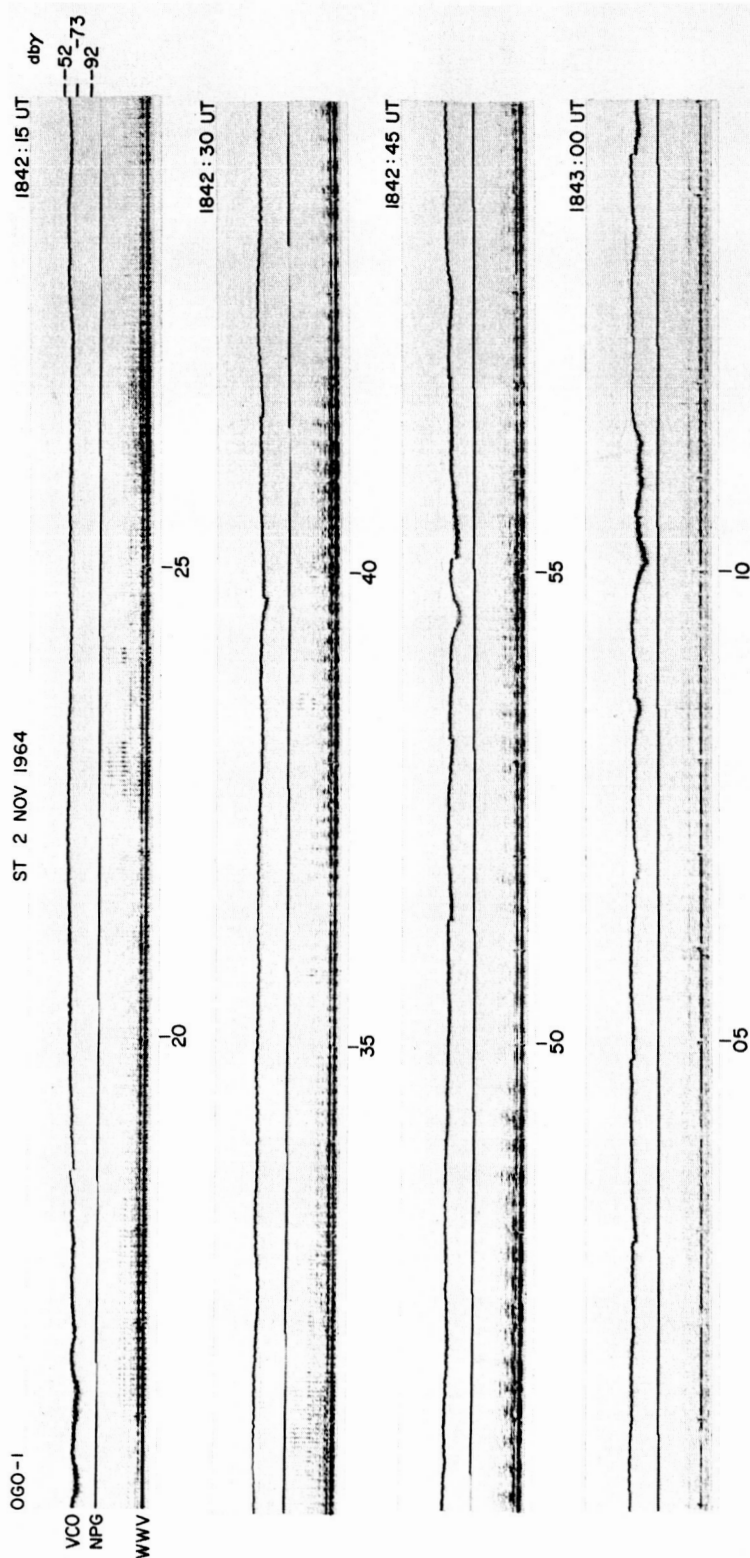


FIG. 20. A CONTINUATION OF THE DATA SHOWN IN FIGS. 18 AND 19. Note that the sudden changes of 100 Hz in the NPG transmitted signal sometimes (but not always) results in amplitude changes in the NPG signal received at the satellite (as indicated by the VCO). This perhaps indicates frequency-selectivity of the whistler-mode paths to the satellite.

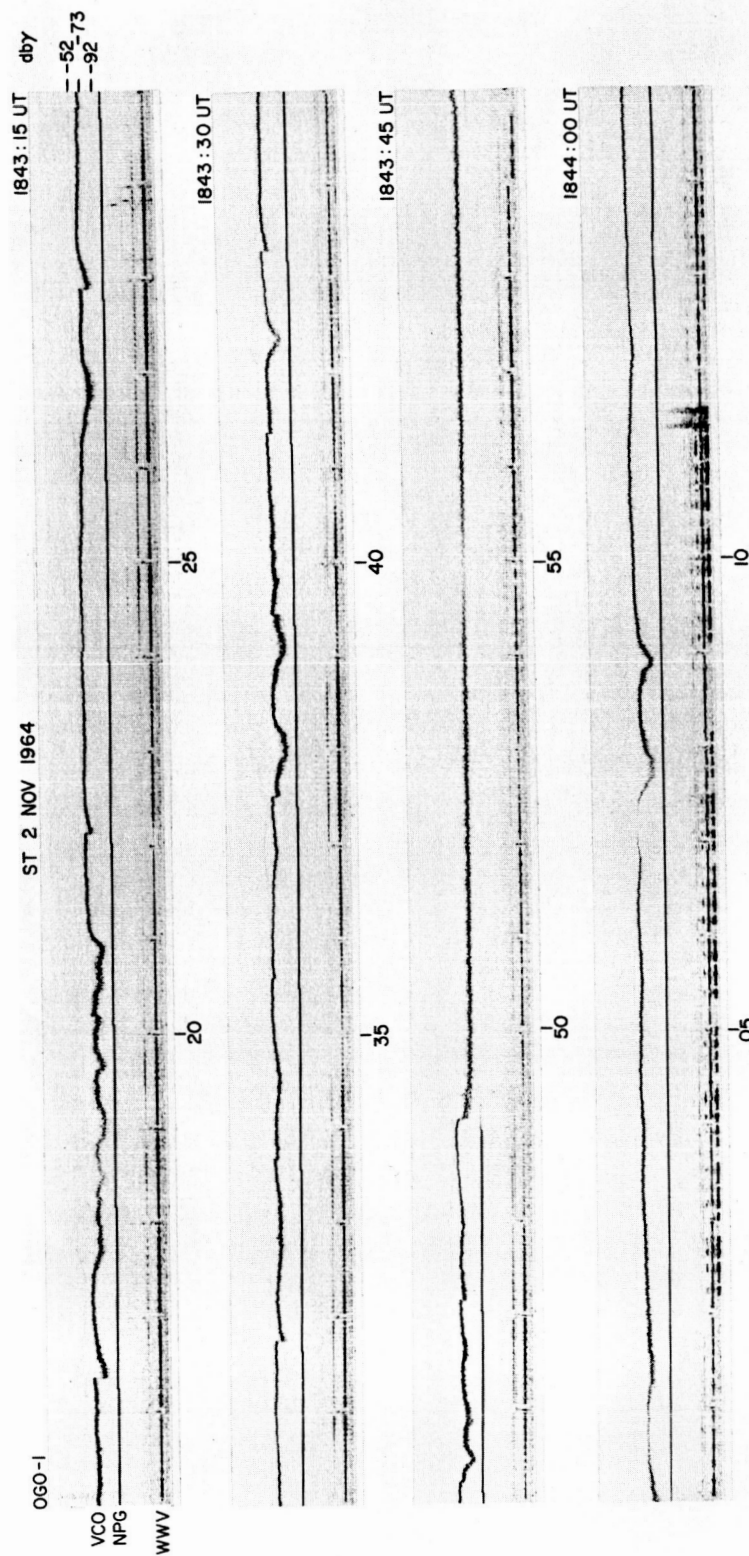


FIG. 21. A CONTINUATION OF THE DATA SHOWN IN FIGS. 18, 19 AND 20. Note that NPG ceases "FM" transmission at approximately 1843:49 UT and then returns to the air with CW (key-down) transmission at approximately 1844:00 UT.

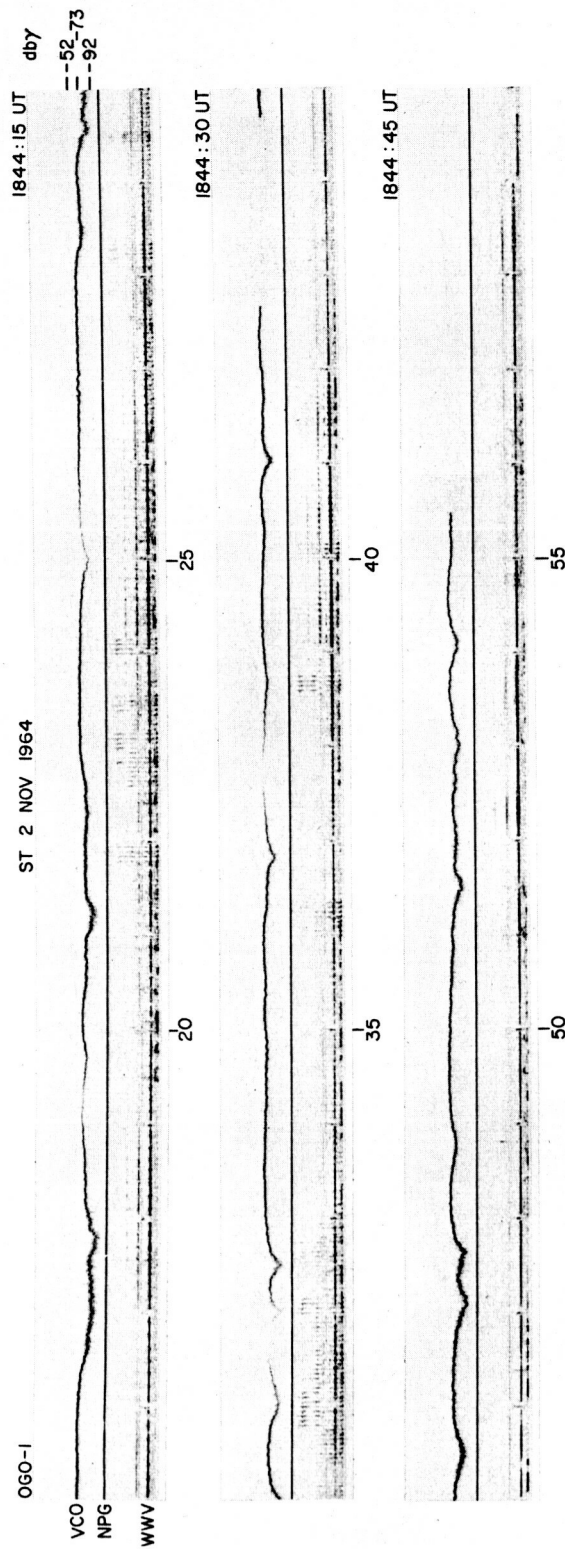


FIG. 22. A CONTINUATION OF THE DATA SHOWN IN FIGS. 18, 19, 20 AND 21. NPG continues to send CW transmission, but due to a failure of the tracking mechanism of the telemetry receiving antenna, the satellite VCO signals are lost at approximately 1844:55 UT.

For the time being, attention is directed only to the mechanics of data presentation. Note in Figs. 4 through 7 that the output of all three receivers, plus serial decimal time, all obtained from the PCM telemetry, appear on 4 separate channels of a multi-channel strip chart recorder. This system of data presentation is used by all of the NASA satellite tracking stations. A major advantage of this type of display for this study is the fact that additional confidence in the legitimacy of the Band 3 data may be obtained by observing simultaneously the outputs of the Band 1 and Band 2 receivers. For instance, the noise bursts in the Band 1 and Band 2 outputs in Figs. 5 and 6 appear only faintly in the Band 3 output. It is clear that the signals from Band 3 during this time do indeed emanate from NAA. However in Fig. 7, it is observed that the satellite has entered a region of wide-band noise since the outputs of all three receivers fluctuate in synchronism. Were the outputs from Band 1 and Band 2 not available, it is quite possible that one might mistake the Band 3 output in Fig. 7 as representing legitimate (although noisy) data.

In Figs. 8 through 15, where it is desired to show the output of the Band 3 receiver over relatively long periods of time, Bands 1 and 2 and the time channel have been omitted. Serial decimal time has of course been extracted and appears at the beginning and end of each record.

Note in Figs. 8 and 9 that signals from NAA gradually "fade out," which is perhaps what one might expect as the satellite steadily moves to higher altitudes. However, Figs. 10 through 15 remove all confidence in a simple "fade out" pattern of the signal versus distance. Here, intense "bursts" of highly discrete signals (one may easily read the Morse code in the "bursts") are observed as the distance from the vlf station to the satellite increases.

Figure 16 shows a single 16mm frame which is typical of the method utilized by Stanford Research Institute (SRI) to display vlf data obtained from the PCM telemetry. With the SRI system, the vlf data from all three receivers, along with all pertinent satellite positional information, time, etc., are displayed on a cathode ray tube and then photographed on 16mm film. In the high bit rate (such as shown by Fig. 16) each frame covers 2.3 seconds of real time data, and the beginning time of each frame is

indicated to the nearest millisecond.

An advantage of the SRI system is the fact that one may examine a single frame at a time, having a large amount of pertinent positional and supporting information at his disposal which certainly facilitates both data reduction and interpretation. Or, one may run the film at any desired speed, thereby quickly obtaining an excellent overall view of what the receiver outputs are presenting versus time.

Figure 17 shows a typical display of data taken from the SP telemetry recorded at Stanford. On data recorded at Stanford, serial decimal time is not available, hence time signals from either NBA, WWVB, or WWV/WWVH are inserted. Also on the Stanford record, the ground signal from the vlf station to which the OGO-I Band 3 receiver is tuned is inserted. Note in Fig. 17 that this is a highly desirable feature, since it enables an accurate determination to be made of the time delay between the time a transmission from a vlf ground station reaches Stanford (at the speed of light, c) and the time at which that same transmission reaches the satellite (at group velocity via the whistler mode).

In Fig. 17 (which is a Rayspan record) the frequency of the satellite VCO is determined by the amplitude of the vlf signals received by the Band 3 receiver. The frequency of the VCO decreases approximately as the logarithm of the amplitude. It is therefore translated at Stanford using an oscillator frequency of approximately 40 kHz so that on the Rayspan record a signal appears at roughly 7 kHz which increases in frequency with increasing amplitude. The ground signal and time are also translated so that they appear on the record as shown. The chief advantage of the Stanford record is that it allows accurate time-delay determination.

Figures 18 through 22 show a long period of CW transmission from NPG. This is the longest CW transmission in all of the data, and is shown in its entirety in order to demonstrate the depth and frequency of fading of the OGO-I whistler-mode signals for a particular ionospheric location.

From 1840:15 UT until 1843:49 UT in Figs. 18, 19, 20, and 21, NPG is transmitting a special "FM" pulse schedule. In this mode the power output is nearly constant, but the transmitter carrier frequency is swept linearly in time from 18.55 kHz to 18.65 kHz every two seconds. Since

the satellite Band 3 receiver has a 500 Hz bandwidth, this total carrier frequency shift of 100 Hz (center frequency ± 50 Hz) should not result in any observable change in amplitude at the receiver output. In other words, the "FM" schedule is, for the purpose of amplitude studies, the same as a true key-down (CW) transmission.

A discussion in Section F of this chapter outlines the need for relating the maximum and average values of the measured data. The data shown in Figs. 18 through 22 were utilized, along with all other available key-down periods from both satellites in order to determine this relationship. Typical key-down fading patterns of whistler-mode signals received at low altitudes by OGO-II are shown in Figs. 52, 53, and 54 of Chapter V.

The satellite tracking stations and the U.S. Navy vlf stations from which data were used throughout this study are listed in Table 2. This permits easy identification of the code abbreviations used in many of the illustrations.

E. SOURCE OF ERRORS

As mentioned earlier, calibration of the vlf receivers is performed on every 16th sweep when the receivers are in the sweeping mode. It is an easy matter to compare amplitudes of these calibration signals using the strip-chart or 16mm film records obtained from the PCM telemetry. This procedure supplies evidence that the calibration level has not changed, and that amplitudes of vlf signals indicated by these two methods of data reduction are accurate to within ± 1 db [L. H. Rorden and B. P. Ficklin, private communication].

Unfortunately, one may not place such high confidence in the amplitudes of vlf signals as indicated by the VCO via the special purpose telemetry. Because of changes in operating power necessitated by improper satellite stabilization as described in Section D, temperatures inside the main body have fluctuated as much as 20°C . This may have caused the center frequency of the VCO to drift as much as 2 kHz, with the result that prelaunch calibration curves of VCO frequency versus amplitude are not accurate. This temperature fluctuation has also caused the master local oscillator frequency to drift somewhat, with the result that the sequence of commands necessary to tune the Band 3 receiver to a given frequency is not constant.

TABLE 2. LOCATIONS OF PERTINENT STATIONS.

Code	Location	Geographic Coordinates		Geomagnetic Latitude
BY	Byrd Station, Antarctica	80.0°S	120.0°W	70.6°S
DA	Darwin, Australia	12.4°S	131.0°E	23.0°S
SKA	Fairbanks, Alaska	65.0°N	147.5°W	64.5°N
JO	Johannesburg, South Africa	26.5°S	28.0°E	27.0°S
QU	Quito, Ecuador	0.2°S	78.5°W	11.0°N
RO	Rosman, North Carolina	35.0°N	83.0°W	47.0°N
SA	Santiago, Chile	33.5°S	70.7°W	22.0°S
ST	Stanford, California	37.4°N	122.2°W	43.7°N
NAA	Cutler, Maine 17.8 kHz 1,000 kw	44.6°N	67.3°W	56.0°N
NPG	Jim Creek, Washington 18.6 kHz 250 kw	48.2°N	121.9°W	54.0°N

The temperature effect on the VCO calibration is obviously a serious one. However, since there are occasions when the same vlf data are being recovered simultaneously from both telemetry channels, it has been possible to compare amplitudes as indicated by the VCO with amplitudes as indicated simultaneously by the digital channel, and thereby synthesize a new calibration curve for the VCO at a given temperature. Thus it is possible to determine with a fair degree of accuracy the amplitudes of vlf signals as indicated by the VCO during periods of time when these same data are not available from the PCM telemetry.

Cross correlation of amplitudes as indicated by the VCO and the PCM telemetry at times when both are available have shown, except for one instance, that the VCO may be interpreted correctly within approximately +5 db. The exception, which occurred on 1 April 1965, contained a

discrepancy of approximately 15 db between the VCO and the digital data. On this occasion the VCO frequency was erratic and the discrepancy could not be resolved. In all of the data reduction work, where redundant data were available, amplitudes indicated by the digital channel and PCM telemetry were accepted as the most accurate.

The temperature effect on the master local oscillator proved to be more of an inconvenience than a source of error. Had the spacecraft temperature been stable as planned, tuning up to any given frequency would have been simply a matter of sending the proper sequence of commands from the ground. With the unexpected temperature variation, the tuning procedure became more complicated.

To tune the Band 3 receiver to a given frequency it became necessary to monitor the master local oscillator frequency by use of the 150-foot parabolic dish antenna operated by the Stanford Radar Astronomy Center, while at the same time requesting specific satellite commands by telephone from the OGO control center at Greenbelt, Maryland. Thus it was possible to tune the receiver to any given frequency with complete assurance that the tuning had been conducted successfully.

Another potential source of error involves the orientation of the satellite loop antenna with respect to the earth's magnetic field. It can be shown [Ratcliffe, 1959] that for the QL (quasi-longitudinal) case the magnetic field vector of the whistler-mode wave is circularly polarized in the plane of the wavefront, and is perpendicular to the wave normal. If one assumes strictly field-aligned propagation with small wave normal angles, then the H vector of the wave will be rotating in a plane that is essentially perpendicular to the earth's magnetic field lines. Therefore the loop antenna would not be expected to receive these signals whenever the axis of the loop was aligned (or nearly so) with the geomagnetic field.

The assumption of small wave normal angles is not unreasonable for 18 kHz signals which have propagated up only one side of a field line. One may expect that the wave normal angles of such waves are considerably less than 45° [R. L. Smith, private communication]. This assumption is further justified by the ray tracing results contained in Chapter VII.

Furthermore, it is recalled that the loop sensitivity is a cosine function of the angle between the plane of the loop and the wave normal, and its sensitivity would be reduced only 3 db for an angle of 45° .

Whether or not an alignment of the loop axis and the earth's magnetic field does indeed occur is an easy matter to determine. The loop axis (satellite z-axis) is estimated to lie between -5° to -18° declination and $+44^{\circ}$ right ascension. The spatial coordinates of the direction of the earth's magnetic field for all portions of the OGO-I orbit are printed out in the ephemeris derived from the after-the-fact-orbit-attitude tapes produced by Goddard Space Flight Center (GSFC). A comparison of these two sets of coordinates resolves the problem. Such a comparison has been made for all periods of time when fixed-frequency vlf data were being obtained from the Band 3 receiver. On only one occasion did they approach coincidence sufficiently closely that the loop would not be expected to respond accurately to field-aligned signals. This happened at approximately 0350 UT on 1 April 1965. However, the NAA signals had faded out from natural causes approximately 20 minutes earlier. It is therefore believed that loop orientation may be ruled out as a possible source of error in this study.

The unexpected spinning of the satellite with a 12 second period is another possible error source. As noted above, the loop axis orientation is known to have a declination of between -5° and -18° and a right ascension of $+44^{\circ}$. Independent measurements place the most probable spin axis orientation at -9° declination and $+42.5^{\circ}$ right ascension. Hence the spin axis is sufficiently parallel to the loop axis that although the loop "wobbles" a bit as the satellite spins the deviation is so slight that no observable effect would be expected. None has been observed in the data, and therefore spin has also been ruled out as a source of error. As a matter of fact, this "wobble" is a good test of whether the vlf signals arrive at an angle close to the null of the loop antenna. If they did, the "wobble" would cause modulation of the data. Since no modulation has been observed in the data, the assumption of small wave normal angles made above appears even more justifiable.

Inability to accurately read the SRI film presentation, due to such things as aberrations in the projection process, probably introduces a

2 or 3 db uncertainty. This is a random error which probably must be accepted.

Since the strip-chart recorders may be accurately calibrated for full-scale deflection at the time each record is made, and the voltage level of the calibration signal in the satellite is accurately known, it is believed that the accuracy of these records is within 1 or 2 db.

F. DATA REDUCTION

Telemetry signals from the OGO satellites are received at the ground data acquisition stations, demodulated, and recorded on magnetic tape. These tapes are then sent to GSFC for further processing and individual experiment decommutation. The data processing branch at GSFC carries responsibility for the preliminary processing and reduction of the flight experimental data up to and including decommutation. Data processing beyond this point is the responsibility of the individual experimenters. In the case of the Helliwell vlf experiment, data processing of the PCM telemetry is the responsibility of SRI. Processing of the special purpose telemetry used in this study has been accomplished by the Radioscience Laboratory at Stanford University. A flow diagram of the OGO System Operations is shown in Fig. 23.

The method of data presentation shown by Figs. 4 through 15 needs no clarification. These data were taken directly from the PCM telemetry records at GSFC by the author using the Data Word Selector Equipment and multi-channel chart recorders available there. The assistance of Mr. R. Brittner of GSFC is gratefully acknowledged.

Similarly, the Rayspan method shown in Figs. 17 through 22 is widely used by the Stanford Radioscience Laboratory and is conventional in its application to the OGO data. The SRI method shown in Fig. 16 was developed specifically for the processing of OGO PCM data, and a brief discussion of this method follows.

The SRI method involves a four-pass computer processing system; the first three passes on a Burroughs B5500 computer, the final pass on a Control Data Corporation 160-A. The first pass processes the satellite attitude-orbit magnetic tape data. The second pass processes the real

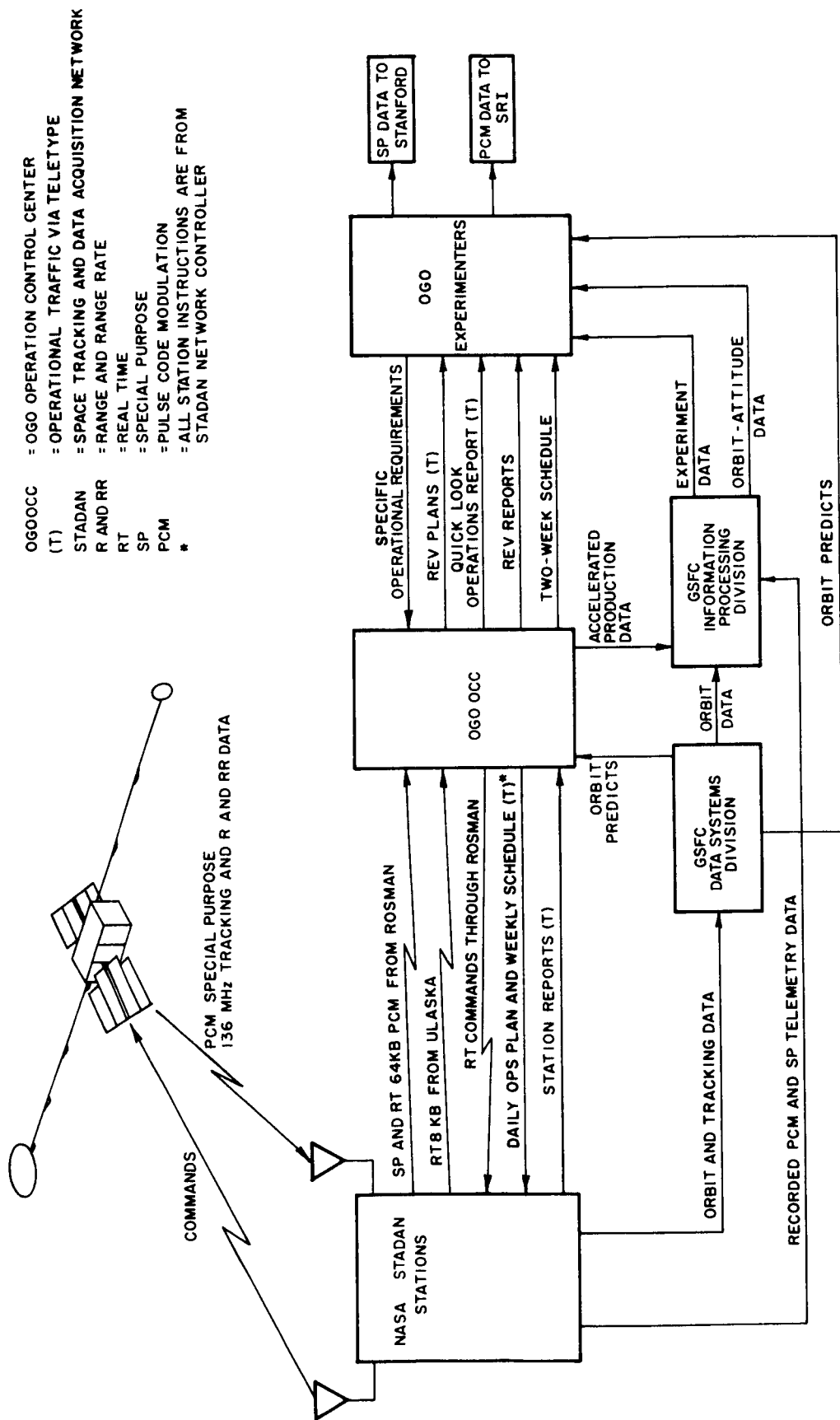


FIG. 23. A FLOW DIAGRAM OF THE ROUTINE OGO SYSTEM OPERATIONS.

and stored-time digital experimental magnetic tape data. The third pass results in the production of a display tape for the CDC computer. This pass integrates the experimental data with the associated time-ordered satellite attitude-orbit parameters, thus producing an output tape containing information to be used as an input to the CDC computer. The fourth and final pass results in the production of a 16mm film, one frame of which is shown in Fig. 16. This film displays the contents of the CDC display tape which was generated during pass number three. The computer program for pass number four is designed to take the information from the magnetic display tape and present this information on the face of a cathode ray tube where it is filmed. The final result (16mm film as shown in Fig. 16) enables one to examine large quantities of data rapidly if the film is projected at the customary rate of 16 or 24 frames per second, or to examine each frame in detail if single-frame projection is used. To obtain the PCM telemetry data contained in this study the author scaled an estimated 5,000 frames such as shown in Fig. 16.

In scaling the data, the maximum signal intensity of each frame is recorded; these maximum values are shown by the continuous lines in all plots of field intensity versus universal time for OGO-I, and field intensity versus magnetic latitude for OGO-II (see Figs. 34 through 44, and Figs. 56 through 89). While one would prefer to have the average value of field intensity from each frame rather than the peak value, this is virtually impossible for two reasons: 1) the large number of frames of data to be scaled, and the inherent difficulty of quickly yet accurately determining the average value for each frame; and 2) only a small portion of the data is key-down (CW) transmission. Probably more than 99% of the data represents conditions where the vlf station is transmitting traffic (interrupted CW). Hence, there are many periods in most frames where no signal is being transmitted. The duration of these "silent" periods is variable and depends on such things as the sequence of dots and dashes used in the message, and on the method of keying the transmitter (hand-keying, or tape). Also, for frames where the signal intensity is near the background noise level it is difficult to determine precisely whether the lack of signal is due to a "silent" transmission period or due to fading of the signal being scaled.

The usefulness of the peak value, its possible relation to the average value, and further arguments in favor of its use will now be presented.

Since the object of this study is to compare calculated intensities (which are based on average power) with measured intensities, one obviously would like to have the average value from each frame. However, it is difficult indeed to accurately scale an average value from a frame of data, without becoming involved in a laborious and prohibitively time-consuming process. On the other hand, it is a relatively easy matter, and probably accurate to within 1 or 2 db, to simply lay a straight-edge across a frame of data (using only frames representing key-down transmissions) and read the median value. Then the problem becomes one of determining how the average relates to the median; a relationship which depends on the statistics of the signal envelope. Unfortunately, the statistics of the envelope are not known at this time. Therefore, as an alternative, it was decided to conduct a study of all available key-down periods of data in order to determine the ratio between the maximum and the median of the received signal. This provides an indication of what one would expect the average to be.

To do this, one first of all notes that the received signal is not contaminated by additive noise. Assurance that this is the case for the records being scaled comes from the fact that the signal intensity is at least 20 db above the background noise level for all key-down periods scaled. Hence, it is probably safe to assume that the statistics of the envelope are determined by the statistics of the fading of the signal. In addition, one must be careful to utilize in a given study only those data which were obtained by a common sampling rate. For instance, it is necessary to separate the OGO-I and OGO-II data for the key-down periods studied here, since one frame of data for OGO-I represents 2.3 seconds of real time, but one frame of data for OGO-II represents approximately 73 seconds of real time.

A useful comparison may now be drawn. If, for example, one assumes that Rayleigh fading is involved (this would mean that the received envelope is Rayleigh distributed) it is easy to determine that the ratio of average to median is approximately 1.14. See for instance, Parzen [1960], Omura and Kailath [1965]. It is probably reasonable to assume for

the purposes of this discussion that the ratio of median to average of the OGO data is near unity.

Until the statistics of the signal are better defined this appears to be a reasonable point to conclude the discussion. If one assumes that the received signal is the summation of components from many paths, then the assumption of gaussian signal and a Rayleigh envelope is well justified [H. M. Hall, private communication].

The results of scaling all of the available key-down periods for both OGO-I and OGO-II data appear in Figs. 24 and 25. These measured median values are also plotted on the field strength records in Chapters IV and VI.

In order to interpret the data properly one must know something about the integration time constants of the receiver being used aboard the OGO satellites. Three factors determine the receiver capability to respond properly to a received signal: 1) the integration time constant of the IF band pass filter; 2) the integration time constant of the detector output filter; and 3) the sampling rate of the telemetry system. The integration time constant of the detector output filter and the sampling rate both depend upon the bit rate of the real-time equipment group used in each satellite. For OGO-I all of the PCM data contained in this study were obtained from the Band 3 receiver using the 64 kilobit/second data rate. In this configuration the integration time constant of the detector output filter is 2 ms, the integration time constant of the IF band pass filter is 1.6 ms, and the sampling period is 9 ms (111 samples per second). Hence, the limiting factor is the sampling rate.

This is not a particularly serious limitation when one considers that the rise times of the modulation envelope of the vlf transmitters utilized in this study are on the order of 10 to 15 milliseconds [W. Cornell, private communication]. In addition, the most rapid fading observed in the OGO-I data by means of the VCO whose response is not limited by the above factors (as discussed below) seems to have a minimum period on the order of 100 milliseconds. Therefore, it is probably safe to assume that most of the characteristics of the received signal are passed by the equipment and that the amplitude variations shown by the OGO-I data represent true fading, not effects caused by band limiting.

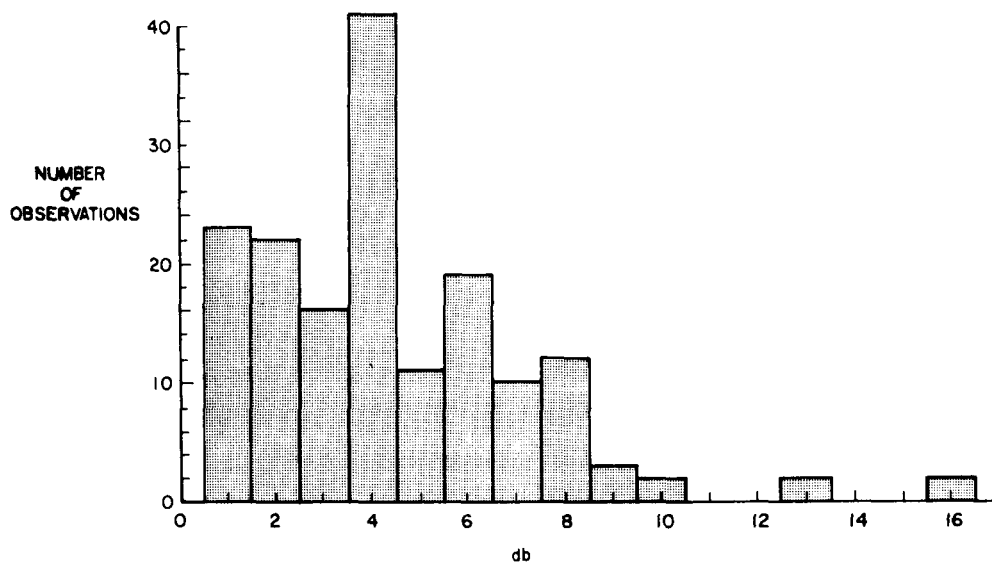


FIG. 24. RATIO OF PEAK TO MEDIAN VALUES (IN DB) AS SCALED FROM KEY-DOWN PERIODS OF DATA FROM OGO-I. Sampling period = 2.3 seconds.

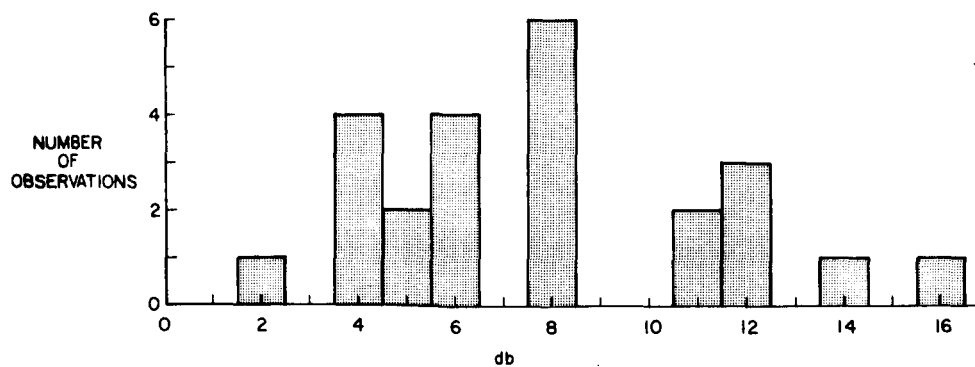


FIG. 25. RATIO OF PEAK TO MEDIAN VALUES (IN DB) AS SCALED FROM KEY-DOWN PERIODS OF DATA FROM OGO-II. Sampling period = 73 seconds.

For the OGO-II amplitude data, which were obtained from the phase track receiver in the stored data mode (4 kilobit/second data rate), the limiting factor is the sampling rate. In this configuration, the amplitude and phase of the phase track receiver are sampled 6.94 times per second. Therefore one would expect amplitude ambiguities to be introduced by the receiver for fading rates that exceed a few cycles per second. Data from the special purpose telemetry system are not subject to the restraints of the equipment outlined above. The bandwidth of this channel is 500 Hz through the IF circuits; however, this is reduced to 300 Hz by an input filter at the VCO. Hence, it should be possible to observe fading rates as high as several hundred cycles per second with the SP system. No fading rates this high have been observed. The maximum observed rates appear to be on the order of 10 to 20 Hz and are shown in Figs. 52 and 53.

G. PRESENTATION OF THE DATA

By scaling records such as those shown in Figs. 4 through 22, all of the available fixed-frequency data from the PCM telemetry which OGO-I has measured have been obtained, along with all similar data which have been obtained at Stanford via the SP telemetry. These measured data (peak values) have been plotted as field intensity versus time, along with pertinent satellite positional information, in Figs. 34 through 44.

Using the procedures outlined in Chapter III, field intensities have been calculated for every satellite location where the above measurements were made. These calculated values are plotted along with the measured values in Figs. 34 through 44.

It is not clear what method should be applied to the measured data in order to indicate its most probable average value. The factors influencing this choice are discussed in detail in Section F above. Based on these arguments and in view of the limited data available, it appears that a reasonable correction factor may be obtained by taking the average of the db difference between the peak and median values shown in Figs. 24 and 25. There is no particular reason why this method is suggested in preference to another except that it at least appears to be an acceptable method of obtaining an unbiased estimate of the ratio between peak to average values

of the measurements. Using this method, correction factors of approximately 7.8 db for the OGO-II measurements and 4.3 db for the OGO-I measurements are obtained.

For all field intensity records containing key-down periods (which were scaled for median values) the measured median value is indicated on each record. (See Fig. 69 for instance.) Except for these few cases, only the peak values of the measurements appear on the field strength figures. The reader should keep this in mind when comparing measured and calculated values in Chapter IV and Chapter VI.

III. FIELD STRENGTH CALCULATIONS

A. INTRODUCTION

In this chapter we define a model whistler-mode path between a vlf transmitter and a satellite. We then review the contributions from other researchers regarding each of the major loss sources in this model, and utilize their results to calculate field intensities expected at any given satellite position. These calculations will then be compared to the measured data in Chapters IV and VI, and refinements to improve the model suggested in Chapter VII.

With the location of both end-points of the path specified, field intensity at the satellite may be calculated on the basis of a model path having three major sources of loss: 1) excitation of the whistler-mode at the foot of the field line passing through the satellite; 2) absorption of the signal in passing through the ionosphere, and 3) divergence within the ionosphere. This model path will hereafter be referred to as the first-approximation model. It should be noted again that item (1) includes the earth-ionosphere waveguide loss between the vlf transmitter and the foot of the field line as well as the losses due to reflection at the boundary. These losses are lumped in this manner in the first-approximation model in order to utilize the results of Cray which are shown in Fig. 27.

The results of researchers in each of these three general areas will be discussed separately, and then the results utilized in typical total-path field strength calculations.

B. EARTH-IONOSPHERE WAVEGUIDE

The first segment of the propagation path between a vlf ground station and the satellite in the first-approximation model is the earth-ionosphere waveguide. This is defined as the space between the conducting spherical shells formed by the earth and the lower edge of the ionosphere. It is now well established that whistler-mode signals can propagate for several thousand kilometers underneath the ionosphere [Helliwell, et al, 1962; Parks, et al, 1964; and others].

As energy from a vlf transmitter spreads out beneath the ionosphere

continual leakage into the ionosphere occurs and whistler-mode waves will be excited wherever the polarization of the waves is appropriate.

Field intensities along the guide can be determined approximately by either of two methods: 1) a series of waveguide modes [Wait, 1957]; or 2) by a series of rays [Budden, 1961]. Ray theory (geometrical optics) has been widely used in whistler work and will be used here. Ray-path geometry is shown in Fig. 26.

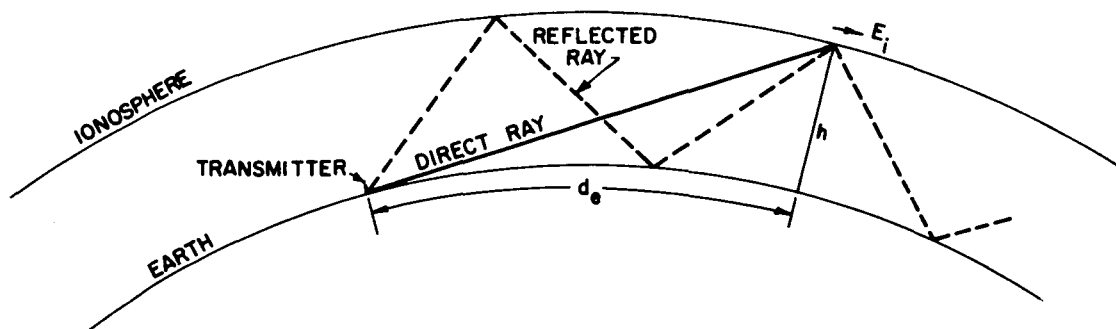


FIG. 26. RAY PATH GEOMETRY FOR PROPAGATION IN THE EARTH-IONOSPHERE WAVEGUIDE. Only the direct and one-hop rays are shown. Normally several reflected rays are required to accurately describe the total field.

Crary [1961] calculated, for a wide range of frequencies, the field strength at the ground produced by a source situated just within the ionosphere. He also calculated the field intensity of the transmitted ionosphere whistler-mode wave versus distance (d_e) from a short vertical antenna on the ground. This is the type of antenna used by the Navy vlf stations. His results were published by Helliwell [1965] and are shown here in Fig. 27.

The lower boundary of the waveguide is represented by the conductivity of the ground, and the upper boundary by a double-valued expression for refractive index which may be written [Budden, 1961]

$$n^2 = 1 - i \left(\frac{\omega_r}{\omega} \right) e^{\frac{+i\tau}{\omega}} \quad (3.1)$$

where

$$\frac{\omega_r}{\omega} = \frac{\omega_o^2}{\omega(\nu^2 + \omega_L^2)^{\frac{1}{2}}} \quad (3.2)$$

and

$$\tan \tau = \frac{\omega_L}{\nu} \quad (3.3)$$

Each ray experiences amplitude and phase changes at the earth and ionosphere reflection points. Knowing the characteristics of the ground and the ionosphere, Fresnel coefficients at the ground and reflection and conversion coefficients at the ionosphere may be calculated. The intensity of each ray just inside the homogeneous sharply bounded model of the ionosphere is thus obtained. Although each ray enters the ionosphere at a slightly different angle of refraction, this difference in angle is usually small and the field components of each ray may be summed (after considering their time phase) as though their wave normals were coincident.

A mismatch between the polarization of the whistler-mode (ordinary) wave, which is circularly polarized, and the elliptically polarized incident wave causes additional loss during coupling into the ionosphere. To satisfy the boundary conditions, an extraordinary wave of opposite polarization is generated.

For frequencies below the gyrofrequency and for $\omega_o \gg \omega$ the ordinary wave has an essentially progressive nature, and represents the whistler-mode of propagation. The extraordinary wave is essentially evanescent, and its amplitude decreases exponentially with height. All of the above effects plus reflection losses at the sharp boundary were taken into consideration by Crary.

To obtain the results shown in Fig. 27, Crary used two ionospheric models; one for summer night, the other for summer day. The parameters of these two models are shown in Table 3. The summer night values in Table 3 correspond to an effective f_H of 1.34 MHz, $f_o = 352.0$ kHz, and $\nu = 4.855 \times 10^6$. For the summer day model the values correspond to an $f_H = 1.35$ MHz, $f_o = 350$ kHz, and $\nu = 3.165 \times 10^7$.

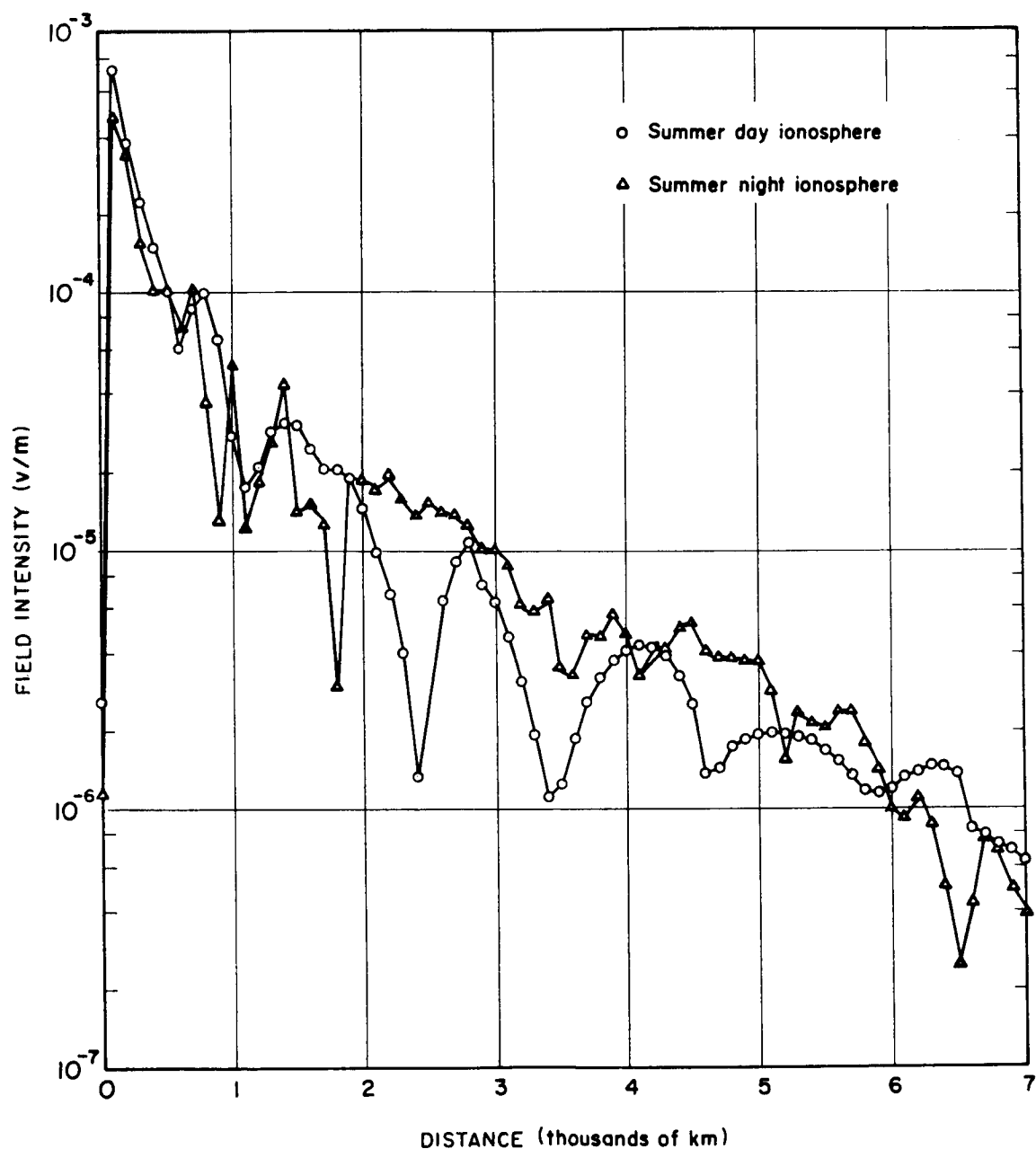


FIG. 27. FIELD INTENSITY OF TRANSMITTED IONOSPHERE WAVE VERSUS DISTANCE FROM A SHORT VERTICAL ANTENNA AT THE GROUND RADIATING 1 KW AT 15.5 kHz [Helliwell, 1965].

TABLE 3. PARAMETERS USED IN FIELD-STRENGTH CALCULATIONS.

Ionosphere		Ground
Summer Night	Summer Day	
$\omega_r = 5 \times 10^5 \text{ sec}^{-1}$ $\tau = 60^\circ$ $h' = 90 \text{ km}$ $n \approx 2.23$	$\omega_r = 1.5 \times 10^5 \text{ sec}^{-1}$ $\tau = 15^\circ$ $h' = 70 \text{ km}$ $n \approx 2.21$	$\sigma \approx 4.5 \text{ mho/m}$ $k \approx 80$

To simplify the treatment Crary did not allow for diffraction around the earth's surface for near tangential rays [Wait and Murphy, 1957] nor for the spherical convergence of rays bouncing between a spherical earth and a concentrically spherical ionosphere [Allcock, 1964]. Crary also made the simplifying assumptions that each individual ray component may be considered a plane wave, the QL approximation is valid, and that the lower edge of the ionosphere may be adequately represented by an equivalent homogeneous model with a sharp lower boundary and a vertical magnetic field. This assumption, although it has been used by many researchers [Davies, 1965], is only a first approximation because some observations can not be explained by the sharp boundary. It has been found by Wait [1960, 1962], Barron [1959], and Johler and Harper [1962] that a two-layered model is necessary to explain the observed attenuation rate in the frequency range from 500 Hz to 1.5 kHz. For frequencies in the range 8 kHz to about 20 kHz, however, the sharply bounded model is convenient for a simple description of what must be a complicated reflection process. Extensive justifications for the idealized model have been given by Wait and Walters [1964].

Helliwell [1965] calculates the reflection loss of a circularly polarized wave in free space incident vertically on the lower boundary of a homogeneous sharply bounded model ionosphere for which $\mu(0) = 4$. He finds that the reflection coefficient for this case represents a power loss of about 2 db and notes that the loss will, of course, vary with refractive index and angle of incidence.

The alternative approach is to utilize a full-wave treatment as discussed by Pitteway [1965], Piggott, et al [1965] and Pitteway and Jespersen [1966]. Piggott, et al [1965] for a frequency of 16 kHz shows a midday reflection coefficient for the penetrating mode (whistler mode) of less than 0.05 for all angles of incidence between approximately -45° and $+45^{\circ}$. Thus only a fraction of a db is lost due to reflections. For the nighttime model the reflection coefficient corresponds to no more than a 2 db loss for all angles of incidence between approximately -25° and $+40^{\circ}$. The authors point out that a study of the wave-fields reveals that this is due to efficient transmission of the whistler-mode through the ionosphere.

Certainly the above results indicate that the transmission coefficients are very high and that most of the loss comes not from reflections and uncertainties at the boundary, but from absorption in passing through the ionosphere. One is probably justified in assuming that ionospheric phenomena such as sporadic-E perhaps introduce more uncertainty than the sharp boundary assumption.

Using ray-theory and the sharp boundary assumption, Crary calculated the total field just inside the boundary as the sum of n sky-wave components. Each succeeding component is of lower amplitude than the previous one, due to the $1/R$ amplitude factor and the multiplication of additional reflection coefficients, which are always less than unity. Hence, a series is formed with terms of successively decreasing magnitude. In Crary's calculations, the first six rays for $n = 0$ through 5 were always calculated. The field from each component was then resolved into its three axial components and each axial component then added to the sum of that axial component built up by previous rays. His calculations terminated only when the amplitude of the last ray was less than 1% of the smallest of the three sums.

Figure 27 represents the results of Crary's work which are directly applicable to this study. For the first-approximation model, the field intensity of the transmitted whistler-mode ionosphere wave, E_i , at any given earth-ionosphere waveguide distance, d_e , is obtained from this figure.

C. ABSORPTION

The second major source of loss in the first-approximation model occurs from absorption as the whistler-mode wave passes through the lower and the upper ionosphere. Because of collisions between electrons and other particles, the wave loses energy as it propagates. Some of the energy is lost as heat in the medium and some as disordered electromagnetic radiation. Most of the absorption occurs in the lower ionosphere at regions between 70 and 120 km where collisions between electrons and neutral particles dominate. However some absorption also occurs in the upper ionosphere in the F-region as a result of coulomb collisions between electrons and charged particles. Both regions should be considered in determining total absorption of the wave.

Since the vlf frequencies of this study are well above the lower hybrid resonance [Smith, et al, 1966] through all of the ray path the effect of ions is neglected. Ion interaction with the wave is small for frequencies well above the lower hybrid resonance.

In Chapter I it was shown that the complex refractive index, n , using the QL approximation can be written

$$n^2 = 1 + \frac{X}{iZ - 1 + |Y_L|} \quad (3.4)$$

To investigate absorption of the whistler-mode wave in a slowly varying medium the complex refractive index is written as

$$n = u - i\chi . \quad (3.5)$$

Letting F be some field quantity in the wave, such that

$$F = F_0 e^{i\omega(t - nz/c)} \quad (3.6)$$

where n = refractive index, and z is measured in the direction of the wave-normal, we may write

$$F = F_0 e^{-(\alpha\chi z/c)} e^{i\omega(t - \mu z/c)} \quad (3.7)$$

This represents a wave traveling with velocity c/μ and attenuated to $e^{-\chi}$ in a distance $z = \lambda/2\pi$, where λ = wavelength in free space.

The absorption coefficient, α , is now seen to be related to the imaginary part (χ) of the refractive index by

$$\alpha = \frac{\omega\chi}{c} \text{ nepers/m} \quad (3.8)$$

where $c = 3 \times 10^8$ m/sec.

From Eq. (3.4) and Eq. (3.5), we may write for quasi-longitudinal propagation

$$(u - i\chi)^2 = 1 + \frac{X}{iZ - 1 + |Y_L|} \quad (3.9)$$

Equating real and imaginary parts of Eq. (3.9), and assuming that $|Y_L| \gg 1$ gives

$$\alpha = \frac{\omega}{\sqrt{2}c} \left[\sqrt{(1 + G|Y_L|)^2 + (GZ)^2} - (1 + G|Y_L|) \right]^{\frac{1}{2}}, \quad (3.10)$$

where

$$G = \frac{X}{Y_L^2 + Z^2} = \frac{\omega_0^2}{\omega_L^2 + \nu^2} \quad .$$

Helliwell [1965] points out that this expression permits few simplifications of practical value, but that it is necessary to employ the relation

$$\alpha \cong \frac{\omega G Z}{2c \sqrt{1 + G |Y_L|}} \quad (3.11)$$

if

$$(1 + G |Y_L|)^2 \gg (GZ)^2 . \quad (3.12)$$

Otherwise, the difference of the terms in the brackets in Eq. (3.10) becomes so small that, even in a digital computer, errors result.

For heights greater than 100 km Helliwell [1965] points out that

$$G |Y_L| \gg 1 \quad \text{and} \quad |\omega_L| \gg \nu$$

and then Eq. (3.10) reduces to

$$\alpha = \frac{\omega_o \nu}{2c |\omega_L|^{3/2}} \omega^{\frac{1}{2}} . \quad (3.13)$$

For a horizontally stratified ionosphere and a wave propagating vertically the total absorption is obtained by integrating Eq. (3.13) in the direction of the wave normal. Total absorption in decibels is given by

$$A = 8.69 \times 10^3 \int_{h_o}^{h_i} \alpha \, dh , \quad (3.14)$$

where h_o and h_i are the heights in km over which the absorption is to be determined.

Equation (3.13) shows that the absorption coefficient depends on the variation of electron density N and collision frequency ν with height, and also upon the variation of the earth's magnetic field B with height

and with magnetic latitude. The integration is therefore performed numerically on a digital computer after models for N and ν have been selected.

Helliwell [1965] performed this integration using three electron density models for the lower ionosphere (60 to 200 km) representing normal daytime, normal nighttime, and polar blackout conditions. His models are shown in Fig. 28. For the upper ionosphere (200 to 1500 km), he used a single model having a daytime f_oF_2 of 12.5 MHz and a nighttime f_oF_2 of 5.5 MHz.

Using these models and the above procedure, Helliwell calculated the absorption of a vertically incident wave integrated through the lower and upper ionosphere as a function of geomagnetic latitude. He did this for two frequencies, 2 kHz and 20 kHz both for nighttime and daytime. His results are shown in Fig. 29. The 20 kHz graph is directly applicable to this study, since integrated absorption at either 17.8 kHz (NAA) or 18.6 kHz (NPG) will not be greatly different than absorption at 20 kHz.

Total absorption in db for the first-approximation model is obtained from Fig. 29.

Other ionospheric models are considered in Chapter VII, and the integration is performed for 18 kHz.

D. DIVERGENCE

The third and final segment of the propagation path involves the divergence (or spreading) of the wave as it propagates through the ionosphere and up to the satellite. A brief review of the contributions of earlier researchers to this problem will now be presented.

L. R. O. Storey, in 1953, showed that the anisotropy of the ionosphere causes the direction of energy flow (ray direction) of whistler-mode waves to lie within a limiting cone whose axis is along the direction of the earth's magnetic field. For wave frequencies very low compared to the local gyrofrequency (i.e., for small values of normalized frequency Λ , where $\Lambda = f/f_h$), the half-angle of this limiting cone is $19^\circ 29'$. It can be shown [Poevlerlein, 1948], that the ray will be perpendicular to the refractive index surface as discussed below.

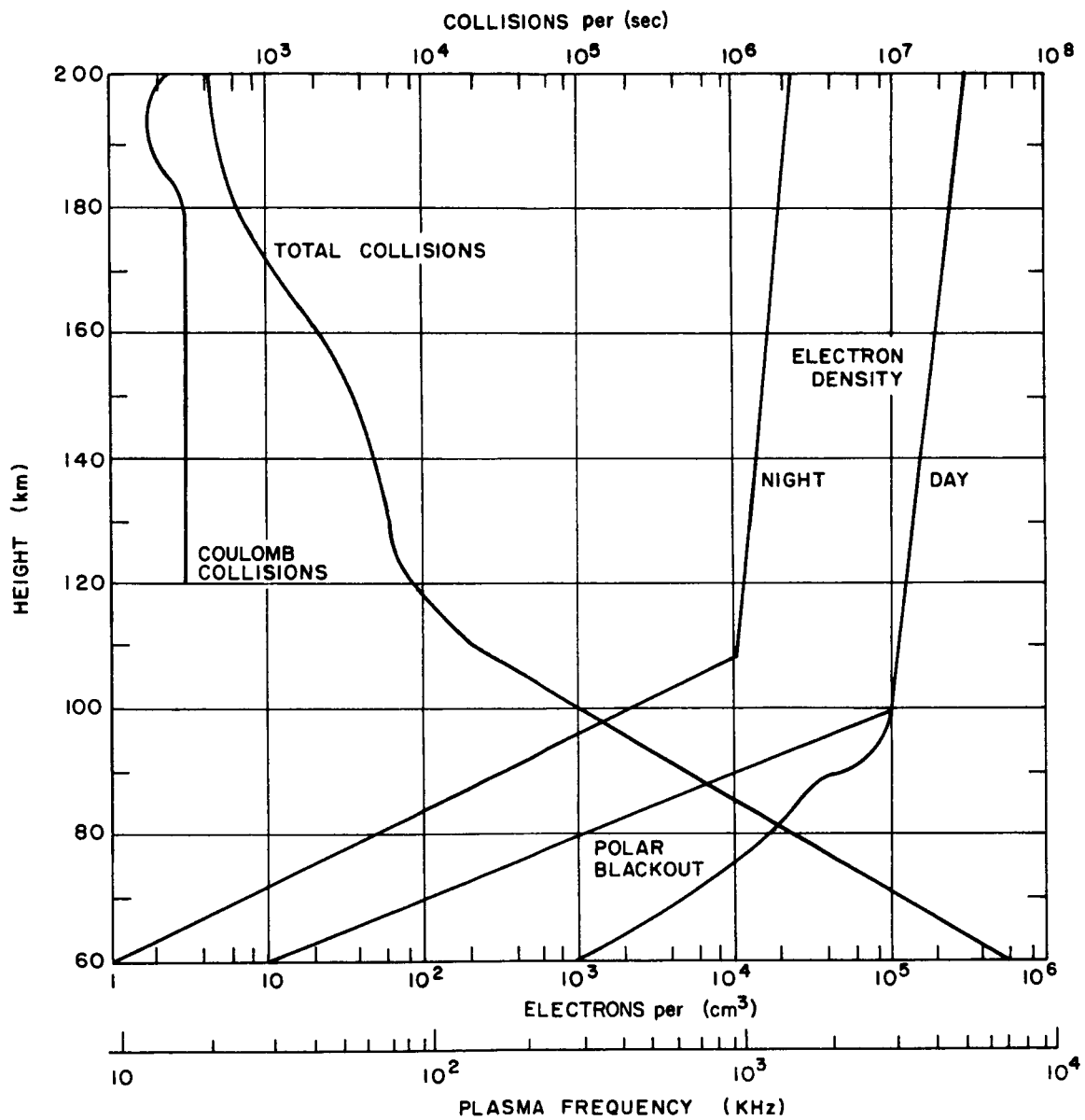


FIG. 28. DERIVED MODELS OF THE LOWER IONOSPHERE
[Helliwell, 1965].

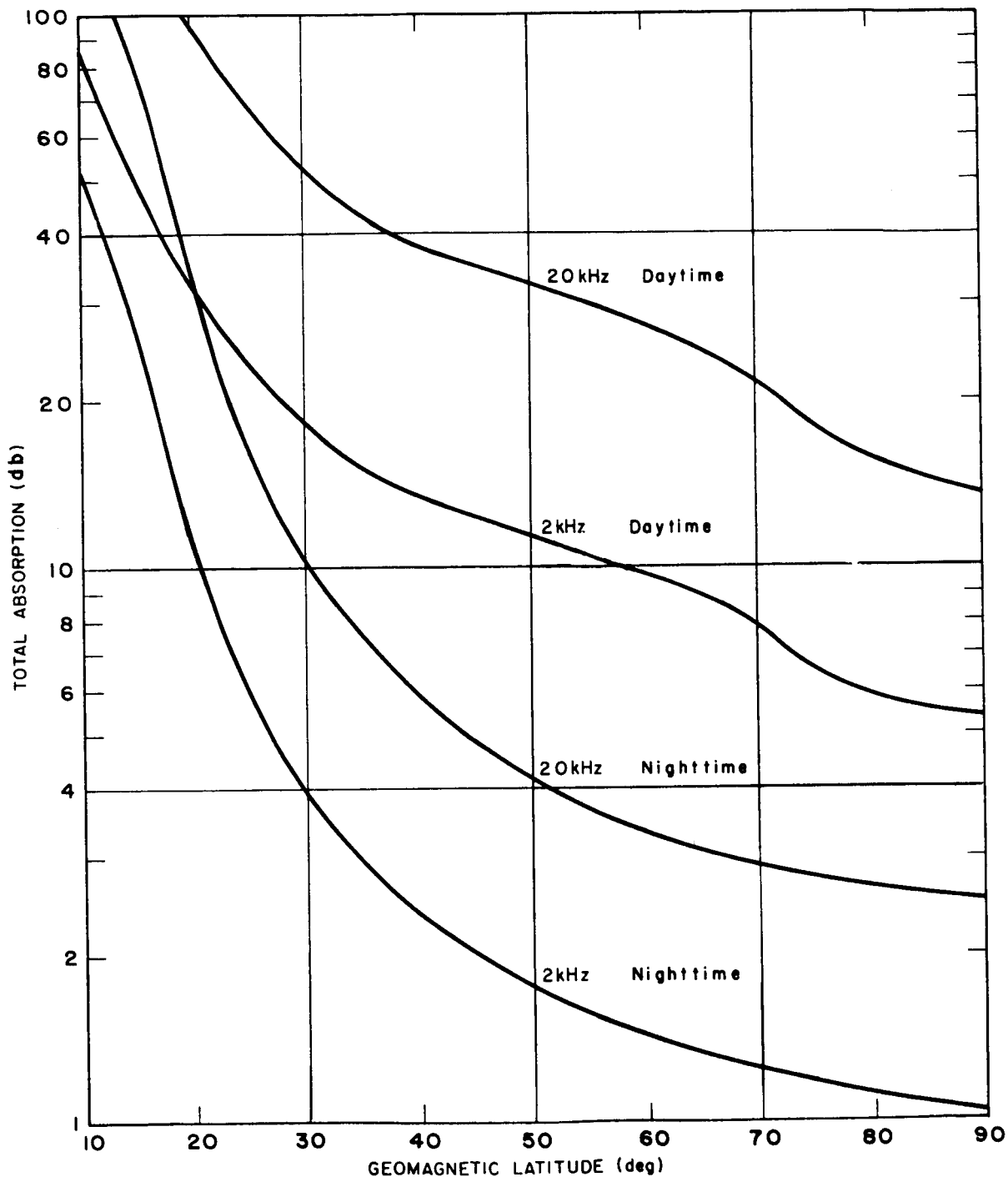


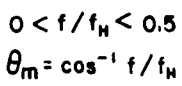
FIG. 29. ABSORPTION OF A VERTICALLY INCIDENT WAVE INTEGRATED THROUGH THE LOWER AND UPPER IONOSPHERE AS A FUNCTION OF LATITUDE [Helliwell, 1965].

Storey discussed in detail certain properties of the ray path through the ionosphere. He showed that, since the refractive index is a function of direction only through the wave-normal angle with respect to the magnetic field (which is to say that the medium is uniaxial in its anisotropy), the ray will lie in the plane defined by the wave-normal direction and the magnetic field. This is to say that the ray path will always lie in a plane containing the direction of the static magnetic field. Storey also demonstrated that $\tan \alpha = -\frac{1}{2} \tan \theta$ when $f_o^2 \gg f f_H$, and when $f_H \gg f$, where α is the angle between the wave normal and the ray direction and θ is the angle between the earth's magnetic field and the wave normal. This result means that the ray direction must always lie between the wave normal and the direction of the earth's field.

From these basic concepts come the fundamental principles of graphical ray tracing which enable one to determine the relationship between the wave normal and the ray, and thus, trace the path of the ray through a model ionosphere. In general, the ray direction differs markedly from the direction of the wave normal.

The refractive index surfaces which apply to whistler-mode propagation can be computed easily from a modified form of Eq. (3.4) and these surfaces can then be used to determine the direction of reflected and transmitted waves at a sharp boundary. This is the method of ray tracing outlined by Smith [1960b]. A typical refractive index surface for $0 < \Lambda < 0.5$ is shown in Fig. 30 where the refractive index (μ_1 and μ_2) is represented by a vector drawn from the origin to any point on the surface. The wave normal has the same direction as this vector, and the ray is always perpendicular to the surface at the point where the vector intersects the surface. The maximum ray angle versus normalized frequency Λ , and the ray direction versus wave-normal direction after Smith [1960a] and Helliwell [1965] are shown in Fig. 31 and Fig. 32. The minimum limiting ray angle of 11° is obtained when $\Lambda = 0.189$ in Fig. 32.

In examining data for this study, on only one occasion were whistler-mode signals observed when Λ was greater than approximately 0.45. This occurred at 0107 UT on 24 Nov. 1964 when the signals from NAA began fading in when the gyrofrequency at the top of the field line was approximately 25 kHz, or $\Lambda = 0.71$. Figure 32 shows that the limiting ray direction



This strong steering effect at frequencies below the gyrofrequency has been described as magnetoionic guiding. This is not to be confused with the term geomagnetic ducting, a process by which field-aligned irregularities of ionization tend to trap whistler-mode energy in a manner analogous to a light tube. Smith [1960b, 1961b] and Smith, et al [1960] have provided a theory of trapping of whistlers in field-aligned columns of enhanced ionization and have demonstrated graphical ray tracing techniques. They have shown that in ducts the ray path is then defined by the boundaries of the enhanced (or depressed) columns of ionization.

SEL-66-094

dimension would be more than sufficient to counteract the two-dimensional focusing shown by Yabroff.

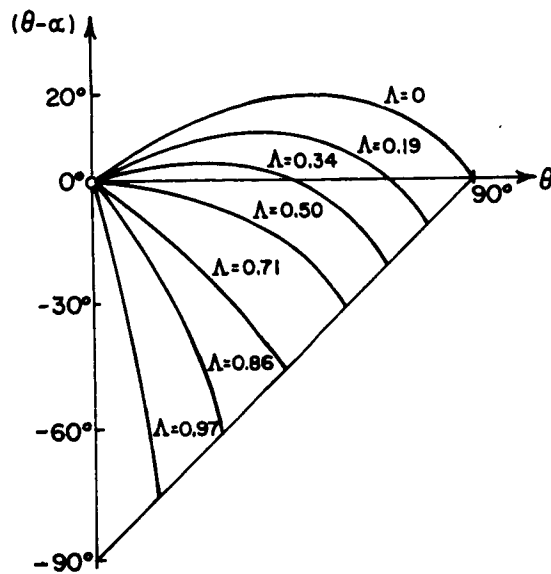


FIG. 31. RAY DIRECTION VERSUS WAVE-NORMAL DIRECTION, PARAMETRIC IN NORMALIZED FREQUENCY [Helliwell, 1965].

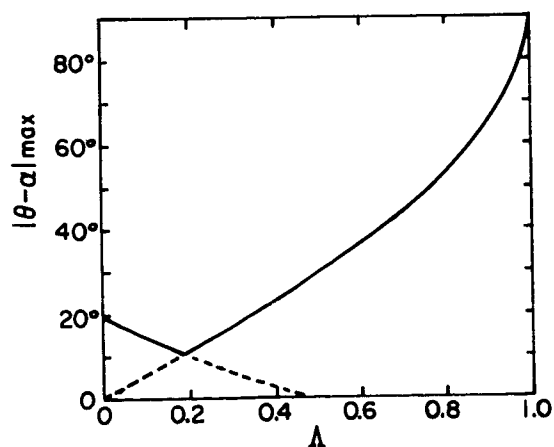


FIG. 32. MAXIMUM RAY ANGLE VERSUS NORMALIZED FREQUENCY [Helliwell, 1965].

The experimental evidence supporting ducted propagation on discrete field-aligned paths is extensive and varied [Carpenter and Smith, 1964]. These data can not be explained if the outer ionosphere is smoothly varying and void of irregularities capable of supporting discrete propagation paths. The use of ray theory and ducting is well justified by the internal consistency of the experimental results over a wide range of frequencies.

It should be pointed out that there is probably no real significance to the fact that whistler-mode signals are not normally observed in these data for Λ greater than approximately 0.45. The OGO-I orbit is inclined approximately 35° to the equatorial plane, and reaches magnetic latitudes of $\approx 40^\circ$ at altitudes where Λ approaches 0.4. Unfortunately, this is the approximate location where non-whistler-mode "broadband" noise bursts [Rorden, et al, 1966a] are observed. This noise often masks the nighttime vlf station signals received by OGO-I just at the time when the ratio of wave frequency to gyrofrequency (Λ) becomes interesting. For this reason, OGO-I data contained in this study are not generally useful in studying the gyrofrequency cutoff of whistler-mode propagation.

The fundamental difficulty of ray tracing in an anisotropic medium has long been recognized by theoreticians. The modern ray tracing equations were developed by Haselgrove [1954]. Prior to that time there was apparently no satisfactory way of ray tracing in an anisotropic medium where the magnetic field had a large curvature. The Haselgrove equations were applied to whistler-mode paths by Maeda and Kimura [1956], Hines, et al [1959], Yabroff [1961], and Kimura [1966]. Both Kimura and Hines, et al included the effects of ions in their calculations. Kimura demonstrated the effect of ions on the ray paths of waves having frequencies below the lower hybrid resonance. R. L. Smith and B. C. Edgar of the Stanford Radioscience Laboratory have recently improved the Kimura and Yabroff ray tracing programs by adding new features which reduce the tendencies in both of the above programs to over-estimate the corrections to the refractive index vector when this vector is near the resonance cone or near the turn-around point.

This program is utilized in Chapter VII to determine ray paths to the satellites and hence, the loss due to divergence in the received

signals. These results are then compared to the divergence loss indicated by geometrical spreading in the first-approximation model described below, and also to the divergence loss indicated by the virtual source method.

In the meantime, it was decided that the sophisticated techniques of ray tracing would not be used in the first-approximation model, but would be utilized later (in Chapter VII) as a refinement to the model. Instead, the problem of divergence loss was simplified (perhaps over-simplified) by assuming that the vlf signals propagate exactly along the lines of force of the earth's magnetic field. Using this assumption, the limiting cone for the ray direction is defined simply by the geometrical spreading of the geomagnetic field. The method of calculating divergence loss for the first-approximation model using this assumption will now be considered.

Using the centered dipole approximation for the earth's magnetic field [Mlodnosky and Helliwell, 1962], we have

$$f_H = f_{Heq} \left(\frac{R_O}{R} \right)^3 (1 + 3 \sin^2 \phi)^{\frac{1}{2}} \quad (3.15)$$

where

- f_H = electron gyrofrequency
- f_{Heq} = electron gyrofrequency at the equator
($R = R_O$, $\phi = \phi_O$) = 880 kHz
- R = geocentric radius
- R_O = mean earth radius = 6370 km
- ϕ = geomagnetic latitude.

Since

$$f_H = \frac{eB}{2\pi m}, \text{ i.e., } f_H \propto B$$

we may write for Fig. 33

$$B = B_{eq} \left(\frac{R_O}{R} \right)^3 (1 + 3 \sin^2 \phi)^{\frac{1}{2}}, \quad (3.16)$$

- where e = charge on an electron
- m = mass of electron
- B = imposed magnetic field = μH

μ = permeability of the medium

B_{eq} = imposed magnetic field at the equator at the earth's surface

R_1 = distance to A_1 .

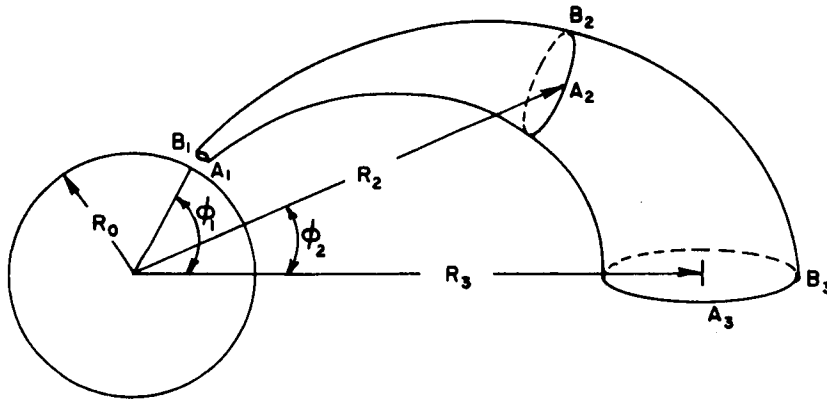


FIG. 33. TO ILLUSTRATE DIVERGENCE OF A FIELD-ALIGNED WHISTLER-MODE WAVE.

Then,

$$\frac{B_3}{B_1} = \frac{B_{eq} (R_0/R_3)^3}{B_{eq} (R_0/R_1)^3 (1 + 3 \sin^2 \phi_1)^{\frac{1}{2}}}, \quad (3.17)$$

which may be written, for values of R_1 approximately equal to R_0 , as

$$\frac{B_3}{B_1} \cong \frac{(R_0/R_3)^3}{(1 + 3 \sin^2 \phi_1)^{\frac{1}{2}}}. \quad (3.18)$$

If we assume strictly ducted propagation with the whistler-mode energy following field lines exactly, the spreading factor as the signal propagates from area A_1 to area A_3 in Fig. 33 will be determined by the ratio of A_3 to A_1 .

Since,

$$A_3 \propto 1/B_3 \quad (3.19)$$

and

$$A_1 \propto 1/B_1 \quad (3.20)$$

we may write Eq. (3.18) as

$$\frac{A_3}{A_1} = (1 + 3 \sin^2 \phi_1)^{\frac{1}{2}} (R_3/R_0)^3 . \quad (3.21)$$

Then the loss due to spreading becomes

$$10 \log (A_3/A_1) \text{ db} . \quad (3.22)$$

The spreading loss for any intermediate point such as A_2 in Fig. 33 may be determined in a similar manner.

Note that Eq. (3.21) and Eq. (3.22) utilize the satellite parameters of geomagnetic latitude and geocentric radius. If one knows the gyro-frequency at a given satellite location, then from Eq. (3.19) and Eq. (3.20) the spreading loss from Eq. (3.22) becomes simply

$$10 \log (f_{H1}/f_{H2}) \text{ db} \quad (3.23)$$

where

f_{H1} = electron gyrofrequency at location A_1 in Fig. 33

and

f_{H2} = electron gyrofrequency at the satellite.

E. IMPEDANCE TRANSFORMATION EFFECTS

Vlf signals are detected at the satellite by means of a 9.5 foot diameter loop antenna which measures the magnetic field component of the signal in the direction of the satellite axis. Intensities are given in

db with respect to 1 gamma rms.

In a magnetoionic plasma, the magnetic field strength H is presumed always to be equal to the flux density B divided by the permeability of free space. However, the ratio of electric to magnetic field strength E/H equals Z , the local wave impedance. This impedance is the free-space impedance Z_0 , divided by the local refractive index, which is a function of the parameters of the medium. For instance, an infinite plane wave propagating in free space, with a magnetic flux density of 1 gamma would have an electric field strength of 0.3 v/m and a magnetic field strength of 7.96×10^{-4} amperes/meter.

The work of Crary, discussed in Section B above, provides a means of determining the field intensity in the ionosphere just above the earth-ionosphere boundary of a wave launched into the whistler mode from a short vertical antenna on the ground. In Crary's calculations it was assumed that the refractive index of the ionosphere, just above the boundary, was 2.23. It is now necessary to consider impedance transformation effects between this point of launching and the loop antenna aboard OGO-I.

For the region just above the boundary, we may write

$$H_i = \frac{E_i}{Z_i} = \frac{E_i}{Z_0/n_1} = \frac{E_i n_1}{Z_0}, \quad (3.24)$$

where

E_i = electric field intensity of the transmitted ionosphere wave

H_i = magnetic field intensity of the transmitted ionosphere wave

Z_0 = free-space wave impedance

Z_i = local wave impedance at the point of launching

n_1 = refractive index of the medium at the point of launching.

Similarly, at the satellite, we may write

$$H_2 = \frac{E_2}{Z_2} = \frac{E_2}{Z_0/n_2} = \frac{E_2 n_2}{Z_0}, \quad (3.25)$$

where

E_2 = electric field intensity of the wave at the satellite

H_2 = magnetic field intensity of the wave at the satellite

Z_2 = local wave impedance at the satellite

Z_0 = free space wave impedance

n_2 = refractive index of the medium at the satellite.

From the foregoing, it is apparent that the ratio of the electric to the magnetic field of the wave will continually change as it propagates from the earth-ionosphere boundary to the satellite, and will be determined at each point by the refractive index at that point. Helliwell [1965] has shown that under conditions of whistler-mode propagation, the change of refractive index for longitudinal propagation near the lower part of the F2 layer is less than 10 per cent in one wavelength. It is not unreasonable then to consider this region of the medium to be slowly varying for the purposes of this discussion. In the E-region this assumption is less valid, and obviously is a very debatable question, properly handled only by a full wave treatment such as outlined by Pitteway and Jespersen [1966]. However, if one is not interested in details of the wave structure in this transition region (the E-region) then it should be possible to choose a suitable boundary which will allow adequate representation of the wave at regions removed from the boundary.

Under slowly varying conditions reflections can be neglected to a first approximation, and propagation of the wave from the boundary to the satellite may be compared to waves on a tapered transmission line where the ratio of E to H changes gradually. With no energy being reflected or absorbed the power density in the traveling wave must remain constant. Hence we may write

$$P_1 = P_2$$

or

$$E_1 \times H_1 = E_2 \times H_2$$

In general

$$P = \text{constant} = \frac{E^2}{Z} = H^2 Z \quad (3.26)$$

Then from Eqs. (3.24), (3.25), and (3.26), we have

$$P_i = H_i^2 Z_i = \frac{E_i^2 n_1^2}{Z_o^2} \cdot \frac{Z_o}{n_1} = \frac{E_i^2 n_1}{Z_o} , \quad (3.27)$$

and

$$P_2 = H_2^2 Z_2 = \frac{H_2^2 Z_o}{n_2} . \quad (3.28)$$

But $P_i = P_2$, therefore

$$\frac{H_2^2 Z_o}{n_2} = \frac{E_i^2 n_1}{Z_o} . \quad (3.29)$$

Solving for H_2 we have

$$H_2 = \frac{E_i}{Z_o} (n_1 n_2)^{\frac{1}{2}} \text{ amperes/m} \quad (3.30)$$

where H_2 = magnetic field intensity at the satellite.

E_i is readily obtained from Fig. 27, $n_1 = 2.2$ and $Z_o = 377$.

The effects of absorption and divergence as calculated in Sections C and D may be included by inserting a reduction factor, R_H , in the denominator of Eq. (3.30). We then have

$$H_2 = \frac{E_i (n_1 n_2)^{\frac{1}{2}}}{Z_o R_H} \quad (3.31)$$

where

$$(\text{Absorption Loss} + \text{Spreading Loss}) \text{ db} = 20 \log R_H$$

or

$$R_H = \log^{-1} [(\text{Absorption Loss} + \text{Spreading Loss})/20] . \quad (3.32)$$

The plan is now complete. All of the factors in Eq. (3.31) except n_2 are known or may be obtained from the methods outlined in this chapter. Hence, if the refractive index at the satellite can be determined, Eq. (3.31) may be used to compute the intensity of the field which the OGO-I loop should measure.

The determination of n_2 and the application of the above methods for calculating H_2 are illustrated by two examples in the following section. These calculated values are then compared to the values measured by OGO-I.

F. TOTAL PATH CALCULATIONS

Using the first-approximation model discussed above, total-path attenuation has been computed, and for easy comparison with measured values, has been plotted as the dashed lines in Figs. 34 through 44.

The following two examples illustrate the method by which these calculations are made.

Example 1

NAA 17.8 kHz	1,000 kw	0122 UT	24 Nov. 1964
$R = 17.243$ kkm		$d_e = 0.635$ kkm	
$\phi = -9.8^\circ$		$d_f = 22.0$ kkm	
$\lambda = -66.1^\circ$		$f_H = 41.1$ kHz	
$L = 2.9$			

The foot of the field line in the northern hemisphere is at 40°N and 71°W (51° geomagnetic latitude, where the local time is ≈ 8 pm).

(a) From Fig. 27

$$E_i = (10^{-4})(1,000)^{\frac{1}{2}} = 3.16 \times 10^{-3} \text{ v/m}$$

(b) From Fig. 29, total absorption through the lower and upper ionosphere is approximately 4 db.

(c) From Eq. (3.21), we may compute the power spreading factor:

$$R/R_o = \frac{17,243}{6,370} = 2.71$$

$$\frac{A_3}{A_1} = (2.71)^3 (1 + 3 \sin^2 40^\circ)^{\frac{1}{2}} = 29.7 .$$

From Eq. (3.22), this represents a spreading loss of

$$10 \log 29.7 = 14.7 \text{ db} .$$

It should be noted here that the same result may be obtained from Eq. (3.23) utilizing the electron gyrofrequency at the field line foot and at the satellite. Then we have

$$\text{db} = 10 \log \frac{1225 \text{ kHz}}{41.1 \text{ kHz}} = 14.7 \text{ db} .$$

The losses due to absorption and spreading are

$$14.7 \text{ db (spreading)} + 4 \text{ db (absorption)} = 18.7 \text{ db} .$$

(d) To consider the effects of impedance transformation as outlined in Section E, it is necessary to determine the refractive index of the medium at the satellite.

Angerami and Carpenter [1966] show the 1963 equatorial summer-time electron density $[N_e(\text{eq})]$ at night and at $L = 2.9$ to be approximately 5×10^2 electrons per cc.

It is well established that electron densities in the magnetosphere experience diurnal, seasonal and solar cycle variations [Carpenter, 1962b] and that densities at sunspot maximum may be nearly twice as high in December as in June [Smith, 1961a]. Since data in this example were taken in November of 1964, a year of sunspot minimum, we will estimate [Angerami, private communication] the value of N to be approximately 1.6 times higher than that given by Angerami and Carpenter or $N = 8 \times 10^2$ el/cc.

Plasma frequency at the satellite is then

$$f_o = 9(800)^{\frac{1}{2}} = 254 \text{ kHz} .$$

Since $f_o \gg f_H$ and $\theta \approx 0$ we may write from Eq. (1.6)

$$\begin{aligned} n &\approx \frac{f_o}{[ff_H(1-f/f_H)]^{\frac{1}{2}}} \\ &= \frac{2.54 \times 10^5}{[(1.78 \times 10^4)(4.11 \times 10^4)(1-0.433)]^{\frac{1}{2}}} \\ &= 12.4 \end{aligned}$$

(e) From Eq. (3.31) we calculate the value of H at the satellite:

$$\begin{aligned} H &= \frac{(3.16 \times 10^{-3})[(2.2)(12.4)]^{\frac{1}{2}}}{(3.77 \times 10^2)(8.6)} \\ &= 5.1 \times 10^{-6} \text{ amperes/m.} \end{aligned}$$

The factor 8.6 in the denominator of the above equation represents the reduction factor, R_H , in magnetic field intensity due to absorption and spreading. From part (c) we have a total loss of 18.7 db from absorption and spreading, hence we may write from Eq. (3.32)

$$18.7 \text{ db} = 20 \log R_H$$

$$R_H = 8.6$$

As pointed out in Section E, 1 gamma corresponds to a magnetic field strength of 7.96×10^{-4} amp/m. Therefore we may reference the computed signal intensity at the satellite as follows:

$$\begin{aligned} \text{db} &= 20 \log \frac{7.96 \times 10^{-4}}{5.1 \times 10^{-6}} \\ &= 43.9 \text{ db below 1 gamma.} \end{aligned}$$

This calculated value is plotted in Fig. 34.

Example 2

NAA 17.8 kHz 1,000 kw 0107 UT 24 Nov. 1964
R = 21.128 kkm $d_e = 0.606$ kkm
 $\phi = -5.5^\circ$ $d_f = 25.386$ kkm
 $\lambda = -71.7^\circ$ $f_H = 23.6$ kHz
L = 3.4

The location of the foot of the field line in the Northern hemisphere is 44°N and 75°W (55° geomagnetic latitude, where the local time is 8:07 pm).

(a) From Fig. 27

$$E_i = (7 \times 10^{-5})(1,000)^{\frac{1}{2}} = 2.21 \times 10^{-3} \text{ v/m}$$

(b) From Fig. 29, total absorption is approximately 3.7 db.

(c) From Eq. (3.21), the power spreading factor is 57.1 which from Eq. (3.22) represents a spreading loss of 17.6 db.

(d) From Angerami-Carpenter [1966] the 1963 equatorial summertime electron density for $L = 3.4$ nighttime is approximately 4×10^2 el/cc. Using the same arguments as in step (d) of Example 1, this is modified to a value of 6.4×10^2 el/cc. Plasma frequency is then 227 kHz. From Eq. (1.6)

$$n = 22.4 .$$

(e) From Eq. (3.32) we calculate the value of H at the satellite.

$$\begin{aligned} H &= \frac{(2.21 \times 10^{-3})[(2.2)(22.4)]^{\frac{1}{2}}}{(3.77 \times 10^2)(13.4)} \\ &= 3.1 \times 10^{-6} \text{ amp/m.} \end{aligned}$$

Referencing this to 1 gamma we have

$$\begin{aligned} \text{db} &= 20 \log \frac{7.96 \times 10^{-4}}{3.1 \times 10^{-6}} \\ &= 48.2 \text{ db below 1 gamma.} \end{aligned}$$

Note that when this value is plotted in Fig. 34, it is almost 40 db above the measured value. Indeed this particular example was chosen because it represents one of the few occasions in all of the OGO-I data where the calculated value greatly exceeds the measured value. It is believed that this may be new evidence of cyclotron absorption, a phenomenon which has not been considered in the first-approximation model. This possibility is discussed in Chapter IX.

These two examples illustrate the methods used to calculate all plotted field intensities at the satellite, but for one exception; the variation of electron density with latitude. This factor did not enter into Examples 1 or 2 since the satellite latitude was near zero degrees in each case. For calculations at latitudes not near the equatorial plane, the Angerami-Carpenter electron densities were modified (increased) according to a graphical procedure recommended by Dr. Angerami.

Since the diffusive equilibrium model of electron density seems to fit whistler data best for L-values inside the knee (L-values less than approximately 4) densities were modified according to this model.

Using the procedures outlined above, field intensities have been calculated for every satellite location where vlf fixed-frequency whistler-mode signals have been observed in OGO-I and are plotted, along with the measured values, in Chapter IV.

IV. THE OGO-I DATA

A. INTRODUCTION

All of the vlf data obtained from OGO-I by the methods illustrated in Figs. 4 through 22 have been scaled and plotted and are presented in Figs. 34 through 44. Universal time is used as the independent variable with magnetic field strength (db below 1 gamma) along the ordinate. All pertinent satellite positional information is included on each figure. The solid line represents peak intensities of the measured data from OGO-I, the dashed line represents values calculated utilizing the first-approximation model of Chapter III. In Chapter VII, the earth-ionosphere waveguide loss, the absorption loss, and the divergence loss are all reconsidered and more sophisticated techniques are utilized to improve the first-approximation model. The dash-dot line represents values calculated after these modifications to the model have been made.

B. OGO-I FIELD INTENSITIES VERSUS UNIVERSAL TIME

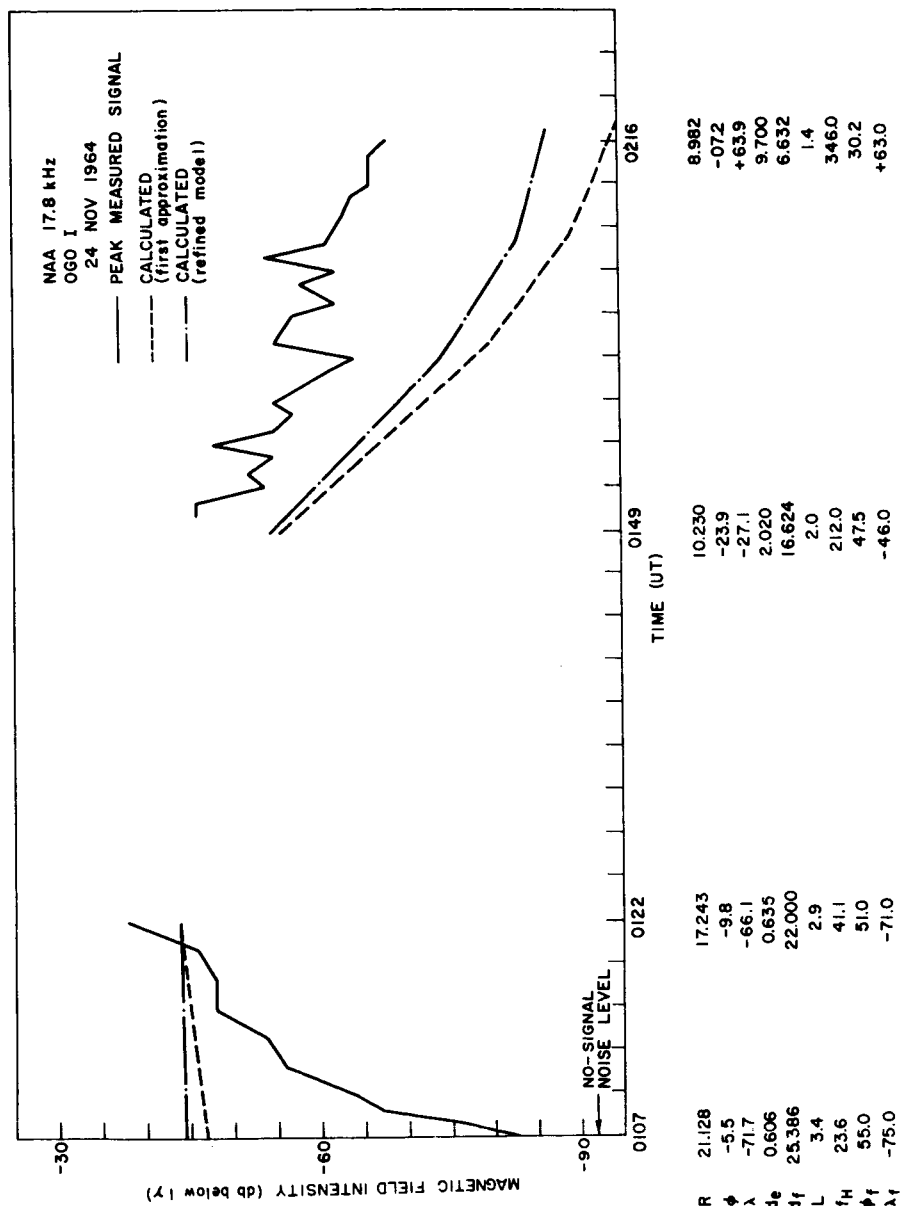


FIG. 34. OGO-I MAGNETIC FIELD STRENGTH VERSUS TIME FOR NAA ON 24 NOV. 1964. R = geocentric distance (kkm); ϕ = Northern geomagnetic latitude and λ = Eastern longitude (degrees) of subsatellite point; d_e = great-circle distance (kkm) from NAA to the foot of the field line in the Northern hemisphere; d_f = distance (kkm) along the field line from the Northern foot to the satellite; L = L-value; f_H = electron gyrofrequency (kHz) at the satellite; ϕ_f = Northern geomagnetic latitude and λ_f = Eastern longitude of the field line foot. The solid line represents peak measured values, the dashed line represents values calculated using the first-approximation model, and the dash-dot line represents values calculated using the refined model.

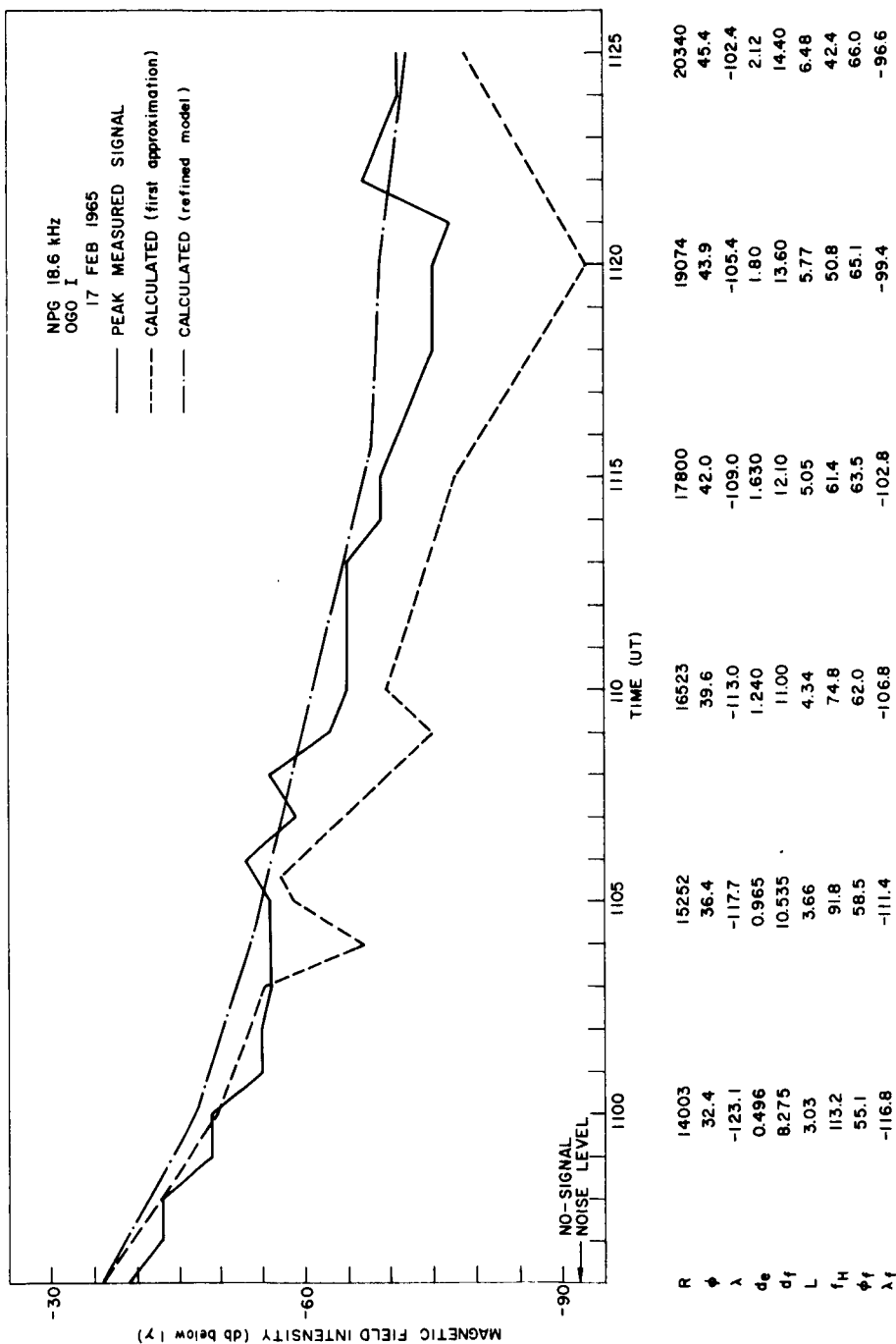


FIG. 35. OGO-I MAGNETIC FIELD STRENGTH VERSUS TIME FOR NPG ON 17 FEB. 1965. R = geocentric distance (kkm); ϕ = Northern geomagnetic latitude and λ = Eastern longitude (degrees) of subsatellite point; d_e = great-circle distance (kkm) from NPG to the foot of the field line in the Northern hemisphere; d_f = distance (kkm) along the field line from the Northern foot to the satellite; L = L-value; f_H = electron gyrofrequency (kHz) at the satellite; ϕ_f = Northern geomagnetic latitude and λ_f = Eastern longitude of the field line foot. The solid line represents peak measured values, the dashed line represents values calculated using the first-approximation model, and the dash-dot line represents values calculated using the refined model.

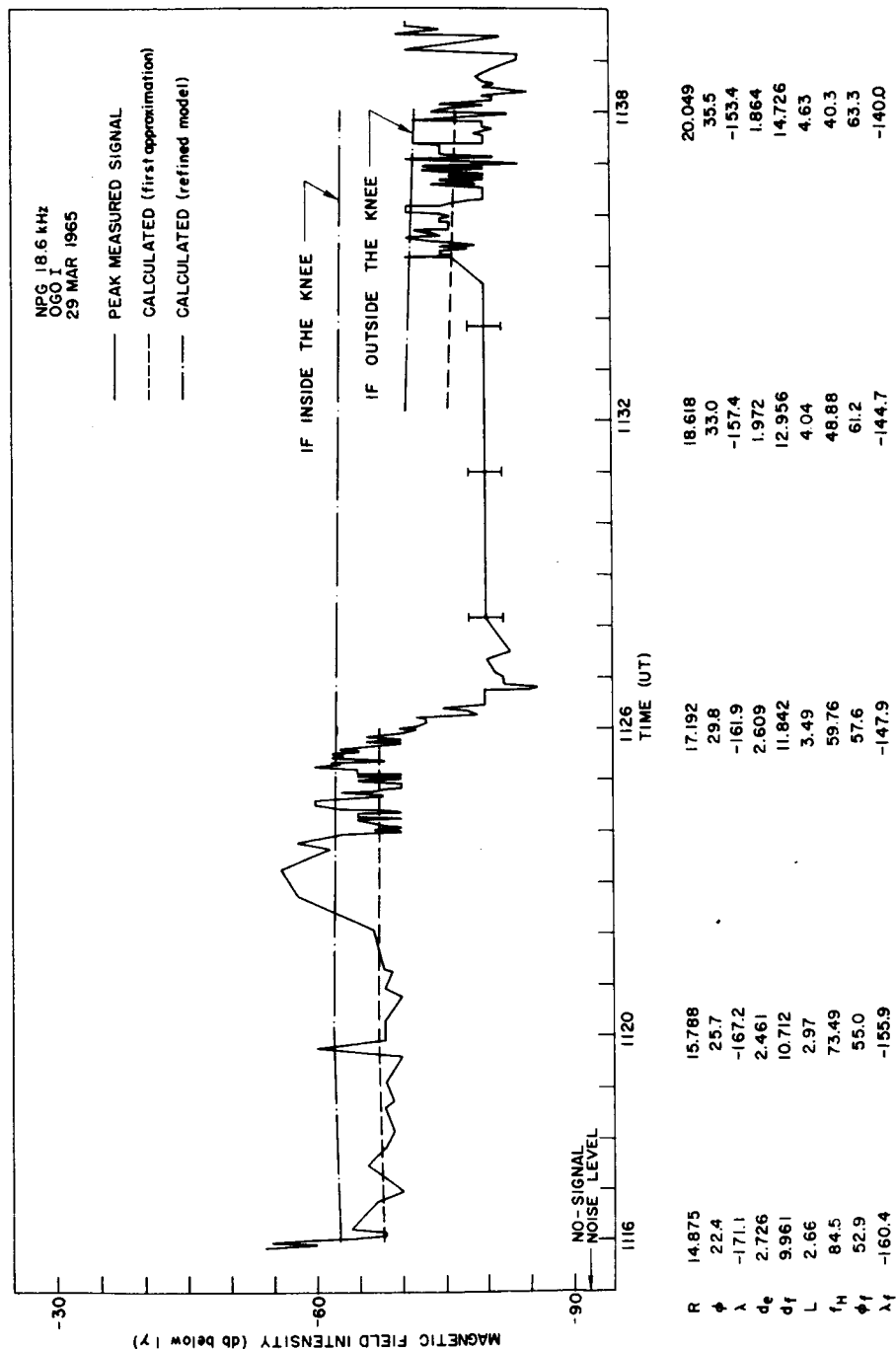
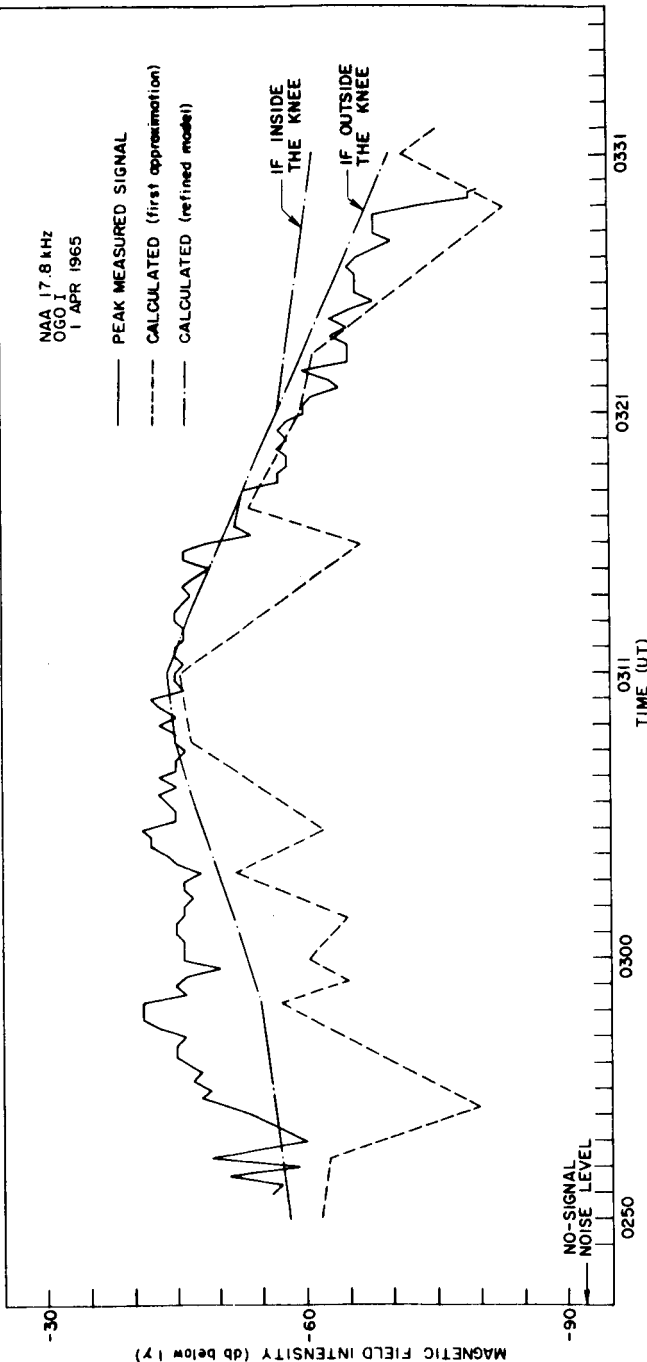


FIG. 36. OGO-I MAGNETIC FIELD STRENGTH VERSUS TIME FOR NPG ON 29 MAR. 1965. R = geocentric distance (kkm); ϕ = Northern geomagnetic latitude and λ = Eastern longitude (degrees) of subsatellite point; d_e = great-circle distance (kkm) from NPG to the foot of the field line in the Northern hemisphere; d_f = distance (kkm) along the field line from the Northern foot to the satellite; L = L-value; f_H = electron gyrofrequency (kHz) at the satellite; ϕ_f = Northern geomagnetic latitude and λ_f = Eastern longitude of the field line foot. The solid line represents peak measured values, the dashed line represents values calculated using the first-approximation model, and the dash-dot line represents values calculated using the refined model.



R	10.647	11.812	13.860	16.064	18.396
ϕ	3.6	19.9	32.1	38.8	42.7
λ	-90.5	-74.1	-59.9	-49.7	-41.6
d_e	2.330	1.205	0.538	1.279	1.871
d_f	7.499	7.386	8.934	11.260	12.377
L	1.70	2.16	3.10	4.14	5.22
f_H	183.5	156.0	111.3	76.6	53.2
ϕ_f	38.9	45.2	54.6	60.0	63.9
λ_f	-83.3	-72.6	-60.8	-52.0	-45.7

FIG. 37. OGO-I MAGNETIC FIELD STRENGTH VERSUS TIME FOR NAA ON 1 APR. 1965. R = geocentric distance (kkm); ϕ = Northern geomagnetic latitude and λ = Eastern longitude (degrees) of subsatellite point; d_e = great-circle distance (kkm) from NAA to the foot of the field line in the Northern hemisphere; d_f = distance (kkm) along the field line from the Northern foot to the satellite; L = L-value; f_H = electron gyrofrequency (kHz) at the satellite; ϕ_f = Northern geomagnetic latitude and λ_f = Eastern longitude of the field line foot. The solid line represents peak measured values, the dashed line represents values calculated using the first-approximation model, and the dash-dot line represents values calculated using the refined model.

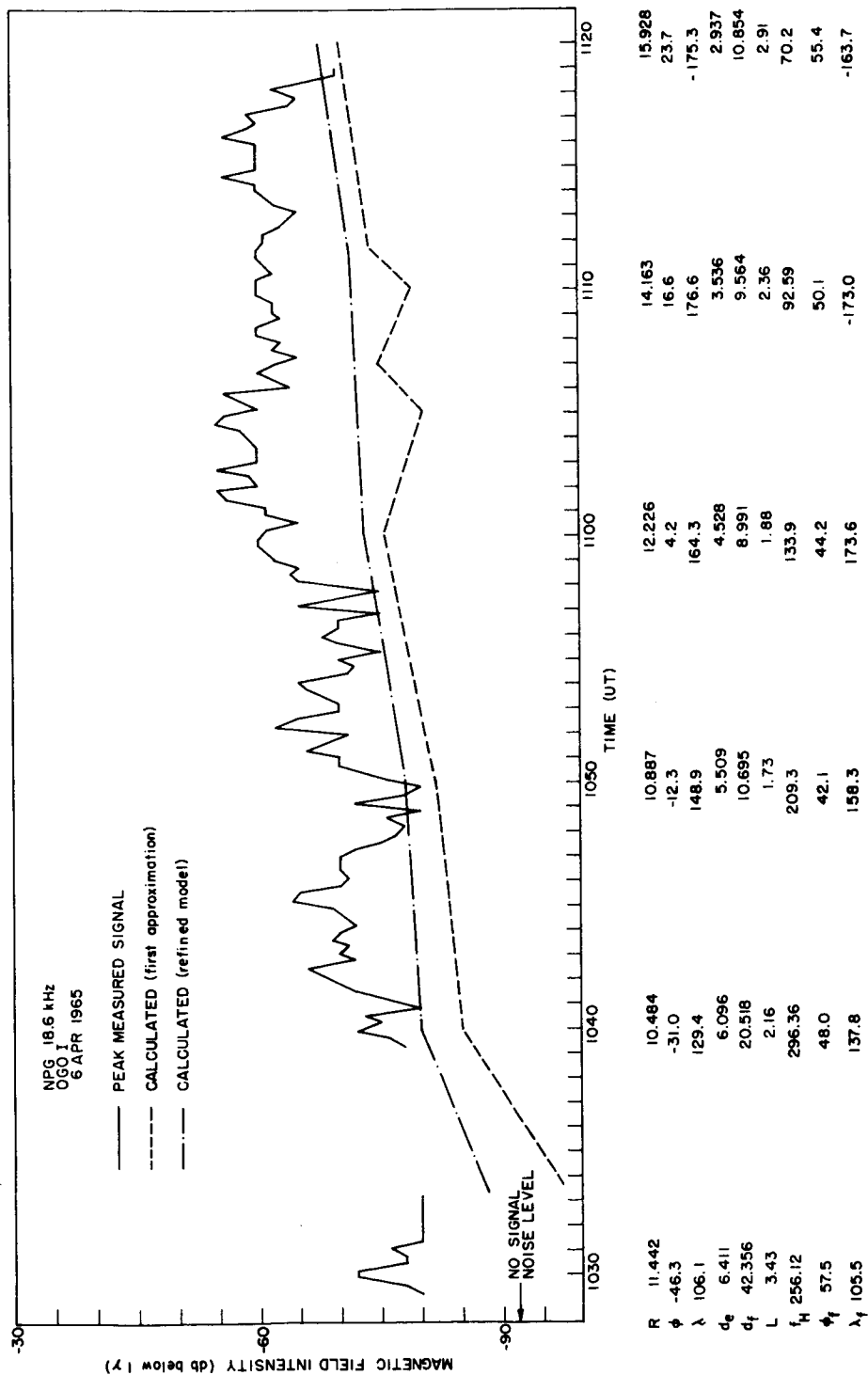


FIG. 38. OGO-I MAGNETIC FIELD STRENGTH VERSUS TIME FOR NPG ON 6 APR. 1965. R = geocentric distance (kkm); ϕ = Northern geomagnetic latitude and λ = Eastern longitude (degrees) of subsatellite point; d_e = great-circle distance (kkm) from NPG to the foot of the field line in the Northern hemisphere; d_f = distance (kkm) along the field line from the Northern foot to the satellite; L = L-value; f_H = electron gyrofrequency (kHz) at the satellite; ϕ_f = Northern geomagnetic latitude and λ_f = Eastern longitude of the field line foot. The solid line represents peak measured values, the dashed line represents values calculated using the first-approximation model, and the dash-dot line represents values calculated using the refined model.

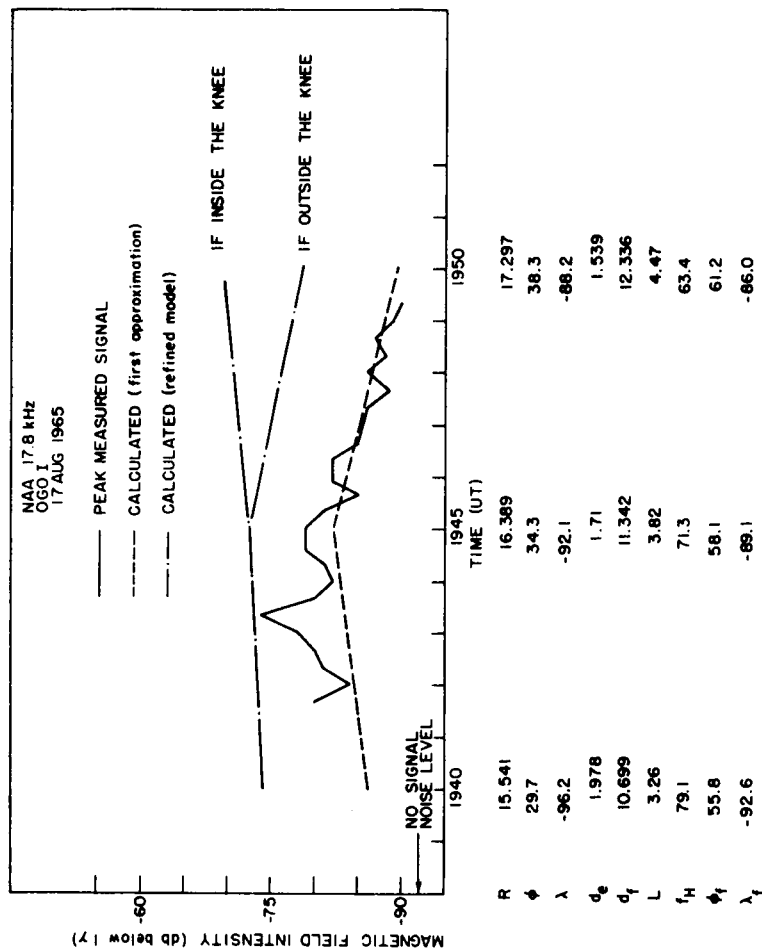


FIG. 39. OGO-I MAGNETIC FIELD STRENGTH VERSUS TIME FOR NAA ON 17 AUG. 1965. R = geocentric distance (kkm); ϕ = Northern geomagnetic latitude and λ = Eastern longitude (degrees) of subsatellite point; d_e = great-circle distance (kkm) from NAA to the foot of the field line in the Northern hemisphere; d_f = distance (kkm) along the field line from the Northern foot to the satellite; L = L-value; f_H = electron gyrofrequency (kHz) at the satellite; ϕ_f = Northern geomagnetic latitude and λ_f = Eastern longitude of the field line foot. The solid line represents peak measured values, the dashed line represents values calculated using the first-approximation model, and the dash-dot line represents values calculated using the refined model.

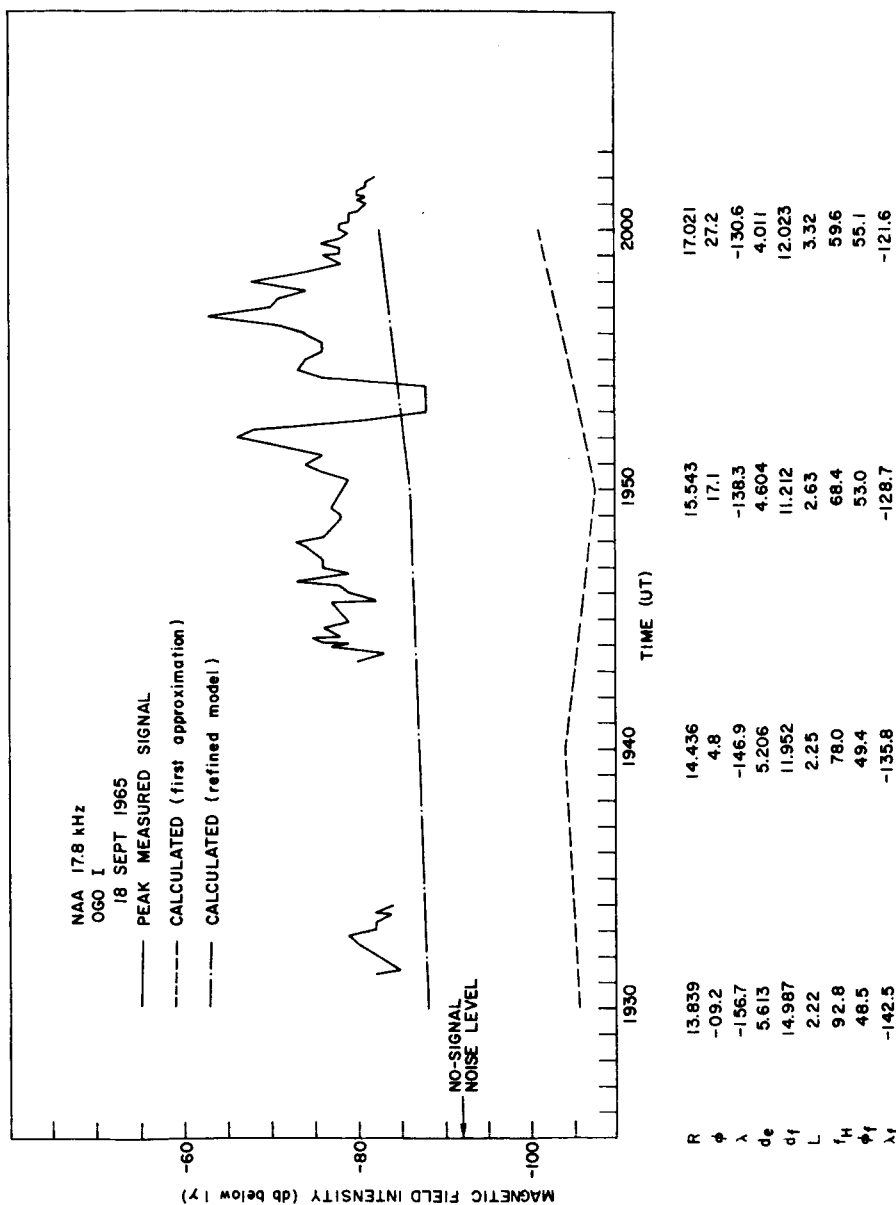


FIG. 40. OGO-I MAGNETIC FIELD STRENGTH VERSUS TIME FOR NAA ON 18 SEP. 1965. R = geocentric distance (kkm); ϕ = Northern geomagnetic latitude and λ = Eastern longitude (degrees) of subsatellite point; d_e = great-circle distance (kkm) from NAA to the foot of the field line in the Northern hemisphere; d_f = distance (kkm) along the field line from the Northern foot to the satellite; L = L-value; f_H = electron gyrofrequency (kHz) at the satellite; ϕ_f = Northern geomagnetic latitude and λ_f = Eastern longitude of the field line foot. The solid line represents peak measured values, the dashed line represents values calculated using the first-approximation model, and the dash-dot line represents values calculated using the refined model.

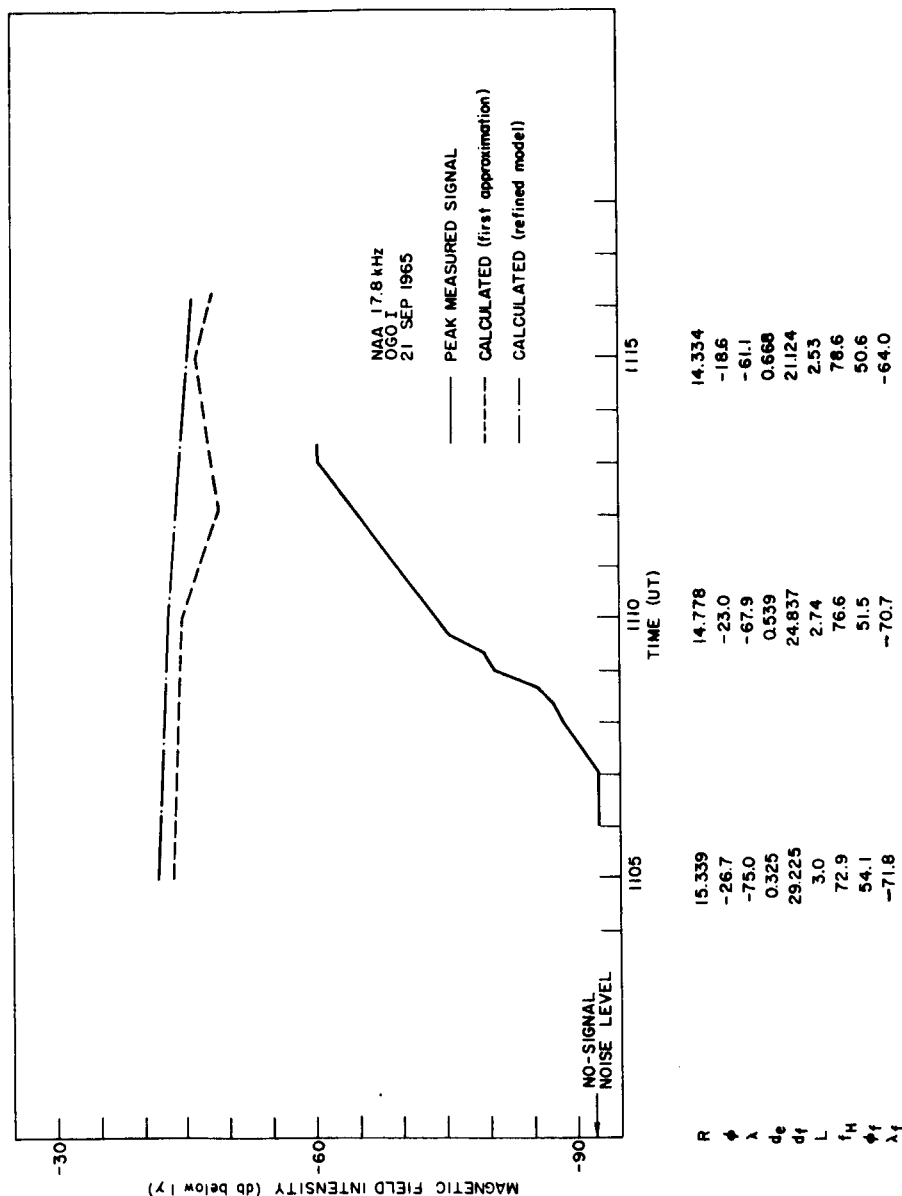


FIG. 41. OGO-I MAGNETIC FIELD STRENGTH VERSUS TIME FOR NAA ON 21 SEP. 1965. R = geocentric distance (kkm); ϕ = Northern geomagnetic latitude and λ = Eastern longitude (degrees) of subsatellite point; d_e = great-circle distance (kkm) from NAA to the foot of the field line in the Northern hemisphere; d_f = distance (kkm) along the field line from the Northern foot to the satellite; L = L-value; f_H = electron gyrofrequency (kHz) at the satellite; ϕ_f = Northern geomagnetic latitude and λ_f = Eastern longitude of the field line foot. The solid line represents peak measured values, the dashed line represents values calculated using the first-approximation model, and the dash-dot line represents values calculated using the refined model.

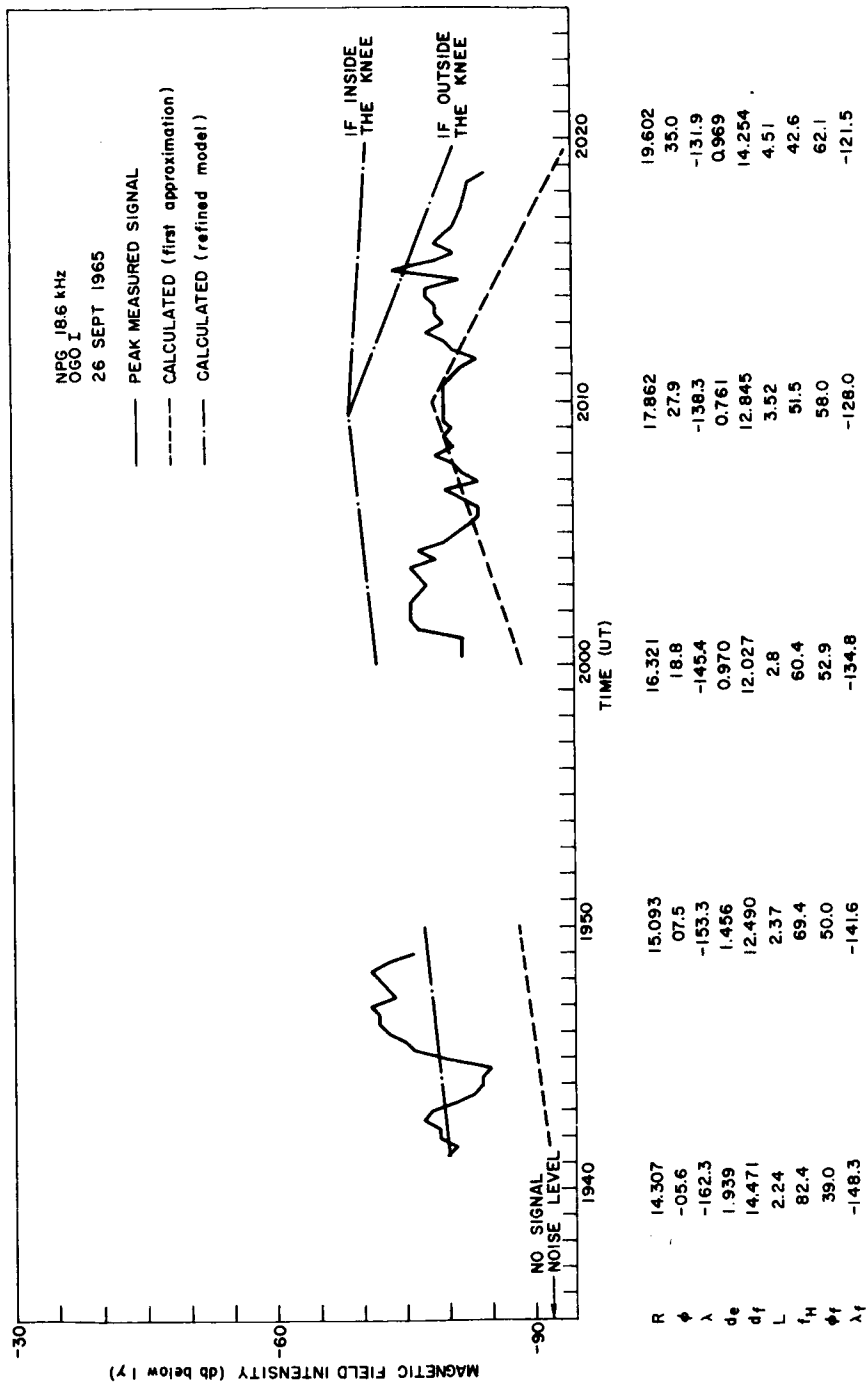


FIG. 42. OGO-I MAGNETIC FIELD STRENGTH VERSUS TIME FOR NPG ON 26 SEP. 1965. R = geocentric distance (kkm); ϕ = Northern geomagnetic latitude and λ = Eastern longitude (degrees) of subsatellite point; d_e = great-circle distance (kkm) from NPG to the foot of the field line in the Northern hemisphere; d_f = distance (kkm) along the field line from the Northern foot to the satellite; L = L-value; f_H = electron gyrofrequency (kHz) at the satellite; ϕ_f = Northern geomagnetic latitude and λ_f = Eastern longitude of the field line foot. The solid line represents peak measured values, the dashed line represents values calculated using the first-approximation model, and the dash-dot line represents values calculated using the refined model.

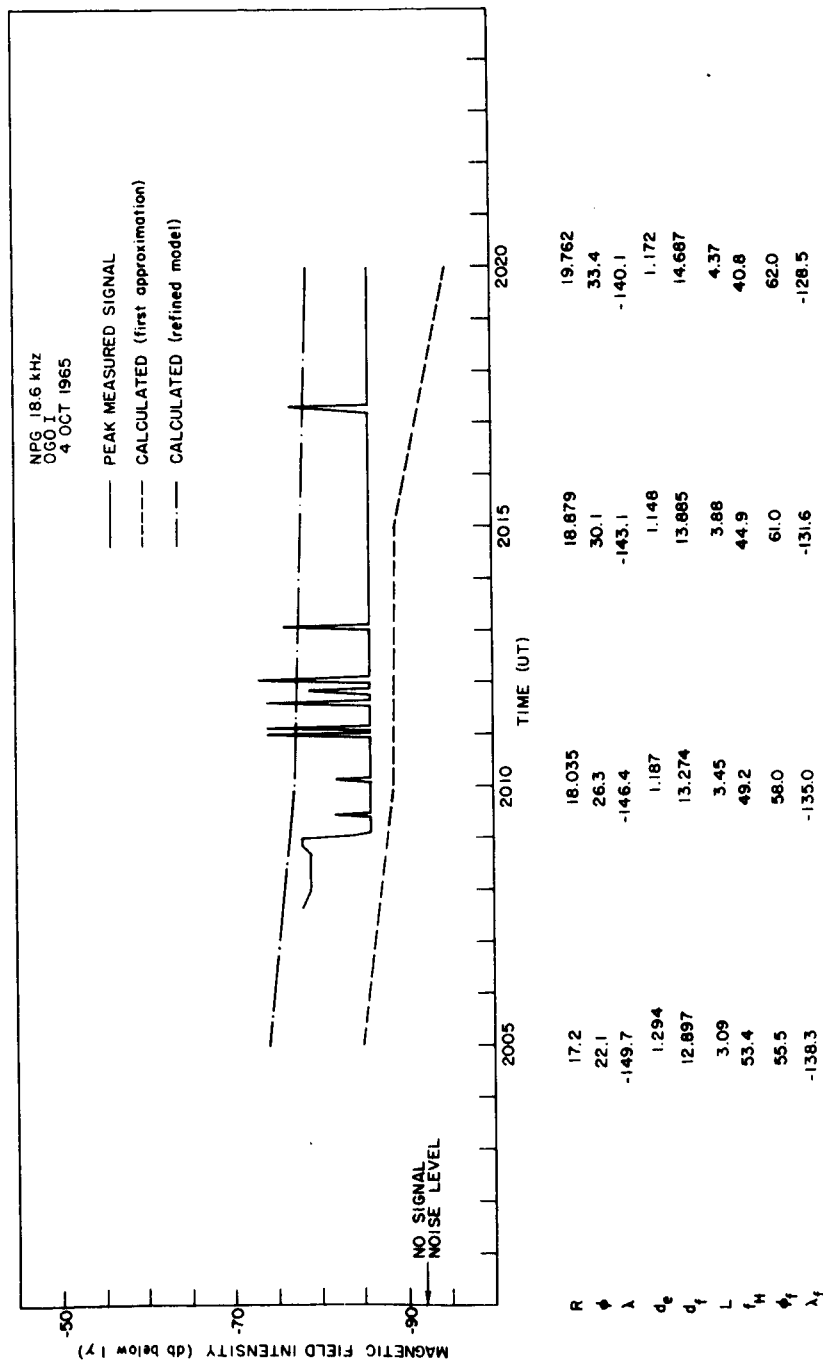


FIG. 43. OGO-I MAGNETIC FIELD STRENGTH VERSUS TIME FOR NPG ON 4 OCT. 1965. R = geocentric distance (kkm); ϕ = Northern geomagnetic latitude and λ = Eastern longitude (degrees) of subsatellite point; d_e = great-circle distance (kkm) from NPG to the foot of the field line in the Northern hemisphere; d_f = distance (kkm) along the field line from the Northern foot to the satellite; L = L-value; f_H = electron gyrofrequency (kHz) at the satellite; ϕ_f = Northern geomagnetic latitude and λ_f = Eastern longitude of the field line foot. The solid line represents peak measured values, the dashed line represents values calculated using the first-approximation model, and the dash-dot line represents values calculated using the refined model.

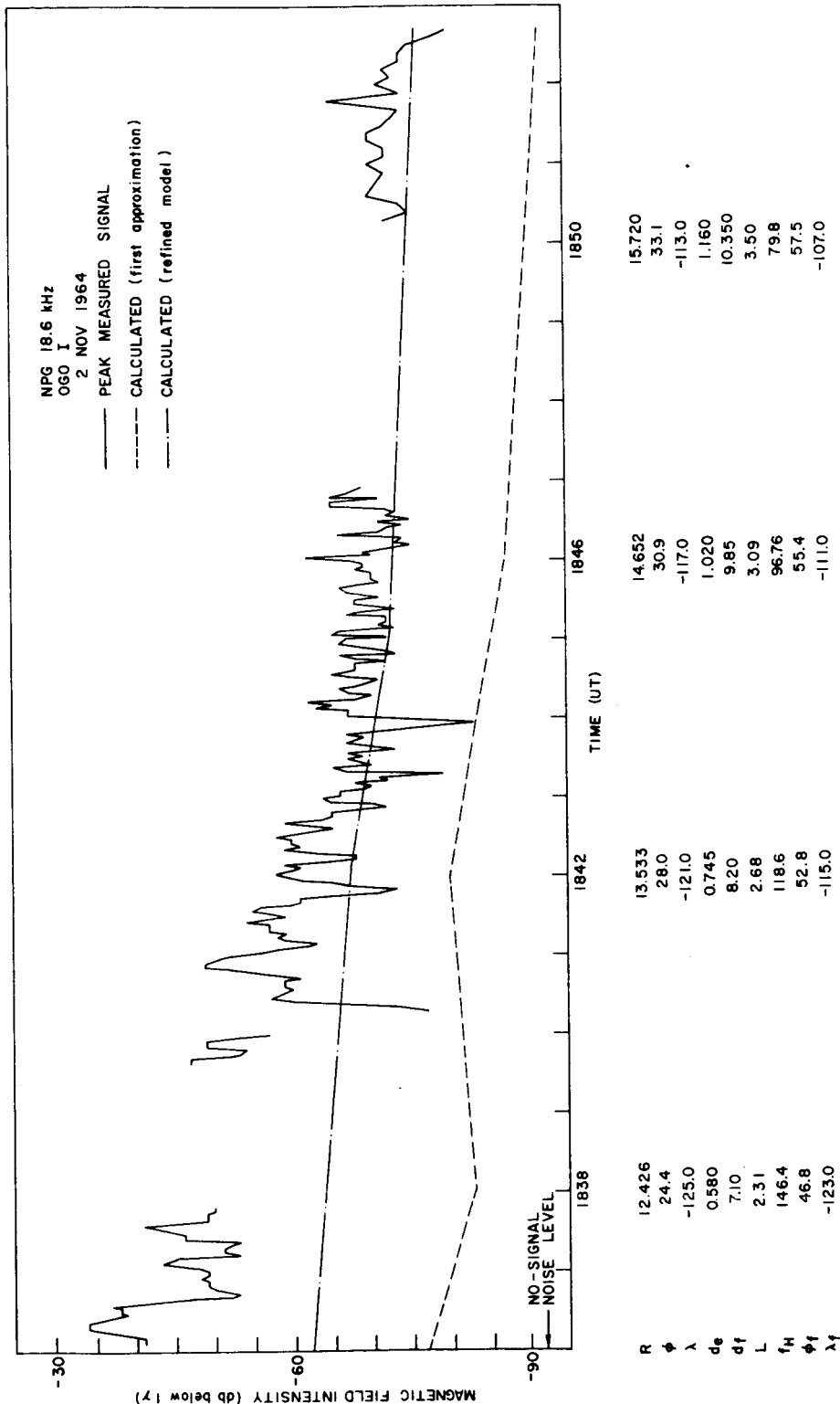


FIG. 44. OGO-I MAGNETIC FIELD STRENGTH VERSUS TIME FOR NPG ON 2 NOV. 1964. R = geocentric distance (kkm); ϕ = Northern geomagnetic latitude and λ = Eastern longitude (degrees) of subsatellite point; d_e = great-circle distance (kkm) from NPG to the foot of the field line in the Northern hemisphere; d_f = distance (kkm) along the field line from the Northern foot to the satellite; L = L-value; f_H = electron gyrofrequency (kHz) at the satellite; ϕ_f = Northern geomagnetic latitude and λ_f = Eastern longitude of the field line foot. The solid line represents peak measured values, the dashed line represents values calculated using the first-approximation model, and the dash-dot line represents values calculated using the refined model.

V. THE OGO-II EXPERIMENT

A. THE SATELLITE

The second Orbiting Geophysical Observatory (OGO-II) was launched from the Pacific Missile Range at 1312 UT on 14 October 1965. The spacecraft and its equipment, in so far as the Helliwell 5002 vlf experiment is concerned, is essentially the same as OGO-I described in Chapter II.

Except for the shape and orientation of the vlf loop antenna, the general configuration of the spacecraft is as shown in Fig. 3. On OGO-II, the vlf antenna is not a circular loop as on OGO-I, but is hexagonal in shape and of such dimensions that it can be contained within a circle whose perimeter is 30 feet; in other words, a hexagon whose maximum diagonal distance is approximately 9.5 feet. In addition, the loop axis is not aligned with the "z" axis of the spacecraft as on OGO-I (see Fig. 3), but rather with the spacecraft "x" axis. In the stabilized flight mode, the "z" axis of the spacecraft always points towards the earth.

The various relationships that exist in QL whistler-mode propagation between the earth's magnetic field and the wave components were discussed in Chapters I and II. For the low-altitude orbit of OGO-II, one is normally justified in assuming that all whistler-mode wave normals start off essentially in a meridional plane along a radius vector (except near the equator), and at 18 kHz will not be changed in direction greatly before reaching the satellite [R. L. Smith, private communication]. Figure 45 shows the spacecraft orientation in stabilized flight mode 3, where it is apparent that for small wave normal angles in the earth-satellite meridional plane, the null condition of the loop will never obtain, and the loop should provide maximum response to whistler-mode signals regardless of the latitudinal position of the spacecraft. Indeed, for sensing the H vector of field-aligned signals with the spacecraft in stabilized flight and the "z" axis pointing towards the earth, this is a more desirable loop orientation than that used in OGO-I.

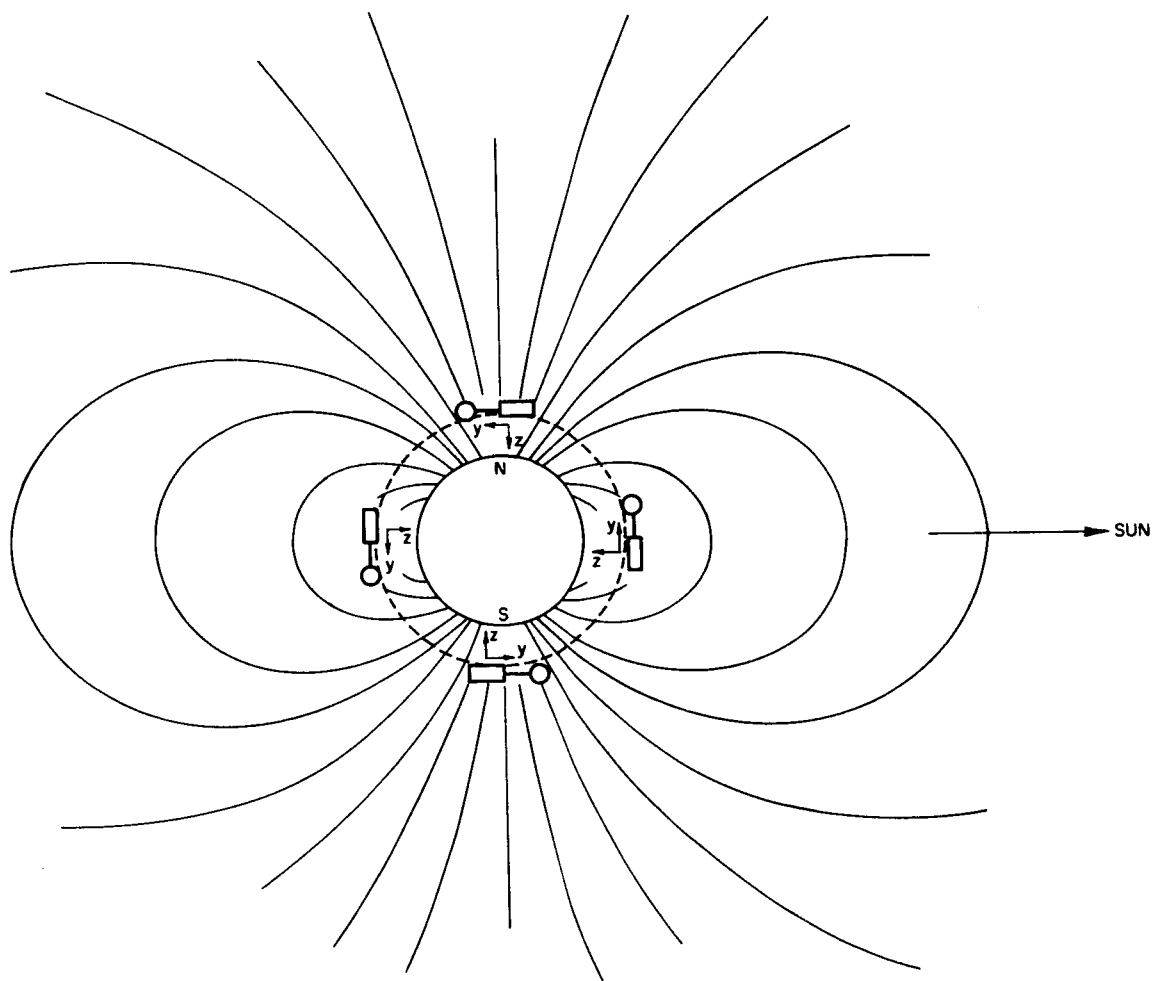


FIG. 45. OGO-II SPACECRAFT AND VLF LOOP ANTENNA ORIENTATION IN STABILIZED FLIGHT MODE 3.

B. THE ORBIT

The nominal OGO-II orbit was planned to be polar and nearly circular; however, an unexpected increase in burn-time of one of the launch vehicle rocket engines placed OGO-II in a somewhat elliptical orbit. Initial perigee was 415 km, and initial apogee was 1507 km. The inclination of the orbit was 87 degrees and the orbital period was 104 minutes. The orbital parameters are shown in Table 4, which was prepared from data supplied by Goddard Space Flight Center.

TABLE 4. OGO-II DEFINITIVE ORBITAL PARAMETERS.

DAY UT	12/29/65 00:00	1/12/66 00:00	1/19/66 00:00	1/26/66 00:00	2/9/66 00:00	3/16/66 00:00
SEMI-MAJOR AXIS KILOMETERS	007339.79	007339.65	007339.59	007339.51	007339.40	007339.07
ECCENTRICITY	0.07441	0.07436	0.07441	0.07445	0.07461	0.07468
INCLINATION DEGREES	087.363	087.362	087.362	087.360	087.361	087.363
MEAN ANOMALY DEGREES	310.395	015.001	227.937	081.388	149.572	147.677
ARGUMENT OF PERIGEE DEGREES	303.710	260.953	239.597	218.252	175.618	069.421
MOTION MINUS DEGREES PER DAY	03.0480	03.0481	03.0481	03.0482	03.0485	03.0492
R. A. OF ASCEND. NODE DEGREES	261.824	257.867	255.889	253.910	249.948	240.050
MOTION MINUS DEGREES PER DAY	00.2834	00.2836	00.2836	00.2836	00.2839	00.2836
ANOMALISTIC PERIOD MINUTES	0104.29668	0104.29382	0104.29258	0104.29079	0104.28845	0104.28150
MOTION MINUS MINUTES PER DAY	0.00021	0.00017	0.00027	0.00016	0.00021	0.00020
HEIGHT OF PERIGEE KILOMETERS	000415.22	000415.46	000415.08	000414.66	000413.41	000412.61
HEIGHT OF APOGEE KILOMETERS	001507.58	001507.07	001507.33	001507.58	001508.62	001508.76
VELOCITY AT PERIGEE KM PER HOUR	028584	028583	028584	028586	028590	028593
VELOCITY AT APOGEE KM PER HOUR	024624	024626	024625	024624	024625	024619
GEOC. LAT. OF PERIGEE DEGREES	-56.199	-80.580	-59.494	-38.204	04.377	69.26

C. EQUIPMENT

Although the basic vlf equipment aboard OGO-II is essentially the same as on OGO-I, substantial refinements were made. These are discussed in detail by Ficklin, et al [1965] and only those pertinent to this study will be discussed briefly here.

As discussed in Chapter II the vlf equipment package contains three step-frequency superheterodynes plus a broadband receiver. In addition, OGO-II carries a double-converting heterodyne phase tracking receiver using two phase-locked local oscillators. This receiver has a 50 Hz bandwidth, and may be tuned upon command from the ground to receive signals at 100 Hz increments in the range 14.4 to 26.3 kHz. As in OGO-I the Band 3 receiver may be tuned to any frequency between approximately 12.5 and 100 kHz in 256 discrete steps. This receiver has a bandwidth of 500 Hz. Tuning of the Band 3 receiver is independent of the tuning of the phase track receiver. Therefore, it is possible, for instance, to have the Band 3 receiver receiving NPG and the phase track receiver simultaneously receiving NAA. The value of this useful feature was nullified somewhat (at least for the earlier revolutions) by a malfunction which altered the normal sequence of impulse commands necessary to tune the Band 3 receiver to a given frequency. As a result, all tuned frequencies of the Band 3 receiver were one step (approximately 342 Hz) below the intended value. Hence, when it was believed that the Band 3 receiver was tuned to NPG (18.6 kHz) it was actually tuned to $18.6 - 0.342$ or approximately 18.258 kHz. In this condition, the center frequency of the receiver is 342 Hz below NPG and 458 Hz above NAA. With a 500 Hz bandwidth, both NAA and NPG appeared in the Band 3 output. For this reason, all of the amplitude data from OGO-II presented in this study were taken from the phase track receiver via film records produced by SRI from the PCM telemetry.

The above is not intended to imply that data from the Band 3 receiver via the VCO and special purpose telemetry are not useful. Valuable information concerning such phenomena as the cut-off of whistler-mode signals with latitude, discussed in Chapter VIII is obtained even though specific amplitudes are not known accurately.

Although features were added to make data retrieval more efficient,

the methods of telemetry and data retrieval from OGO-II are essentially the same as for OGO-I, as are the mechanics of data presentation. These were all discussed in detail in Chapter I. Typical displays of OGO-II data are presented in the following chapter.

Additional refinements involve methods of calibrating, adding the vlf signals to the spacecraft telemetry, and monitoring, but these need not be discussed here.

Calibration and accuracy are discussed in Section E.

D. OBTAINING THE DATA

It was planned to have OGO-II earth-stabilized, with the "z" axis always pointing towards the earth. The attitude control system (ACS), which utilizes reaction wheels, as well as gas jets, performed all of its required post-launch operations quite well. However, the tendency of the horizon scanners to track thermal gradients due to cold atmospheric clouds rather than the earth's horizon caused the argon gas supply to be consumed at a higher-than-expected rate. A quantity of gas normally adequate for one year of stabilized flight was consumed in the process of providing only approximately 3 days of stabilized flight during the first ten days after launch.

The first 144 revolutions of OGO-II were well stabilized, but after that the gas supply was exhausted and the spacecraft developed various additional problems resulting from undervoltage conditions caused by eclipse periods and the inability of the reaction wheels alone to provide proper stabilization and orientation. All components (solar arrays, batteries, regulators, etc.) of the complete power system performed properly for several months. However, perturbations in the attitude of the observatory, due to difficulties with the ACS, greatly reduced the ability of the solar arrays to follow the sun and therefore reduced the power available to experiment loads. On one occasion, the power available was insufficient to support even the minimum "housekeeping" loads, and batteries were discharged to the point where the ACS inverter stopped functioning properly and the 136 MHz tracking transmitter signal was not observed by the monitoring stations. On other occasions, the array tracked

the sun satisfactorily and abundant power was available. These, plus additional problems continue to plague the OGO-II operation. However, at the time of writing of this report, OGO-II is functioning and obtaining useful data.

Table 5 summarizes, by revolution, the ACS modes and the available control during the period of time that data were obtained for this study. This was compiled from the Spacecraft Operations Summary section of the Weekly Operations Report for OGO-II supplied by Goddard Space Flight Center.

TABLE 5. A SUMMARY, BY REVOLUTION, OF THE ACS MODES AND THE AVAILABLE CONTROL FOR OGO-II DURING THE PERIOD OF TIME COVERED BY THIS STUDY.

REV. NOS.	ACS MODE	CONTROL REQ'D.		CONTROL AVAIL.	
		RE. WHEELS	GAS	RE. WHEELS	GAS
0-4	2B	X	X	X	X
5-9	3	X	X	X	X
10-32	2C	X	X	X	X
33-36	3	X	X	X	X
37-103	2C	X	X	X	X
104-114	3	X	X	X	X
115	2A				
116-119	1				
120-127	3	X	X	X	X
128-144	3	X	X	X	

In mode 1 the ACS is inhibited and the spacecraft is drifting. In mode 2A the solar panels are positioned to 180° , receiving maximum illumination from the -y direction. In mode 2B, the sun is acquired and the "-y" axis is pointed towards the sun. In this mode, the spacecraft is slowly spinning around the "y" axis, with a controlled pitch rate of approximately 0.49° per second or about 5 revolutions per hour. Mode 2C is the earth acquisition mode in which the horizon scanners search for a

thermal discontinuity, and upon finding it, "lock on." One additional operation, that of stopping the pitch motion, places the spacecraft in mode 3... stabilized flight. Mode 2C therefore represents a condition where the sun has been acquired, the "-y" axis points towards the sun, and the spacecraft spins around the "y" axis with a controlled pitch rate of approximately 5 revolutions per hour. Mode 3 is stabilized flight with the "z" axis always pointing toward the earth.

At the present time data from the phase track receiver have been processed only through revolution 137, and all vlf amplitude data from OGO-II contained in this study came from 20 revolutions between revolutions 74 and 134. Of these 20 revolutions, all were in stabilized flight mode 3, except for revolutions 74, 75, 76, and 103. These were in mode 2C.

Figure 46 shows that the 5 revolution-per-hour rotation about the "y" axis will drive the loop through its null position to field-aligned signals approximately 16 times during each 104 minute revolution of the spacecraft around the earth. This artificial modulation of the data must be expected in mode 2C, and it is therefore considered in the analysis of revolutions 74, 75, 76, and 103. In all other revolutions from which data for this study were obtained, proper stabilization was assured.

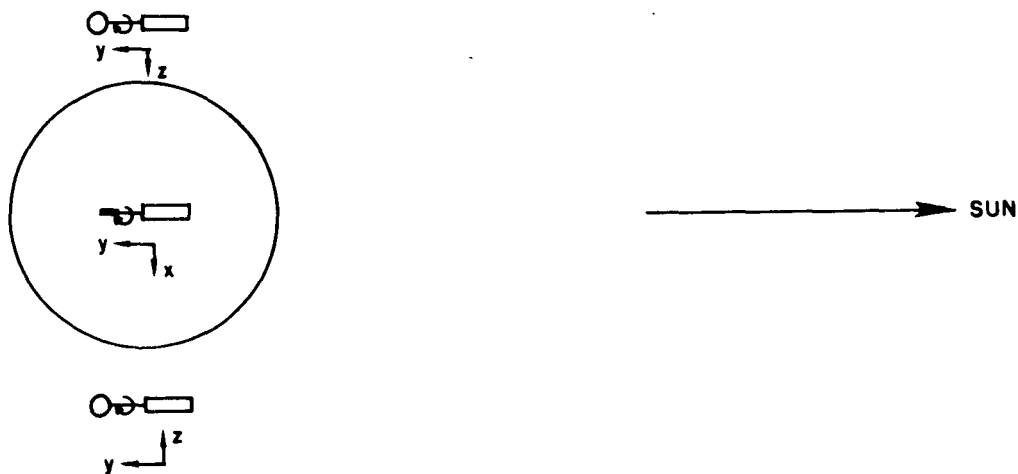


FIG. 46. OGO-II SPACECRAFT AND VLF LOOP ANTENNA ORIENTATION IN FLIGHT MODE 2C. The view is looking down on the North Pole. The earth's magnetic field lines are not shown.

Since revolution 144, when the supply of gas became exhausted, the spacecraft has been operated for long periods of time in a mode designated as 3C. In this mode the spacecraft spins slowly around the "z" axis. The "z" axis does not point towards the earth, but (except for perturbations caused by drag, gravity gradients and solar radiation) is fixed in inertial space.

Reaction wheel momentum is transferred to the spacecraft upon cessation of wheel activity and this changes the yaw-spin period. This period has been decreasing steadily during the past several months from a period of approximately 12 minutes to a period of 3.7 minutes at the present time.

E. SOURCE OF ERRORS

For OGO-II an internal calibration system was incorporated in the receiver. The calibrator may be commanded through its various modes to check out the unit without external stimuli, thereby allowing the same check-out procedure to be used on the ground that is now used with the spacecraft in orbit. In this manner, a good history of the variation of important parameters of the equipment was obtained during several months of testing prior to launch.

There are two circuits in the experiment which generate signals that are phase-locked to the spacecraft clock and are used to internally calibrate the electronic circuits. One circuit generates a spectrum of 500 Hz harmonics and the other 2.5 kHz and its harmonics. The 2.5 kHz calibrator is used to check all of the experiment except Band 1 and to measure the loop antenna impedance. It injects either a voltage or a current into the antenna when it is calibrating. The 500 Hz calibrator is used to check the Band 1 receiver and it injects high-or-low level signals into the Band 1 input filter.

Each calibrator is turned on and off and switched between voltage and current or high and low by the same logic circuitry. There are two modes that are normal for the calibrators... the automatic mode and the command mode.

In the automatic mode, signals are generated for one complete sweep

every 16th sweep of the sweeping receivers as in OGO-I.

Every other calibration sweep will be a voltage-or-current calibration for the 2.5 kHz calibrator, and high or low level respectively for the 500 Hz one.

In the command calibration mode, the calibrators are commanded on by a sequence of commands from the ground. The command calibration function was added to the experiment to allow a quick, thorough check-out of the experiment when in orbit.

Although a detailed study of the calibration level has not yet been made for OGO-II (as was discussed in Chapter II for OGO-I) there is some evidence that the calibration level has not changed and that amplitudes of vlf signals as indicated by the strip-charts and 16mm SRI film records are accurate to within ± 1 db [B. P. Ficklin, private communication]. Since a completely detailed study of the calibration level is not expected to be completed for approximately 6 months, one can only state that careful examination of the data and evidence of calibration accuracy so far obtained indicate no change.

In revolutions 74, 75, 76, and 103, loop orientation is certainly a source of error and one must proceed cautiously in interpreting these data. In data from all other revolutions contained in this study, loop orientation as an error source has been ruled out.

A change of receiver gain with temperature change is the major known source of error in the vlf equipment package. Pre-launch tests showed this error to be on the order of 1 db change in output voltage for a 30°C temperature change. Goddard Space Flight Center Spacecraft Operations Summaries show that all spacecraft temperatures were well within the predicted ranges for the first 144 revolutions, and that the temperature fluctuation of the panel on which the vlf equipment package is located was less than 10°C during this period. Hence, this also has been ruled out as a source of error.

It is believed that inability to accurately read the film presentations, due to such things as aberrations in the projection process, probably represent the greatest source of error. This uncertainty is believed to be 2 or 3 db. In comparing measured values with calculated values throughout this study, it is clear that the uncertainty involved in the calculations

as a result of effects from uncertainty in the models being used (electron density versus height and latitude, for instance) are undoubtedly greater than uncertainties in the measurements.

F. PRESENTATION OF THE DATA

By carefully scaling records such as those shown in Figs. 47 through 51, all of the available fixed-frequency vlf data from the PCM telemetry have been obtained for revolutions up through and including 137. These measured data (peak values) have then been plotted as field intensity versus dipole latitude, along with pertinent satellite positional information and time, in Figs. 56 through 89 of Chapter VI.

The records presented in this section are selected not only to illustrate the manner in which the data from OGO-II are presented, but primarily because of the fundamental importance of the phenomena they represent. For instance, Figs. 47 and 48 clearly show a whistler-mode cutoff at approximately 60° geomagnetic latitude, which is one of the important new results of this experiment. Figure 49 shows a signal enhancement of more than 25 db near the NPG antipode, and the beginning of an intense noise which is often seen at high latitudes. Figures 50 and 51 show high intensity signals from NPG over an earth-ionosphere waveguide distance of almost 9 kkm, and also illustrate one of the few instances in all of the data where the latitudinal cutoff is not entirely effective and signals are observed to magnetic latitudes as high as 80° . These data will not be discussed further at this point, but will be considered in Chapters VIII and IX.

Figures 52 through 55 are typical of the many Rayspan records produced at Stanford from the SP telemetry which have been studied. While these records have not been utilized in specific amplitude determination, they have been valuable in studying the cutoff of whistler-mode signals versus latitude and the fading patterns of vlf signals. These results are also included in Chapters VIII and IX.

Utilizing the procedures outlined in Chapter III, field intensities have been calculated for many satellite locations where OGO-II obtained data. These calculations are based on the refined model, as discussed in Chapter VII, and are plotted as the dash-dot lines along with the peak measured values in Chapter VI.

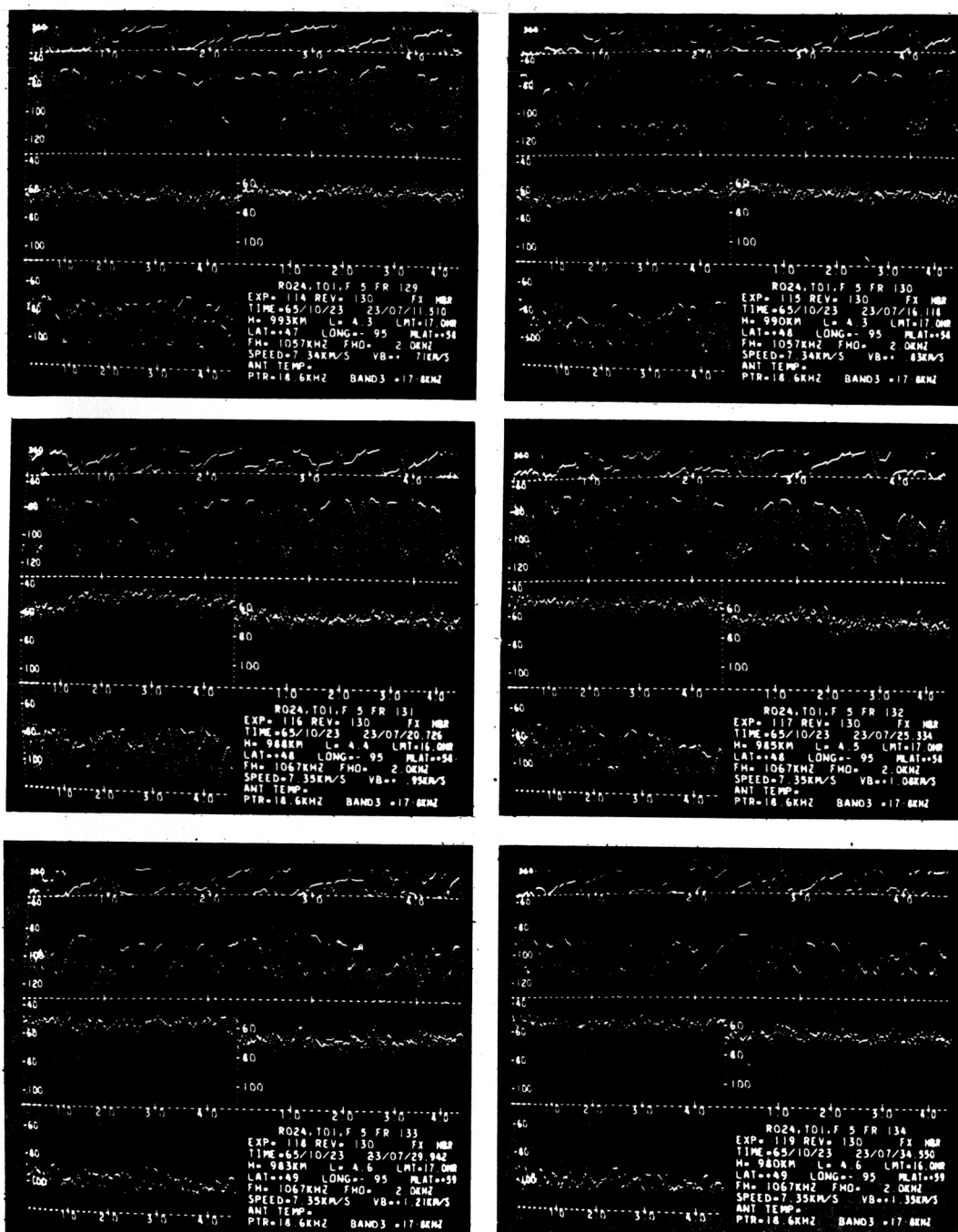


FIG. 47. TO ILLUSTRATE A SHARP LATITUDINAL CUT OFF OF WHISTLER-MODE SIGNALS OBSERVED IN OGO-II. The top two traces in each frame represent phase and amplitude, respectively, of the phase track receiver which is tuned to NPG. The bottom trace represents amplitude of the Band 3 receiver which, due to mis-tuning, contains signals from both NAA and NPG. Note in FR 129 that the magnetic latitude is 58° and that the NPG amplitude is as high as 63 db below 1v. The NAA signals essentially disappear from Band 3 in FR 132.

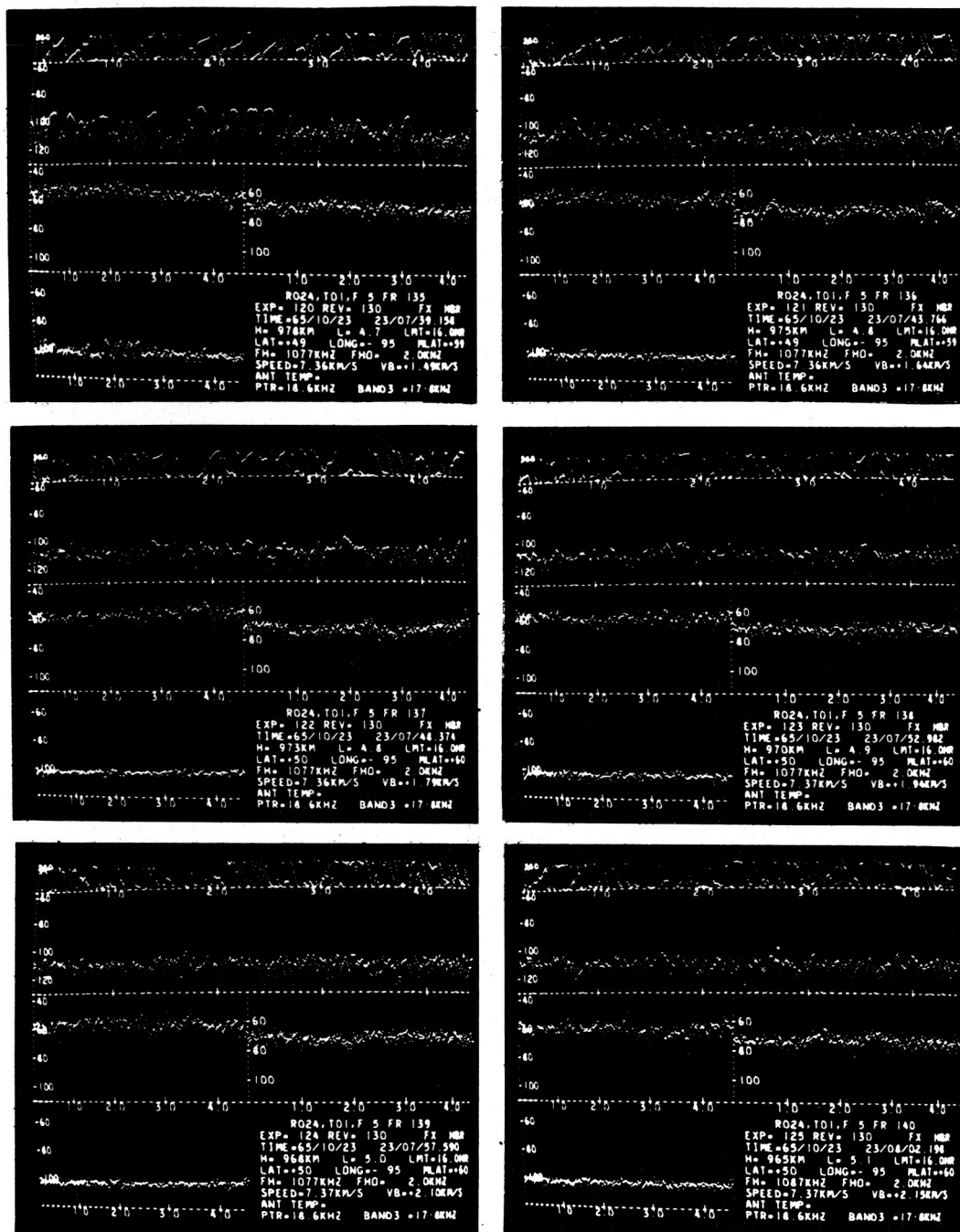


FIG. 48. A CONTINUATION OF THE DATA SHOWN IN FIG. 47. Note that FR 135 contains no evidence of NAA signals in the Band 3 receiver and that the NPG signals in the phase track receiver become noticeably weaker. The NPG signals continue to fade, and are no longer recognizable in FR 139 and FR 140 where the magnetic latitude is 60° and the maximum amplitude is 102 db below 1γ . Each frame represents 4.6 seconds of real time. The center two traces of each frame represent the output of the Band 1 and Band 2 receivers.

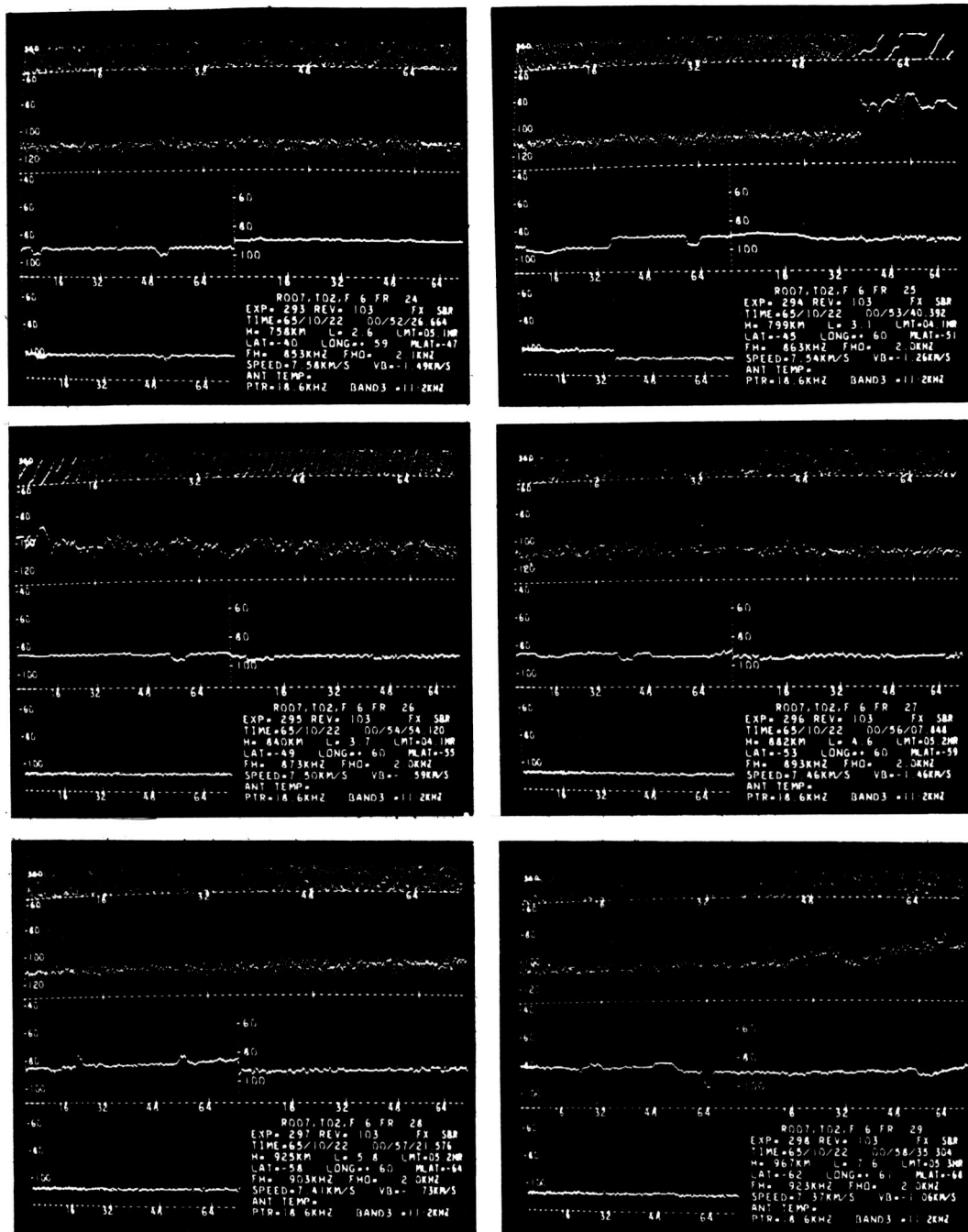


FIG. 49. TO ILLUSTRATE A SIGNAL ENHANCEMENT OF APPROXIMATELY 25 db NEAR THE NPG ANTIPODE. NPG (second trace from the top in each frame) ends a silent period and begins CW transmission in FR 25 when the satellite is within 200 km of the antipode. The signals fade rapidly in subsequent frames as the satellite flies south, and enters the region of intense noise in FR 29. In this sequence each frame represents approximately 73 seconds of real time.

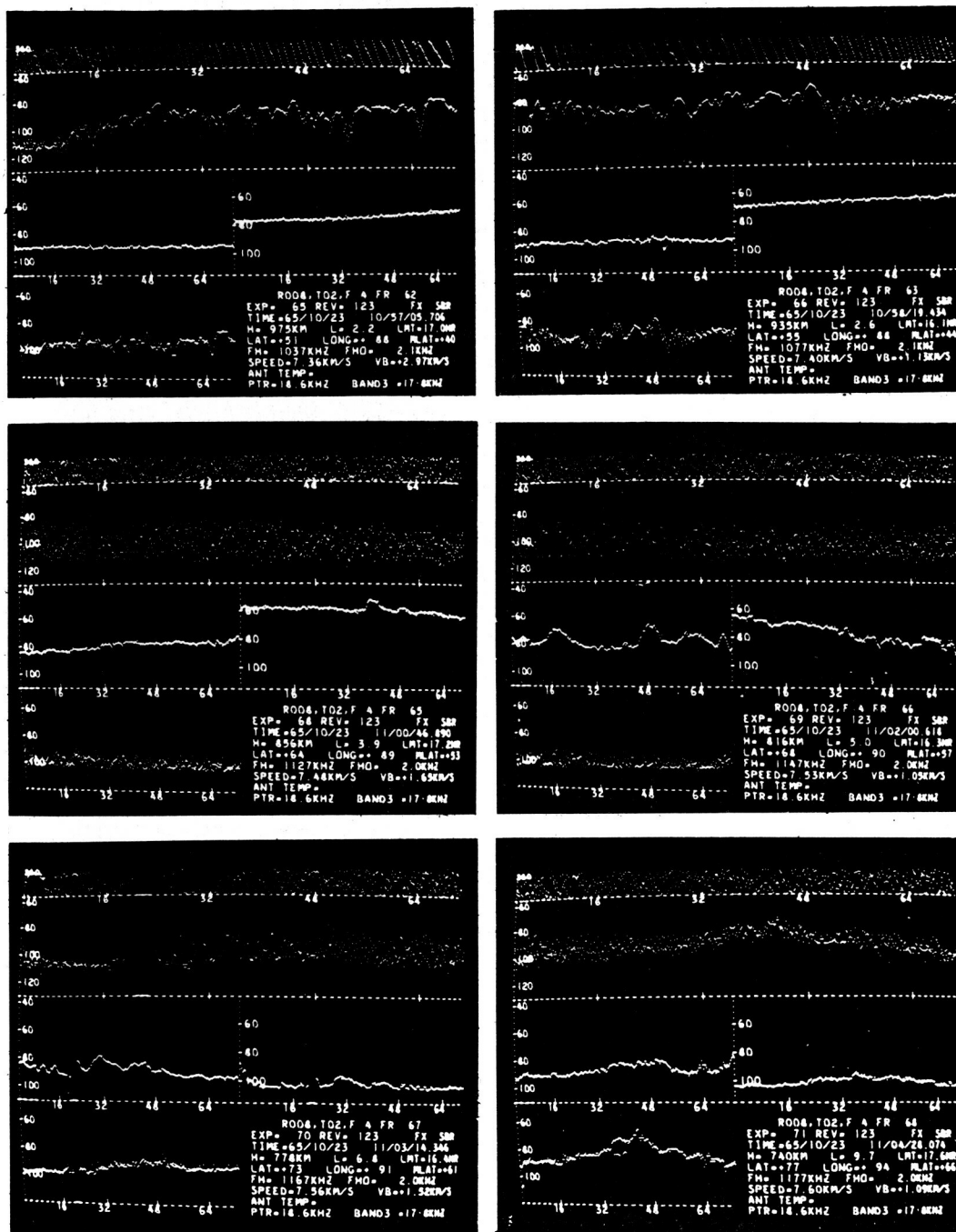


FIG. 50. TO ILLUSTRATE HIGH INTENSITY NPG SIGNALS (SECOND TRACE FROM THE TOP) OVER AN EARTH-IONOSPHERE WAVEGUIDE DISTANCE OF ALMOST 9 kkm. The satellite is flying north over Siberia. In FR 67 NPG signals fade rapidly, with intense noise beginning in FR 68. NPG is transmitting CW in FR 62 and FR 63 and begins sending traffic in FR 65. Each frame represents 73 seconds of real time.

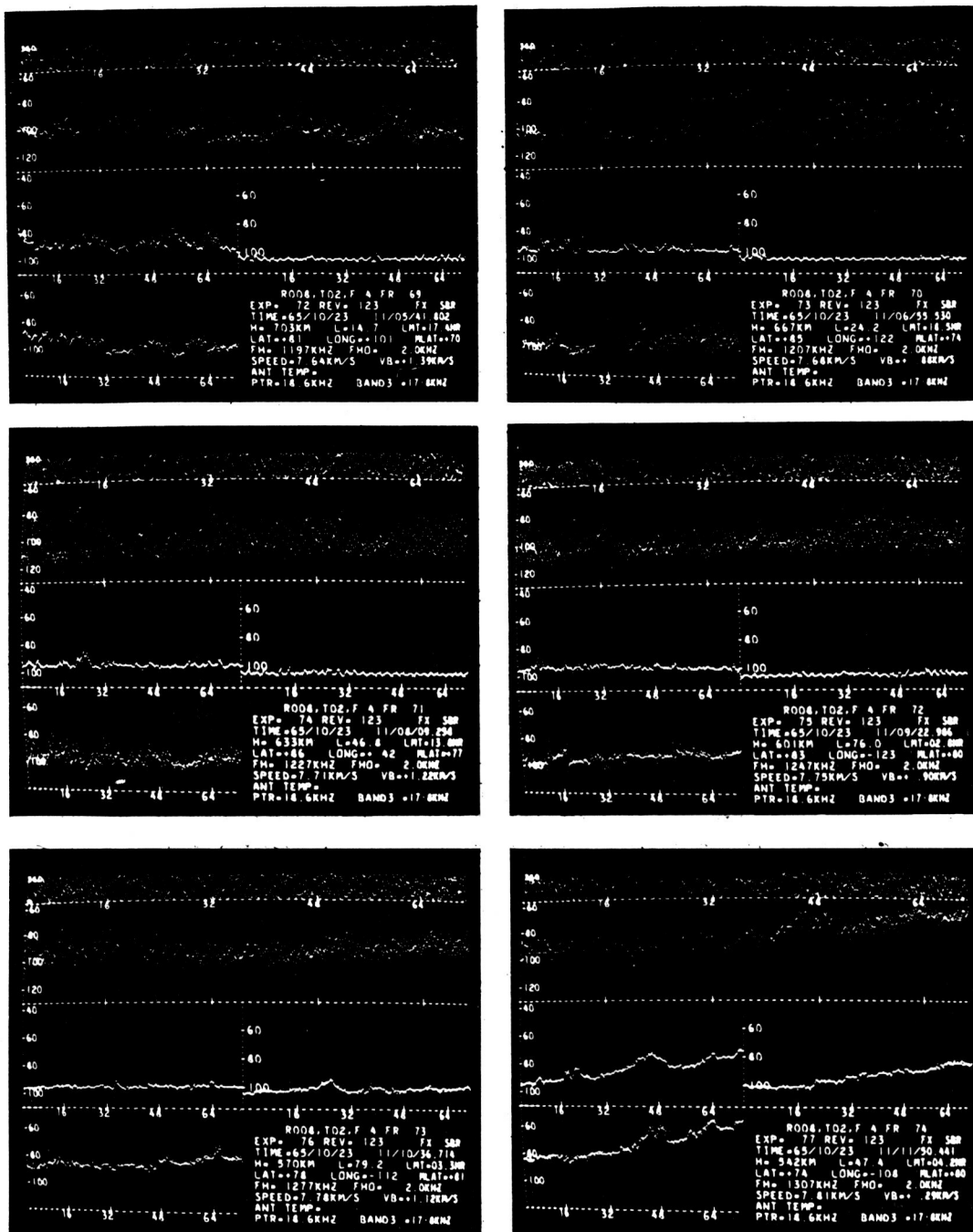


FIG. 51. A CONTINUATION OF THE DATA SHOWN IN FIG. 50, DEMONSTRATING ONE OF THE FEW INSTANCES WHERE THE LATITUDINAL CUT OFF IS NOT OBSERVED, THE INTENSE NOISE (WHICH BEGAN IN FR 68 OF FIG. 50) DOES NOT PERSIST, AND VLF SIGNALS ARE OBSERVED AT HIGH LATITUDES (UP TO 81° IN FR 73). In FR 74 the satellite has crossed the polar region and intense noise is seen on the Western Hemisphere (nighttime) side of the earth.

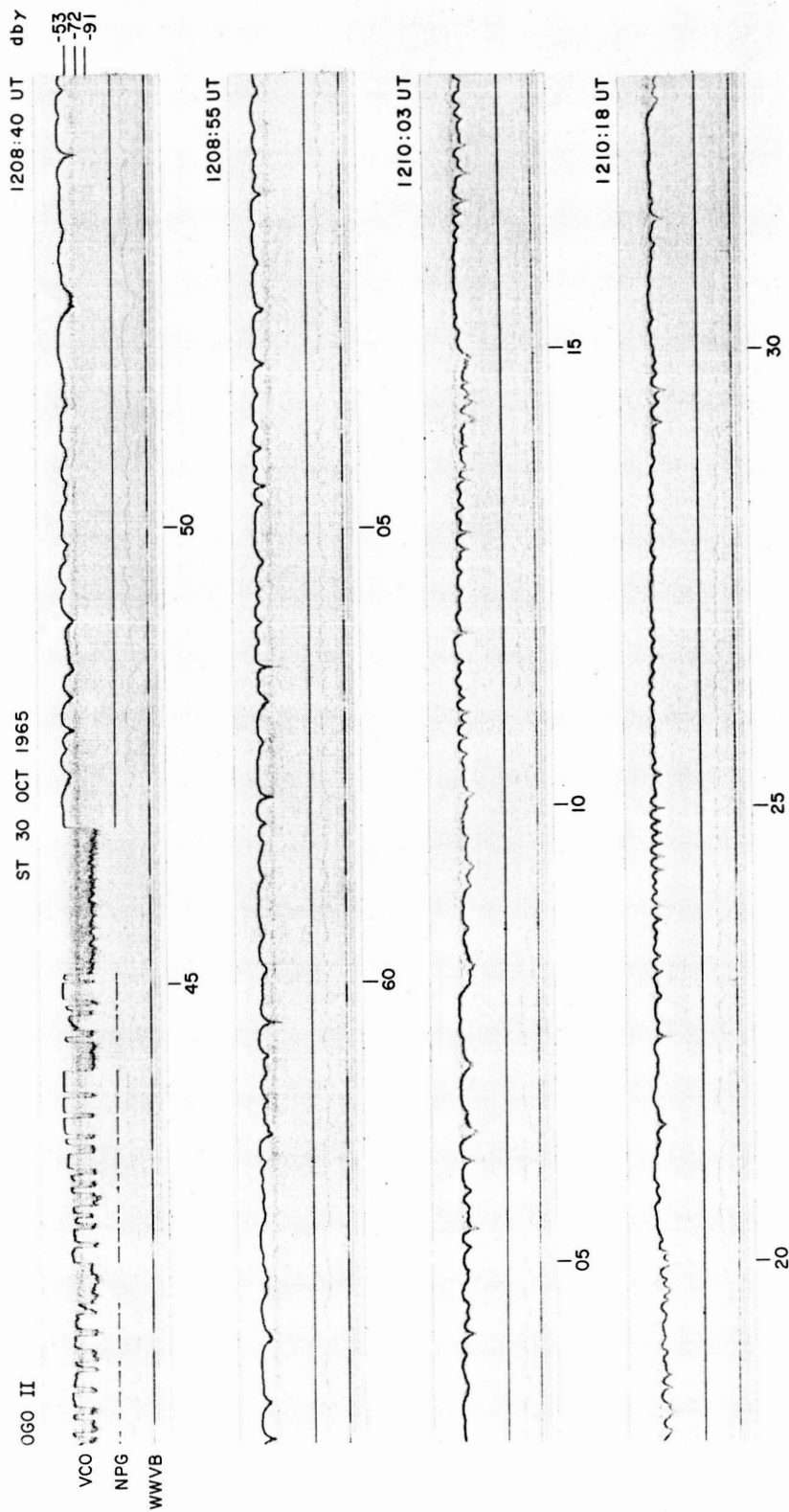


FIG. 52. FAIRLY RAPID FADING PATTERNS DURING PERIODS OF CW TRANSMISSION FROM NPG AS INDICATED BY THE OGO-II SATELLITE VCO VIA THE SPECIAL PURPOSE TELEMETRY. The NPG and WWVB signals are obtained from receivers at Stanford and are inserted simultaneously as the VCO signal is being received from the satellite telemetry. The satellite is at 125°W and 50°N (55° magnetic), flying south at an altitude of 422 km.

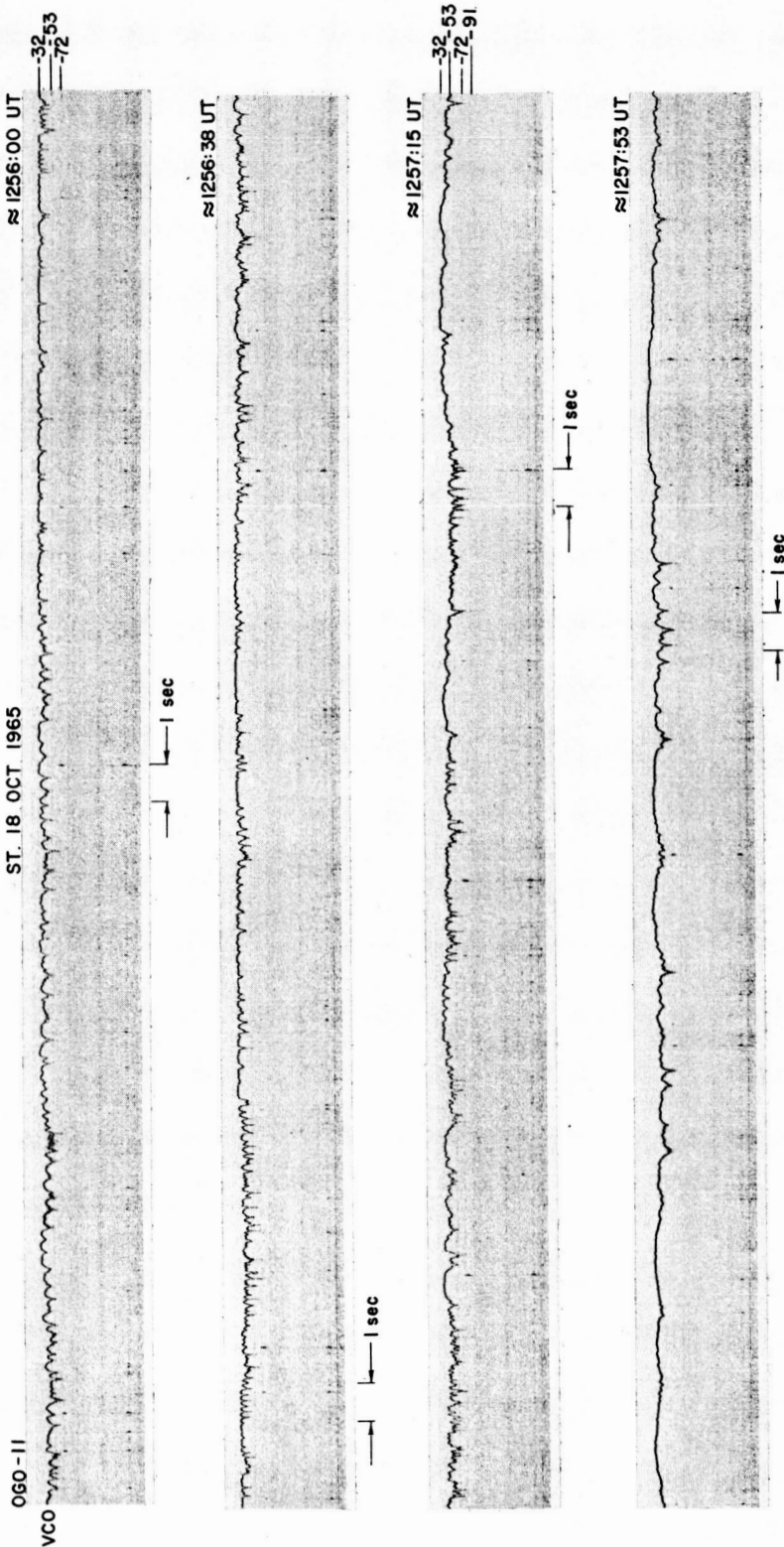


FIG. 53. TO ILLUSTRATE SOME OF THE DEEPEST AND MOST RAPID FADING PATTERNS OBSERVED BY OGO-II. An equipment malfunction prevented time signals and the NPG ground signals from being recorded. The satellite is at 122°W and 48°N (54° magnetic), flying south at an altitude of 500 km.

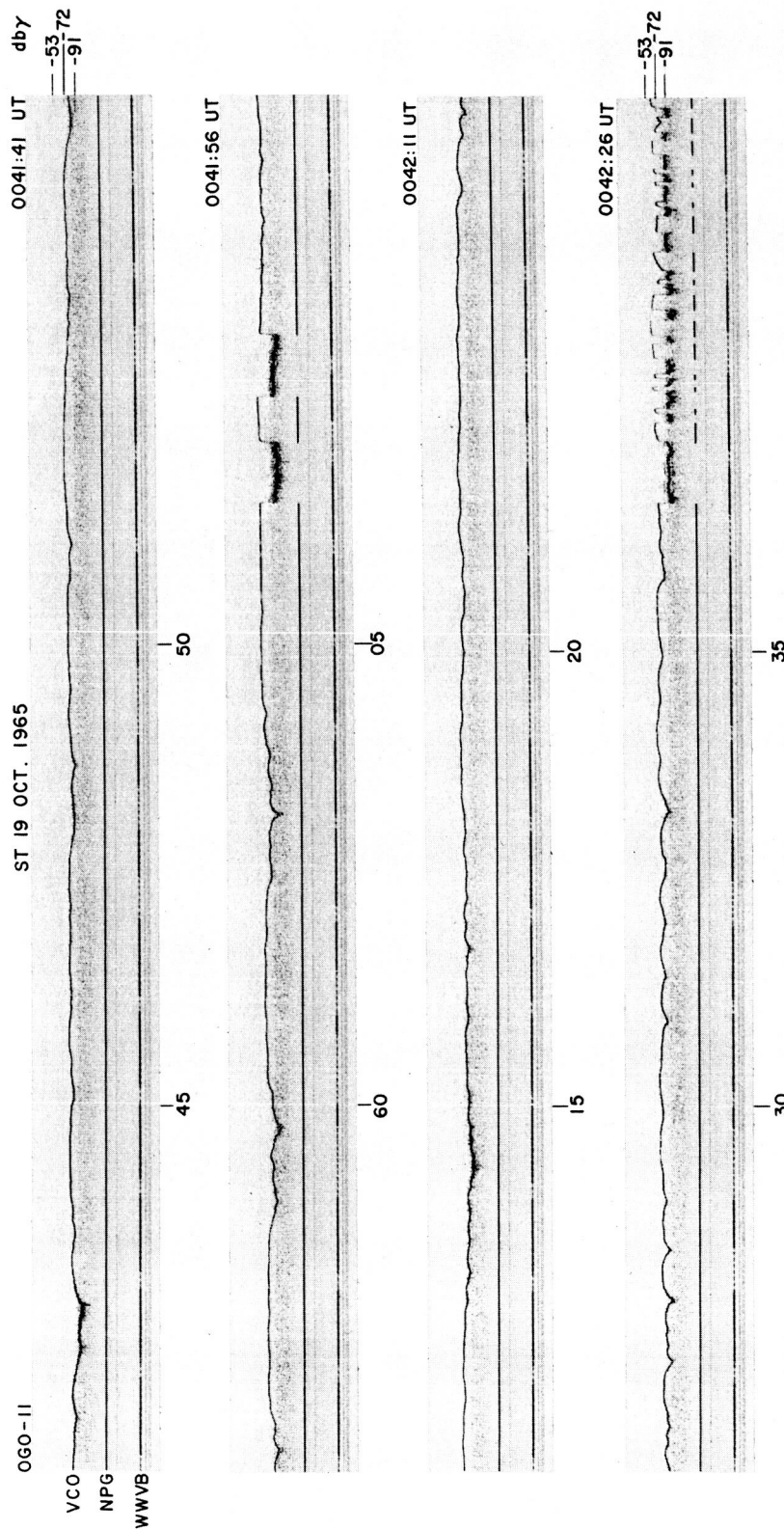


FIG. 54. TO ILLUSTRATE FADING PATTERNS OBSERVED BY OGO-II WHICH RESEMBLE THE FADING OBSERVED BY OGO-I. (See Fig. 22) The NPG and WWVB signals are obtained from receivers at Stanford and are inserted simultaneously as the VCO signal is being received from the satellite telemetry. The satellite is at 114°W and 35°N (43° magnetic), flying north at an altitude of 1250 km.

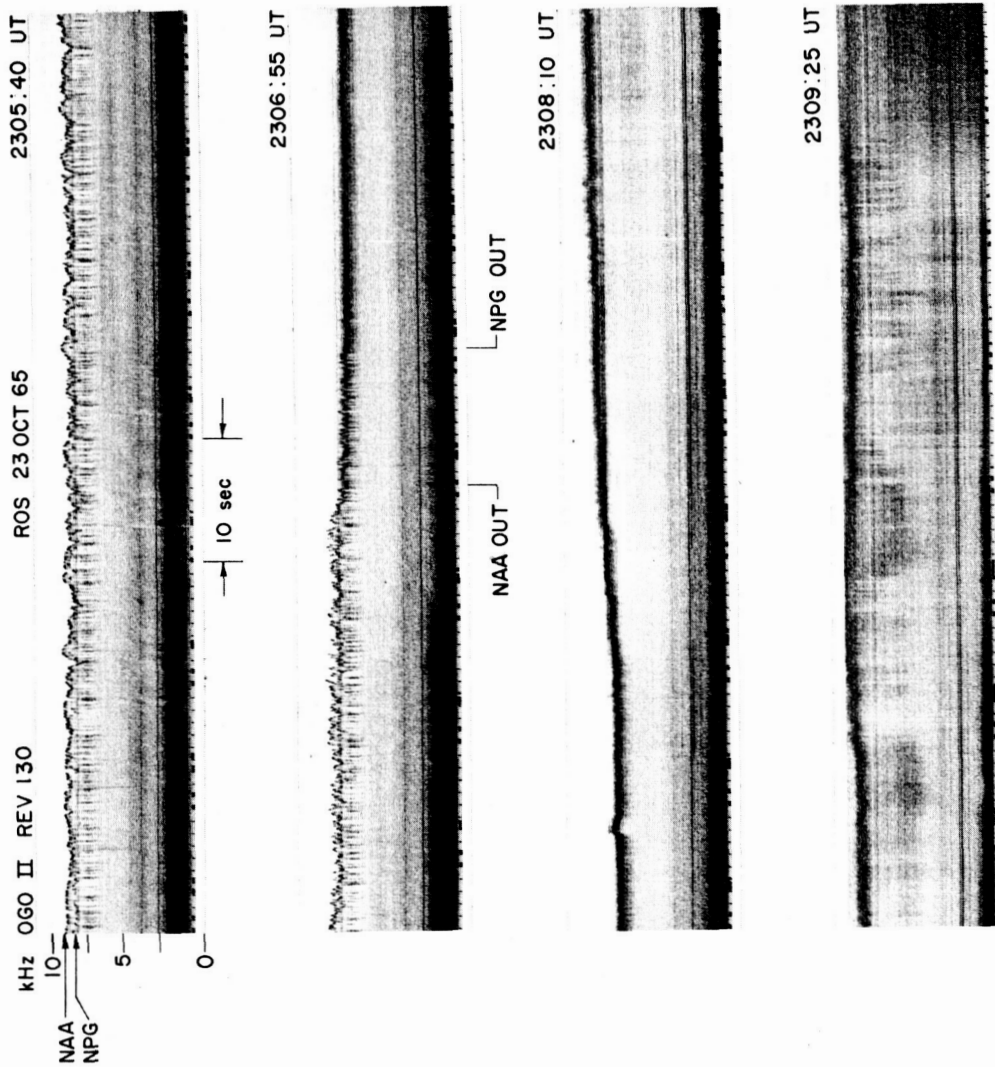


FIG. 55. A RAYSPAN RECORD OF THE LATITUDINAL CUTOFF PHENOMENA SHOWN IN FIGS. 47 AND 48. The Band 3 output (containing both NPG and NAA) is superimposed on the output of the broadband receiver. Note the fade out of NAA and NPG signals in the Band 3 receiver, followed by a brief quiet period, and then intense noise. The satellite positional parameters are as shown in Figs. 47 and 48.

VI. THE OGO-II DATA

A. INTRODUCTION

All of the vlf amplitude data obtained from the OGO-II PCM telemetry and processed by SRI have been scaled and plotted and are presented in Figs. 56 through 89. Magnetic dipole latitude is used as the independent variable with magnetic field strength (db below 1 gamma) along the ordinate. Pertinent satellite positional information is included on each figure. The solid line represents the peak intensities of the measured signals from the vlf stations. The dashed lines represent peak intensities of the noise signals received during periods of time when no signals were apparent from the vlf stations. The dash-dot lines represent values calculated by utilizing the first-approximation model after modification as outlined in Chapter VII.

The sub-satellite points, for each revolution where vlf data were obtained, accompany the field intensity versus magnetic latitude graphs in Figs. 56 through 89.

B. OGO-II FIELD INTENSITIES VERSUS DIPOLE LATITUDE

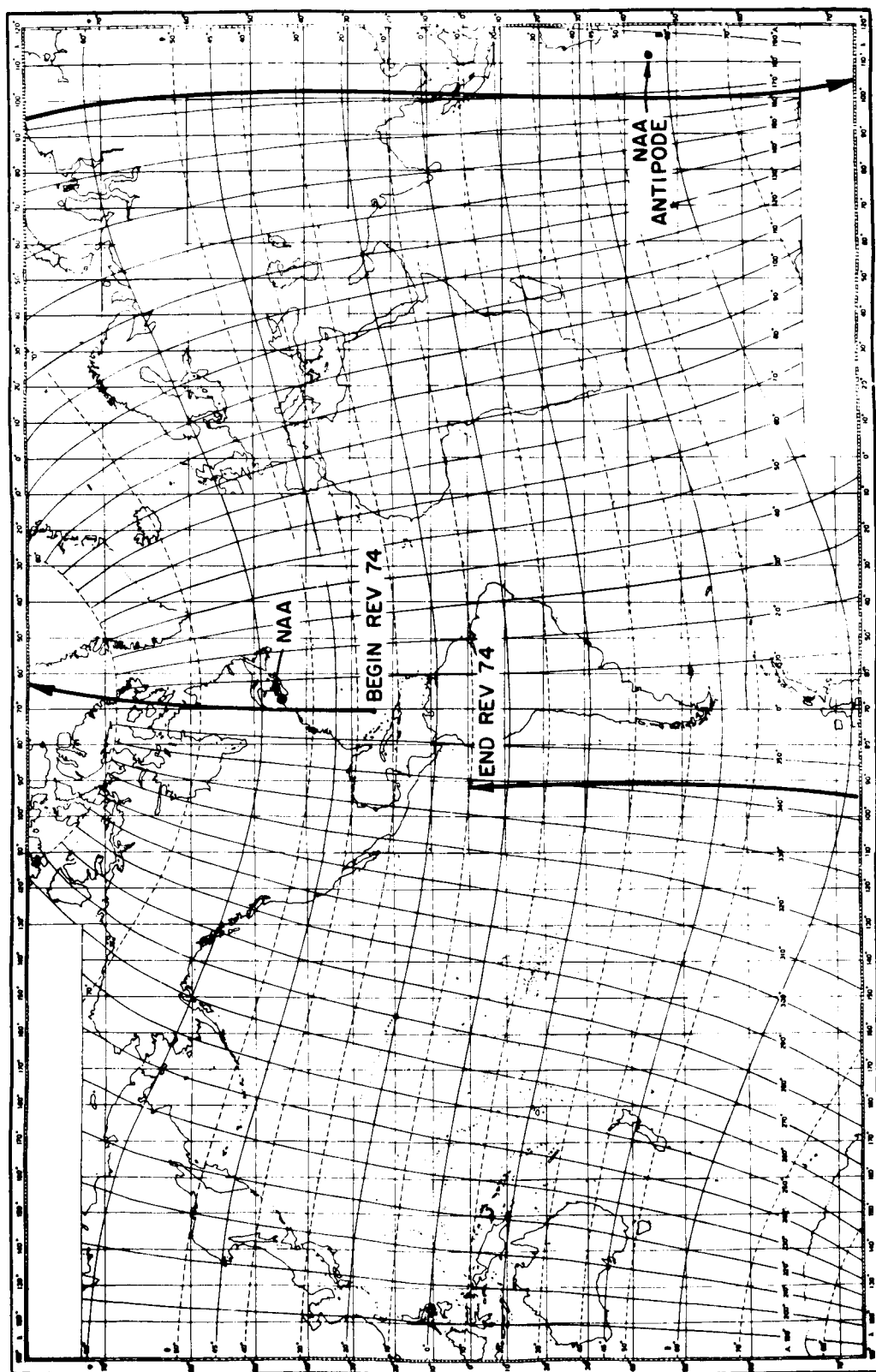


FIG. 56. OGO-II ORBITAL SUBSATELLITE PLOT WHERE VLF DATA WERE OBTAINED DURING REV. 74.

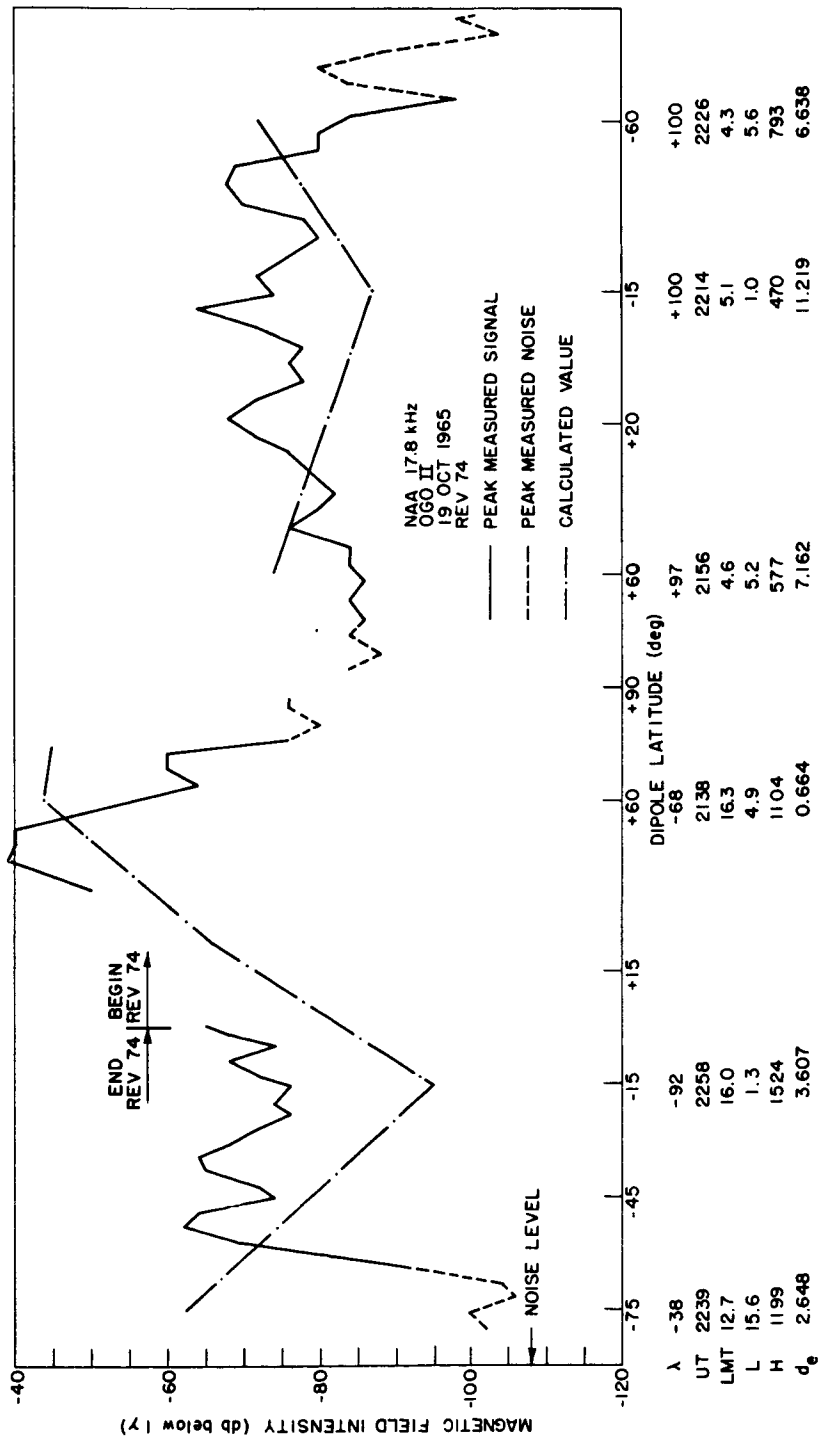


FIG. 57. OGO-II MAGNETIC FIELD STRENGTH VERSUS DIPOLE LATITUDE FOR NAA ON 19 OCT. 1965. λ = Eastern longitude (degrees); UT = universal time; LMT = local mean time at the satellite; L = L-value; H = satellite altitude (km); d_e = great-circle distance (km) from NAA to the foot of the field line in the Northern hemisphere. The calculated values were made using the refined model.

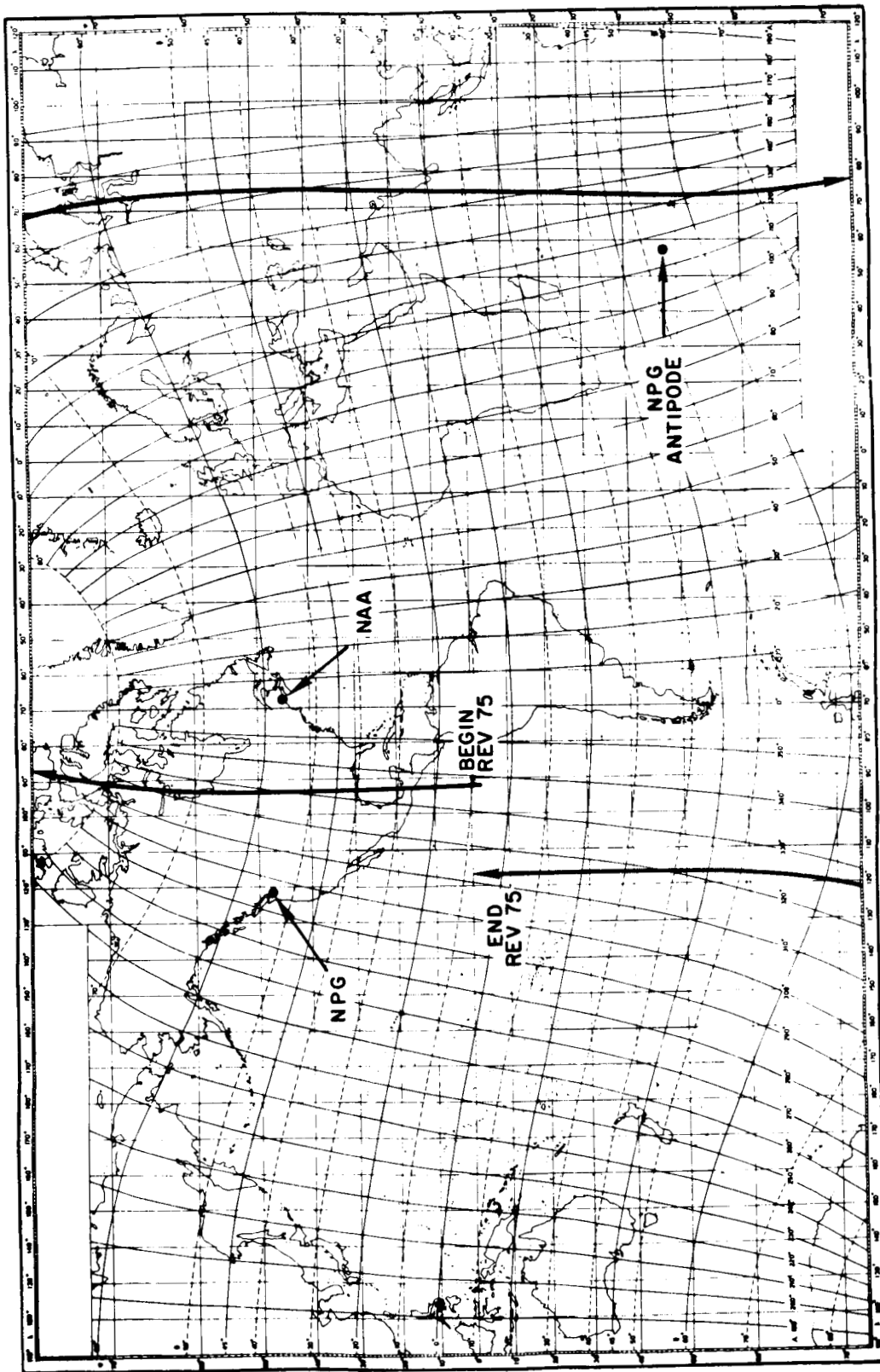


FIG. 58. OGO-II ORBITAL SUBSATELLITE PLOT WHERE VLF DATA WERE OBTAINED DURING REV. 75.

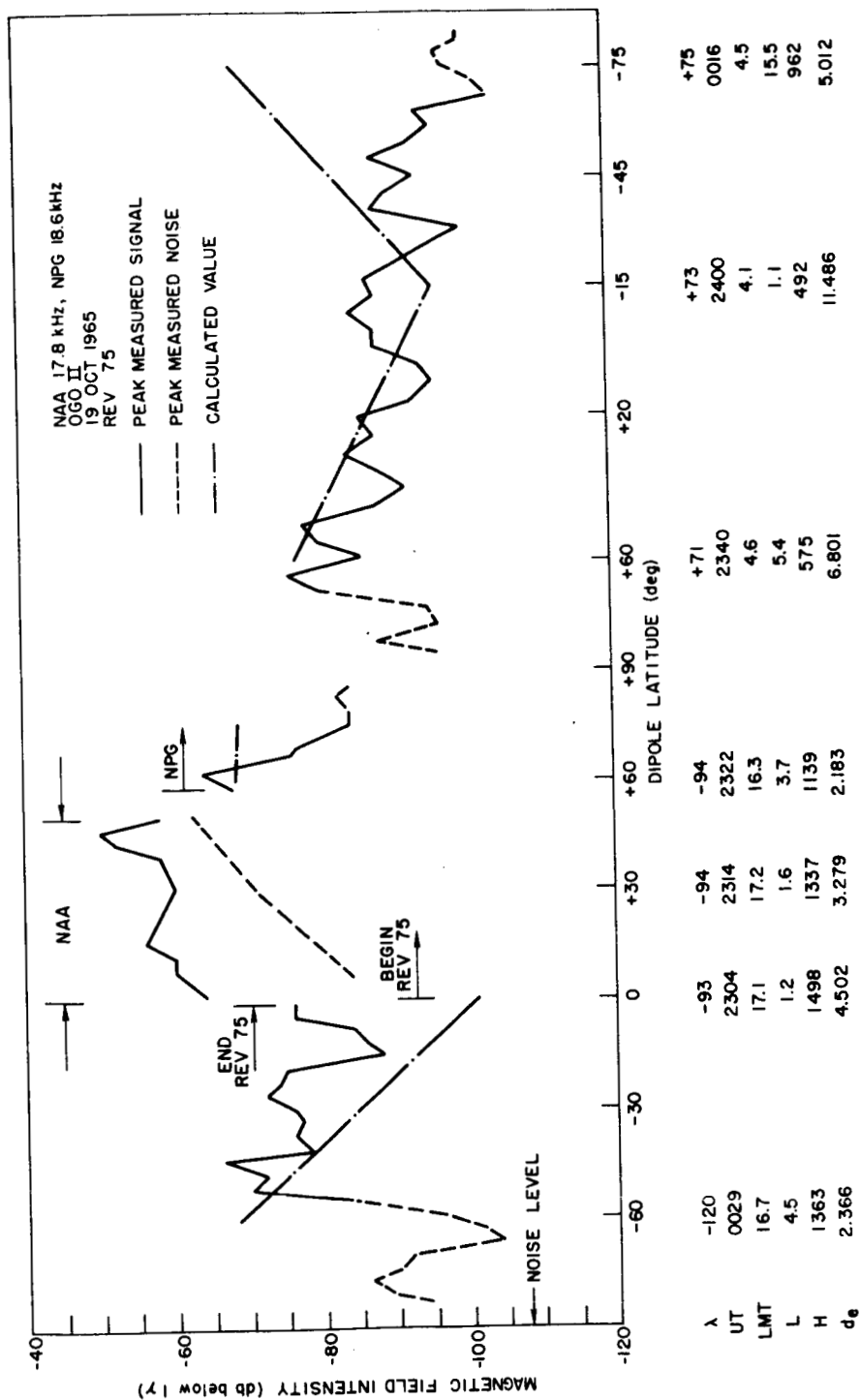


FIG. 59. OGO-II MAGNETIC FIELD STRENGTH VERSUS DIPOLE LATITUDE FOR NAA AND NPG ON 19 OCT. 1965.
λ = Eastern longitude (degrees); UT = universal time; LMT = local mean time at the satellite;
L = L-value; H = satellite altitude (km); d_e = great-circle distance (kkm) from NAA and NPG
to the foot of the field line in the Northern hemisphere. The calculated values were made
using the refined model.

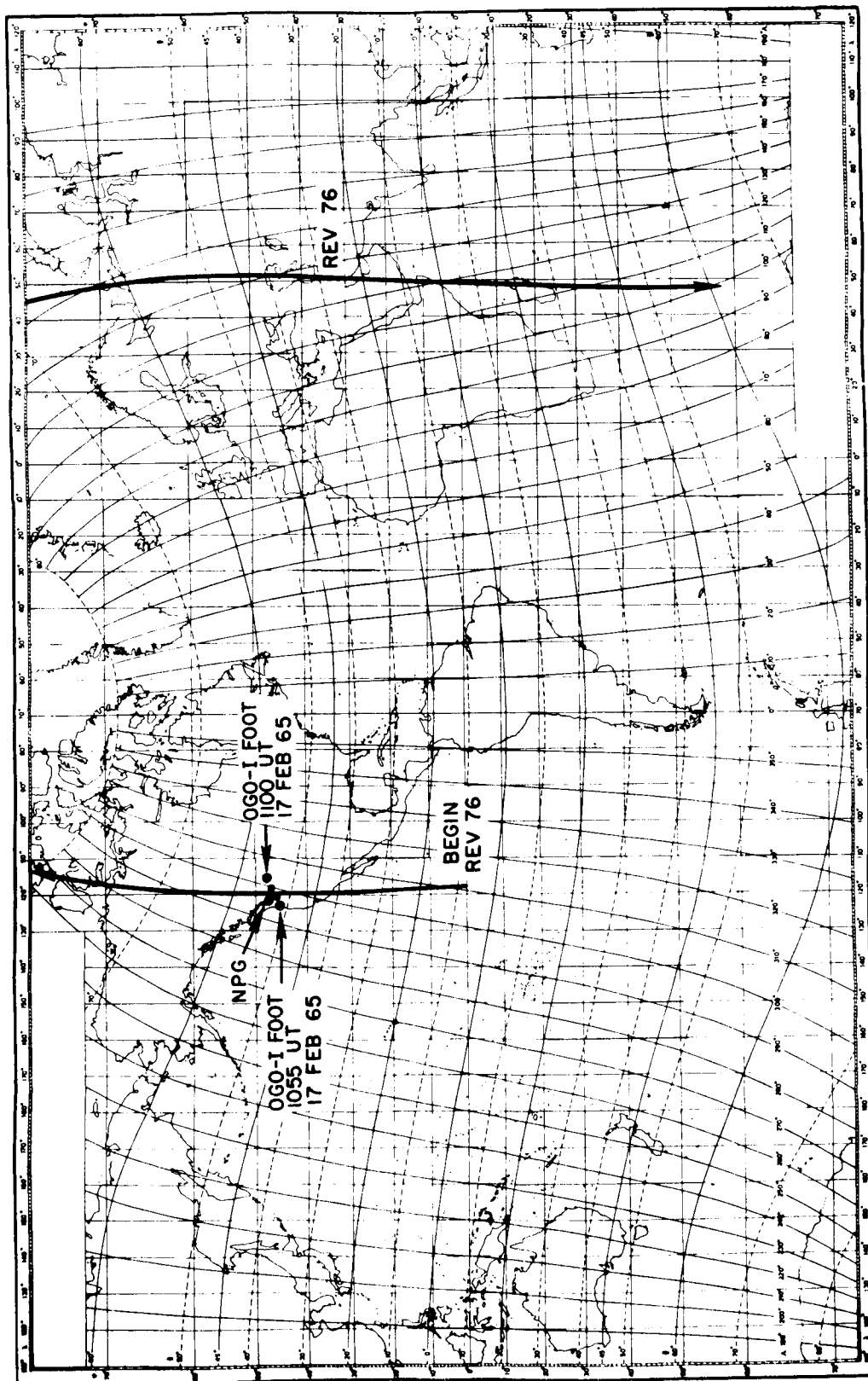


FIG. 60. OGO-II ORBITAL SUBSATELLITE PLOT WHERE VLF DATA WERE OBTAINED DURING REV. 76.

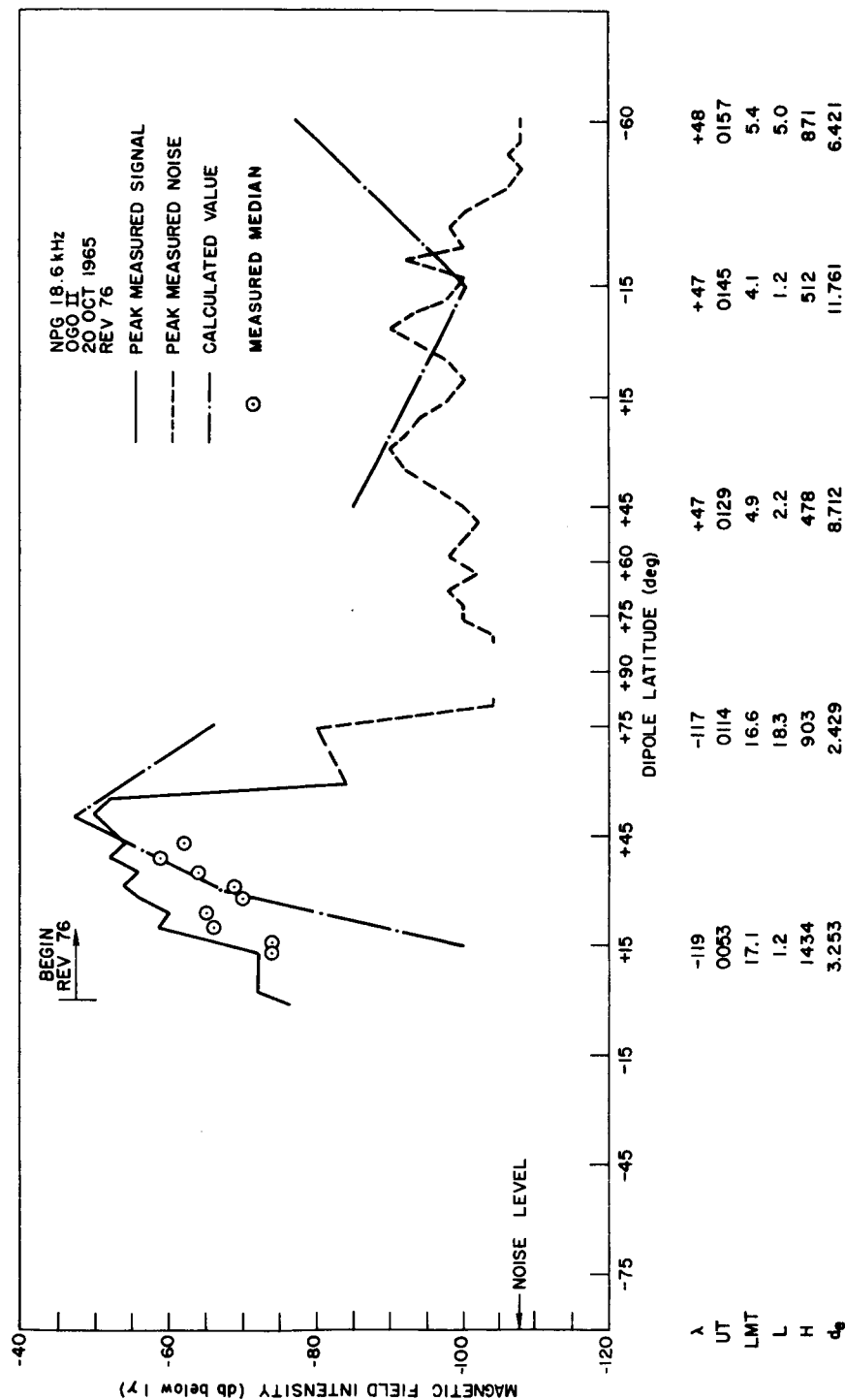


FIG. 61. OGO-II MAGNETIC FIELD STRENGTH VERSUS DIPOLE LATITUDE FOR NPG ON 20 OCT. 1965. λ = Eastern longitude (degrees); UT = universal time; LMT = local mean time at the satellite; L = L-value; H = satellite altitude (km); d_g = great-circle distance (kkm) from NPG to the foot of the field line in the Northern hemisphere. The calculated values were made using the refined model.

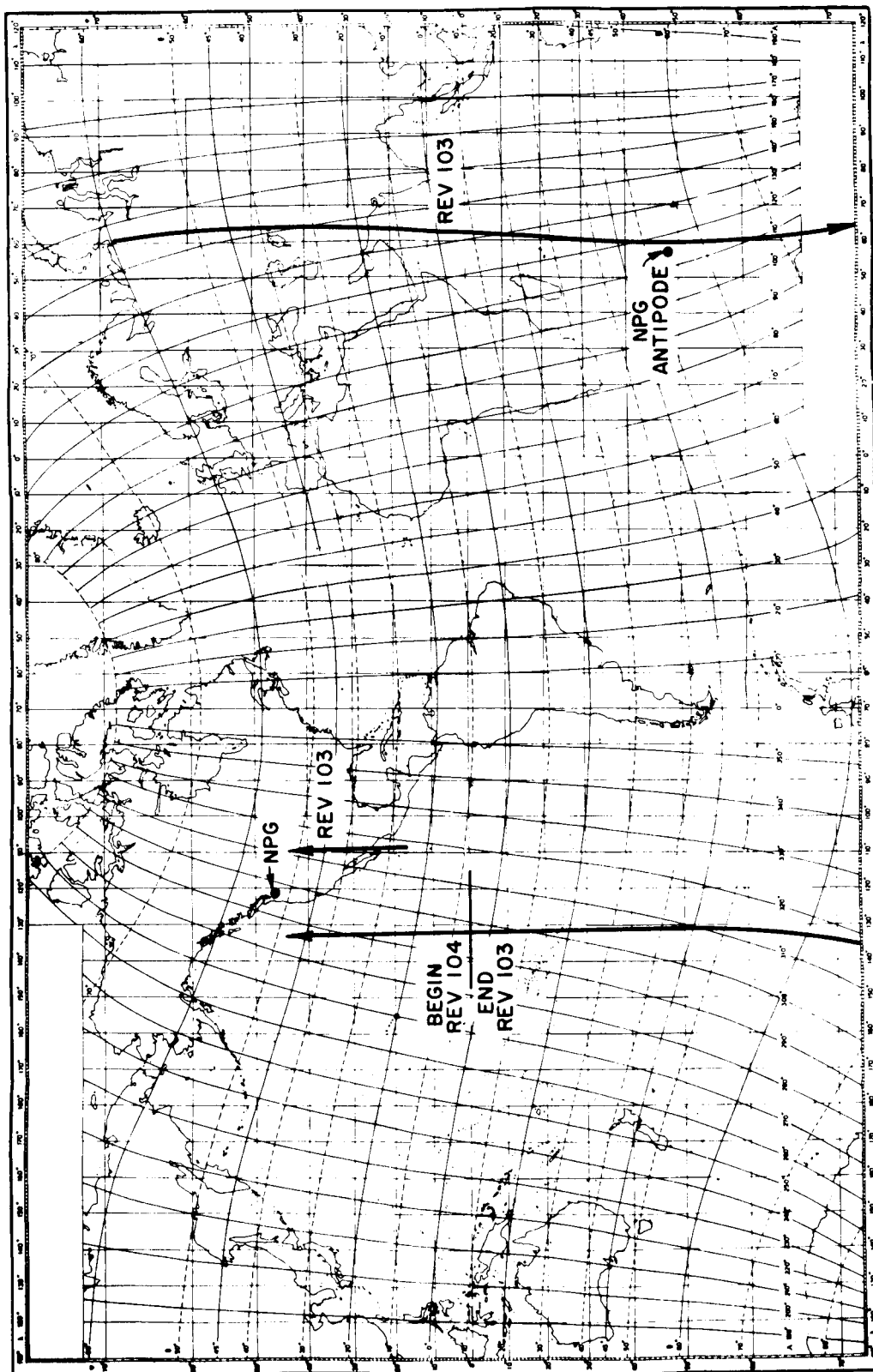


FIG. 62. OGO-II ORBITAL SUBSATELLITE PLOT WHERE VLF DATA WERE OBTAINED DURING REV. 103 AND 104.

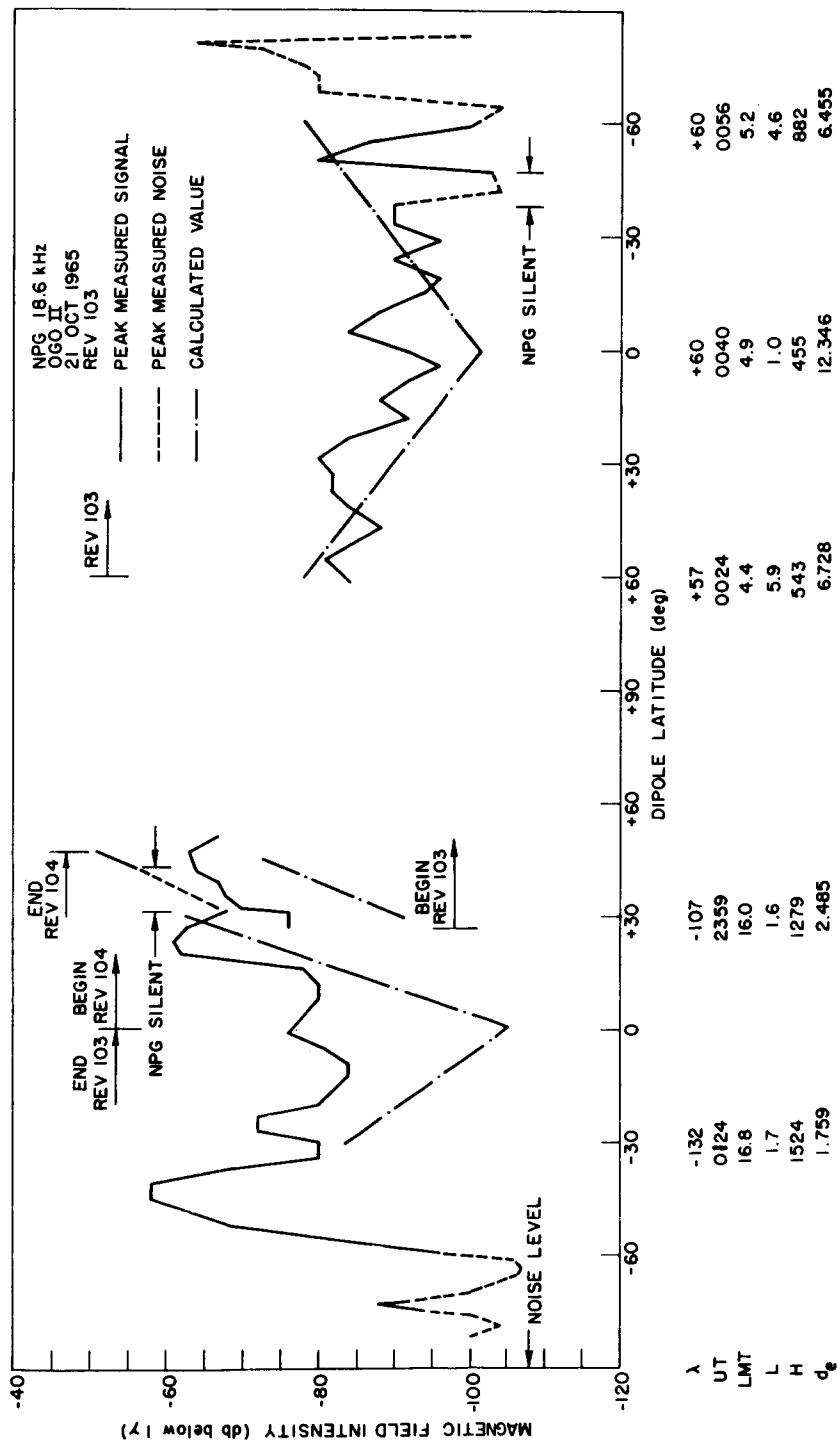


FIG. 63. OGO-II MAGNETIC FIELD STRENGTH VERSUS DIPOLE LATITUDE FOR NPG ON 21 OCT. 1965. λ = Eastern longitude (degrees); UT = universal time; LMT = local mean time at the satellite; L = L-value; H = satellite altitude (km); d_e = great-circle distance (km) from NPG to the foot of the field line in the Northern hemisphere. The calculated values were made using the refined model.

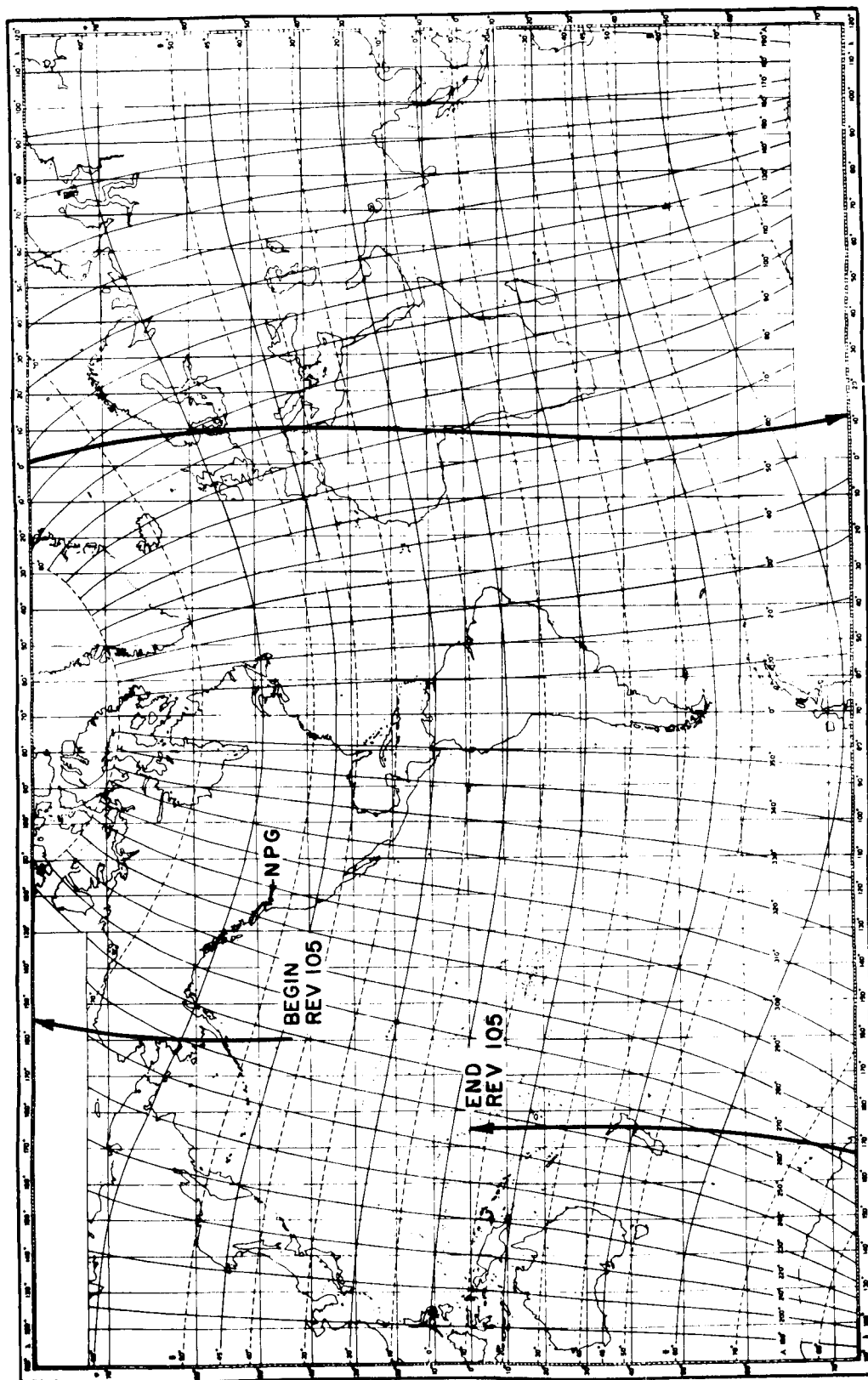


FIG. 64. OGO-II ORBITAL SUBSATELLITE PLOT WHERE VLF DATA WERE OBTAINED DURING REV. 105.

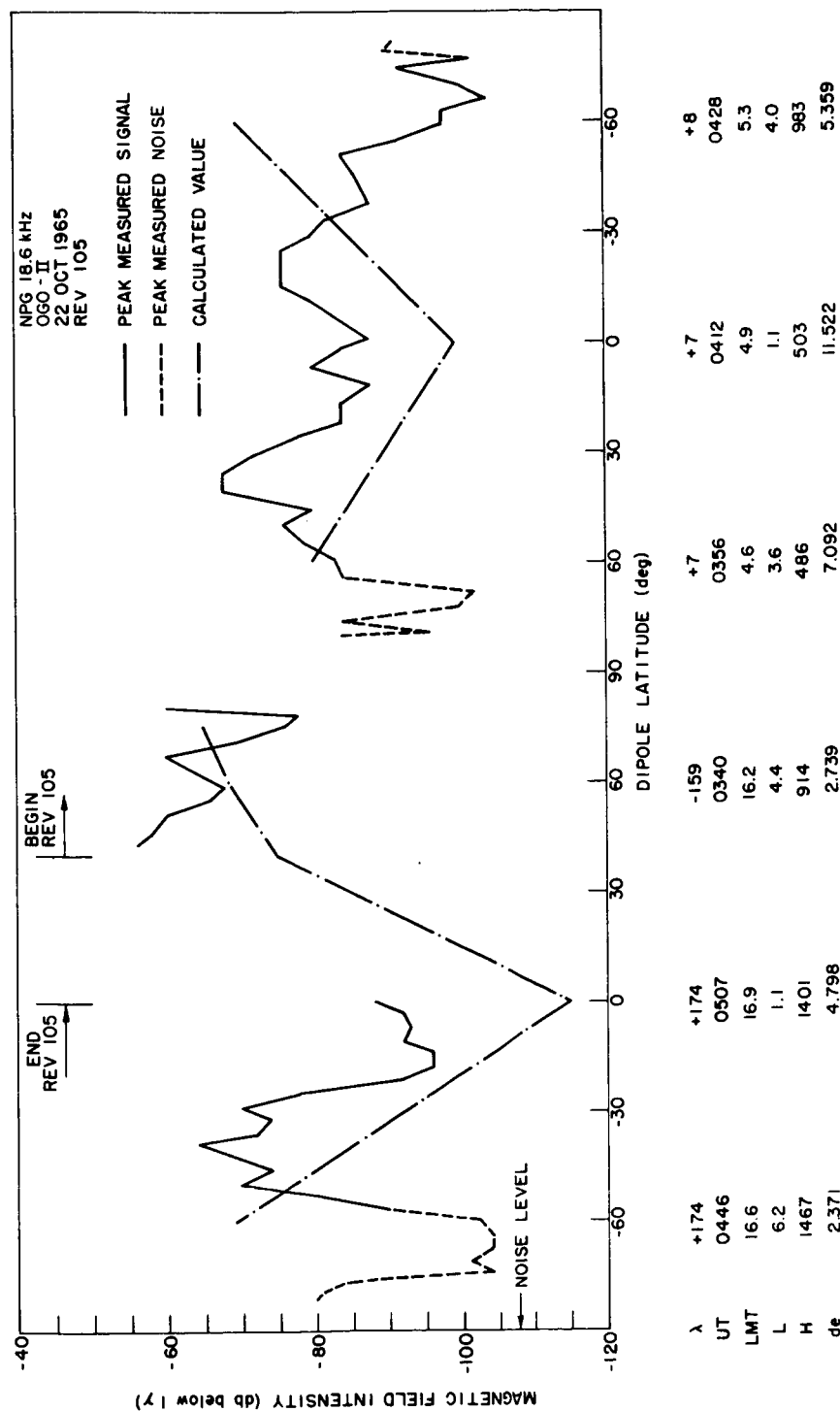


FIG. 65. OGO-II MAGNETIC FIELD STRENGTH VERSUS DIPOLE LATITUDE FOR NPG ON 22 OCT. 1965. λ = Eastern longitude (degrees); UT = universal time; LMT = local mean time at the satellite; L = L-value; H = satellite altitude (km); d_e = great-circle distance (km) from NPG to the foot of the field line in the Northern hemisphere. The calculated values were made using the refined model.

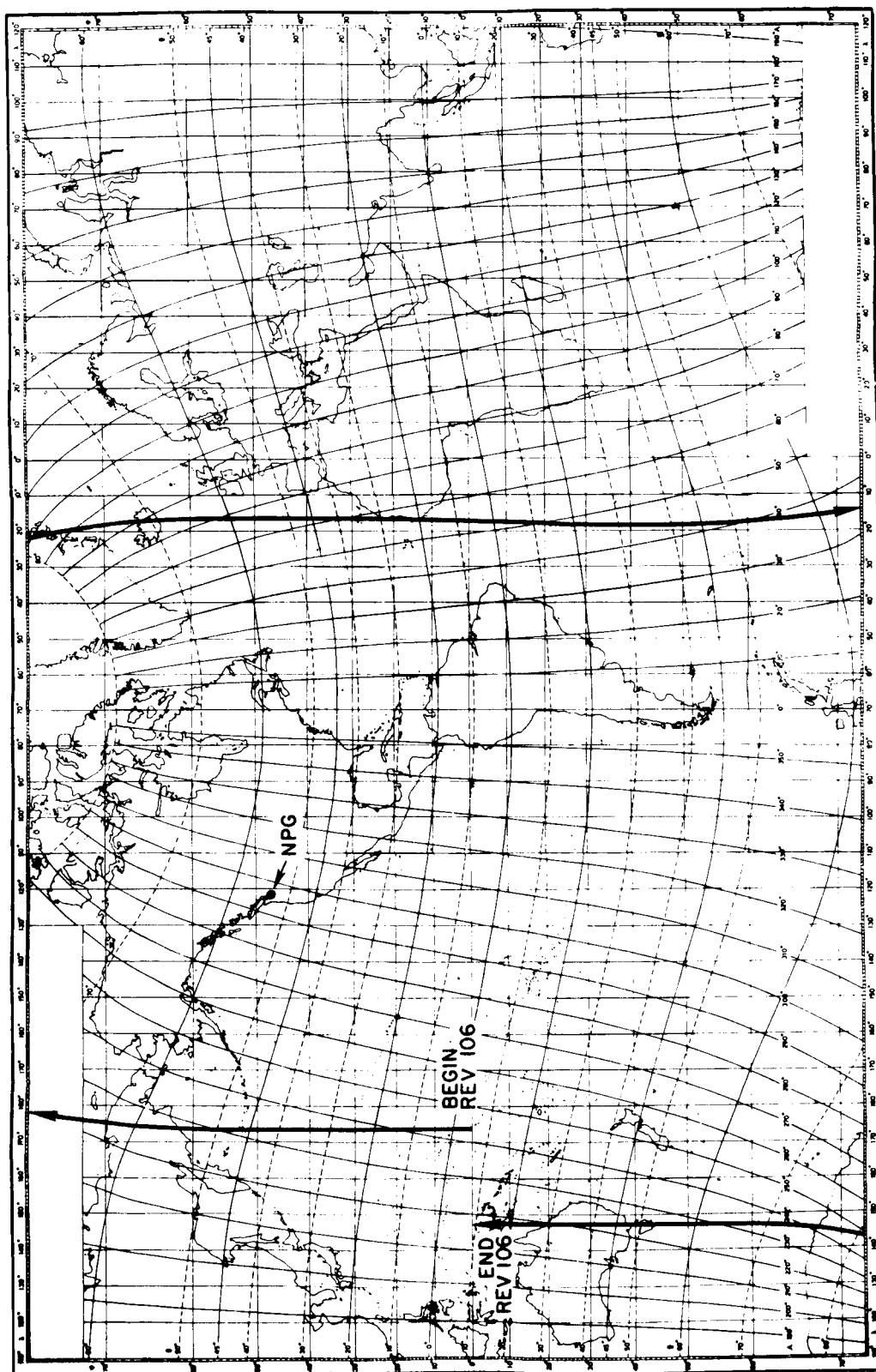


FIG. 66. OGO-II ORBITAL SUBSATELLITE PLOT WHERE VLF DATA WERE OBTAINED DURING REV. 106.

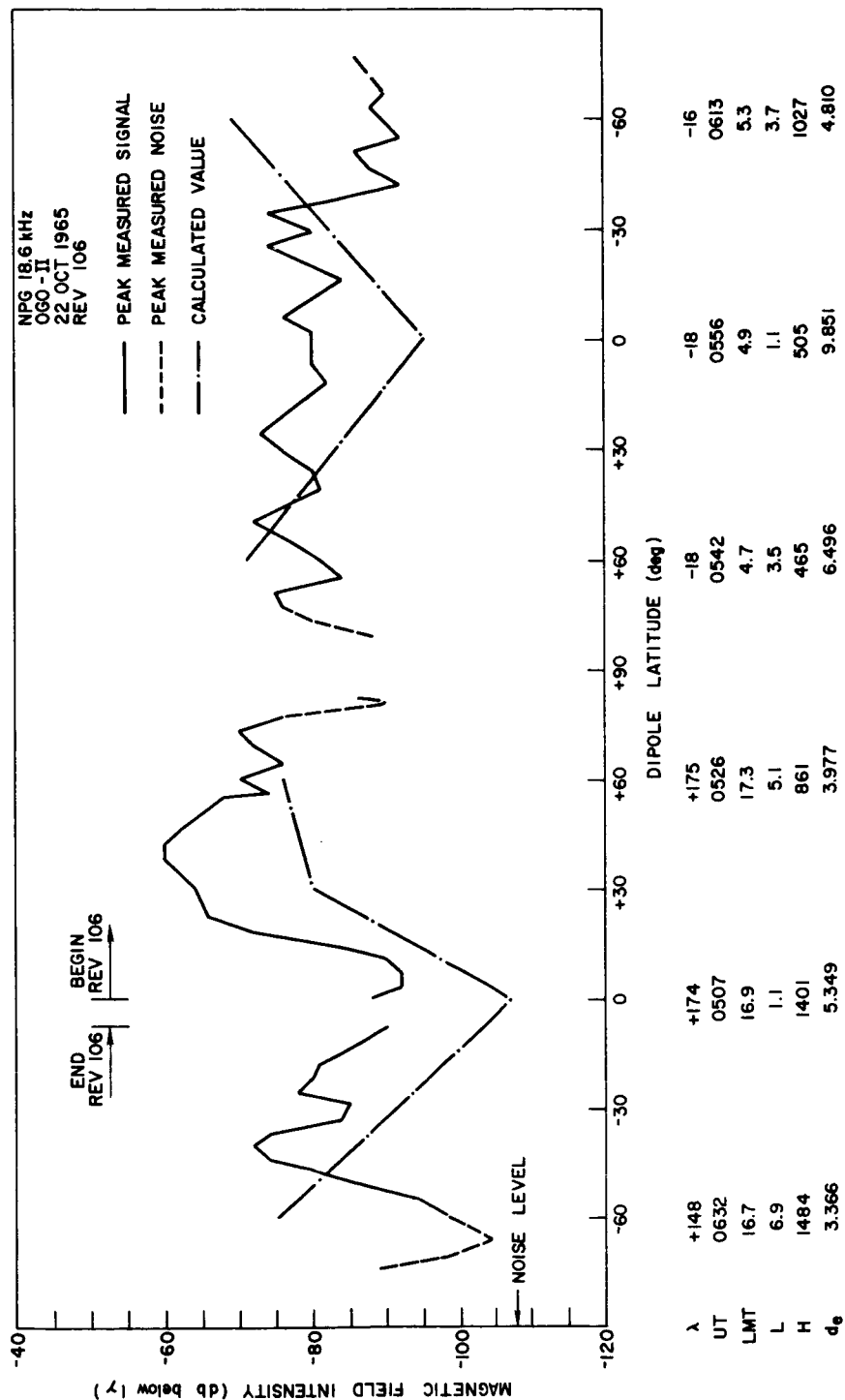


FIG. 67. OGO-II MAGNETIC FIELD STRENGTH VERSUS DIPOLE LATITUDE FOR NPG ON 22 OCT. 1965. λ = Eastern longitude (degrees); UT = universal time; LMT = local mean time at the satellite; L = L-value; H = satellite altitude (km); d_e = great-circle distance (kkm) from NPG to the foot of the field line in the Northern hemisphere. The calculated values were made using the refined model.

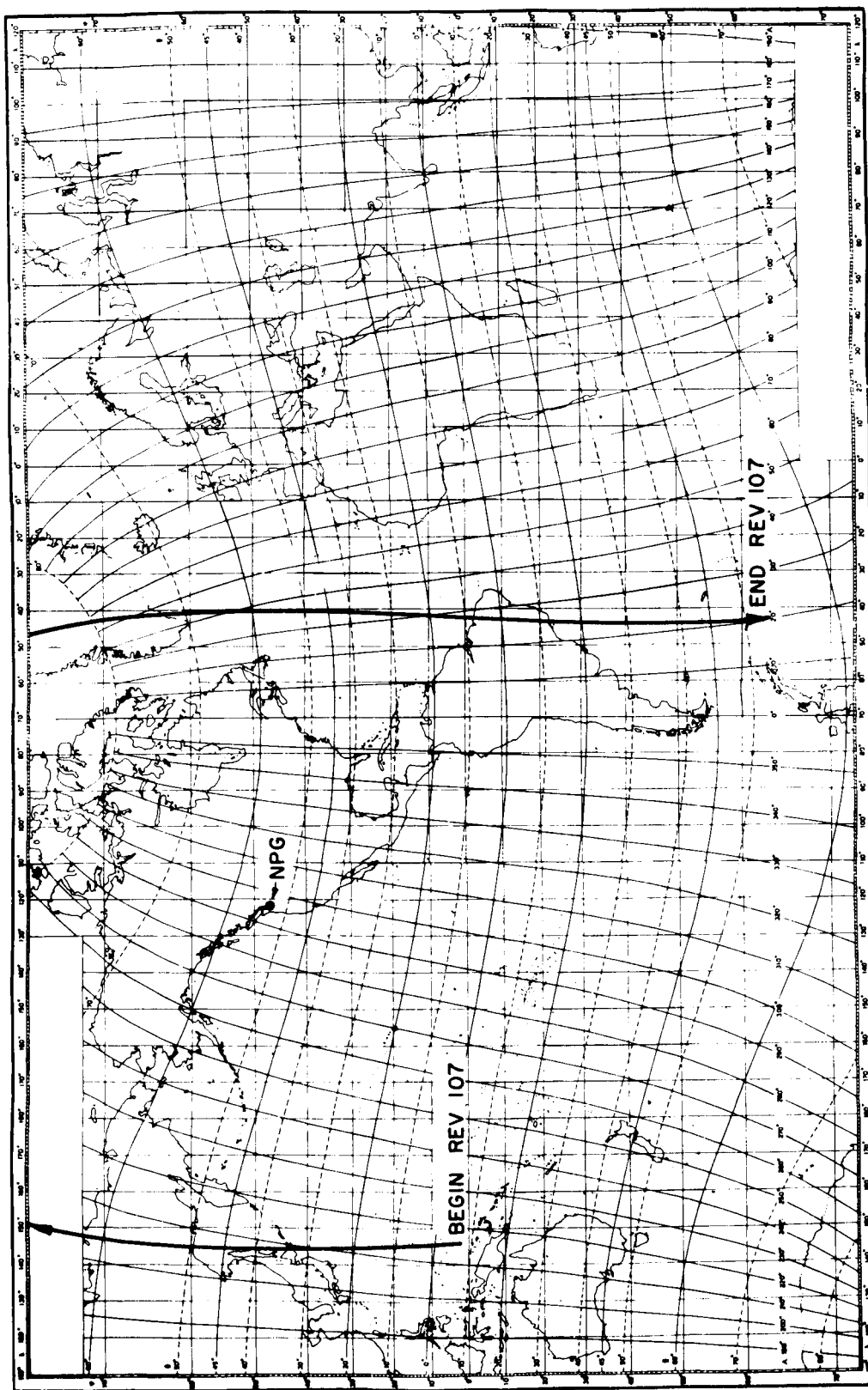


FIG. 68. OGO-II ORBITAL SUBSATELLITE PLOT WHERE VLF DATA WERE OBTAINED DURING REV. 107.

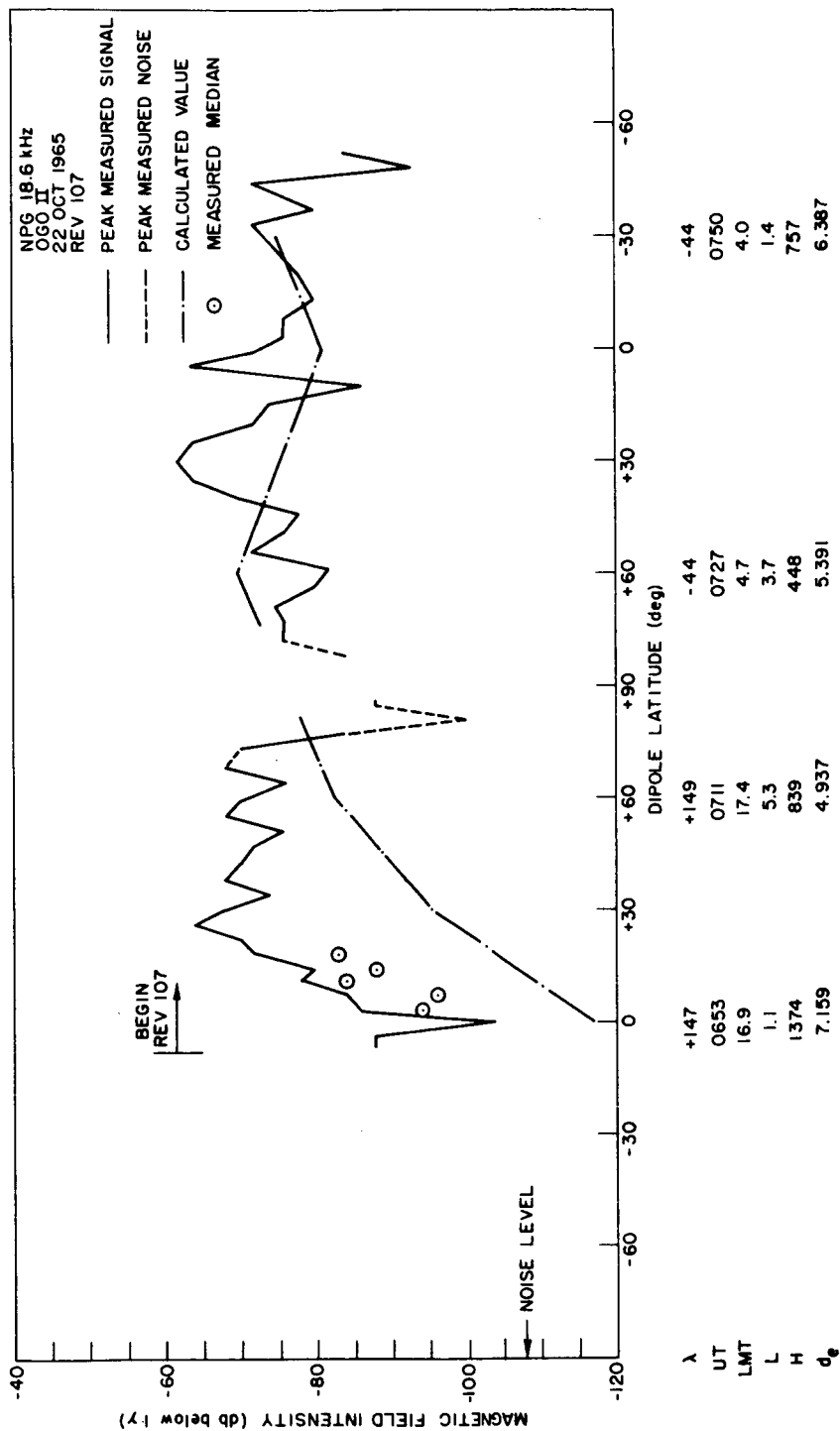


FIG. 69. OGO-II MAGNETIC FIELD STRENGTH VERSUS DIPOLE LATITUDE FOR NPG ON 22 OCT. 1965. λ = Eastern longitude (degrees); UT = universal time; LMT = local mean time at the satellite; L = L-value; H = satellite altitude (km); d_e = great-circle distance (km) from NPG to the foot of the field line in the Northern hemisphere. The calculated values were made using the refined model.

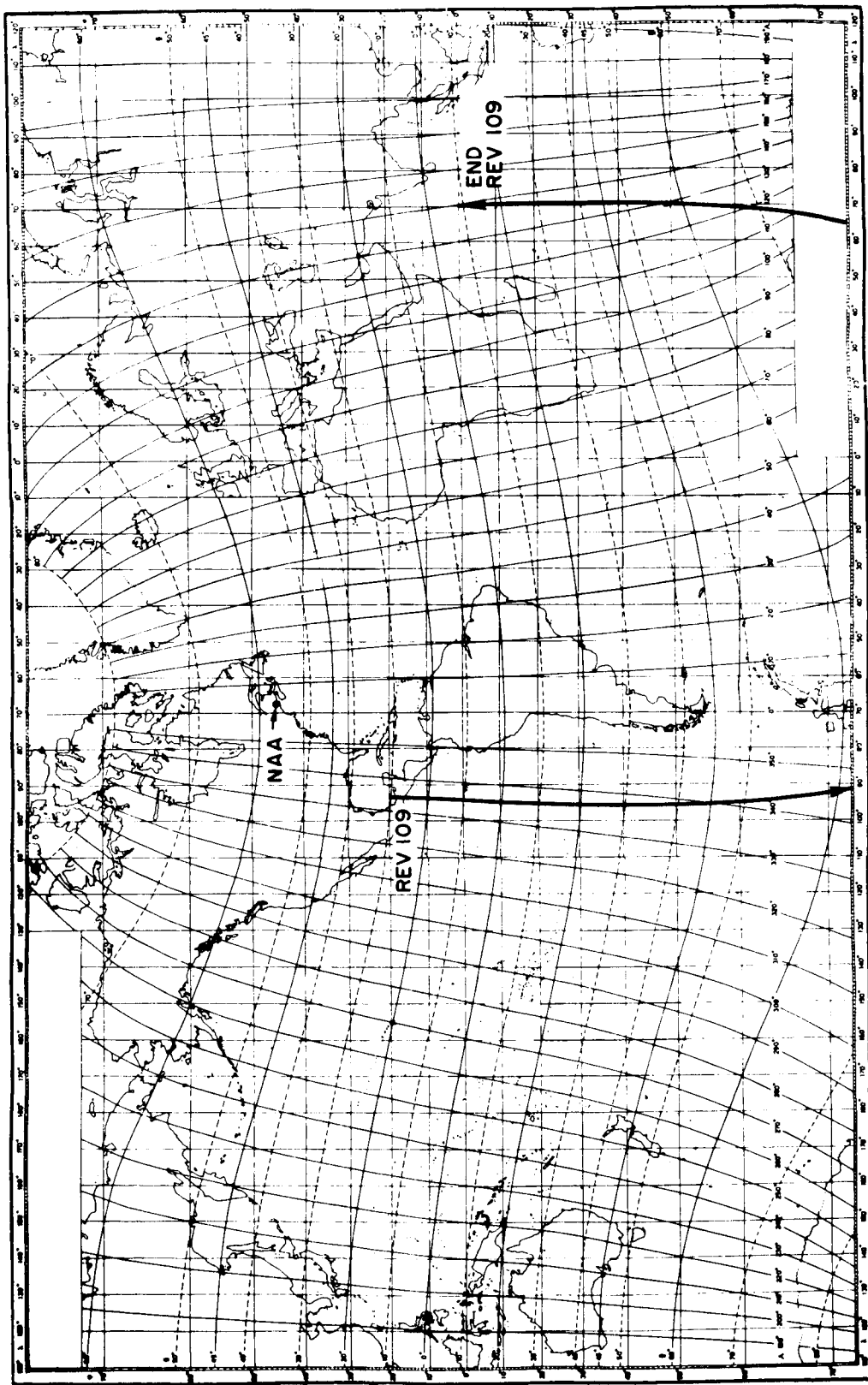


FIG. 70. OGO-II ORBITAL SUBSATELLITE PLOT WHERE VLF DATA WERE OBTAINED DURING REV. 109.

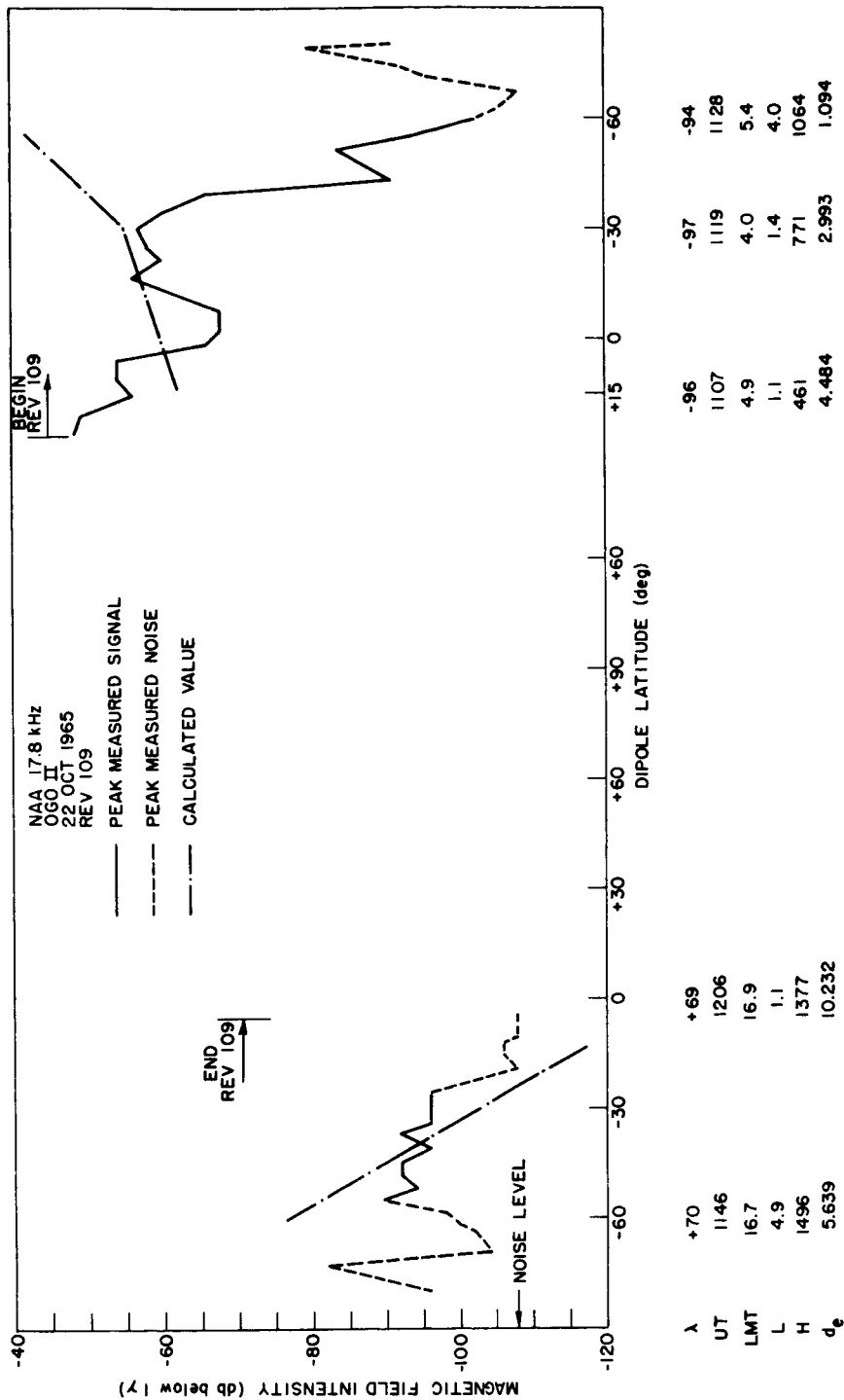


FIG. 71. OGO-II MAGNETIC FIELD STRENGTH VERSUS DIPOLE LATITUDE FOR NAA ON 22 OCT. 1965. λ = Eastern longitude (degrees); UT = universal time; LMT = local mean time at the satellite; L = L-value; H = satellite altitude (km); d_e = great-circle distance (km) from NAA to the foot of the field line in the Northern hemisphere. The calculated values were made using the refined model.

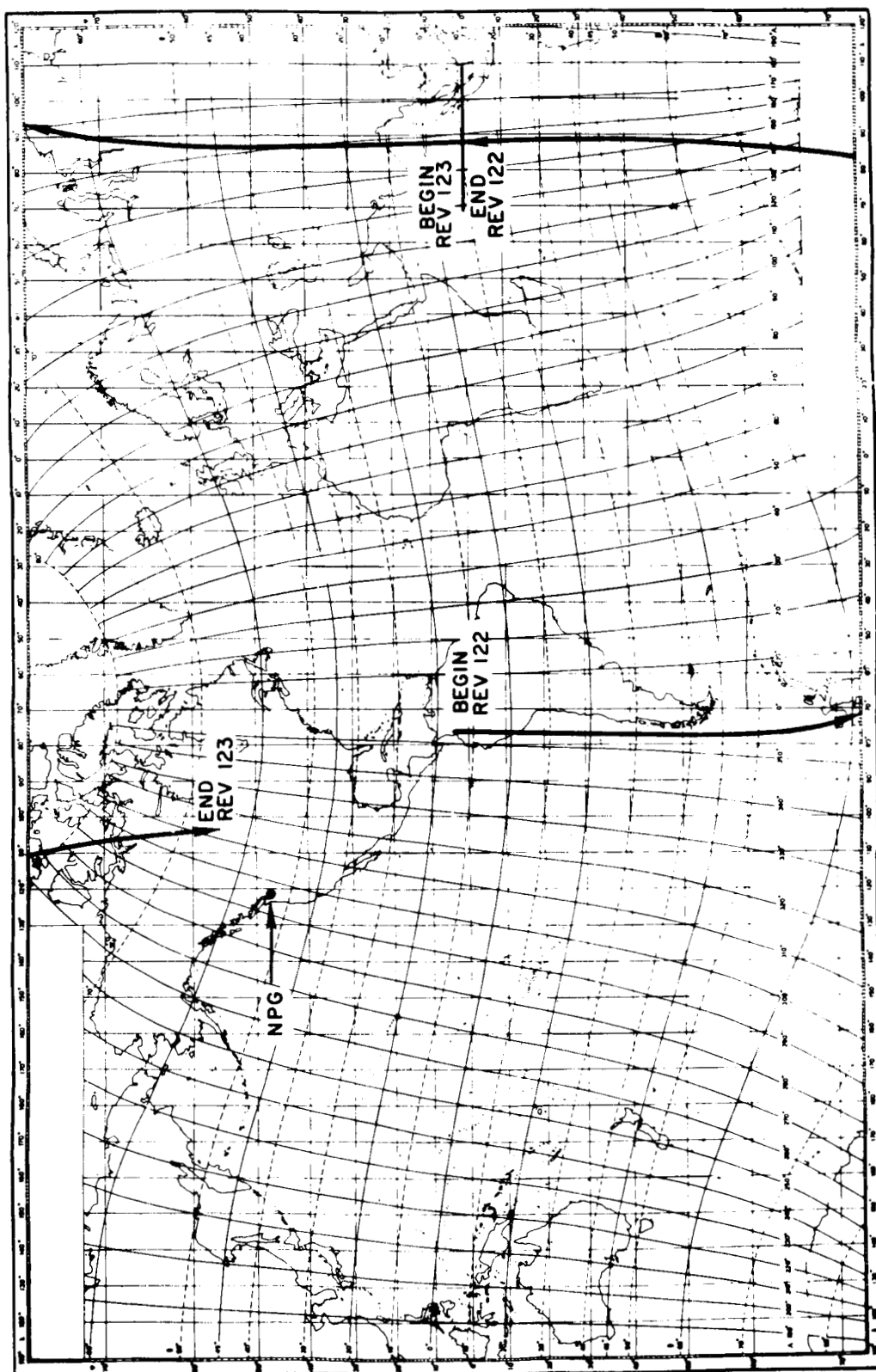


FIG. 72. OGO-II ORBITAL SUBSATELLITE PLOT WHERE VLF DATA WERE OBTAINED DURING REV. 122 AND 123.

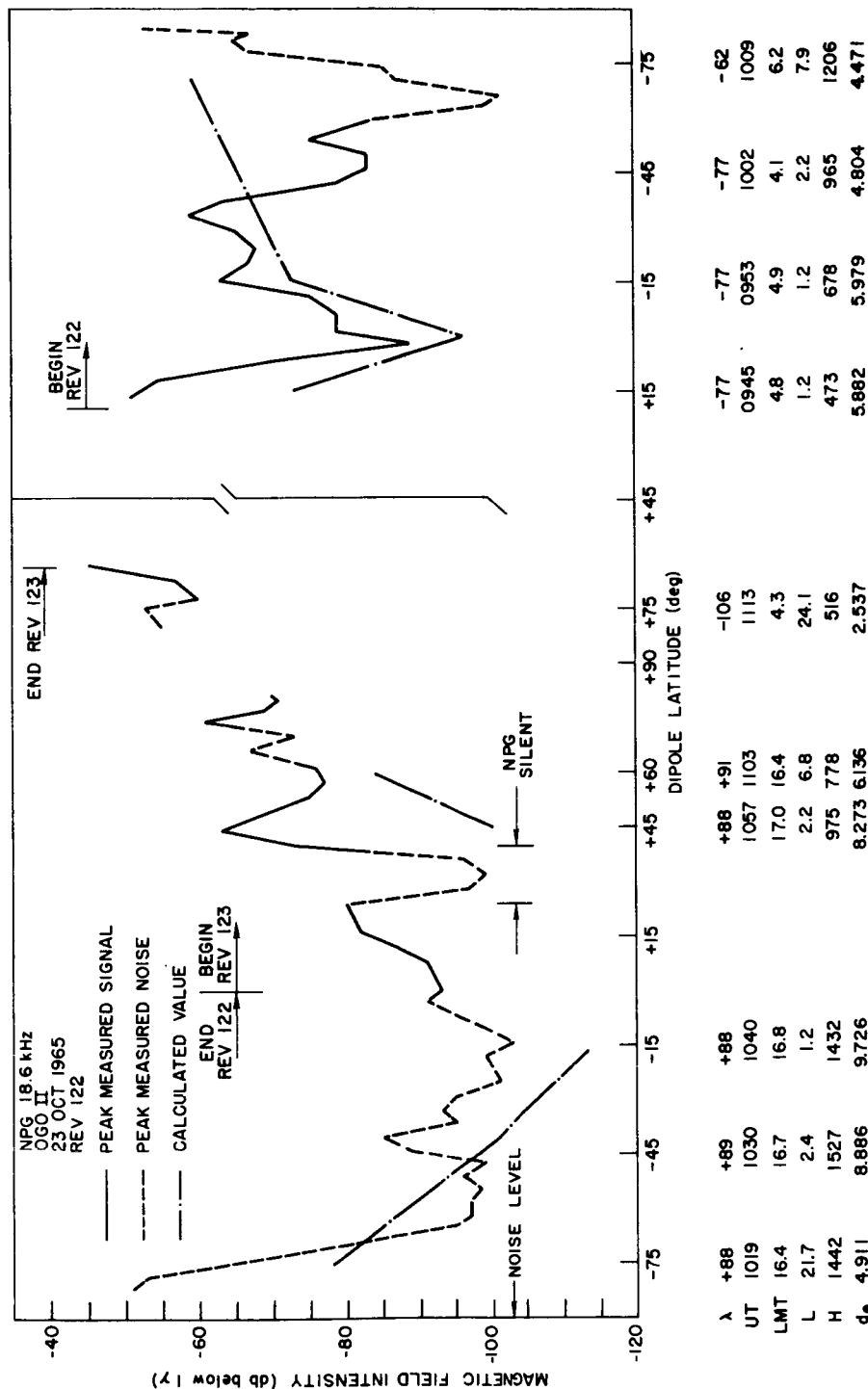


FIG. 73. OGO-II MAGNETIC FIELD STRENGTH VERSUS DIPOLE LATITUDE FOR NPG ON 23 OCT. 1965. $\lambda =$ Eastern longitude (degrees); UT = universal time; LMT = local mean time at the satellite; L = L-value; H = satellite altitude (km); d_g = great-circle distance (km) from NPG to the foot of the field line in the Northern hemisphere. The calculated values were made using the refined model.

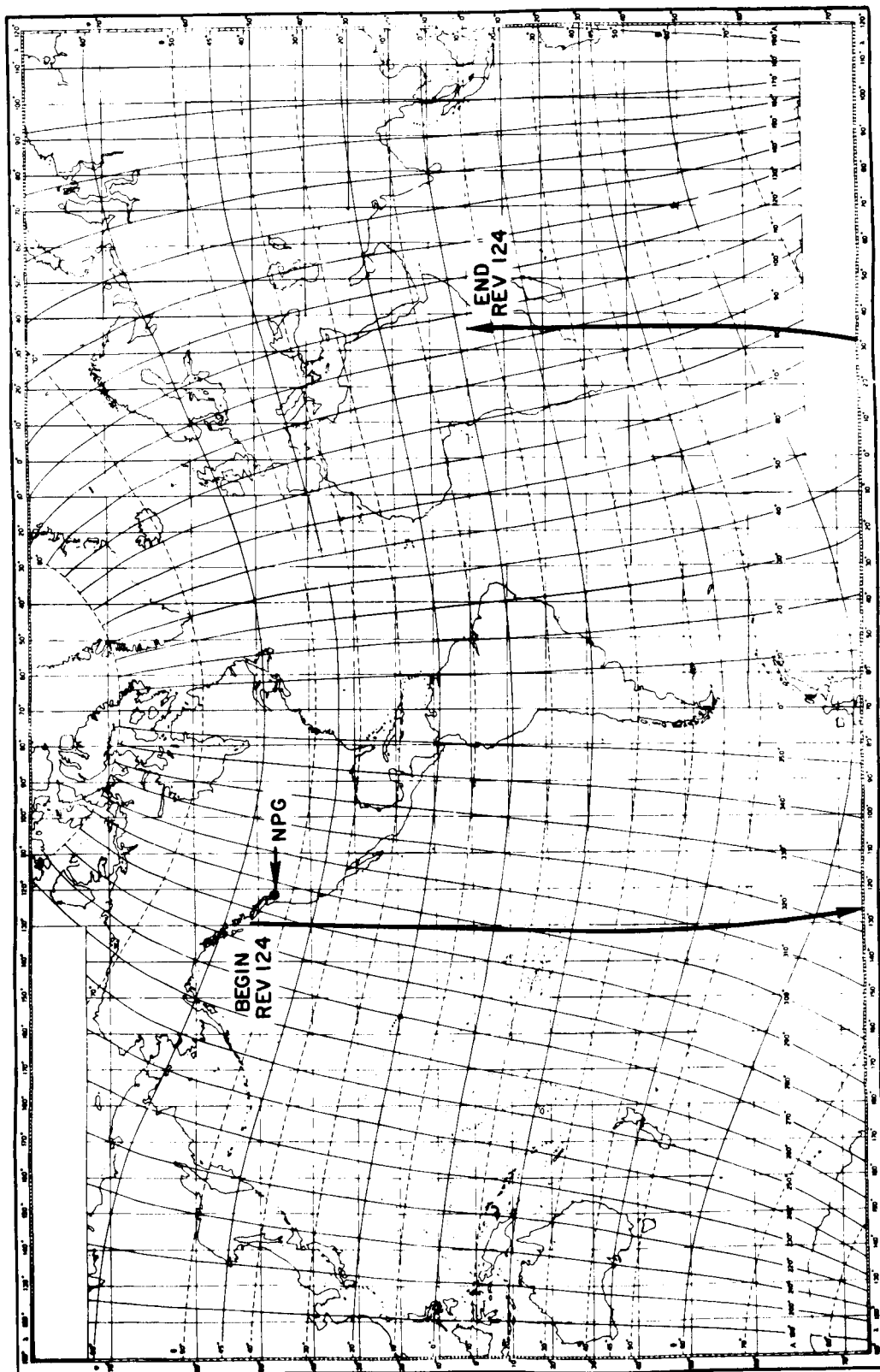


FIG. 74. OGO-II ORBITAL SUBSATELLITE PLOT WHERE VLF DATA WERE OBTAINED DURING REV. 124.

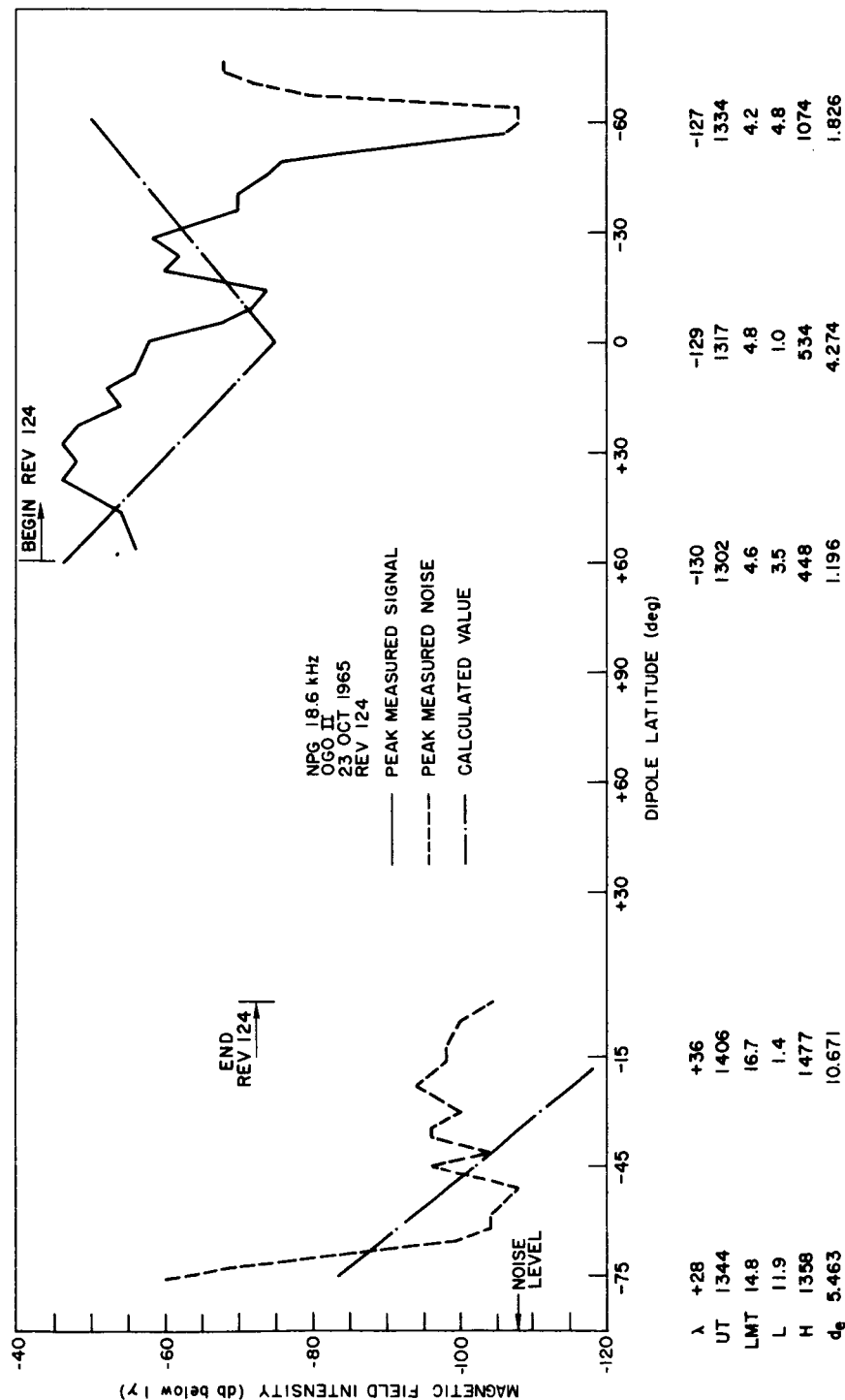


FIG. 75. OGO-II MAGNETIC FIELD STRENGTH VERSUS DIPOLE LATITUDE FOR NPG ON 23 OCT. 1965. λ = Eastern longitude (degrees); UT = universal time; LMT = local mean time at the satellite; L = L-value; H = satellite altitude (km); d_g = great-circle distance (kkm) from NPG to the foot of the field line in the Northern hemisphere. The calculated values were made using the refined model.

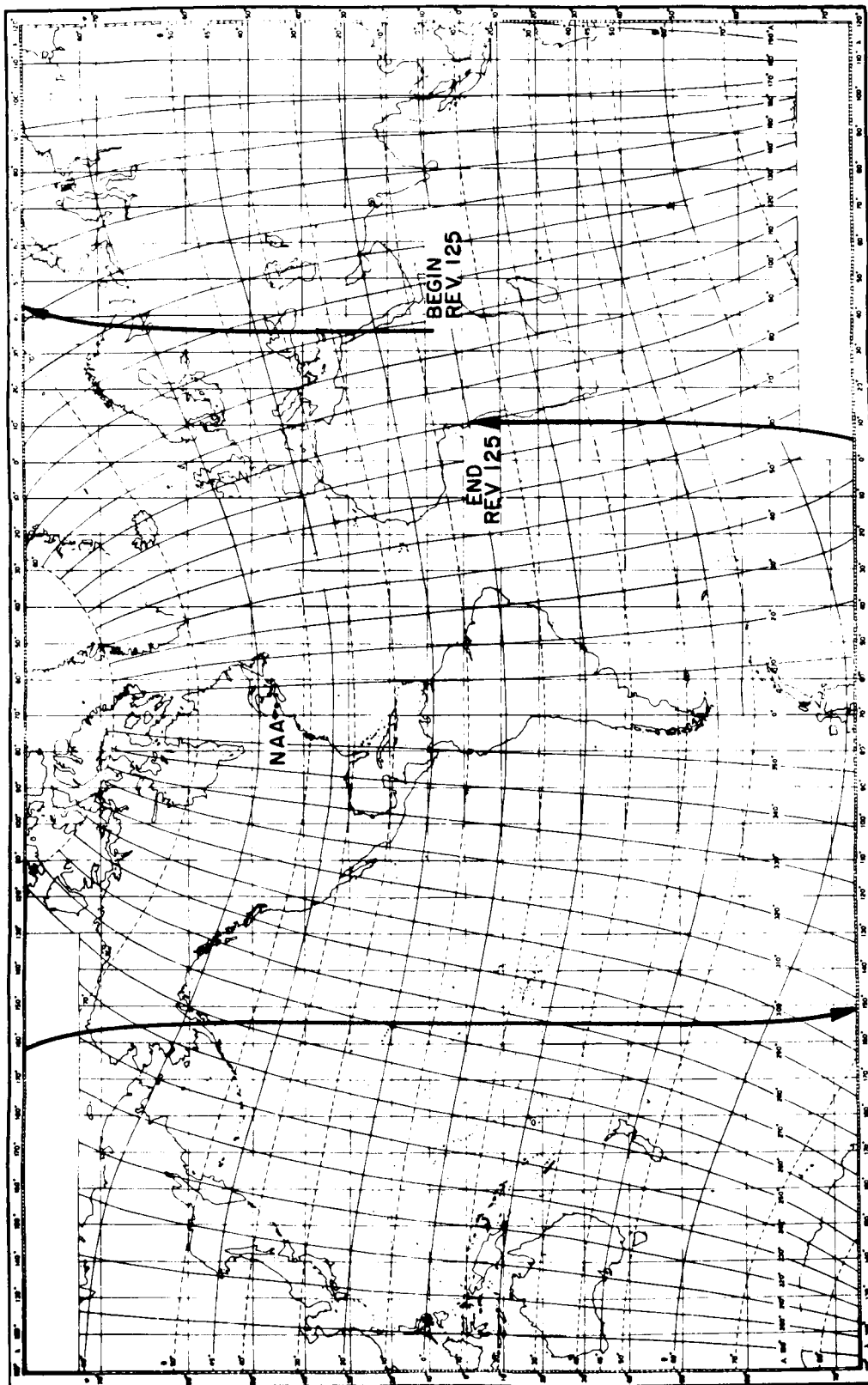


FIG. 76. OGO-II ORBITAL SUBSATELLITE PLOT WHERE VLF DATA WERE OBTAINED DURING REV. 125.

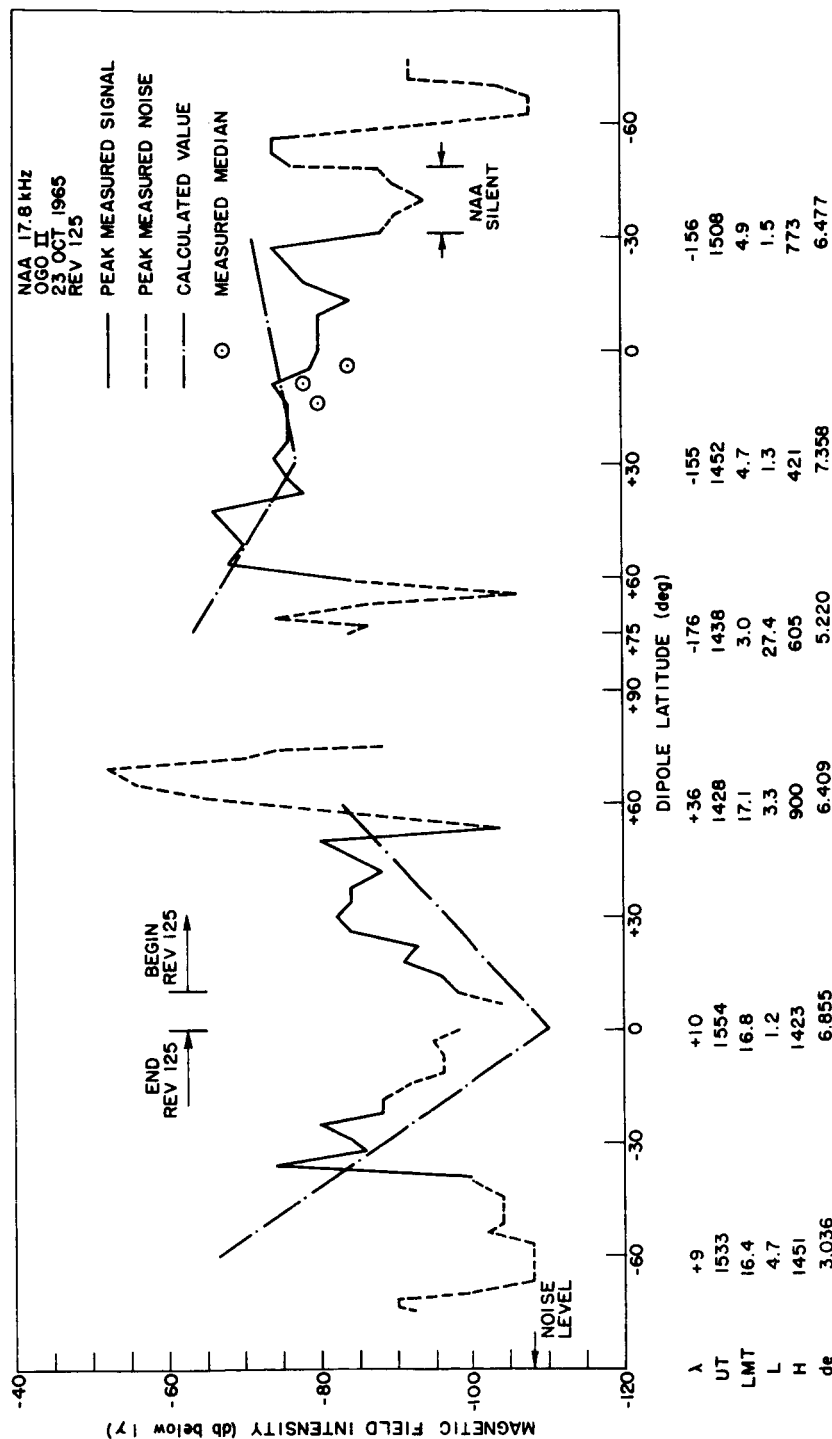


FIG. 77. OGO-II MAGNETIC FIELD STRENGTH VERSUS DIPOLE LATITUDE FOR NAA ON 23 OCT. 1965. $\lambda =$ Eastern longitude (degrees); UT = universal time; LMT = local mean time at the satellite; L = L-value; H = satellite altitude (km); d_e = great-circle distance (km) from NAA to the foot of the field line in the Northern hemisphere. The calculated values were made using the refined model.

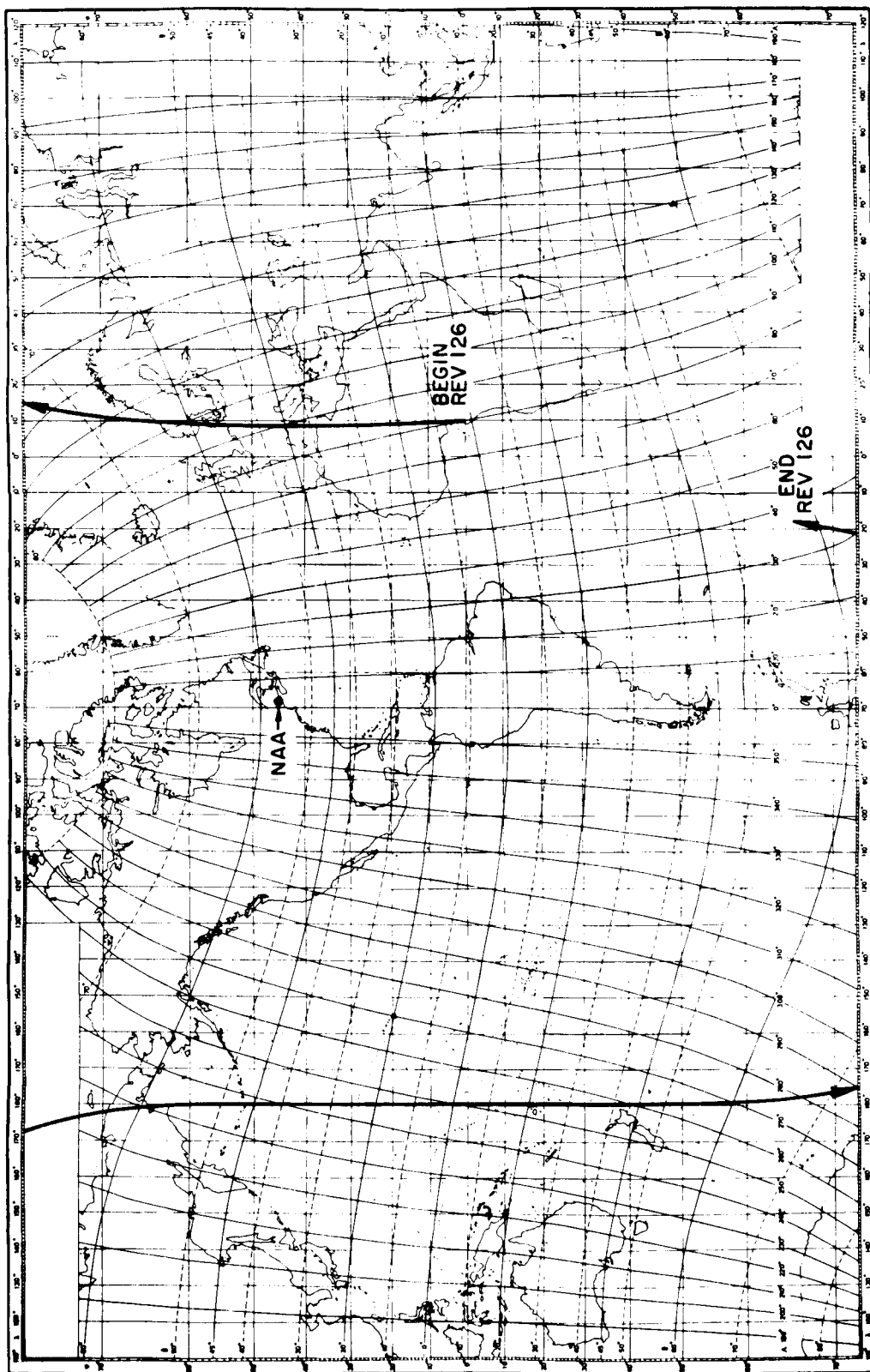
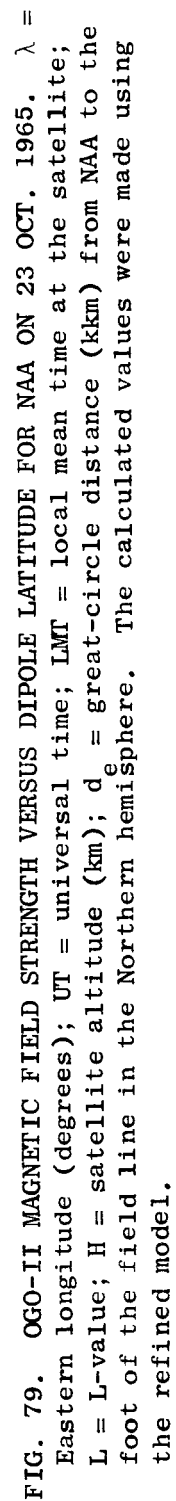


FIG. 78. OGO-II ORBITAL SUBSATELLITE PLOT WHERE VLF DATA WERE OBTAINED DURING REV. 126.



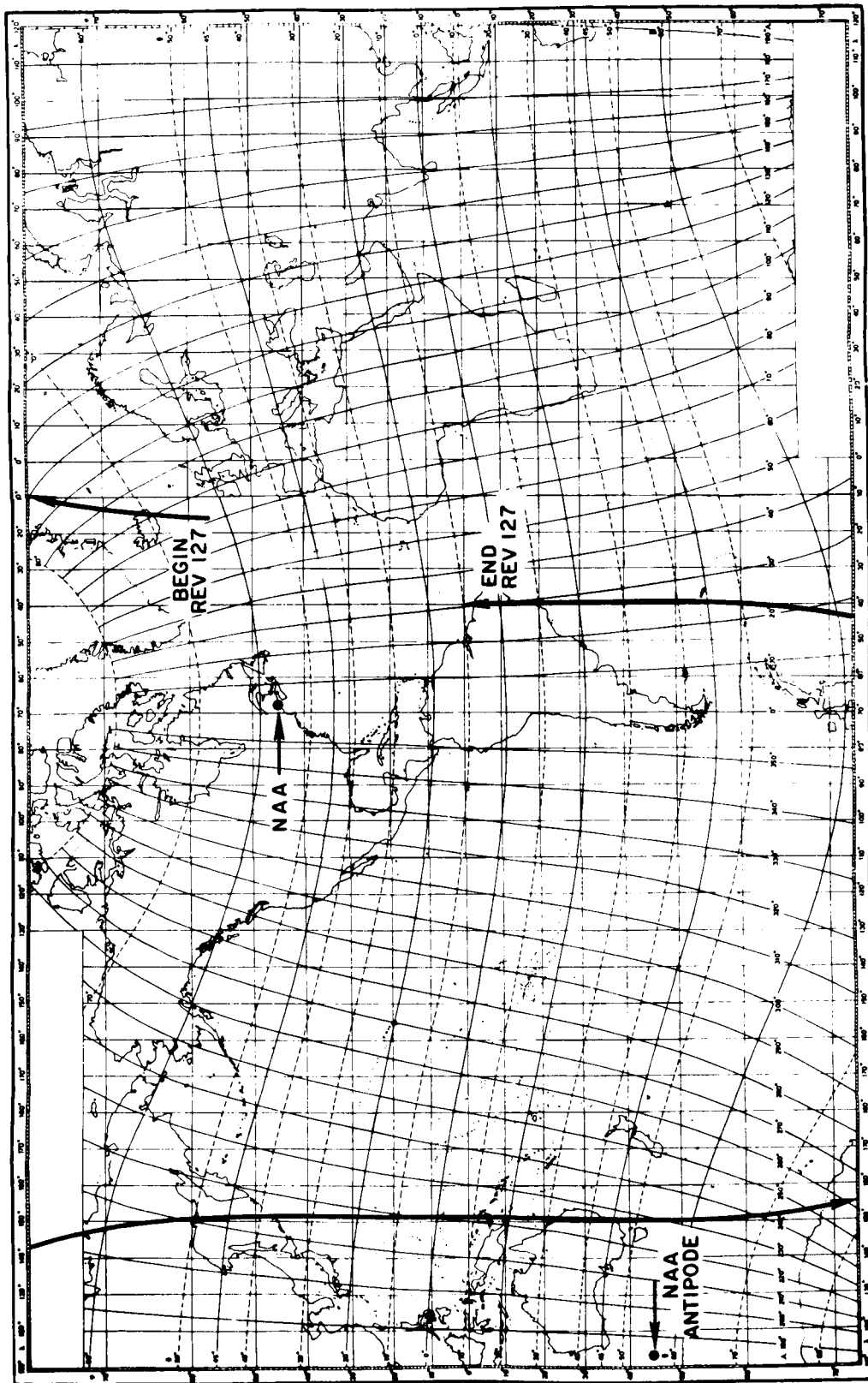


FIG. 80. OGO-II ORBITAL SUBSATELLITE PLOT WHERE VLF DATA WERE OBTAINED DURING REV. 127.

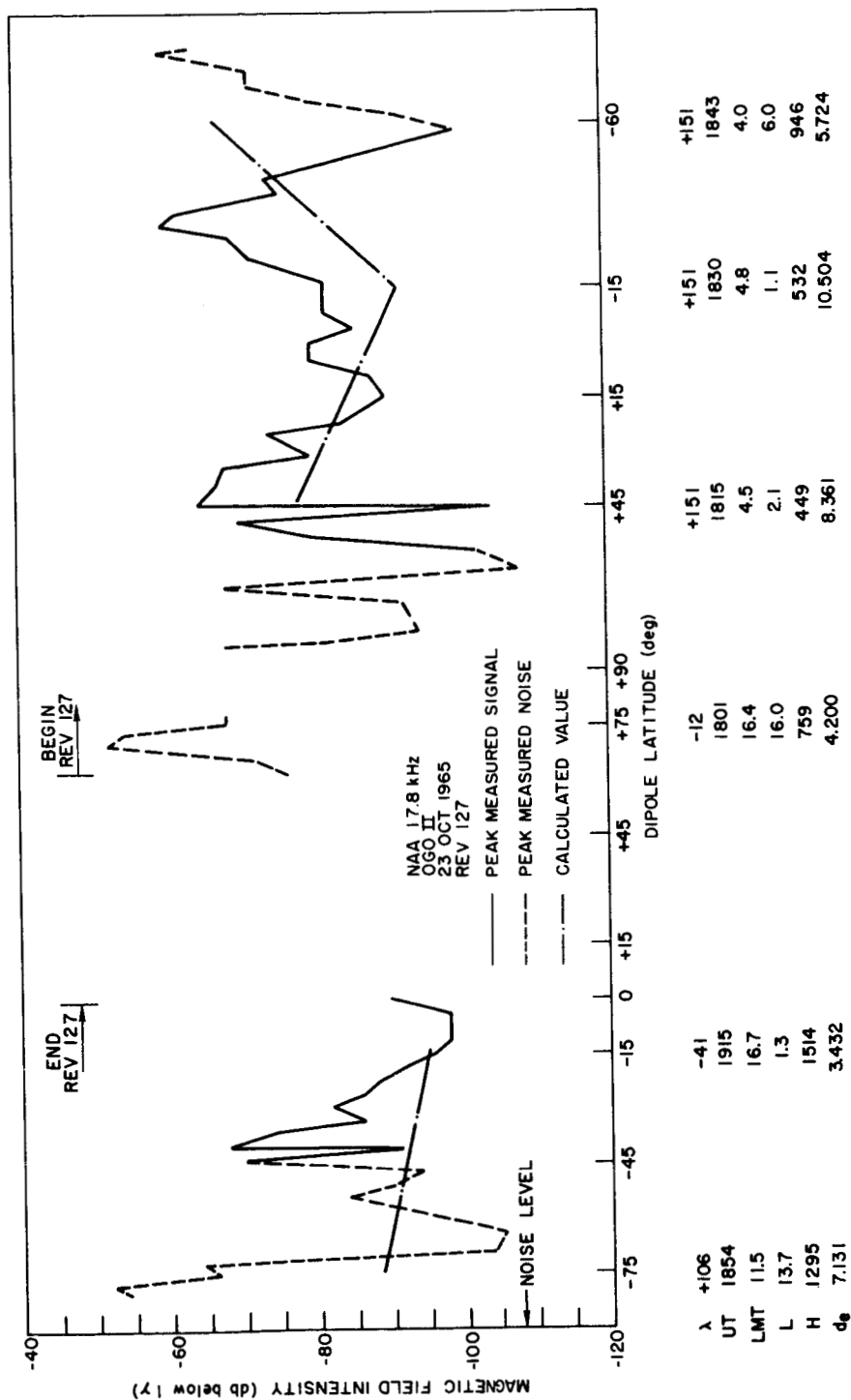


FIG. 81. OGO-II MAGNETIC FIELD STRENGTH VERSUS DIPOLE LATITUDE FOR NAA ON 23 OCT. 1965. $\lambda =$ Eastern longitude (degrees); UT = universal time; LMT = local mean time at the satellite; L = L-value; H = satellite altitude (km); d_e = great-circle distance (km) from NAA to the foot of the field line in the Northern hemisphere. The calculated values were made using the refined model.

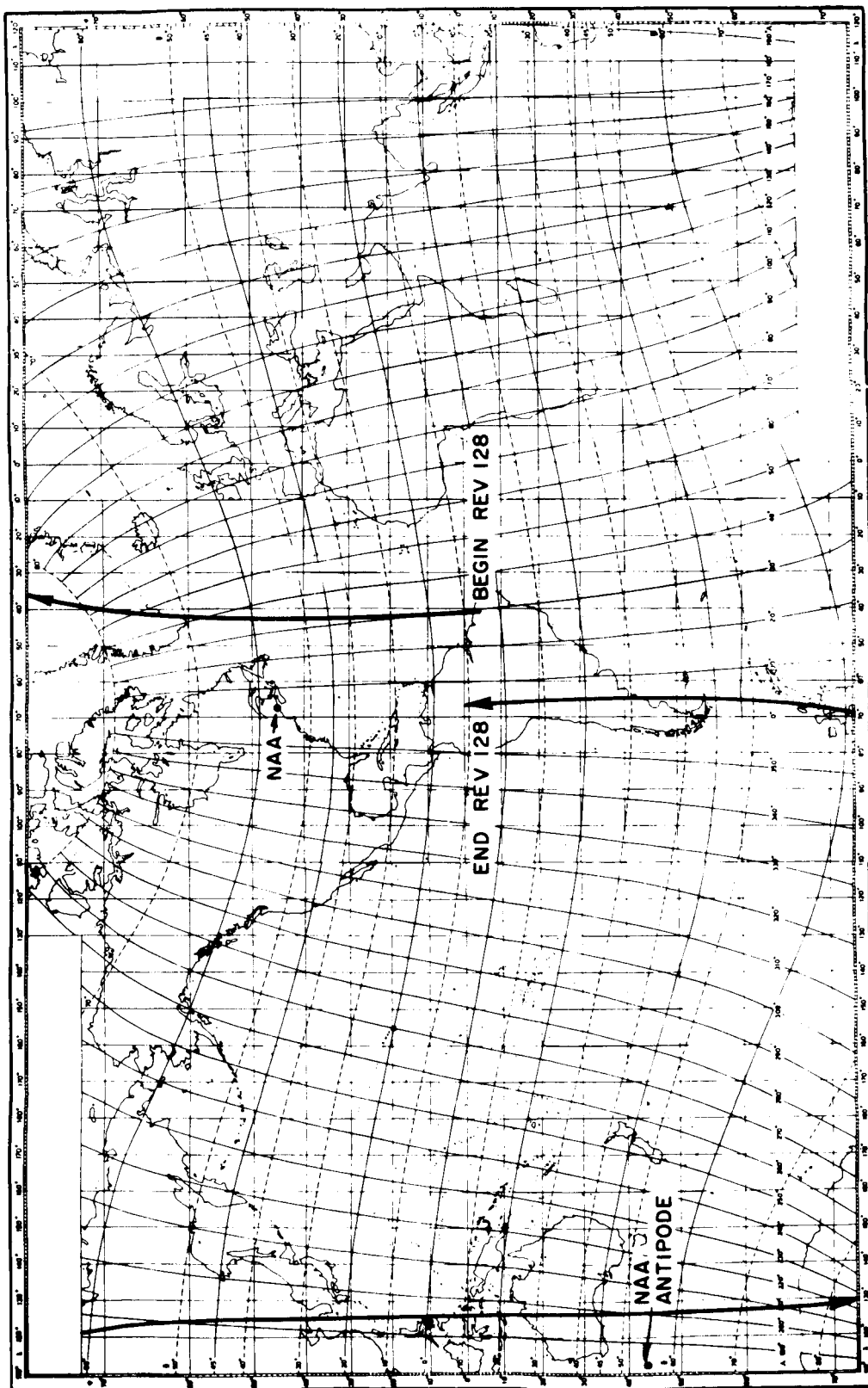


FIG. 82. OGO-II ORBITAL SUBSATELLITE PLOT WHERE VLF DATA WERE OBTAINED DURING REV. 128.

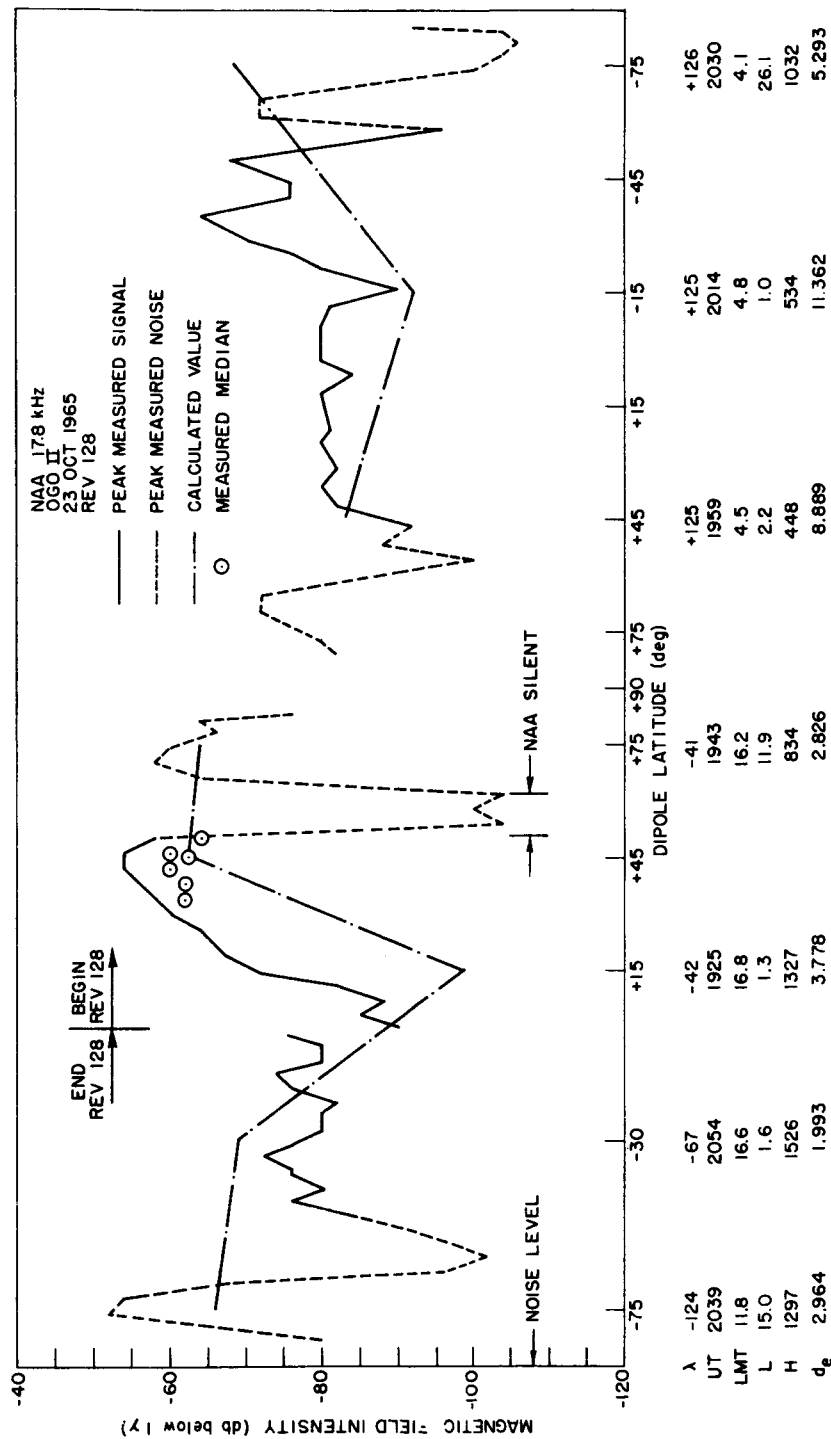


FIG. 83. OGO-II MAGNETIC FIELD STRENGTH VERSUS DIPOLE LATITUDE FOR NAA ON 23 OCT. 1965. λ = Eastern longitude (degrees); UT = universal time; LMT = local mean time at the satellite; L = L-value; H = satellite altitude (km); d_e = great-circle distance (kkm) from NAA to the foot of the field line in the Northern hemisphere. The calculated values were made using the refined model.

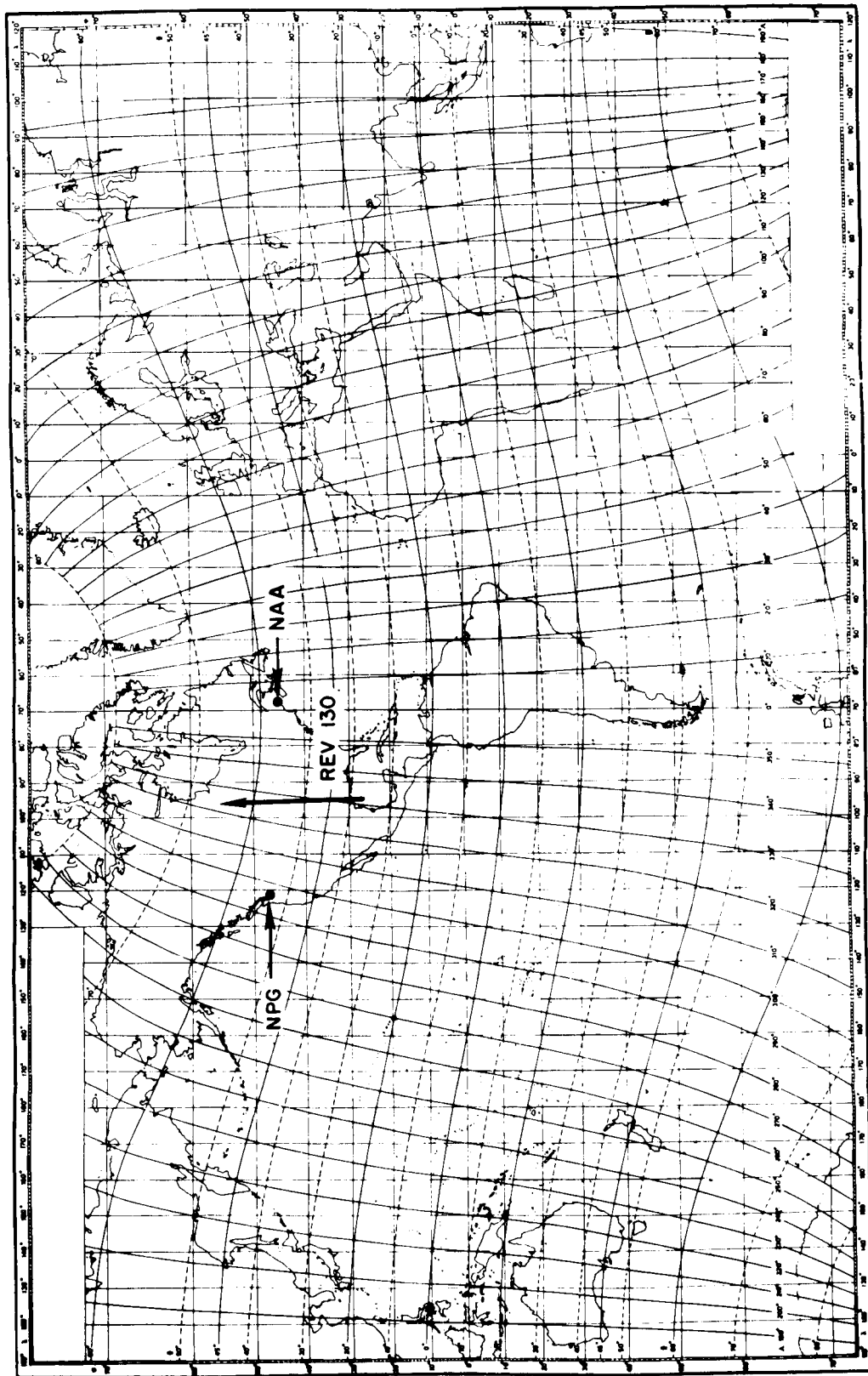


FIG. 84. OGO-II ORBITAL SUBSATELLITE PLOT WHERE VLF DATA WERE OBTAINED DURING REV. 130.

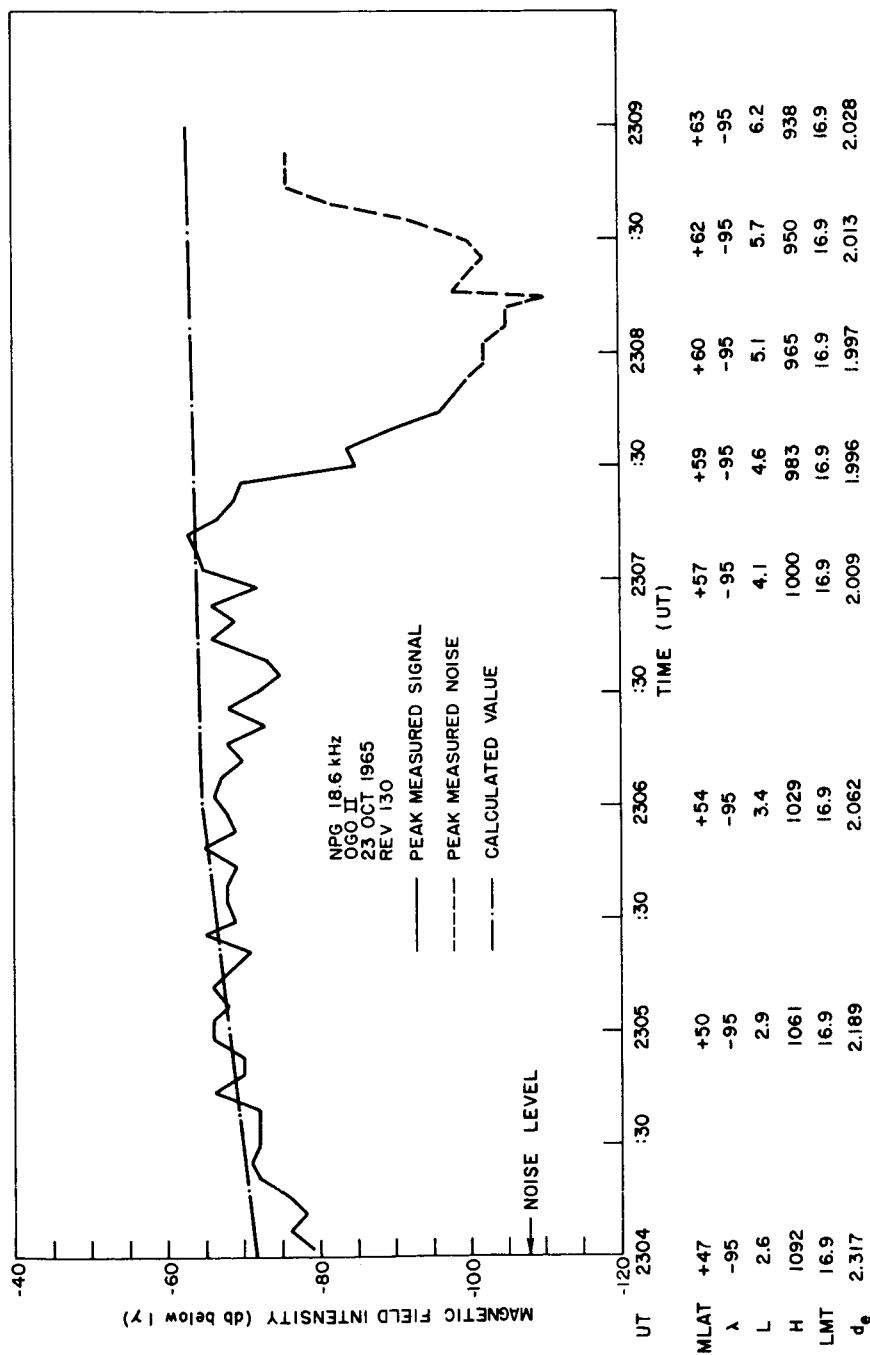


FIG. 85. OGO-II MAGNETIC FIELD STRENGTH VERSUS UNIVERSAL TIME FOR NPG ON 23 OCT. 1965. MLAT = magnetic latitude; λ = Eastern longitude (degrees); L = L-value; H = satellite altitude (km); LMT = local mean time at the satellite; d_e = great-circle distance (kkm) from NPG to the foot of the field line in the Northern hemisphere. The calculated values were made using the refined model. Note the sudden fade out of NPG signals at \approx 2307:20 UT.

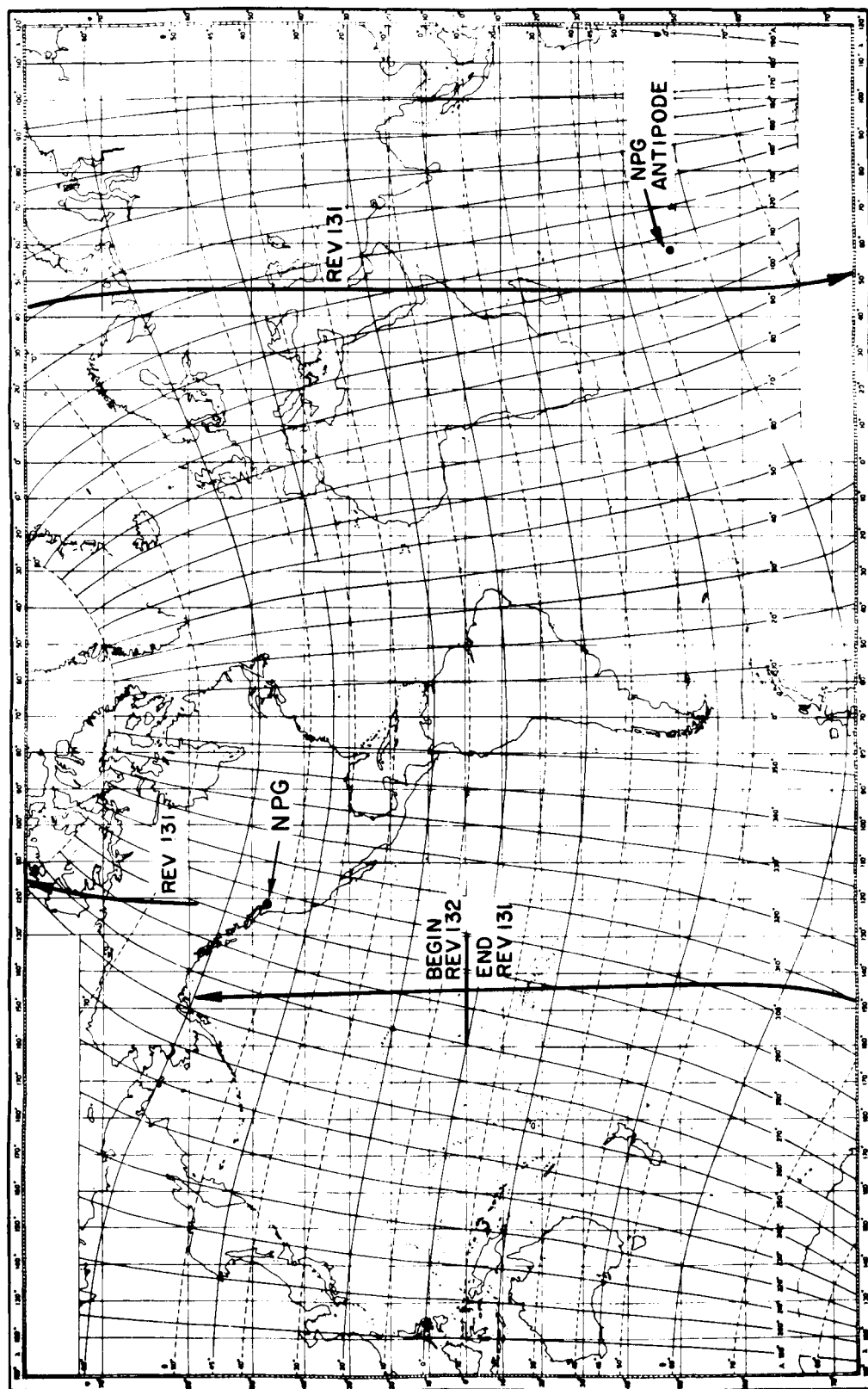


FIG. 86. OGO-II ORBITAL SUBSATELLITE PLOT WHERE VLF DATA WERE OBTAINED DURING REV. 131 AND 132.

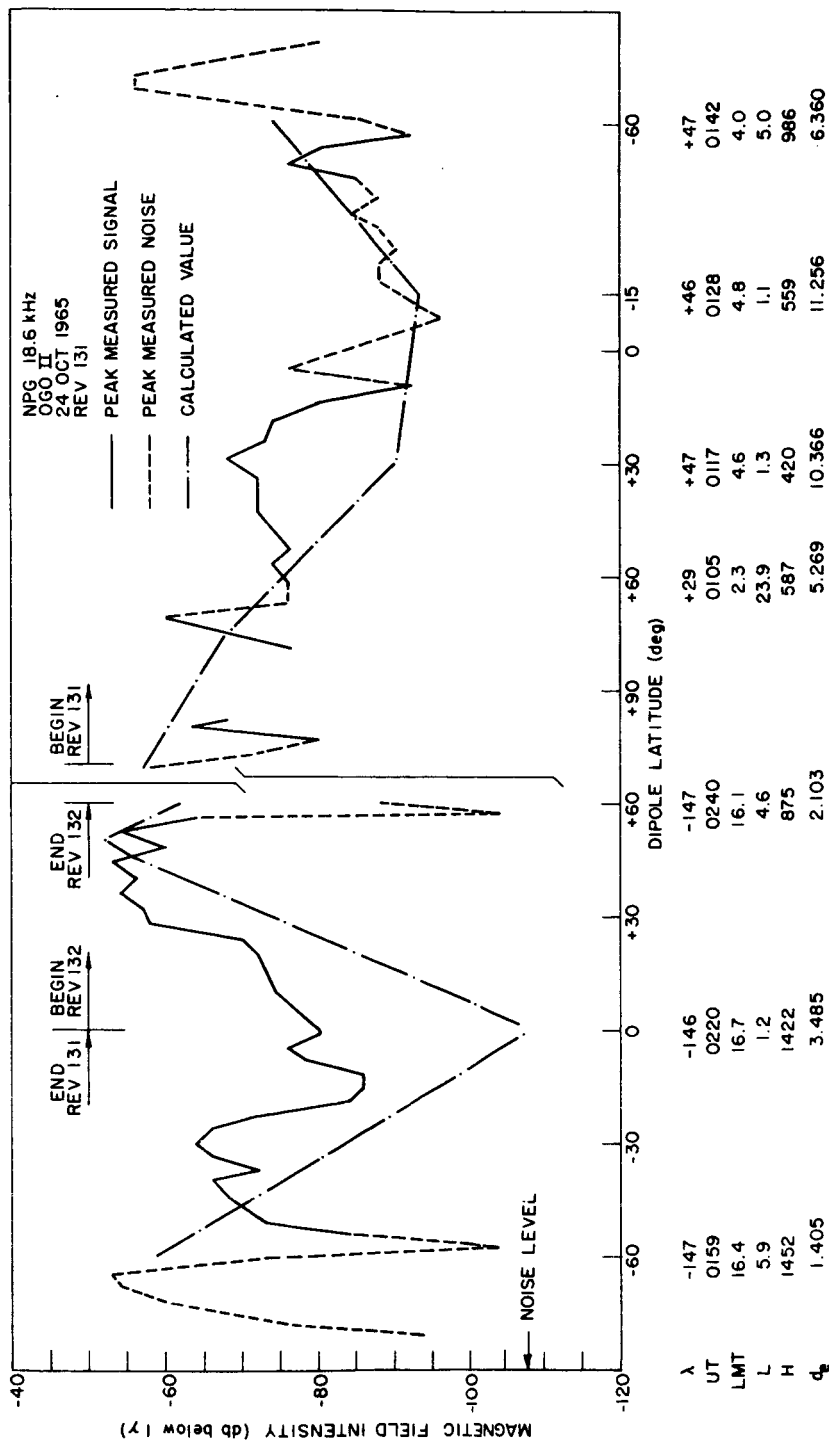


FIG. 87. OGO-II MAGNETIC FIELD STRENGTH VERSUS DIPOLE LATITUDE FOR NPG ON 24 OCT. 1965. λ = Eastern longitude (degrees); UT = universal time; LMT = local mean time at the satellite; L = L-value; H = satellite altitude (km); d_p = great-circle distance (kkm) from NPG to the foot of the field line in the Northern hemisphere. The calculated values were made using the refined model.

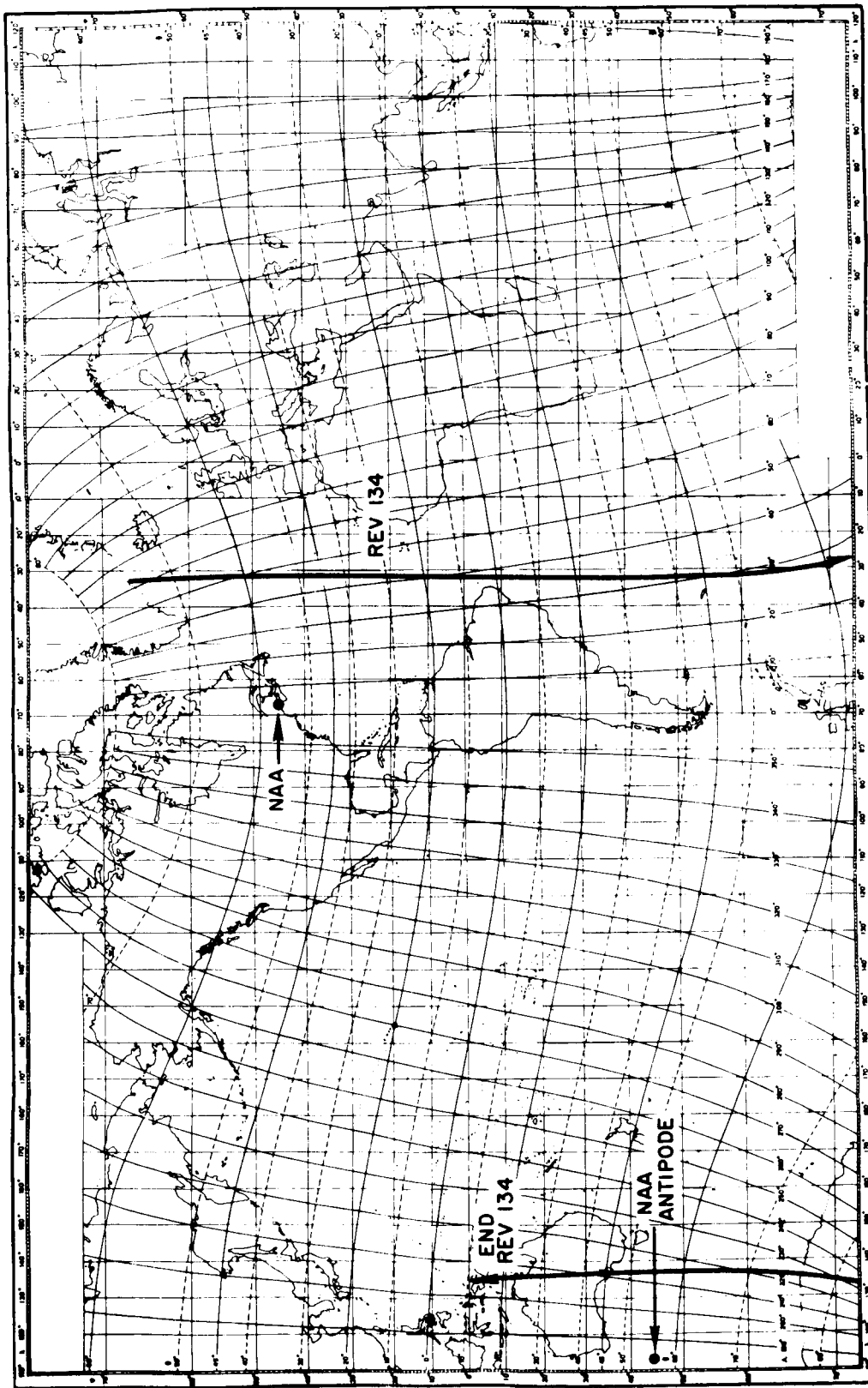


FIG. 88. OGO-II ORBITAL SUBSATELLITE PLOT WHERE VLF DATA WERE OBTAINED DURING REV. 134.

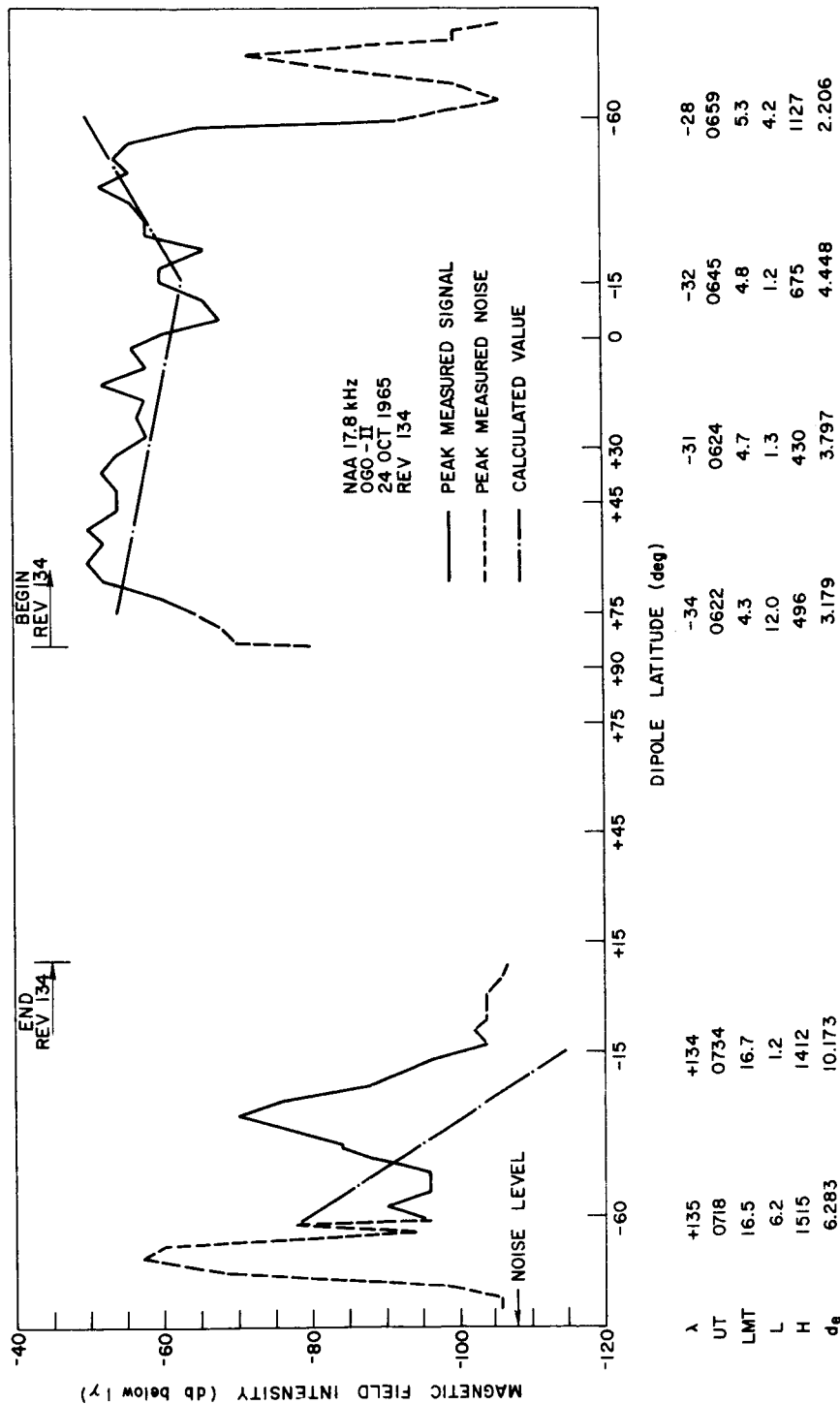


FIG. 89. OGO-II MAGNETIC FIELD STRENGTH VERSUS DIPOLE LATITUDE FOR NAA ON 24 OCT. 1965. λ = Eastern longitude (degrees); UT = universal time; LMT = local mean time at the satellite; L = L-value; H = satellite altitude (km); d_e = great-circle distance (kkm) from NAA to the foot of the field line in the Northern hemisphere. The calculated values were made using the refined model.

VII. REFINEMENT OF THE MODEL

A. THE EARTH-IONOSPHERE WAVEGUIDE LOSS

In comparing calculated and measured values of Chapter IV and Chapter VI, two important observations may be noted, both of which suggest a review of the earth-ionosphere waveguide loss used in the first-approximation model.

First, the large fluctuations of field strength versus distance in Crary's calculations (Fig. 27) are not observed in the data from either OGO-I or OGO-II. Fluctuations of this magnitude are observed, but they seldom correlate in distance with Fig. 27. Large fluctuations in the calculations are common for both the daytime and nighttime models, and are created by interference patterns between different modes of transmission. It is strange that these large fluctuations, if indeed they do exist, are not seen (correlated with distance) in the data.

Secondly, comparisons between calculated and measured field intensities for OGO-I often show measured intensities greater than those predicted by the calculations. It appears from the results of the following two sections that uncertainties in absorption and divergence are not usually sufficient to explain the observed difference.

Allcock [1966] has calculated the propagation characteristics of an 18.6 kHz signal propagating in the earth-ionosphere waveguide between a transmitter on the ground and a point just below the ionosphere. Allcock assumed, as did Crary, that the lower boundary of the ionosphere is a sharply bounded homogeneous medium of constant refractive index. His calculations allowed for two effects not treated by Crary, viz., diffraction around the earth's surface for near tangential rays [Wait and Murphy, 1957] and the net convergence of rays bouncing between a spherical earth and a concentrically spherical ionosphere [Allcock, 1964]. While Crary's calculations included the transmission losses at the ionosphere-free space boundary, Allcock removed this complication in order to give a general simplified picture of the form of variation of field strength with distance.

Allcock's results show that the scale of the interference pattern is less than that shown by Crary. The magnitude of the dips in the Allcock

nighttime pattern are on the order of 3 to 6 db out to a distance of approximately 700 km. His results show a 7 or 8 db dip at approximately 900 km, while the corresponding nighttime dip at this distance as shown by Crary is almost 15 db. Between 1 kkm and 3 kkm the Allcock pattern varies only 2 or 3 db while Crary shows two sudden drops in magnitude of approximately 14 db nighttime and 20 db daytime respectively in this same distance interval.

Allcock concludes that the undulations in the interference pattern are small, and that the general trend of the variation with distance can usefully be found by plotting the rms value of the resultant field strength, $\left[\sum |E_{n,d}|^2 \right]^{\frac{1}{2}}$, as a function of distance. From this procedure he finds that the difference between the curve for daytime transmission and that for nighttime transmission is quite small, usually less than 2 db. Except for distances between 300 and 800 km, the daytime field strength is larger than the nighttime field strength.

Allcock's calculations give the field strength of the incident signal near the lower boundary of the ionosphere. He points out that the actual signal detected by rocket-borne receiving equipment just below the ionosphere will be different from this, since there will also be a signal reflected from the ionosphere nearby. These two signals must be combined vectorially to give the resultant signal that is received. Thus the 0-hop ray is no longer independent of the reflection coefficient of the ionosphere. As an example, Allcock made calculations for a loop antenna oriented in the plane of propagation and situated just below the ionosphere. He found that the effect of the proximity of the ionospheric boundary is to decrease the received signal strength, except for very small values of d . The day to night variation is still small, the maximum difference being about 5 db at a distance of 400 km, the nighttime signal being stronger than the daytime signal.

It is not clear why Crary's and Allcock's calculations should differ so widely. However, the following factors should be considered.

1. Crary's ray summations always included the six components for $n = 0$ through 5. Additional components were then included until the amplitude of the last ray was less than 1% of the amplitude of the previous sum. Allcock's curves were computed by summing the direct (0-hop),

1-hop, and 2-hop rays. He states that the effect of neglecting the contributions of the 3-hop and higher order rays will not amount to more than about 1 db within the range 100 to 3,000 km.

2. Crary (private communication) points out that his calculations included the effects of the earth's magnetic field and the cross coupling between the two polarizations of the incident and reflected waves. Allcock apparently did not include this effect.
3. In the method used by Crary and by Allcock, the value of ω_r (a parameter which takes into account the refractive index of the medium) determines the reflection coefficient of the ionosphere. A reduction in ω_r would lower the reflection coefficient and thereby tend to smooth out the variation of field strength with distance. This effect was shown by Crary [1961]. However, upon comparing the ionospheric models used by Allcock and by Crary, one finds that Allcock's nighttime value for ω_r is 8×10^5 rad/sec, while Crary used 5×10^5 rad/sec. Thus it appears that differences in the two ionospheric models which were used do not account for the difference in the calculations.
4. It appears unlikely that the two effects treated by Allcock, but not by Crary (diffraction around the earth's surface for near tangential rays, and the net convergence of rays bouncing between a spherical earth and a concentrically spherical ionosphere) could cause the difference; particularly at the shorter distances where differences are pronounced.
5. Crary's summation of the rays was made just above the boundary after the rays had entered the ionosphere. Depending upon the angles of incidence and refraction, these rays would have different wave normal angles above the boundary than they had below and would produce different interference patterns.
6. If the large variation of field strength with distance does indeed exist just above the boundary, it is possible that other factors might prevent the observance of this phenomenon by the satellites. For instance, it appears reasonable that scattering of the waves at lower regions in the ionosphere could tend to "smear out" the large variations, thereby preventing their being observed by the satellites. This hypothesis possibly could be checked by rockets or by a satellite flying at minimum altitude.

It should be noted that both Allcock and Crary neglected the non-reciprocity of propagation of vlf radio waves over an east-west path [Crombie, 1958; Wait and Spies, 1960] in order to simplify their treatment. Azimuthal dependency arises from inclusion of the longitudinal component of the electric field of the whistler-mode wave in the ionosphere, and from the variation of attenuation with azimuth as mentioned in the following section. Neither Crary nor Allcock considered these effects in their calculations. Allcock notes that this will not affect the calculations

for the incident 0-hop ray which is dominant to distances of 1.5 to 2 kkm. However, he points out that a consideration of experimental data on ground-to-ground transmission [Watt and Croghan, 1964] suggests that neglect of non-reciprocity considerations may lead to significant errors at larger distances. As Allcock notes, the incident wave is not sensitive to azimuth. However, it should be pointed out that the transmitted wave will have azimuthal dependency.

Davies [1965] presents a survey of the work of Heritage, et al [1947], Crombie [1958], Barron [1959], Barber and Crombie [1959], Wait and Spies [1960], Johler and Harper [1962], and Wait [1962], and concludes the following:

1. The most favorable propagation conditions for a signal of frequency between 15 and 20 kHz occur for west-to-east propagation over sea at night. The attenuation rate under these conditions is a minimum and is about 1 db/kkm.
2. The maximum attenuation rate for this frequency range occurs for a land path from east-to-west during daylight and is about 3.5 to 4 db/kkm.
3. Experimental observations consistently show night values of attenuation lower than the day values.
4. In general, propagation in the 15 to 20 kHz frequency range over land adds about 1.0 to 1.5 db/kkm to the nighttime value. The non-reciprocity causes about 1 db/kkm more attenuation for east-west propagation as compared with west-east propagation. There is some evidence which indicates that attenuation is higher in the auroral zone and over large expanses of ice such as Greenland [A. G. Jean, private communication].

It is instructive to compare the Crary and Allcock calculations with the above. Allcock shows attenuation rates decreasing with distance from a maximum rate of approximately 7 db/kkm between 1 and 2 kkm, to about 3 db/kkm between 4 and 5 kkm, the distance at which his calculations terminate. By estimating a best-fit rms value for Crary's nighttime results (Fig. 27), one finds the attenuation rates to be approximately the same as Allcock's for distances up to 3 or 4 kkm, but to be substantially higher than Allcock's for greater distances. For example, the attenuation rate shown by Crary is at least 8 db/kkm between 5 and 7 kkm.

One concludes from the above that since Fig. 27 was utilized in the first-approximation model, the earth-ionosphere waveguide losses calculated for large distances are probably too high.

In order to determine the wave guide attenuation indicated by the OGO data, it is necessary to normalize the data in such a manner as to remove the other two major effects; losses due to spreading, and losses due to absorption in passing through the ionosphere. This normalization is not difficult and may be accomplished satisfactorily for either satellite, although the process for each is different. In general, the OGO-I orbit is such that losses due to spreading and absorption (both a function of latitude) change relatively slowly with time and are easy to isolate. This is not the case for the low-altitude polar orbit of OGO-II where latitude and hence absorption changes very rapidly with time.

An example of how this normalization process is performed on the OGO-I data is now shown, utilizing Fig. 34 for NAA on 24 November 1964. During the time interval 0149 UT to approximately 0203 UT (approximately midnight to 0200 LMT at the foot), the location of the foot of the field line in the Northern hemisphere changed as follows:

1. The distance from NAA to the foot increased approximately linearly with time from 2 kkm to 6.5 kkm.
2. The longitude of the foot moved Eastward across the Atlantic Ocean while the latitude of the foot remained within $\pm 5^\circ$ of 50° geomagnetic latitude, with latitude at the end of the interval only approximately 3° higher than at the beginning.
3. As the foot location moved almost due East from NAA, essentially all of the earth-ionosphere waveguide path was over sea water for the entire interval.

From (2) above and Fig. 29, it is seen that the signal will experience approximately $\frac{1}{2}$ db less absorption at the end of the time interval than at the beginning.

During this interval, the satellite was in the Southern hemisphere flying towards the north-east and its position (latitude and altitude) changed in such a manner that the gyrofrequency at the satellite increased from 212 kHz to approximately 325 kHz. From the methods of Chapter III, the difference in divergence of the signal is approximately 2.2 db with the divergence loss being less at the end of the interval.

From the foregoing, one may conclude that over the time interval involved, the signal intensity at the satellite was increased by approximately 2.7 db due to changes in absorption and divergence. Removing the effects

of these two factors should thus provide the normalized rate of attenuation due to earth-ionosphere waveguide losses alone.

When the data of Fig. 34 are normalized in this manner, one obtains an average earth-ionosphere waveguide attenuation rate of approximately 2.7 db/kkm over this interval of 2. to 6.5 kkm. Recall that this is for a west-to-east propagation path over sea water at night.

It should be noted that the rate of earth-ionosphere waveguide attenuation is non-linear, becoming successively smaller with distance as indicated by both Crary and Allcock. This is due to the two-dimensional spreading of the signal in the earth-ionosphere waveguide. For distances used in the above calculations, this loss varies approximately as the inverse square root of the distance, thereby adding another 3 db loss each time the distance is doubled. This loss is of course inherently included in all experimental observations, but is sometimes omitted (or removed) when presenting these data or the results of theoretical calculations based on waveguide mode theory. For example, although the conclusions of Davies are based on experimental observations, the loss due to two dimensional spreading has been removed. Davies minimum attenuation rate is approximately 1 db/kkm for east-to-west propagation over sea water at night. When one adds to this rate the effects of two dimensional spreading good agreement (within $\frac{1}{2}$ db/kkm) is obtained between his conclusions and the OGO-I data for the earth-ionosphere waveguide loss of the above example.

Normalization of the OGO-II data is accomplished in the following manner. In Chapter V it was pointed out that the OGO-II orbit is essentially polar and has a period of 104 minutes. Therefore on each successive revolution the satellite will cross any given latitude at a longitude 26° West of where it crossed this given latitude on the previous revolution. Therefore, where data from successive revolutions are available, one obtains two situations (one on the dayside and one on the nightside of the earth) where the difference in signal intensity measured at a given latitude is due almost entirely to the difference in the length of the earth-ionosphere waveguide path. By choosing a dipole latitude of approximately 50° for these comparisons, one obtains the following advantages:

1. The differential earth-ionosphere waveguide distance will be nearly due East or due West of either NAA or NPG. This permits a study of

the non-reciprocity of propagation over an east-west path.

2. Absorption of the signal in passing through the ionosphere will be virtually the same on each successive revolution. This follows from the flatness of the absorption curve at latitudes as high as 50° (see Fig. 29) and also from the fact that at 50° magnetic latitude, the position of the foot of the field line at heights where maximum absorption occurs will not be sensitive to variations in satellite height on successive revolutions.

Since the satellite altitude does not change appreciably at a given latitude between successive revolutions, differences in divergence of the signal, assuming field-aligned propagation, will be less than 1 db and may be neglected.

To illustrate the above procedure, consider the OGO-II data from revolutions 74 and 75 (Figs. 57 and 59). On revolution 74 at approximately 2136 UT, the satellite reached a northern magnetic latitude of 50 degrees at a distance of approximately 400 km west of NAA. The measured peak value of NAA field intensity was 40 db below 1 gamma. On the next revolution, the satellite reached a northern magnetic latitude of 50 degrees at approximately 2320 UT at a longitude 26 degrees west of the position noted above. The measured peak value of NAA field intensity was 58 db below 1 gamma. At this latitude (approximately 40° geographic) a 26 degree change in longitude represents a distance change of approximately 2.22 kkm.

The indicated earth-ionosphere waveguide attenuation rate over this distance interval is therefore

$$\frac{(58 \text{ db} - 40 \text{ db})}{2.22 \text{ kkm}} \cong 8.1 \text{ db/kkm}.$$

This is for an east-to-west path over land during the daytime. Note that this result gives an average rate of attenuation (the slope of the attenuation versus distance curve) over the distance interval involved.

In order to compare the absolute value (not just the slope) of these measured attenuation rates from OGO-I and OGO-II with Crary's calculated values of Fig. 27, additional normalization is required. First, it is necessary to remove the effects of absorption and divergence (as discussed above) from the measured values, and to normalize the measurements to a radiated power of 1 kw. Secondly, it is necessary to reduce the magnitudes

of the peak measured values by an amount corresponding to the correction factors calculated in Chapter II. These correction factors provide an estimate of the ratio between peak to average values of the measured data, and must be utilized whenever one compares calculated values (based on average power) to the peak intensities scaled from the data. All of these factors have been considered in the normalization process.

By the methods outlined above, all of the OGO-I and OGO-II data have been utilized to produce the earth-ionosphere waveguide attenuation rates shown in Table 6 and in Figs. 90 and 91. Uncertainties in the normalization process and in the scaling of records probably introduce sizeable errors. Error bars on each of the attenuation rates shown in Figs. 90 and 91 indicate the best estimate of these uncertainties.

TABLE 6. ATTENUATION RATES IN THE EARTH-IONOSPHERE WAVEGUIDE
AS INDICATED BY NORMALIZING THE OGO DATA. Rates are in db/kkm.

Distance Interval	Direction of Propagation	Land		Sea	
		Day	Night	Day	Night
0.5 to 1.0 kkm	West-to-East	12			
1 to 2 kkm	West-to-East				
	East-to-West	8.1			
	North-to-South		7.3		
2 to 6.5 kkm	West-to-East				2.7
4 to 5 kkm	East-to-West	5.8			
6 to 9 kkm	West-to-East	3.8	2.16 1.4		2.7
	East-to-West			2.73 5.4	3.6 4.9

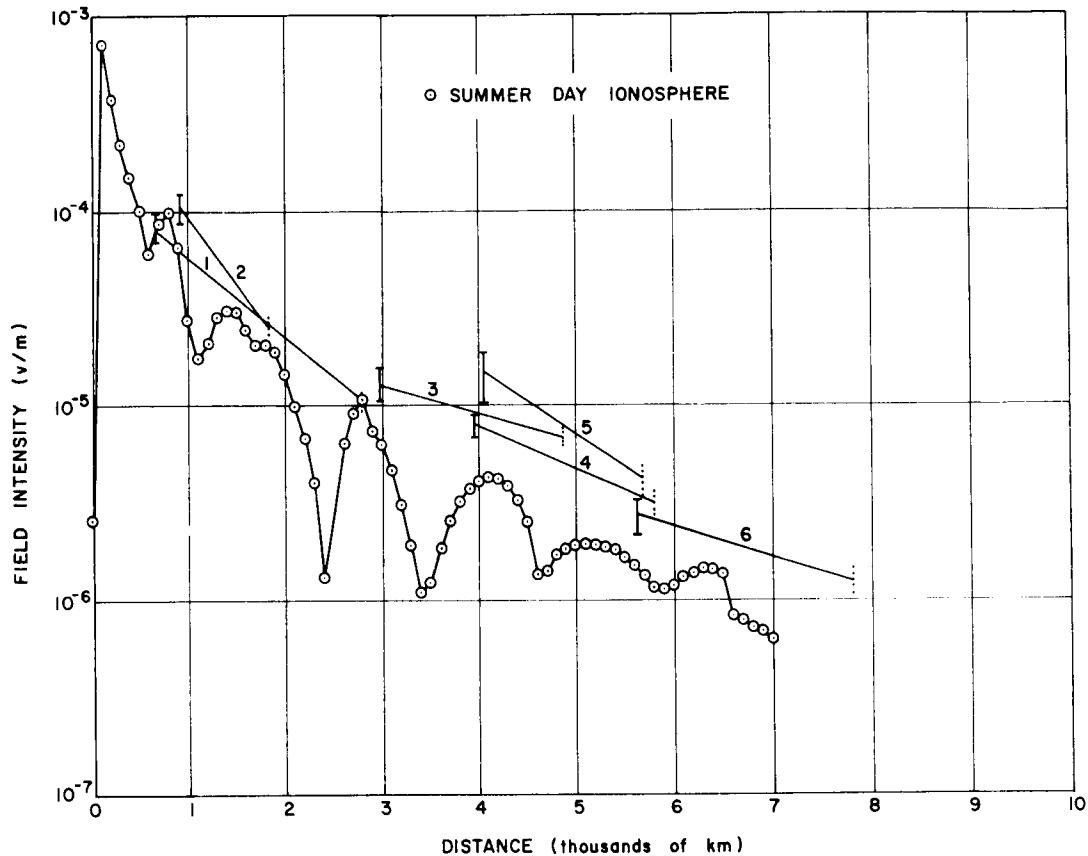


FIG. 90. FIELD INTENSITY OF DAYTIME TRANSMITTED WAVE (JUST ABOVE THE BOUNDARY) VERSUS DISTANCE FROM SHORT VERTICAL ANTENNA AT GROUND RADIATING 1 kw. The line segments are normalized measurements from the satellites. The dotted error bars represent uncertainties in the attenuation rate (slope). The solid bars indicate uncertainties in absolute magnitudes of the normalized measurements. 1 = OGO-II Rev. 74 and 75, east-to-west over land. 2 = OGO-I, 2 November 1964, west-to-east over land. 3 = OGO-II Rev. 105 and 106, east-to-west over land. 4 = OGO-II Rev. 106 and 107, east-to-west over sea water. 5 = OGO-I, 18 September 1965, east-to-west over land. 6 = OGO-II Rev. 125 and 126, west-to-east over land.

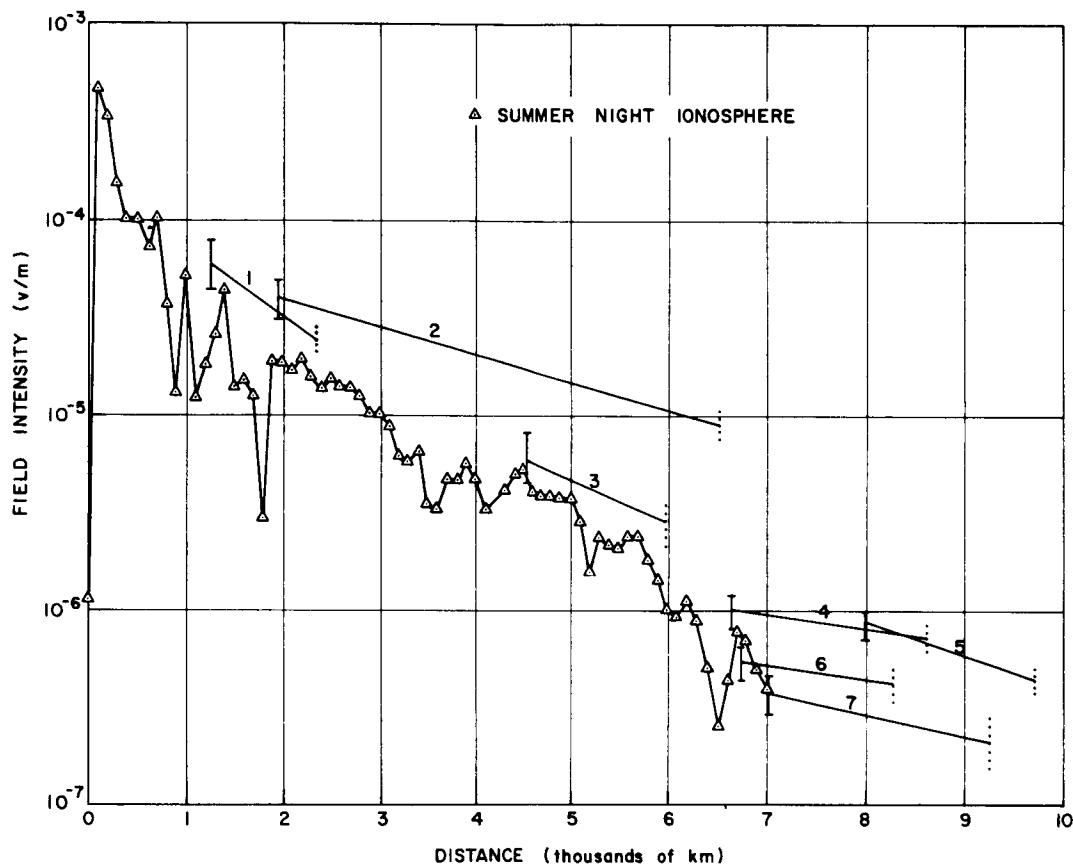


FIG. 91. FIELD INTENSITY OF NIGHTTIME TRANSMITTED WAVE (JUST ABOVE THE BOUNDARY) VERSUS DISTANCE FROM SHORT VERTICAL ANTENNA AT GROUND RADIATING 1 kw. The line segments are normalized measurements from the satellites. The dotted error bars represent uncertainties in the attenuation rate (slope). The solid bars indicate uncertainties in absolute magnitudes of the normalized measurements. 1 = OGO-I, 1 April 1965, north-to-south over land. 2 = OGO-I, 24 November 1964, west-to-east over sea water. 3 = OGO-I, 6 April 1965, east-to-west over sea water. 4 = OGO-II Rev. 105 and 106, west-to-east over a mixed path. 5 = OGO-II Rev. 126 and 127, east-to-west over sea water. 6 = OGO-II Rev. 74 and 75, west-to-east over land. 7 = OGO-II Rev. 125 and 126, east-to-west over sea water.

B. ABSORPTION LOSS

Another apparent weakness of the first-approximation model involves the large value of daytime absorption through the upper ionosphere (200 to 1500 km). As pointed out in Chapter III, the absorption curves of Fig. 29 were calculated on the basis of a daytime f_oF_2 of 12.5 MHz and a nighttime f_oF_2 of 5.5 MHz. A study of the Ionospheric Data Charts, Part A of the CRPL F-Series for the period October 1964 through August 1965 indicates that a more accurate value for f_oF_2 at mid-latitudes during the time OGO-I data for this study were obtained would be 6 MHz daytime, and 3 MHz nighttime.

Utilizing these adjusted f_oF_2 values the integrated absorption curves were re-calculated and are shown in Fig. 92, where for quick reference the absorption curves for the first-approximation model (Fig. 29) are also shown. In addition total absorption as a function of height for these adjusted values of f_oF_2 are shown in Fig. 93.

Note in Fig. 92 that the adjusted values of f_oF_2 result in approximately 10 db less daytime total absorption for most latitudes. The adjusted values have much less effect on the nighttime calculations. For dipole latitudes above approximately 35° the nighttime difference is less than 2 db.

In the process of re-calculating the absorption curves, several different models of the lower and upper ionosphere were used and the effect of each model on total absorption was determined. One of these composite models utilized the lower-ionosphere electron density and collision frequency height distributions of Piggott, et al [1965]. The maximum difference between total daytime absorption at any latitude using the Helliwell model of Fig. 28 or the Piggott, et al model was approximately 6 db. The Helliwell model produced the lower value of absorption, which was expected, since his values of electron density versus height in the lower daytime ionosphere are slightly less than those of Piggott, et al.

Comparison of the measured and calculated field intensities in Figs. 34 through 44 show that OGO-I usually measures daytime intensities greater than those predicted by the calculations. Therefore it would not seem

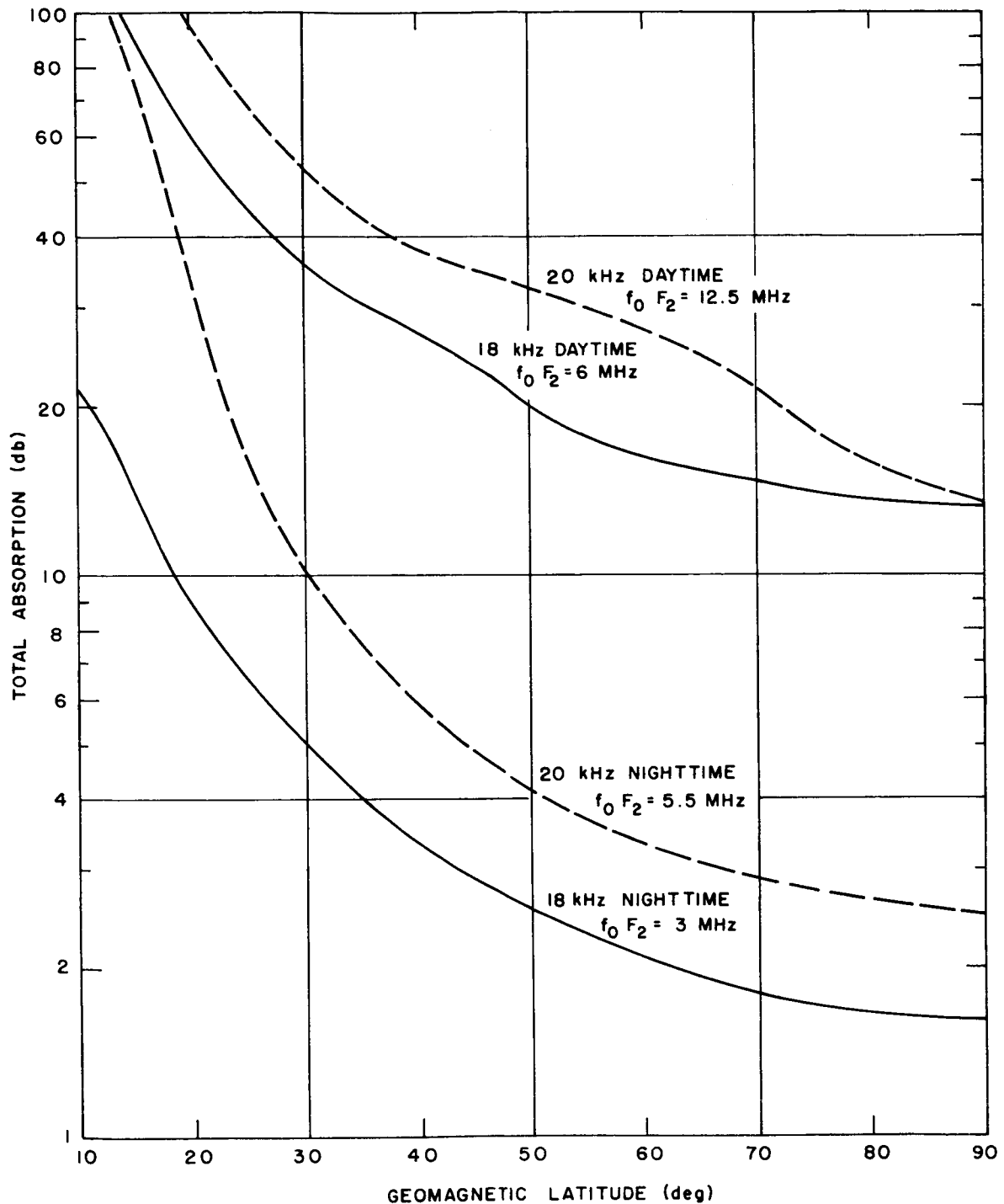


FIG. 92. ABSORPTION OF A VERTICALLY INCIDENT WAVE INTEGRATED THROUGH THE LOWER AND UPPER IONOSPHERE AS A FUNCTION OF LATITUDE SHOWING THE EFFECTS OF A REDUCTION IN $f_o F_2$. The 20 kHz curves are the same as shown in Fig. 29.

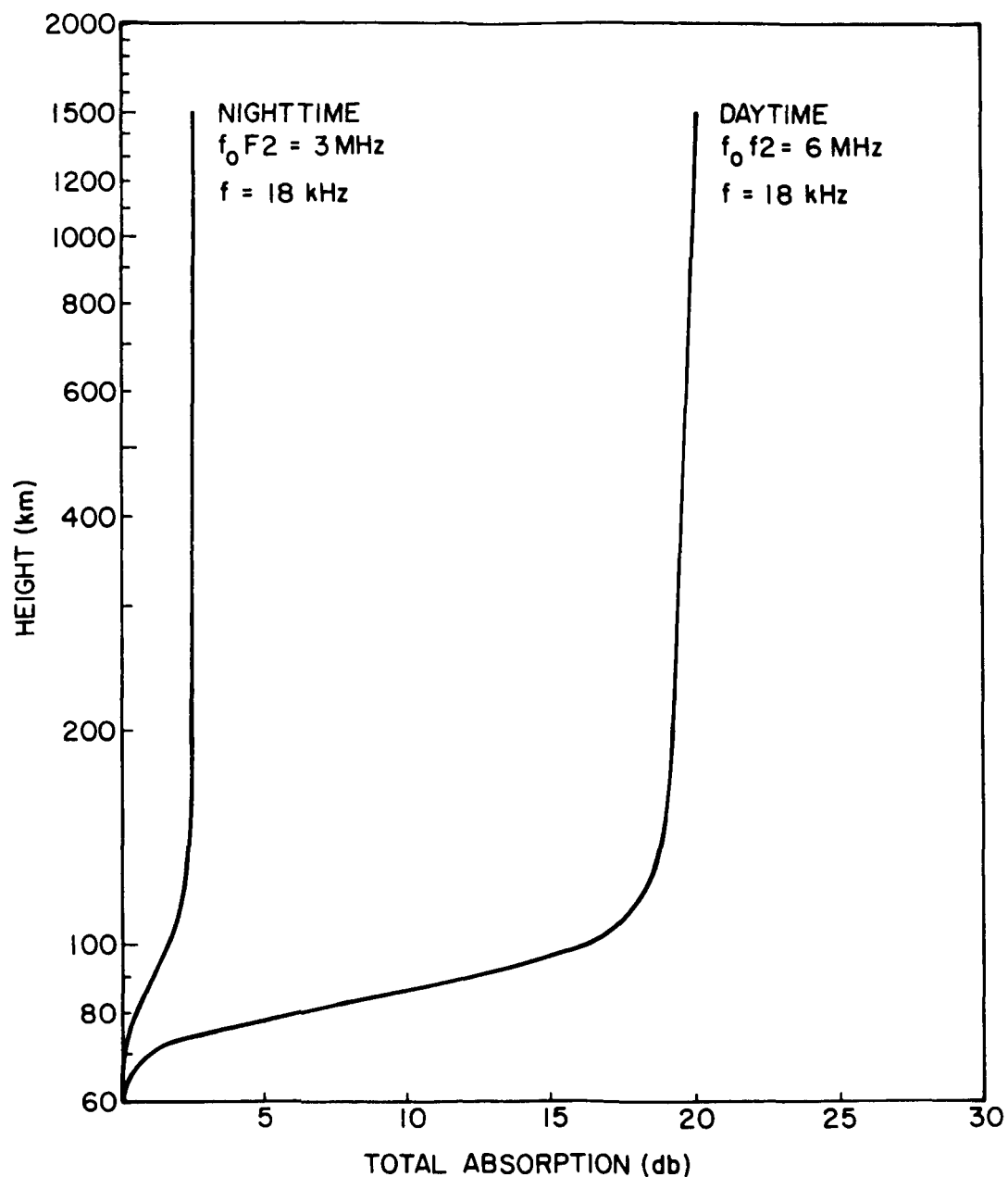


FIG. 93. TOTAL ABSORPTION AS A FUNCTION OF HEIGHT FOR A VERTICALLY INCIDENT WAVE INTEGRATED THROUGH THE LOWER AND UPPER IONOSPHERE. N and ν are assumed to vary with height as shown in Fig. 28.

advisable to choose or construct models in such a manner as to increase the absorption and thereby create an even larger discrepancy between the measured and calculated values.

In the absorption theory from which the numerical results for this study were obtained, it was assumed that the waves were homogeneous. Since the refractive index can be complex as shown by Eq. (1.1), the transmission angle can be complex; indeed this must be the case in order to satisfy Snell's law at the boundary [Budden, 1961]. This condition results in the planes of constant phase not being aligned with the planes of constant amplitude. Such a wave is called an inhomogeneous plane wave [Budden, 1961].

R. L. Smith has calculated the attenuation rate for several inhomogeneous waves. He concludes that the attenuation rate of the vertically incident homogeneous wave is within 40 per cent and 60 per cent of the rate for inhomogeneous waves having elevation angles of 45 degrees and 10 degrees, respectively. His results were published by Helliwell [1965]. These calculations are sensitive to azimuth, and for most azimuthal angles the differences between the homogeneous and inhomogeneous cases are considerably less than stated above. Helliwell [1965] points out that although the assumption of homogeneous waves obviously introduces a rather large error, it is probably not larger than the errors produced by deviations from the ionosphere models employed.

C. DIVERGENCE LOSS

In the first-approximation model, divergence loss was determined by assuming that the ray direction was confined exactly to the field line. Therefore, the divergence loss was determined by the geometrical spreading of the field. This assumption will now be reviewed, and other methods of determining divergence loss considered.

First, the ray tracing program of Smith and Edgar discussed in Chapter III will be used to determine all possible ray paths to a given OGO-I location, and the results utilized to determine divergence loss of the signal. Next, the divergence loss for this same satellite location will be determined by a comparison of data from OGO-I and OGO-II. The loss

indicated by each of these methods will then be compared to the divergence loss indicated by simple geometrical spreading of the geomagnetic field.

In choosing the OGO-I location to which the above methods are to be applied, 1100 UT to 1120 UT on 17 February 1965 was selected for two important reasons.

1. The foot of the field line during this time is close to NPG (within 1 kkm), and the satellite is at a modest altitude (approximately 7.6 kkm at 1100 UT and approximately 12.7 kkm at 1120 UT). Under these conditions there can be little uncertainty about where the signals penetrate the ionosphere.
2. The path of the foot of the field line in the Northern hemisphere during this time interval intersects the path of the field line foot for revolution 76 of OGO-II on 20 October 1965.

Item (2) above is highly significant since such a rendezvous in space between the two satellites provides the first known measurement of actual divergence loss of whistler-mode signals. With OGO-II at approximately 1 kkm (above all significant absorption as shown in Fig. 93), and OGO-I on the same field line but at an altitude of more than one earth radius, the difference in intensity of the two measurements would be almost wholly attributable to divergence if the rendezvous had coincided in time as well as in space. Unfortunately, the intersection of the foot of the field line paths occurs for daytime (approximately 1700 LMT) for OGO-II and nighttime (approximately 0200 LMT) for OGO-I. Nevertheless, the results shown in Fig. 92 provide day-night differences in total absorption by which the two measurements may be related and divergence loss determined.

1. Ray Tracing

Ray tracing was carried out using the diffusive equilibrium model of electron density [Angerami, 1966] which seems to fit whistler data best inside the "knee." The model utilized a base density of 10,000 el/cc at 1,000 km, a temperature of 1600 °K, and a composition of 50% oxygen, 25% hydrogen and 25% helium.

The manner in which ray tracing is used to determine divergence loss will now be discussed. At 1100 UT on 17 February 1965, OGO-I was at the location shown in Fig. 94. Beginning at this satellite location, a wave normal angle is assumed with respect to the radius vector, and the ray tracing program utilized to trace the ray backwards towards the earth.

In this manner the latitude at which this wave must be launched is determined. The program supplies many important parameters along the ray path including the wave normal direction and the latitude at the launch point. Table 7 shows some of these parameters for a variety of wave normal directions at the satellite.

For the diffusive equilibrium model, the magnitude of the refractive index is found to be on the order of 10 to 20 for heights of 200 to 300 km. From Fig. 95, a simple Snell's law solution shows that for grazing incidence of the wave below the boundary, the direction of the wave normal above the boundary (δ_L) must be less than approximately 5.7 degrees.

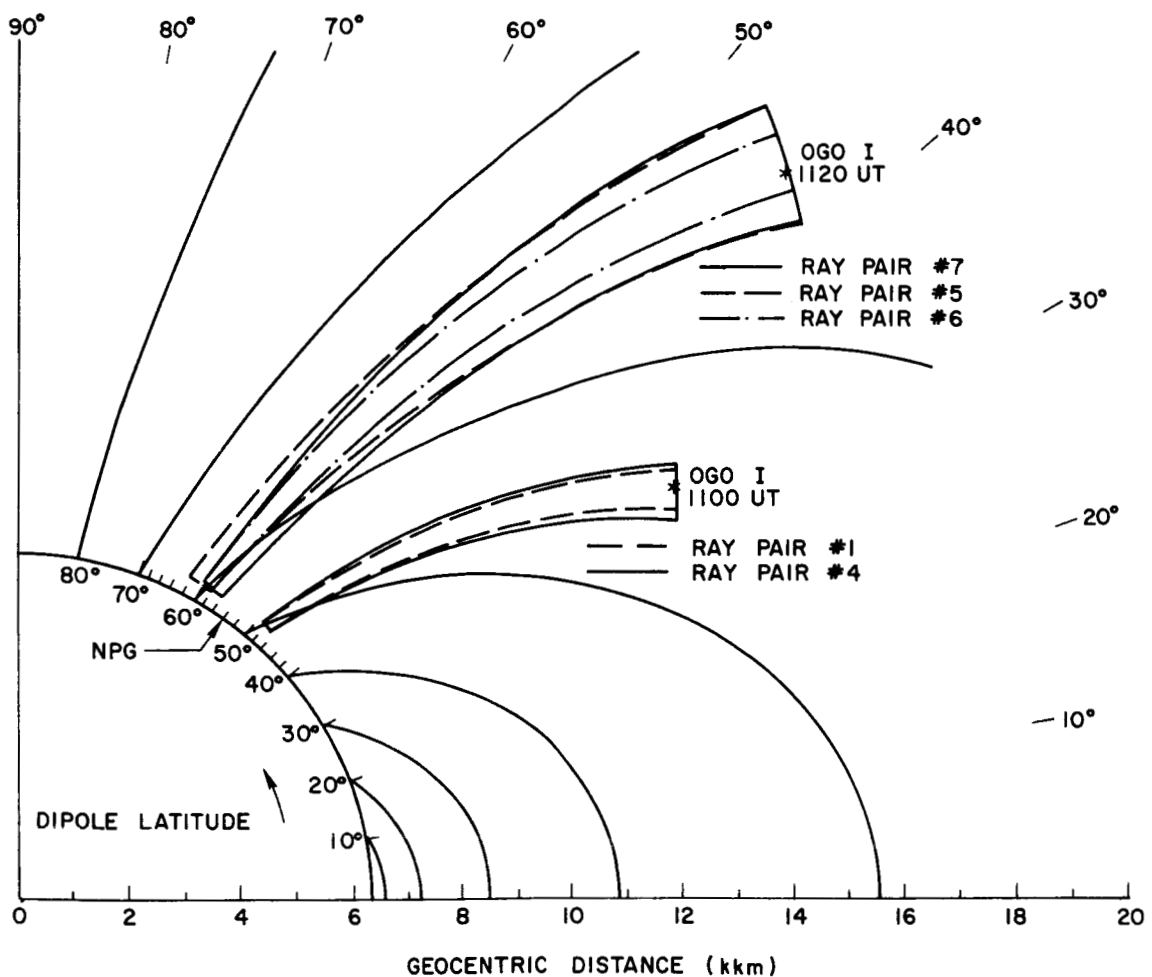


FIG. 94. DIVERGENCE IN THE MAGNETIC MERIDIAN AS OBTAINED BY TRACING PAIRS OF RAYS FROM A HEIGHT OF 250 KM TO THE OGO-I SATELLITE LOCATION ON 17 FEBRUARY 1965. The latitudes and wave-normal angles of each ray pair are shown in Table 8.

TABLE 7. LAUNCH POINT CHARACTERISTICS FOR A VARIETY OF WAVE NORMAL DIRECTIONS AT THE SATELLITE (OGO-1) FOR 1100 UT 17 FEBRUARY 1965. δ_s and δ_L are measured clockwise from the radius vector to the wave normal at the satellite and at the launch point, respectively. ψ_L is measured clockwise from the magnetic field vector $(B_o)_L$ to the wave normal at the launch point.

Wave Normal Direction at the Satellite δ_s (degrees)	Launch Point		δ_L (degrees)	ψ_L (degrees)
	Altitude (km)	Mag. Lat. (degrees)		
-10	262	49.1	-48.5	-71.9
-5	274	47.1	-39.9	-64.8
0	319	45.1	-29.8	-56.3
5	264	44.4	-18.3	-45.4
10	232	46.1	-7.4	-33.1
11	326	46.5	-4.5	-29.9
12	321	47.3	-2.24	-27.1
13	319	48.1	0.04	-24.1
14	321	49.1	2.34	-21.1
15	326	49.9	4.69	-18.1
16	231	51.2	6.8	-15.1
17	245	52.3	8.9	-12.1
18	262	53.4	11.2	-9.2
19	285	54.5	13.5	-6.2
20	312	55.6	16.2	-2.7
30	281	63.3	40.1	26.0

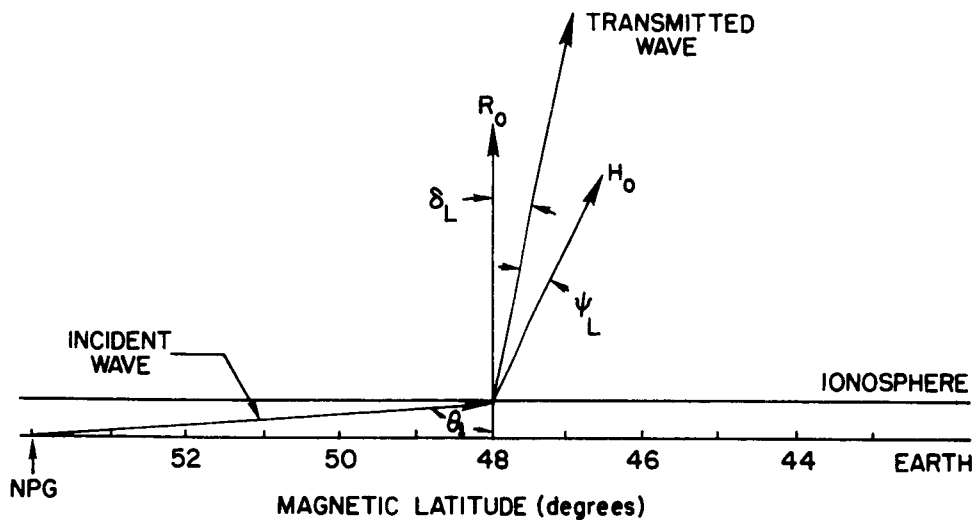


FIG. 95. GEOMETRICAL RELATIONSHIPS OF THE INCIDENT AND TRANSMITTED WAVES, THE EARTH'S MAGNETIC FIELD (H_0) AND THE RADIUS VECTOR (R_0) AT THE LAUNCH POINT. δ_L is the angle between the radius vector and the transmitted wave at the launch point. ψ_L is the angle between H_0 and the transmitted wave at the launch point.

$$n_1 \sin \theta_1 = n_2 \sin \delta \quad (7.12)$$

for $n_1 = 1$ and $n_2 = 10$

$$\delta_L = 5.7^\circ$$

This maximum value for δ_L eliminates as physically realizable possibilities all of the Table 7 wave normal angles at the satellite except for 11 through 15 degrees.

Note that the magnetic latitude of NPG (54°) is higher than the latitude of the launch point of each of the remaining waves. Hence, the geometrical relationships of the incident and transmitted waves, the earth's magnetic field, and the radius vector are as shown in Fig. 95. Since the angle of refraction (δ_L) for this condition can not be less than 0° , it is seen from Fig. 95 that the wave normal of the transmitted wave must lie to the right of the radius vector, and δ_L must be positive. This condition eliminates wave normal angles of 11° and 12° of Table 7, and allows one to draw the conclusion that wave normals at the satellite for this location must properly lie between 13° and 15° .

It should be noted that this result, although not yet an indication of divergence loss, is valuable since it defines a small region at an

altitude of approximately 250 km where a wave must penetrate the ionosphere in order to reach the satellite. The above results and Table 7 show that the penetration point must lie within a magnetic latitude range of 48.1 to 49.9 degrees. To launch a wave which will hit the satellite at any other latitude requires wave normal angles which are not allowed by the restraints discussed above. This result modifies the first-approximation model calculations for both absorption and earth-ionosphere waveguide loss, since there it was assumed that the whistler-mode wave is always launched at the foot of the field line. For the above example the foot of the field line is at 55.1° magnetic latitude, while the actual penetration point must have been between approximately 48° and 50° . This reduces the earth-ionosphere waveguide distance (d_e) from 496 km to approximately 400 km. From Figs. 91 and 92, it is seen that this change in penetration point latitude will result in approximately $\frac{1}{2}$ db more absorption, but approximately 4 db less earth-ionosphere waveguide loss than indicated by the first-approximation calculations. Although this does not appear to be a highly significant point for this example, it does become more significant for path geometry related to other satellite locations. For instance, at 1120 UT the foot of the field line is at 65.1° , but the penetration point as indicated by the above techniques is at approximately 59° . This results in a reduction in earth-ionosphere waveguide distance from approximately 1.8 kkm to approximately 1 kkm, a factor which causes 6 to 8 db less earth-ionosphere waveguide loss than indicated by the first-approximation model. Note in Fig. 35 that the field strength as calculated by the first-approximation model is more than 15 db below the peak measured value at 1120 UT. This discrepancy is reduced by 6 to 8 db when the above results are considered.

Once the latitude and wave normal angle required of a wave to hit the satellite has been determined, it is an easy matter to determine the divergence loss. This is accomplished as follows.

Table 7 shows that a wave launched vertically ($\delta_L = 0^{\circ}$) and at a magnetic latitude of 47° would be expected to pass below the satellite. A wave launched vertically at a latitude of 49° would be expected to pass above the satellite. This is indeed the case as verified by the ray tracing program for the satellite position at 1100 UT shown by ray pair

1 in Fig. 94. Although the ray from NPG which enters the ionosphere at a magnetic latitude of 47° will have a slightly larger angle of refraction (δ_L) than the ray entering at 49° , this difference in angle is very small (usually less than 0.2°), and the error introduced by assuming parallel wave normals may be neglected. For example, a comparison of pair # 1 and pair # 4 in Table 8 shows that the wave normal direction may vary as much as $\pm 1^{\circ}$ from the vertical before the divergence loss is changed by approximately 1 db. The ray tracing program also shows that the error in divergence loss introduced by varying the separation (in latitude) between the launch points by only a few degrees is only a small fraction of a db and may be neglected (compare pair # 2 and pair # 3 of Table 8).

TABLE 8. DIVERGENCE LOSS AS INDICATED BY TRACING PAIRS OF RAYS TO THE OGO-I SATELLITE LOCATION ON 17 FEBRUARY 1965. See Figs. 95 and 96 for the definition of symbols.

Universal Time and Ray Pair Number		Latitude of Launch Point (degrees)	δ_L (degrees)	R_1 km	R_2 km	d_1 km	d_2 km	Divergence Loss (db)
1100 UT	# 1	47 49	0 0	6620	14003	230	732	8.3
	# 2	49 51	4 4	6620	14003	230	749	8.5
	# 3	49 53	5 5	6620	14003	460	1430	8.3
	# 4	47 49	1 -1	6620	14003	230	976	9.5
1120 UT	# 5	58 62	0 0	6620	19074	460	2190	11.4
	# 6	58 60	-2.5 -2.5	6620	19074	230	1062	11.2
	# 7	56 60	-5 -5	6620	19074	460	2160	11.3

The procedure by which the divergence losses shown in Table 8 are obtained from the ray tracing program will now be explained.

By tracing a pair of waves (ray # 1 and ray # 2) launched at slightly different latitudes, the distance d_2 in Fig. 96 is obtained. The distance d_1 is calculated for an altitude of 250 km. The magnitude of this distance depends on the difference in latitude between the launch point of ray # 1 and ray # 2. The amount of divergence in the magnetic meridian is determined by comparing the ratio of d_2 to d_1 . The divergence in the third dimension is included by assuming that the waves will spread longitudinally as the ratio of the geocentric distance to 250 km (R_1) to the geocentric distance to the satellite (R_2). This assumption implies that in the third dimension the rays all lie in the magnetic meridional planes. i.e., we are assuming field line divergence in the third dimension.

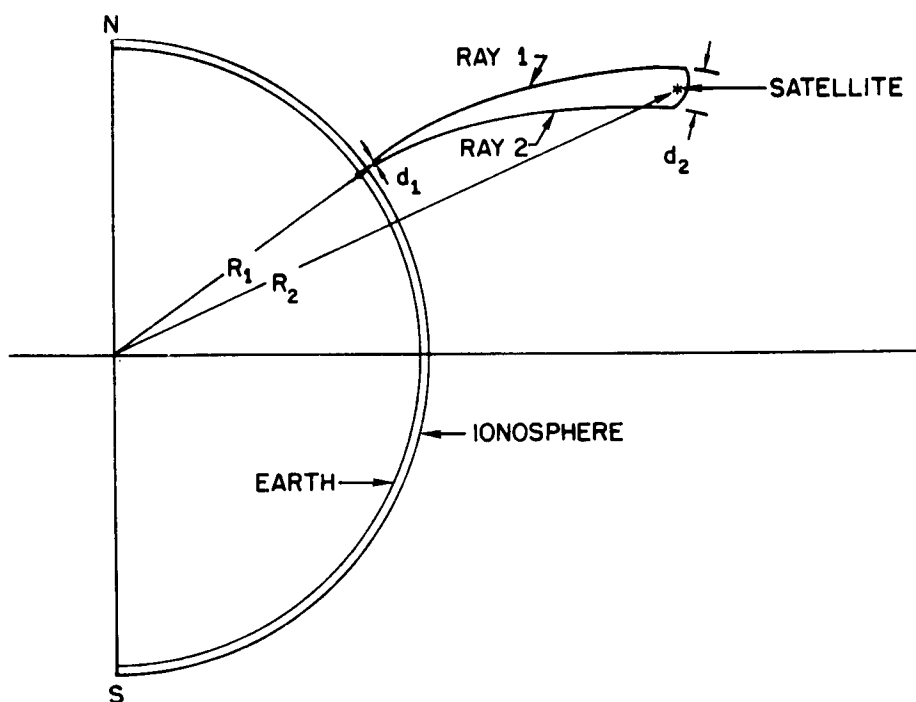


FIG. 96 . TO ILLUSTRATE THE MANNER IN WHICH RAY TRACING AND EQ. (7.13) ARE UTILIZED TO DETERMINE DIVERGENCE LOSS. R_1 = geocentric distance to a height of 250 km (6720 km); R_2 = geocentric distance to the satellite; d_1 = latitudinal distance in km between the launch point of the two rays at a height of 250 km; d_2 = latitudinal distance in km between the two rays at the satellite height as determined by ray tracing.

The divergence loss may then be written as

$$db = 10 \log \left(\frac{R_2}{R_1} \cdot \frac{d_2}{d_1} \right) . \quad (7.13)$$

The results of the above procedure for a variety of wave normal angles and launch point latitudes are shown in Fig. 94, and are summarized in Table 8.

2. Measured Divergence

The divergence loss for the OGO-I satellite position used in the above examples will now be determined by a comparison of OGO-I and OGO-II data.

At 1058 UT (\approx 0300 LMT) on 17 February 1965, the foot of the field line passing through OGO-I was at a magnetic latitude of 53 degrees and a longitude of -119 degrees. At 1007 UT (\approx 1700 LMT) on 20 October 1965 the foot of the field line passing through OGO-II was at a magnetic latitude of 50 degrees and a longitude of -119 degrees (see Fig. 60). The ray tracing results indicate that the signals reaching OGO-I in this region actually penetrate the ionosphere at a latitude slightly lower than the latitude of the foot of the field line. Therefore, it appears reasonable to compare the measured data of OGO-I and OGO-II at the above times and consider the difference as a measurement of divergence loss.

Reference to Figs. 35 and 61 show that the field intensities from NPG as measured by OGO-I and OGO-II at these times were approximately -43 db γ and -50 db γ , respectively. From Fig. 92, it is seen that at a latitude of 50 degrees the difference between daytime and nighttime total absorption is approximately 15 db. This factor must be used to normalize the data before the two measurements are compared. One assumes that if the OGO-II measurement had been made at night rather than in the daytime reduced absorption would have resulted in a measured value approximately 15 db higher. The expected nighttime value would be $-50 + 15 = -35$ db.

The difference expected between two daytime measurements would therefore be 43 db (OGO-I) - 35 db (OGO-II) = 8 db. Since OGO-II was above all significant absorption, this 8 db difference must be primarily

due to divergence of the wave.

It is now instructive to compare the values obtained for divergence loss by each of the methods outlined in this section. These comparisons are shown in Table 9.

TABLE 9. DIVERGENCE LOSS AS INDICATED BY SEVERAL DIFFERENT METHODS FOR OGO-I ON 17 FEBRUARY 1965.

Universal Time	Method Used	Divergence Loss (db)
1100	Ray tracing	8.3
	Geometrical spreading (first-approximation model)	9.5
	OGO-I and OGO-II measurements	8.0
1120	Ray tracing	11.4
	Geometrical spreading (first-approximation model)	13.7

As shown in Table 9 divergence losses calculated by ray tracing and by the geometrical spreading assumption of the first-approximation model are in good agreement (≈ 2 db). The close agreement between the measured divergence loss and the results of these calculations is also demonstrated in Table 9.

The results of this chapter have been utilized to re-calculate field intensities expected at OGO-I locations. These values are plotted as the dash-dot lines in Figs. 34 through 44.

The dash-dot lines in Figs. 56 through 89 represent calculations for OGO-II locations based on the results of this chapter.

VIII. NEW OBSERVATIONS

In the course of analyzing the data from the OGO satellites in order to study whistler-mode propagation, several new phenomena have been discovered. These new observations are now presented and are described in as much detail as is possible with the available data.

While much remains to be learned about these new discoveries, certain important features of each are sufficiently well defined to warrant reporting at this time.

Discussions of the significance and possible interpretation of these phenomena are presented in Chapter IX.

A. LATITUDINAL CUTOFF OF WHISTLER-MODE SIGNALS

One of the important new discoveries of this research is the abrupt latitudinal cutoff of whistler-mode propagation observed by OGO-II. This is best illustrated by Figs. 47, 48, and 85 where signal intensities from both NPG and NAA decrease more than 40 db as the satellite moves from approximately 59° to 60° northern geomagnetic latitude. This phenomenon is also well illustrated by Figs. 61, 69, 77, 79, and 87. This abrupt cutoff has been observed during both nighttime (\approx 0400 LMT) and daytime (\approx 1600 LMT) hours, but has only been observed in the Northern hemisphere, and only during winter months. There is some evidence that the cutoff is sharper and more pronounced during the daytime, and when the geomagnetic planetary K_p index is high. It is important to note that most of the data for this study were taken during October 1965 with only limited data (from the SP telemetry) available for the summer months. The major features of this Northern hemisphere latitudinal cutoff are shown in Table 10.

Do not confuse the cutoff discussed above with the cutoff in the Southern hemisphere such as shown in Figs. 71, 73, 75, 83, and 89. In the Southern hemisphere the NPG and NAA signals received in the satellite are interpreted as arriving by whistler-mode propagation via a field line path from the Northern hemisphere. Hence this cutoff may be explained in terms of the electron gyrofrequency cutoff [Smith, 1960a] or [Smith and Brice, 1964]. The cutoff latitude (determined by the minimum electron

TABLE 10. MAJOR FEATURES OF THE NORTHERN HEMISPHERE LATITUDINAL CUTOFF OF NPG AND NAA SIGNALS OBSERVED BY OGO-II.

LMT	Rev. No.	Northern MLAT Where Cutoff Begins (degrees)	Northern MLAT Where Signals Last Observed (degrees)	K _p	Decrease in Field Intensity Over the Cutoff Range (db)
Approx 1600	74	72	76	0+	17
	75	62	75	0+	20
	76	55	59	0+	32
	106	73	77	1o	15
	107	73	77	1o	30
	122	63	72	3+	15
	125	50	54	4o	25
	126	57	61	3+	24
	130	59	60	3o	40
	132	53	56	4-	40
Approx 0400	105	50	64	0	10
	106	69	74	1o	14
	123	60	72	3+	20
	125	57	61	4o	20
	126	40	50	3+	12
	127	50	58	4-	32
	134	63	73	2+	18

gyrofrequency along the path) of signals received in the Southern hemisphere is of major importance since this will indicate whether or not the signals were ducted. For example, if cutoff occurs for a minimum electron gyrofrequency (f_{H_o}) of approximately 36 kHz ($f/f_{H_o} \approx 0.5$) then it is obvious that we are seeing ducted signals, and good support is thereby given to the duct cutoff theory proposed by Smith [1960a, 1961b] or Smith, et al [1960]. On the other hand if cutoff occurs for much larger ratios of f/f_{H_o} then we assume that a) the signals are not ducted, or b) the signals are not arriving via ducts which terminate immediately overhead.

Table 11 shows the striking features of the Southern hemisphere cutoff of NPG and NAA signals observed by OGO-II. Note that 18 kHz whistler-mode signals are consistently received in the Southern hemisphere at latitudes corresponding to an f_{H^0} of less than 36 kHz. These signals can not be ducted overhead; however they could come from ducts at lower latitudes. Carpenter and Dunckel [1965] have observed whistler-mode signals which reach a given region via a preferred low-latitude path over the equator and which then spread over a latitude range of as much as 10° at 1,000 km. They suggest that these signals are possibly due to leakage or spreading from the base of a lower latitude duct, and perhaps are evidence of propagation transverse to the magnetic field. Carpenter, et al [1964] have reported similar phenomena.

Regardless of whether or not the signals in the present study are ducted, it is clear that the magnetospheric portion of the path can not involve regions where $f/f_{H^0} \geq 1.0$. Using the centered dipole approximation for the earth's field, an equatorial gyrofrequency of 18 kHz occurs at a magnetic latitude of approximately 56° . Therefore the numerous OGO-II signals of Table 11 which were received at Southern magnetic latitudes higher than 56° must have entered the ionosphere at lower latitudes and then propagated poleward to the satellite.

In general (as shown by Table 11) signals are normally observed at significantly higher Southern latitudes during nighttime than during daytime.

B. OBSERVATION OF INTENSE NOISE

Many distinct types of vlf noise observed by satellites are not observed on the ground.

One type involves a noise band which decreases in frequency to a minimum then rises again. This noise has been referred to by Stanford researchers as the "saucer" phenomenon. In the rayspan records, this noise typically lasts for a few seconds, and covers several kHz.

Another type of noise is quite impulsive in spectral form with frequencies of maximum intensity that fluctuate rapidly. This noise is broadband in nature, has a continuously varying lower frequency cutoff,

TABLE 11. MAJOR FEATURES OF THE SOUTHERN HEMISPHERE CUTOFF OF
NPG AND NAA SIGNALS OBSERVED BY OGO-II.

LMT (hours)	Rev. No.	Southern MLAT Where Signals are Last Observed (degrees)	K _p	Satellite Height, H (km)	f _{H_o} (kHz)
Approx 1600	74	63	0+	1199	3.9
	75	53	0+	1363	27.0
	103	60	2o	1524	9.1
	105	58	0	1467	11.5
	106	60	1o	1484	9.1
	109	55	3+	1496	20.0
	125	40	3+	1451	100.0
	127	44	4-	1514	60.0
	128	50	4-	1526	42.0
	131	54	4-	1452	23.0
	134	60	2+	1515	9.1
Approx 0400	74	66	0+	793	2.4
	75	67	0+	962	1.8
	103	58	2o	882	11.5
	105	77	0	983	0.071
	106	67	1o	1027	1.85
	109	59	3+	1064	9.4
	122	59	3+	1050	9.4
	124	57	4o	1074	14.0
	125	56	4o	773	20.0
	126	61	3+	1149	7.7
	127	58	4-	946	11.5
	128	57	4-	1032	14.0
	131	57	4-	986	14.0
	134	59	2+	1127	9.4

and covers a frequency range of many kHz. This intense noise as observed by OGO-II is illustrated in Figs. 79, 81 and 83. The spectral properties of the noise are shown in the rayspan record of Fig. 55 where the narrow-band vlf receiver output is superimposed on the output of the broadband receiver.

As yet both types of noise are unexplained. Both are observed on the Alouette I and II, Injun III, and OGO-II satellites.

The second type of noise described above has been referred to by various workers as "impulsive noise," "vlf hiss," and "auroral hiss;" the latter two terms apparently being used in a different context than the conventional vlf hiss and auroral hiss which has been observed for many years on the ground. In the present work this noise has simply been referred to as "intense noise." Since analysis of these noises is now underway it appears best to refrain from attaching any other name at the present time.

From the narrowband receivers used in this study, it is not possible to define the spectrum of the intense noise. The spectrum must be studied with data from the broadband receiver. However, several important features of the noise are defined by the narrowband data. For instance, these data indicate that when the noise is present it tends to exist in the form of a ring, or band, around the polar regions, and not as a polar cap. The width of the ring is usually from 3 to 10 degrees in latitude. This is illustrated in Figs. 82 and 83 where the following sequence of events occur as the satellite makes one complete revolution of the earth.

1. Between 50° and 60° Northern geomagnetic latitude in the Western hemisphere signals from NAA cutoff.
2. Just beyond the cutoff there is a quiet region.
3. At approximately 67° the satellite enters the ring of intense noise. This noise persists for approximately 12° . At approximately 75° the satellite leaves the noise ring and sees a quiet region, void of both noise and NAA signals. This quiet region appears to exist in the form of a polar cap.
4. As the satellite flies across the Northern polar cap and heads southward into the Eastern hemisphere, it again enters the ring of intense noise at approximately 73° . Here the width of the noise ring is approximately 10° .
5. At approximately 63° the satellite emerges from the noise ring and

sees another quiet region which precedes the fade-in of NAA signals at approximately 45° .

6. Signals from NAA are observed across the Eastern hemisphere to southern magnetic latitudes of approximately 58° . (Note the enhancement of NAA signals as the satellite approaches the NAA antipode.)
7. Another quiet region is observed just beyond the fade-out of NAA signals at approximately 58° .
8. At approximately 60° southern geomagnetic latitude the satellite enters a ring of intense noise which persists for approximately 8° .
9. At approximately 70° the satellite leaves the noise ring and sees no noise and no NAA signals over the Southern polar cap region in either the Eastern or Western hemisphere between magnetic latitudes of approximately 70° and 86° .
10. As the satellite flies over the South Pole and into the Western hemisphere it encounters the noise ring at approximately 75° . Here the intense noise is observed in a band about 5° wide.
11. At approximately 65° the satellite emerges from the noise ring and sees another quiet region prior to the fade-in of NAA signals at approximately 50° southern geomagnetic latitude. The revolution is now complete.

Although the data from some revolutions show deviations from the general pattern illustrated above, this sequence of events is in general typical of the latitudinal profile of signal and noise as the satellite traverses its polar orbit.

An extremely interesting sequence concerning the longitudinal profile of the intense noise is shown by Figs. 76, through 83, where data are shown for four complete and successive satellite revolutions. Attention is directed first to Fig. 77 where the intense noise reaches a maximum in the Northern hemisphere at approximately 70° magnetic latitude and at an eastern longitude of approximately 36° . On the next revolution (Fig. 79) the satellite is 26° further west but it still encounters the intense noise peak at 70° northern magnetic latitude. On the next two successive revolutions (Figs. 81 and 83) although the satellite moves westward 26° with each revolution, the peak of the intense noise ring is always found at essentially the same northern magnetic latitude (70°). This sequence shows that over the latitude range from approximately 40° east to approximately 40° west (and over a time period of more than 5 hours) the peak of the intense noise in the Northern hemisphere pertinaciously remained at 70° magnetic latitude.

An indication of the manner in which the peak magnitude of the noise fluctuates is shown in a sequence of figures beginning with Fig. 73. Note in Fig. 73 that the ring of noise around the South magnetic pole is extremely intense, reaching a peak amplitude of -50 db γ on both the Western and Eastern hemisphere sides of the earth. On the next revolution (Fig. 75), the noise ring (around the South Pole) still exists, but its amplitude has decreased by at least 10 db. On the next revolution (Fig. 77) this noise ring has experienced a dramatic decrease of approximately 30 db. On the next revolution (Fig. 79), the noise has just as dramatically risen by more than 30 db and remains at a high level through the next two revolutions (Fig. 81 and Fig. 83). Although there is evidence that the intense noise is more likely to be observed during magnetically disturbed periods than during magnetically quiet periods (see Table 12) fluctuations in the noise magnitude noted above can not be explained by fluctuations in the K_p index. During the period of interest the 3-hour K_p indices remained between 3+ and 4o.

Major features of the intense noise discussed in this section are shown in Table 12.

C. ANTIPODAL ENHANCEMENTS

On several occasions OGO-II has flown near the antipode of NAA and NPG and has observed pronounced signal enhancements in these regions. An example of NPG antipodal enhancement is shown by Figs. 49 and 63. The locations of the antipode and the subsatellite plot are shown in Fig. 62. Note in Fig. 63 that when the satellite is within 200 km of the antipode, (at an altitude of approximately 1,000 km) NPG signal intensities are as high as -80 db γ . This is approximately 25 db higher than signals observed south of the antipode, and at least 10 db higher than any signals observed within 4,000 km to the north of the antipode.

Another good illustration of NPG antipodal enhancement is shown in Fig. 87, where the satellite passes within approximately 1,000 km of the antipode. Here strong NPG signals are observed over a latitude range of approximately $\pm 5^\circ$ from the antipodal maximum. Only noise exists at greater distances on either side.

TABLE 12. MAJOR FEATURES OF THE INTENSE 18 kHz NOISE OBSERVED BY OGO-II. The width of the noise band is defined as the width (in degrees latitude) 6 db below the peak intensity. Only those noise peaks with magnitude ≥ -95 db γ are shown.

LMT	Rev. No.	MLAT of Peak Noise Intensity (degrees)	Width of Noise Band (degrees)	Peak Intensity of Noise (db below 1 γ)	H (km)	K _p	Hemisphere (North or South)
\approx 1600	75	77	11	-86	\approx 1300	1o	South
	103	73	3	-87		0o	
	105	80	5	-80		4o	
	109	73	4	-82		4o	
	122	82	6	-56		3+	
	124	76	5	-60		3+	
	126	76	3	-62		3+	
	127	78	7	-52		3+	
	128	76	6	-53		3+	
	131	65	7	-53		4-	
	134	71	6	-57		4-	
	125	69	5	-53	\approx 900	3+	North
	126	68	7	-64		3+	
	127	70	5	-52		3+	
	128	70	9	-58		3+	
\approx 0400	74	74	7	-80	\approx 970	0+	South
	103	81	3	-64		0+	
	109	79	3	-80		1o	
	122	83	5	-57		3+	
	124	73	10	-68		3+	
	126	77	3	-60		3+	
	127	79	4	-60		3+	
	128	68	11	-72		3+	
	131	70	7	-56		3+	
	134	77	4	-72		3+	
	75	82	4	-88	\approx 600	0+	North
	105	76	3	-84		1o	
	125	71	3	-74		3+	
	127	67	3	-68		3+	
	128	68	11	-72		3+	

Note in Figs. 63 and 87 that the satellite sees the maximum enhancement at 50° and 49° southern magnetic latitudes, respectively, although the NPG antipode is at 54° magnetic latitude. If whistler-mode signals are excited at low altitudes (the lower boundary of the ionosphere) at 54° by the antipodal enhancement, and subsequently propagate up the field lines, one would expect to see these signals at a lower latitude ($\approx 50^{\circ}$) at a height of 1,000 km. This is precisely what is indicated by the data.

On two other occasions the satellite passed near the NPG antipode, as shown in Figs. 59 and 61. In Fig. 59, where the satellite passes within approximately 1600 km of the antipode, a small enhancement is again observed at 50° southern magnetic latitude. However, in Fig. 61 no enhancement is seen, although the satellite flies within 1100 km of the antipode. This is not surprising when one notes that on this particular pass the satellite saw only a few scattered NPG signals throughout the Eastern hemisphere.

Antipodal enhancements of NAA signals are shown in Figs. 57, 81, 83, and possibly in Fig. 89. An interesting feature of the NAA enhancements is the fact that they seem to be observed at lower latitudes than would be expected. For instance, in Fig. 81 an enhancement of more than 20 db is seen at a southern magnetic latitude of approximately 39° . In Fig. 57, a 12 db enhancement is seen at approximately 45° . The magnetic latitude of the NAA antipode is 56° . The satellite altitude is approximately 1,000 km.

Figure 81 illustrates another interesting phenomenon. It appears likely that the high intensity NAA signals observed in the Northern hemisphere at a magnetic latitude of approximately 44° represent whistler-mode signals which were excited in the Southern hemisphere by the 20 db antipodal enhancement at 39° .

D. EQUATORIAL DIP

Another new discovery, observed for the first time in the data from OGO-II, is the pronounced drop in NPG and NAA field intensity over the magnetic equator. This equatorial dip has been observed on essentially every OGO-II revolution where data were obtained. Seen at all longitudes,

both daytime and nighttime, the drop in intensity is more pronounced during daytime hours. The magnitude of the equatorial dip is typically 12 to 20 db during the daytime, and 5 to 10 db during the nighttime. This phenomenon is well illustrated in Figs. 63, 65, 67, and 87.

Since all signals in this study are interpreted as having reached the satellite via whistler-mode propagation, the equatorial dip observed in the data was not unexpected. As a matter of fact, field strength calculations based on the refined whistler-mode model of Chapter VII indicate that the equatorial dip should be even more pronounced than shown by the measurements.

Since the equatorial dip is predicted by existing theory, and this dip is in fact seen by the satellite, the data are a clear indication that the signals do indeed reach the satellite via the whistler-mode.

E. TERMINAL REGION BURSTS

One of the most puzzling observations of this study concerns the peculiar, unexplained terminal region burst phenomenon observed by OGO-I and shown in Figs. 10, 11, 12, 13, and 43. Figure 10 shows signals from NPG gradually fading out as OGO-I reaches an altitude of approximately 12,500 km. However, as the satellite moves to higher altitudes (Fig. 11) intense bursts of highly discrete signals (one may easily read the Morse code in the bursts) are observed.

In Fig. 12, which covers a time period of two and one half minutes, no discernable signals from NPG arrived at the satellite, although NPG was transmitting continually during this time.

In Fig. 13, one final discrete burst of signal from NPG is observed just before the satellite was commanded into a tape-playback mode, ending the real-time record.

If one assumes this phenomenon to be a spatial variation (perhaps important new evidence of "ducts") then the bursts of signal (in Fig. 11) are separated in space by distances of approximately 30 km minimum to more than 400 km maximum. The width of the "ducts" would be on the order of 10 km to 30 km.

It should be noted that there is only a few db difference in the peak

amplitude of each of the bursts. This is not typical of fading, and would suggest that the phenomenon is more likely due to a loss mechanism.

F. FADING OF WHISTLER-MODE SIGNALS

Data from OGO-I and OGO-II have provided some interesting new observations concerning the intensity and frequency of fading of whistler-mode signals. Fading is best studied during periods of CW (key-down) transmissions from the vlf transmitters; however, these periods are very infrequent in the OGO data. The longest key-down periods are shown in Figs. 18 through 22 for OGO-I and in Figs. 52, 53, and 54 for OGO-II. Each of these records was obtained from the SP telemetry system whose bandwidth is sufficient to faithfully pass fading rates as high as several hundred cycles per second. This is approximately an order of magnitude higher than any fading rates observed, hence it is believed that the fading patterns shown here are genuine.

In Figs. 18, 19, 20, and part of Fig. 21, NPG is sending a special "FM" pulse schedule. In this mode, the transmitter is in a key-down configuration, but the center-frequency of the carrier is swept linearly in time from 18.55 kHz to 18.65 kHz every two seconds. Since the receiver has a 500 Hz bandwidth this frequency shift of the carrier should not produce any observable change in amplitude at the receiver output. Sometimes (but not always) the sudden 100 Hz change in carrier frequency does produce a sudden change in amplitude of the NPG whistler-mode signal at the satellite. This possibly indicates frequency-selectivity of the whistler-mode paths to the satellite. Except for these sudden changes in amplitude which are unquestionably related in some manner to the shift in carrier frequency, the most rapid and intense fading observed in the OGO-I records appears to be on the order of 20 db in approximately one fourth of a second. The satellite positional parameters for Figs. 18 through 22 are shown in Fig. 44 where these data are plotted.

Typical fading patterns of low-altitude whistler-mode signals received by OGO-II are shown in Figs. 52, 53, and 54. Figure 53 illustrates some of the deepest and the most rapid fading observed by OGO-II, where 20 db fadings at the rate of 10 or more per second are common. Figure 54 illustrates a

case where the fading patterns observed by OGO-II are much slower and have essentially the same characteristics as those observed by OGO-I (shown in Figs. 18 through 22).

G. CYCLOTRON ABSORPTION

In general, vlf intensities measured by OGO-I exceed the calculated intensities. However, at 0107 UT on 24 November, 1964 (Fig. 34) measured intensities from OGO-I were more than 40 db below the calculated value. The satellite position at the time of this observation was such that cyclotron absorption appears to be a possible cause of the discrepancy between the measurements and the calculations.

Cyclotron absorption is a mechanism to account for the absorption of energy from a wave by particles in a collision-free plasma, and corresponds to Landau damping, with the major difference being that the resonant particles absorb energy from the wave in a plane perpendicular to the drift motion of the particles along the magnetic field. The absorption of energy from the wave is large when a large number of particles have streaming velocities such that the Doppler-shifted frequency of the wave as "seen" by the particles equals the particle gyrofrequency in magnitude and sense.

Guthart [1964] has considered anisotropic electron distributions that allow cyclotron absorption to be used as the physical mechanism to explain the observed upper cutoff frequency of whistlers.

The data shown in Figs. 34 and 41 appear to be the only evidence from OGO-I where cyclotron absorption may have been observed.

IX. INTERPRETATIONS AND CONCLUSIONS

In this chapter we consider first the contributions of the main body of this research to a better understanding of whistler-mode propagation. The importance of these contributions will be established. Next the new observations will be reviewed and various mechanisms suggested which might lead to possible explanations.

In each of the new observations there is only a limited amount of data. In some cases no mechanism is available, and in others the factors needed for properly checking out proposed mechanisms are lacking. However it is felt that in each case the observation itself is important and warrants reporting at this time, even though we are not in a position to establish firm explanations. The phenomena all remain open for further study, and the author solicits both constructive criticism and new ideas regarding possible explanations.

A. THE EARTH IONOSPHERE WAVEGUIDE LOSS

In Chapter VII, we discussed the two ionospheric models and the rates of earth-ionosphere waveguide loss as developed by Crary and by Allcock. We also discussed the results of a survey made by Davies and presented his attenuation rates.

It was pointed out that the attenuation rates of Allcock and Crary are approximately the same for distances up to 3 or 4 kkm. However at larger distances the rates differ markedly. Allcock shows an earth-ionosphere waveguide attenuation rate of about 3 db/kkm between 4 and 5 kkm, the distances at which his calculations terminate. Crary's rates are substantially higher, being approximately 8 db/kkm between 5 and 7 kkm. Neither Crary nor Allcock considered azimuthal dependency.

The results of the Davies survey showed that (1) the most favorable propagation conditions for a signal of frequency between 15 and 20 kHz occur for west-to-east propagation over sea at night. The attenuation rate under these conditions (after removing the loss due to the effects of two dimensional spreading) is about 1 db/kkm. (2) The maximum attenuation rate for this frequency range occurs for a land path from east-to-west during

daylight and is approximately 3.5 to 4 db/kkm (exclusive of losses due to two dimensional spreading).

The OGO-I data show relatively good agreement with the rates shown by Allcock and Crary to distances of 3 or 4 kkm but indicate that the rate shown by Crary for distances greater than 5 kkm are too high. There is also good evidence in the data that the minimum rate (west-to-east, over sea at night) suggested by Davies is reasonable. Support for the above statements is shown throughout the OGO-I data but most emphatically perhaps in Fig. 34 between the hours of 0149 and 0203 UT. During this time interval, the location of the foot of the field line passing through the satellite moved almost due east across the Atlantic Ocean from NAA. Essentially all of the earth-ionosphere waveguide path was over sea water for the entire interval. Local time at the foot was approximately midnight and propagation was from west-to-east; conditions which according to Davies should minimize the earth-ionosphere waveguide loss. It is easy to normalize out the effects of spreading and absorption during this interval (see Chapter VII). When this is done one obtains a measured earth-ionosphere waveguide attenuation rate of approximately 2.7 db/kkm. Removing the effects of two dimensional spreading, the rate becomes approximately 1.7 db/kkm. This rate compares very favorably with the minimum rate of approximately 1 db/kkm reported by Davies, but unfavorably with Crary's rate of at least 6 db/kkm (after two dimensional spreading effects are removed).

It is important to note at this point that the large discrepancy between measured and calculated intensities on the tail end of the 23 November 1964 run (Fig. 34) is thus easily explained if one uses in the calculations the earth-ionosphere waveguide attenuation rates published by previous authors. e.g., Wait [1962] reports that in the band of frequency from 10 kHz to 30 kHz, the attenuation rates (determined experimentally) vary from approximately 1.0 db/kkm to 4.5 db/kkm, and that these rates are in good accord with theory if earth curvature is accounted for in the calculations. Although uncertainties in the normalization process and in the scaling of records probably introduce sizeable errors, it is clear from Table 6 that in general the OGO data are in agreement with the above.

Another important conclusion is the fact that the large fluctuations of field strength versus distance in Crary's calculations (Fig. 27) are not observed in the OGO data. Fluctuations of this magnitude (on the order of 20 db) are observed, but they seldom correlate in distance with Fig. 27. Allcock's results show that the scale of the interference pattern is less than that shown by Crary. Allcock concludes that the undulations in the interference pattern are small, and that the general trend of the variation with distance can usefully be found by plotting the rms value of the resultant field strength $[\sum |E_{n,d}|^2]^{\frac{1}{2}}$, as a function of distance. The OGO data support this conclusion; however, additional investigation would be useful. It seems possible, for instance, that if the large variation of field strength with distance does indeed exist just above the boundary, other factors might prevent the observance of this phenomenon by the satellites. It appears reasonable that scattering of the waves at lower regions in the ionosphere could tend to "smear out" the large variations, thereby preventing their being observed by the satellites. Perhaps rockets or a satellite flying at minimum altitudes could check this hypothesis.

B. DIVERGENCE LOSS

In Chapter VII divergence losses were determined by ray tracing. These results, when compared to the OGO data, give strong support for the ray tracing model that was used. Agreement within 1 or 2 db was found between the divergence loss as indicated by ray tracing, by simple geometrical spreading (as used in the first approximation model) and by direct measurement. An interesting result is the fact that the divergence loss indicated by ray tracing is 1 or 2 db less than the divergence loss indicated by geometrical spreading. This result would indicate that divergence loss is slightly greater for a ducted than for a non-ducted signal.

An interesting and useful extension of this divergence loss study would be to ray trace in a model ionosphere containing ducts. This would provide information concerning the effect of a duct on wave normal angles which might be very useful in developing an acceptable explanation of the terminal region burst phenomenon.

In the meantime, the results of Chapter VII clearly show that for propagation in an ionosphere containing no ducts a very good approximation for determining divergence loss is to assume that the vlf signals propagate exactly along the lines of force of the earth's magnetic field. Using this assumption, the limiting cone for the ray direction is defined simply by the geometrical spreading of the geomagnetic field.

It should be noted that we would expect to find the same spreading loss for ducted signals, since the cross section of a duct would also be defined by the geometrical spreading of the geomagnetic field.

In addition to the contributions concerning the earth-ionosphere waveguide loss and divergence loss as discussed above, the main body of this research has provided another very significant result. This research has demonstrated that in general one should be able to predict the average intensity of vlf whistler-mode signals in the magnetosphere to within an accuracy of ± 10 db by existing theory. There are instances in the OGO-I data where the calculated and measured intensities differ by more than 10 db; however essentially all of these discrepancies may be explained by reasonable arguments based on either the new observations from OGO-II, or on related phenomena already reported in the literature. Further discussion of this contribution will appear in Section J after the new observations from OGO-II have been discussed.

C. LATITUDINAL CUTOFF OF WHISTLER-MODE SIGNALS

The high latitude cutoff of vlf signals is an experimentally observed fact of considerable significance. This phenomenon is exceptionally interesting because of (a) its impact on possible communication schemes; (b) the possibility that it represents new evidence of some phenomenon in the ionosphere not even predicted, and (c) the questions which arise in attempting to explain its cause.

As noted in Chapter VIII, this abrupt cutoff has been observed during both daytime (≈ 1600 LMT) and nighttime (≈ 0400 LMT) hours. However, the cutoff is sharper and more pronounced during the daytime. The maximum observed drop in signal intensity is 40 db. This occurred during the daytime over a latitude range of no more than 2° beginning at 59° north

magnetic latitude. Based on averages from Table 10 the daytime cutoff typically begins at 61° north magnetic latitude and produces a drop in signal intensity of about 26 db over a latitude range of 5° . The nighttime cutoff typically begins at 56° north magnetic latitude with signal intensity dropping by approximately 18 db over a latitude range of 9° .

The fact that the cutoff is more pronounced during daytime than nighttime seems to be of major importance in looking for a causative mechanism. This fact might suggest that the phenomenon is consistent with an absorption explanation.

One could hypothesize that the NV product in the D and E regions of the ionosphere increases rapidly with latitude near the cutoff region. The hypothesis here is that energetic particles are coming into this region and producing more ionization, and perhaps heating the ionosphere causing an increase in collision frequency. Note the values here. A polar blackout increases the absorption rate in the lower ionosphere by a factor of about 4 for daytime [Helliwell, 1965]. We only need a factor of about 2 to explain 40 db in the daytime.

Another feature of the data which seems to support an absorption hypothesis is the fact that vlf signals are seldom observed at latitudes above the cutoff region. The typical signal-noise profile versus latitude is discussed in Chapter VIII. It is pointed out that just above the cutoff latitude there is a quiet region. This is followed by a belt of intense 18 kHz noise having a latitudinal width of 3 to 10 degrees. Above the noise latitude the satellite sees a quiet region, usually devoid of both noise and vlf signals. This quiet region is observed over the top of the earth in the form of a polar cap. On only one occasion were vlf signals seen at latitudes above the cutoff region. This occurred during revolution 123 as shown in Figs. 72 and 73, when the satellite was at approximately 73° north magnetic latitude and 100° (eastern) longitude. Because of the limited quantity, interpretation of these data is not clear. However, the fact that NPG signals were observed at this location is interesting. One might assume that absorption over the polar cap region on this particular day was unusually low; however the K_p index was not substantially different (3+) from other days when signals were not observed in this region. Additional polar orbiting satellite measurements would be very useful. It is

also possible that measurements from high latitude ground stations or from airplanes flying at high latitudes would help in the study of interpretation of this observation. In the meantime the general absence of vlf signals above the cutoff region lends support to the absorption hypothesis.

Another mechanism which should be considered as a possible explanation of the cutoff is the absorption of vlf waves by electron resonance.

The temperature of the ionosphere at 1,000 km is estimated by most workers to be of the order 10^3 to 10^4 degrees Kelvin [Bell, 1964; Bauer and Bourdeau, 1962]. At this low temperature the typical plasma particle has a mean velocity much less than typical whistler-mode wave velocities and these particles can be considered to be at rest initially. Consequently the magnetoionic theory holds for the gross propagation characteristics of the wave and the refractive index has the usual real part

$$n \approx \left[1 + \frac{\omega_o^2}{\omega(\omega_H \cos \theta - \omega)} \right]^{\frac{1}{2}} .$$

On the other hand, there may be high energy electrons in the plasma at 1,000 km (and below) due to precipitation from higher altitudes. These particles will probably be of low density compared to the ambient density at 1,000 km and will not affect the real part of the refractive index. However, it is conceivable that the imaginary part of n could be affected so that the propagation losses are increased when the high energy particles are present.

The high energy electrons can absorb energy from a vlf wave by at least two resonance interactions [Stix, 1962]:

1. Gyroresonance, in which the wave and particles move in opposite directions and in which the particle sees a doppler-shifted wave frequency equal to its own gyrofrequency.
2. Longitudinal resonance, in which the wave and particles move in the same direction and in which the particle sees a doppler-shifted wave frequency equal to zero.

T. F. Bell [private communication] has considered each case and found no basis for a significant effect.

Another point may be made. It is not likely that changes in electron

density in the upper ionosphere could explain the cutoff. It is shown in Chapter III that electron density at the satellite would have to decrease by a factor of 10^4 in order to account for a 20 db drop in measured signal intensity due to impedance transformation effects. Whistler observations have shown that the electron density equatorial profile exhibits an abrupt decrease, or "knee", at a geocentric distance of about 4 earth radii. However the maximum value of this abrupt decrease is approximately two orders of magnitude and is believed to be considerably less for the same L-value at altitudes of 1,000 km [Angerami, 1966]. Certainly there is no evidence to suggest that abrupt decreases in electron density with latitude exist on a sufficiently large scale to explain the observed cutoff.

In this section the qualitative nature of the factors concerning the observed cutoff have been presented. Obviously no firm answer has been given. Further work will need to be done to determine an acceptable explanation.

D. ANTIPODAL ENHANCEMENTS

The interpretation of antipodal enhancements appears to be straightforward. Because of the sphericity of the earth, vlf waves propagating omni-directionally in the earth-ionosphere waveguide from a short vertical antenna on the ground will meet at a focal point on the opposite side of the earth. This focal point is defined as the antipode, and may be located by passing a straight line through the center of the earth from the transmitting antenna. It is apparent from the data that this concentration of energy at the antipode of the vlf antenna is often sufficient to excite detectable whistler-mode waves. These waves then propagate up the field line to the satellite.

The best illustration of antipodal enhancement is shown in Figs. 49 and 63 where an enhancement factor of approximately 25 db is seen when the satellite flies within 200 km of the antipode. Numerous other antipodal enhancements have been observed (these are discussed in Chapter VIII) but the minimum distance from the satellite to the antipode is greater than for the above example and therefore the enhancement factors are less as one would expect. The data of Fig. 87 lead to an estimate of the physical

size of the enhancement region; an enhancement factor of about 12 db is seen when the satellite is approximately 1,000 km from the antipode.

Another interesting observation discussed in Chapter VIII concerns an enhancement seen both near the antipode and near the magnetic conjugate of the antipode. The enhancement factor near the conjugate was only 5 db less than the enhancement near the antipode. Admittedly, this is not very good data since there is not very much of it, but nevertheless the data available indicate that antipodal enhancements excite whistler-mode waves which then propagate up the field lines and into the opposite hemisphere.

E. INTENSE NOISE

As mentioned earlier, several other researchers have observed various forms of noise which might be related to the intense noise observed here. These observations have been reported (in private communications) by workers at the University of Iowa; the Defence Research Telecommunications Establishment, Ottawa, Canada; and Stanford University.

Barrington and Belrose [1963] published several recordings of ionospheric noise observed by a 600 Hz to 10 kHz bandwidth receiver aboard the Alouette satellite. Their report appears to be the first mention in the literature of ionospheric noise phenomena having characteristics similar to the noise observed in the present study.

Gurnett and O'Brien [1964] using observations by the Injun III satellite showed a close association between vlf hiss, aurora and particle precipitation. Evidence was found that vlf hiss is generated at and above the high latitude trapping boundary for 40 Kev electrons and that it correlated with fluxes of precipitated electrons whose energies are greater than 10 Kev. Gurnett [1966] using the Injun III data, showed that vlf hiss occurred in a zone about 7° wide centered at 77° invariant latitude at 1400 magnetic local time (MLT) and decreasing to 70° invariant latitude at 2200 MLT. Qualitatively, Gurnett found that (1) when a vlf hiss enhancement occurs, it may last for several hours and occur over a spatial extent about 5° wide in latitude and as much as 5 hours in magnetic local time. (2) The occurrence of vlf hiss does not appear to be related to the intensity of

electrons with energy greater than 40 Kev but does appear to be associated with the intense fluxes of soft electrons with energy of about 10 Kev commonly found during early evening. (3) No significant correlation exists between the occurrence of vlf hiss and the planetary geomagnetic K_p index. (4) Vlf hiss occurrence appears to be seasonally dependent with a maximum during local summer. Based on the limited data available, major features of the intense 18 kHz noise observed in this study seem to correlate with items (1) and (4) above, but not with (3). Note that Table 12 shows seasonal dependence of intense noise occurrence, with local summer rates higher than winter. This table also shows general agreement in latitudinal position and width of the noise as reported by Gurnett. However, from Table 12 there does seem to be a correlation between occurrence of the intense noise and the K_p index, in disagreement with Gurnett's findings.

At this point it appears reasonable to assume that the intense 18 kHz noise is related to the auroral vlf hiss observed by Gurnett and others. However, before firm conclusions may be drawn, additional data must be obtained from wideband satellite receivers.

F. CYCLOTRON ABSORPTION

It was noted in Chapter VIII that cyclotron absorption might be the cause of the wide discrepancy between the measured and calculated values for OGO-I at 0107 UT on 24 November 1965 (see Fig. 34).

T. F. Bell [private communication] has considered this possibility with the following interesting results.

For the OGO-I position at 0107 UT in Fig. 34, we make the following assumption:

1. Plasma frequency \approx 200 kHz
2. A Maxwellian electron velocity distribution and constant temperature exist along each field line in the region between $L = 2.9$ and $L = 3.4$ (0107 UT to 0122 UT in Fig. 34). (The Maxwellian velocity distributions are the same for each field line.)
3. Electron temperature = 4×10^4 degrees Kelvin.

Using these assumptions, losses, due to cyclotron absorption over a 10° section of the $L = 2.9$ field line at the equator, are approximately

zero. Over a similar region for the $L = 3.4$ field line cyclotron absorption losses are approximately 40 db, which is approximately the same as the discrepancy between the measured and calculated field intensities. Hence it appears very likely indeed that Fig. 34 shows new evidence of cyclotron absorption. Recall that the large discrepancy near the end of this figure was explained in Section A on the basis of published earth-ionosphere waveguide losses.

The above assumption of a Maxwellian distribution could be checked by a detailed comparison of the calculated losses with the experimental data over the entire period 0107 UT to 0122 UT. In the absence of more data, Maxwellian distribution was chosen. It is possible that these data (and similar data from future experiments) could be used to determine what the electron velocity distributions are and to study the detailed structure of anisotropies.

G. FADING

It is not surprising that fading is observed in the OGO data since the ionosphere is known to be highly irregular. However, some of the features of the fading are rather unusual and need to be discussed. Here we will summarize the unique features and outline some possible factors which might lead to acceptable explanations of the observations.

In general, the fading appears to be of two types: (1) random fading where both the frequency of occurrence and the depth vary over rather wide limits. Fades on the order of 20 db in approximately one fourth of a second are sometimes seen, but usually the fading is neither this deep nor abrupt. Fading observed by OGO-I is of this type and is shown in Figs. 18 through 22. This type has also been observed by OGO-II as demonstrated in Fig. 54. (2) Deep and very rapid fading which is often observed in a highly periodic form. 20 db fadings at the rate of 10 or more per second are often seen. This type has only been observed by OGO-II and is shown in Figs. 52 and 53.

In considering possible interpretations of the observed fading the question arises as to whether the effect is spatial or temporal. Temporal would mean that the satellite is in a given region for a sufficient period of time to observe sudden vlf intensity fluctuations caused by time-changing

effects in the ionosphere. Spatial would mean that the ionospheric effects change rather slowly with time, and that the rapid fluctuations in the data are a result of the satellite motion; i.e., if a second satellite were following the first they would both see the same fluctuations in intensity. Nothing in the data rejects the assumption of spatial variation. This is the effect that will be assumed.

A feature of the ionosphere which might contribute to some of the observed variations in field strength are large scale ionization irregularities. Large patches of enhanced and/or depressed ionization, with dimensions large compared to the wavelength of the vlf signal in the medium, might cause focusing (and defocusing) of the vlf waves. If so, spatial patterns of vlf field intensity would be created. Variations of field intensity versus time would then be produced as the satellite moved through the pattern.

It would be interesting and useful to ray trace through a model ionosphere containing such irregularities. The above hypothesis could possibly be checked in this manner.

It seems reasonable that the extremely deep and sudden fadings seen occasionally in the type (1) records (where the vlf signal intensity drops essentially to the background noise level) might arise from the beating of two prominent multipath components.

The long period of key-down transmission shown in Fig. 18 through Fig. 22 (which is the best available example of type (1) fading) has been scaled in an effort to obtain information about the statistical distribution of magnitudes. In the scaling process the amplitude of the vlf signal was measured every eighth of a second. The results show that the fading amplitude does not have a gaussian distribution. While one is reluctant to draw conclusions from such a small statistical sample of data, this result might suggest that this is an unusual type of fading.

One possibility is that the fading is the result of the "interference pattern" set up by two plane waves. The minimum distance between fadings would be one half wavelength. For the most rapid fading shown in Fig. 53 the period is typically one tenth of a second. Since the velocity of OGO-II is on the order of 7 km/second the indicated wavelength in the medium would be on the order of 1 km. The free space wavelength of an 18 kHz signal

is approximately 17 km, therefore a refractive index of approximately 17 would be required of the medium. This is roughly what we would expect the refractive index to be in this region for QL propagation.

Perhaps the fading is the result of absorption by high energy particles. It is reasonable to assume that the profile of particles which cause absorption varies with L-value. If we postulate the presence of tilts and irregularities which alter the location of the particle mirror points, this might lead to an acceptable physical explanation. However, the calculations of T. F. Bell, mentioned in Section C, seem to weaken this argument.

Further attempts to interpret the fading observations will have to await a more complete investigation when additional data are available.

H. TERMINAL REGION BURSTS

In studying the very limited amount of data concerning this phenomenon one major fact stands out: terminal region bursts have only been observed by OGO-I when the foot of the field line passing through the satellite was at a northern magnetic latitude between 58° and 62° . Notice in Figs. 10, 11, 12, 13 and 43 (the most striking observation available of this phenomenon) that the observation was made during the daytime, in the winter hemisphere. The bursts were observed as the location of the northern field line foot moved between approximately 58° and 61.5° . The similarity to conditions under which the Northern hemisphere latitudinal cutoff is observed by OGO-II is impressive (see Fig. 85).

As mentioned in Chapter VIII, if the bursts are interpreted as a spatial variation, their physical dimensions suggest the possibility of ducts. Van Zandt, Loftus, and Calvert [1966] have observed a temporal and geographical occurrence of conjugate ducts by the high-frequency top-side sounder on Explorer XX. They report a mean duct width of 4.2 km and a mean separation on the order of 100 km. The largest duct was 40 km wide. They find the fractional difference between the electron concentration inside and outside of the duct to be usually less than 1%; the maximum observed was less than 8%.

The physical dimensions of the terminal region bursts appear to be

approximately correct to warrant advancing the possibility of ducts as an explanation. On the basis of impedance change of the medium, electron concentration inside the duct would have to be approximately two orders of magnitude higher than background concentrations in order to cause a 10 db increase in intensity of the vlf signals observed by OGO-I. This is most unreasonable. There is no evidence to suggest concentration enhancements this large. However, there is the possibility that the characteristics of ducted propagation might be such as to permit propagation to higher latitudes than for non-ducted propagation. A logical mechanism for this could be the control of the wave normal angle by a duct. Ray tracing results indicate that there is a considerable deviation of the wave normal with respect to the earth's field outside of a duct. If it were found that a duct restricts the wave normal angles, a considerable reduction in Landau damping might result. Since the author has not yet pursued this hypothesis no defense of the suggestion is made; it is simply raised as a question.

Certainly there is much evidence in the literature giving strong support to the existence of ducts. Much work needs to be done to better determine the characteristics of ducted signals, especially the direction of the wave normal.

I. THE EQUATORIAL DIP

The dip in field intensity over the magnetic equator is believed to be caused by an absorption effect. The dip is observed more often in daytime than nighttime, and is more pronounced in the daytime. We will use the daytime positional information of Figs. 62 and 63 for illustration purposes.

Consider the path of the satellite as it flies north toward the equator during the latter part of revolution 103 and the beginning of revolution 104 as shown in Fig. 62. Recall that in order for signals to reach the satellite they must propagate in the earth-ionosphere waveguide to the vicinity of the foot of the field line in the Northern hemisphere, penetrate the ionosphere, and then propagate along the field line to the satellite. Consider next the path traced by the foot of the field line in the Northern hemisphere as the satellite moves towards the equator in the Southern

hemisphere. Initially the foot will be considerably north and slightly east of NPG. As the satellite approaches mid-latitudes the foot of the field line moves steadily southward and nearer to NPG.

The minimum distance between NPG and the foot of the field line is obtained when the satellite is at a geomagnetic latitude of approximately 48° South. Notice in Fig. 63 that this minimum in earth-ionosphere waveguide distance corresponds to the maximum field intensity observed by the satellite in the Southern hemisphere.

As the satellite continues to move the foot reaches its lowest magnetic latitude of approximately 27° North when the satellite crosses the equator at an altitude of approximately 1400 km. After the satellite crosses the equator the foot of the field line follows very closely the sub-satellite path, swinging northward and to the west of NPG.

Recall that absorption of a vertically incident vlf wave in passing through the ionosphere is strongly dependent on latitude. For instance, Fig. 92 shows a total integrated daytime absorption to be approximately 40 db at a magnetic latitude of 27° as compared to only 20 db at 50° . Hence it is not surprising that the satellite often sees a pronounced drop in intensity of whistler-mode waves as it flies over the equator. As a matter of fact calculations of intensities expected over the equator indicate that the dip should be even greater than the measurements show. This observation may be explained as follows.

Figure 97 shows the geometry of the incident and transmitted waves, and the earth's magnetic field at the earth-ionosphere boundary for the case described above. From Snell's law, assuming grazing incidence and a refractive index of 6 in the D-region where most absorption occurs, we find that the transmitted wave is approximately 9.6° from the vertical. This results in an angle, θ' , between the transmitted wave and the geomagnetic field, H_0 , of approximately 34.4° . All of the absorption calculations in this study (including Figs. 29 and 92) are based on vertical incidence. In other words, the calculations utilize the angle θ rather than θ' in Fig. 97.

For a magnetic latitude of 27° we may estimate the difference in absorption between the two cases as follows. Effectively, (in Fig. 97) the angle between H_0 and the transmitted wave is only 34.4° rather than

44°. Therefore absorption is as though the wave had been launched vertically at a point where the dip angle, I , is $46 + 9.6 = 55.6^\circ$. This corresponds to vertical incidence at a dipole latitude of approximately 37° [Mlodnosky and Helliwell, 1962]. From Fig. 92 it is seen that daytime absorption of a vertically incident wave at a dipole latitude of 27° ($I = 46^\circ$, $\theta = 44^\circ$) is approximately 40 db, while the absorption at a latitude of 37° ($I = 55.6^\circ$, $\theta = 34.4^\circ$) is only approximately 27 db. Thus the fact that calculated values are always less than measured intensities as OGO-II crosses equatorial latitudes is at least qualitatively explained. At higher magnetic latitudes H_o is more nearly vertical and therefore the error caused by the assumption of vertical incidence will be less.

It should be noted that the equatorial dip (based on the above absorption explanation) would be expected to be much less pronounced during nighttime. This effect is shown by the data. For instance, in Figs. 63 and 67, at approximately 0450 LMT it is questionable whether the dip is clearly defined by the measurements.

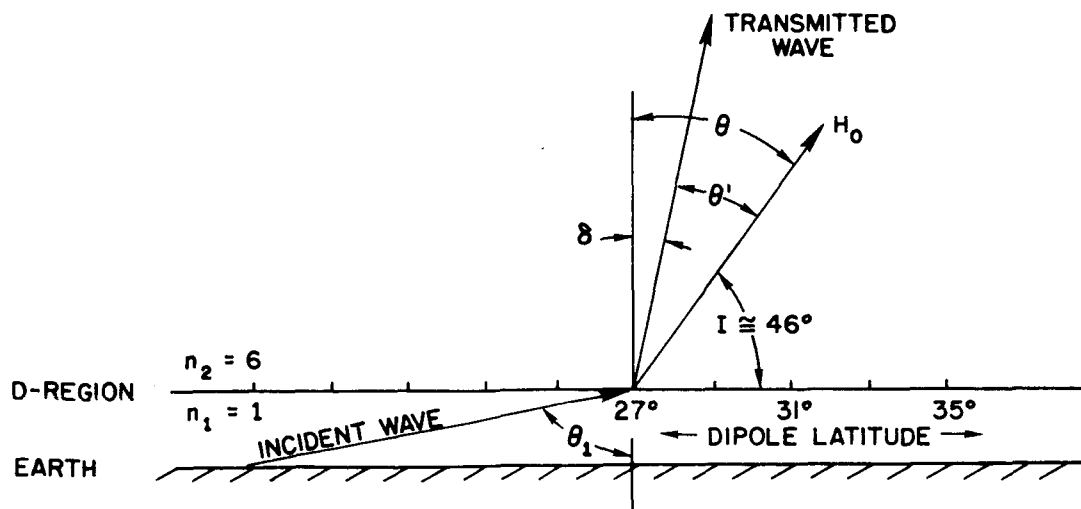


FIG. 97. GEOMETRICAL RELATIONSHIP BETWEEN INCIDENT AND TRANSMITTED WAVE AND THE EARTH'S MAGNETIC FIELD AT A DIPOLE LATITUDE OF 27° .
 I = dip angle, θ_I = angle of incidence, δ = angle of refraction.
 For $\theta_I \approx 90^\circ$ we have $I = 6 \sin \delta$, $\delta \approx 9.6^\circ$.

J. MEASUREMENTS VERSUS CALCULATIONS

One of the significant contributions of this research is the demonstration by controlled experiment that the average intensity of vlf signals in the magnetosphere may usually be predicted to an accuracy of ± 10 db by existing theory. In this section uncertainties in the calculations and in the measurements will be discussed, and a reasonable value for the allowable discrepancy between the two will be established. All of the OGO I measurements and calculated values will then be reviewed with particular attention given to measurements which differ from the calculations by an amount exceeding the allowable discrepancy.

Uncertainties in the calculations arise through uncertainties in the models being used. One obvious component of major importance is the uncertainty in absorption in the D region. This depends in part on uncertainties in the ionospheric models for electron density and collision frequency used in the absorption calculations. Other factors include uncertainties in the rate of earth-ionosphere waveguide attenuation, and in the divergence loss.

In Chapter VII several different models of the ionosphere were used in the integrated absorption calculations. The maximum difference in total absorption at any latitude was less than 6 db. Large uncertainties in the absorption calculations come not only from specific differences between various models (which are based on averages), but from uncertainties in how the ionosphere deviates during short time periods and over small distance intervals from a given model. For instance, observations made by Little and Leinbach [1958] show that regions of anomalous absorption typically have dimensions in excess of 100 km, and during disturbed periods marked differences in absorption can occur between regions 800 km apart. Changes in absorption of as much as 10 db can be expected from anomalous absorption, yet this effect is not a part of the model utilized in the calculations. Similarly, large variations in absorption are known to exist from day to day. But the model, based on averages, also eliminates this effect from the calculations.

Uncertainties in the rate of earth-ionosphere waveguide attenuation are probably much less than uncertainties in absorption. Wait [1962] and

Davies [1965] summarize the earth-ionosphere waveguide attenuation rates determined experimentally by various workers. Wait [1962] performs the theoretical calculations and finds good agreement with the experimental results. For frequencies near 20 kHz the attenuation rates determined both experimentally and theoretically vary from approximately 4.5 db/kkm to 1.0 db/kkm depending upon the time, the direction of propagation, and whether the path is over land or sea. When a specific path is specified the variation between the rates found by various workers is very small, on the order of 1 or 2 db/kkm.

The results in Chapter VII provide good confidence in the ability to predict divergence loss. Uncertainty in divergence is probably no more than 2 or 3 db.

From the above discussion one would probably be justified in estimating that the uncertainty in the calculations is on the order of 10 to 15 db.

Uncertainties in the measurements were discussed in detail in Chapter II. It was concluded that the data are probably accurate to within 2 or 3 db.

In establishing an allowable discrepancy between measured and calculated values, the above would indicate that ± 10 db is a reasonable minimum value. We will therefore adopt ± 10 db as an allowable discrepancy in the regions and at the times of interest in the observations. Each of the OGO-I field intensity charts (Figs. 34 through 44) will now be examined and attention directed to cases where a disagreement greater than approximately 10 db exists between the calculations and the measurements.

In Fig. 34 we have a large discrepancy at the beginning of the run and another large discrepancy of approximately the same magnitude but in the reverse direction at the end of the run. In Section F we presented calculations by T. F. Bell which show that cyclotron absorption could account for losses of approximately 40 db at the beginning of the run. This is approximately the same as the observed discrepancy. Since cyclotron absorption was not included in the calculations based on either the first approximation model or the refined model (the dashed line and the dash-dot line of Fig. 34) it appears that cyclotron absorption is a satisfactory explanation. The large discrepancy on the end of the run was discussed in Section A. It was pointed out that an earth-ionosphere waveguide attenuation

rate of approximately 1.7 db/kkm is indicated by the data in Fig. 34. Since this rate is in excellent agreement with the results of various workers, it appears that the discrepancy is easily resolved. Apparently the earth-ionosphere waveguide attenuation rates for large distances which were used in the calculations (Fig. 27) are too high.

In Fig. 35 the earth-ionosphere waveguide distance is small and the satellite is in a region where cyclotron absorption is not a factor. Note the excellent agreement (on the average) between the calculations and the measurements. The discrepancies (all less than approximately 7 db) probably arise primarily from deviations of the ionosphere from the averages represented by the models. These rapid fluctuations of the measurements may possibly be new evidence of the spatial size of regions of anomalous absorption.

In Fig. 36 the discrepancy between measurements and calculations is well within ± 10 db. From the discussion in Chapter III one would expect a drop in measured field intensity of 10 db due to impedance transformation effects if the satellite entered a region where electron density decreased by two orders of magnitude. Whistler observations have shown that the electron density equatorial profile exhibits such a drop, or "knee," at a geocentric distance of about 4 earth radii. The effect on the calculations for regions inside and outside of the "knee" are shown in Fig. 36. It is apparent that the measured values are in accord with calculations which include the "knee" effect.

In Fig. 37 the greatest discrepancy (near 0258 UT) is approximately 13 db, with the measured value exceeding that calculated. It should be noted that during this time the foot of the field line was almost due south of NAA. Perhaps the discrepancy is at least partially explained by the favorable reduction in the angle of wave normal refraction with respect to the magnetic field when propagation is from north to south. This effect has been observed previously [Rorden, et al, 1964]. This effect is of course not included in a model based on averages.

An interesting feature of Fig. 38 is the fact that the average field intensity consistently remains approximately 15 db higher than the calculated value. Two factors might be involved in the explanation: (a) the earth-ionosphere waveguide distance is large, more than 6 kkm at the beginning of the run. It is well established that the rates used in the calculations (for

large distances) are too high. (b) The earth-ionosphere waveguide path is over sea-water during the entire interval. This fact would accentuate the discrepancy discussed in part (a) above. (c) Penetration of the vlf wave through the ionosphere is perhaps not occurring exactly at the foot but at a higher latitude nearer NPG. This would result in less absorption, and also in a reduced earth-ionosphere waveguide distance. Any or all of these factors are capable of explaining the discrepancy. Each is reasonable.

In Fig. 39 the average discrepancy is on the order of 10 db. Note that calculations based on the first-approximation model provide a better fit than calculations using the refined model. The major difference between the two models for these satellite positional parameters is an approximate 10 db difference in total integrated absorption. The data indicate that absorption was higher than expected during this run. It is probably significant that the foot of the field line was at high magnetic latitudes, between approximately 59° and 61° . This is the region where the latitudinal cutoff is observed by OGO-II. An absorption mechanism was hypothesized in Section C as a possible explanation of the cutoff. It is possible that the discrepancy in Fig. 39 is related to the cutoff phenomenon. Another point that should be considered is the fact that propagation in the earth-ionosphere waveguide is towards the north from NAA. The angle of wave normal refraction with respect to the magnetic field will be large, and therefore we can expect attenuation to be increased. This is the opposite of the effect discussed above for Fig. 37.

In Fig. 40 the most likely explanation of the observed discrepancy appears to be the attenuation rate for the earth-ionosphere waveguide used in the calculations. Note that the field line foot is almost due west from NAA and that the path to the foot extends completely across the United States.

In Fig. 41 it is unfortunate that data were not available for a longer period. Note that the satellite is in the Southern hemisphere and that signals from NAA are first observed when the gyrofrequency at the top of the field line is approximately 30 kHz. Cyclotron absorption, as discussed in Section F, is a likely cause of the observed discrepancy. At the end of the run the discrepancy has been reduced to approximately 10 db. At this point the gyrofrequency at the top of the field line is approximately 45 kHz.

The discrepancy might still involve some cyclotron absorption, or might be attributed to uncertainties in absorption in the D region.

In Fig. 42 excellent agreement between calculated and measured values is found at the beginning of the run. However, as the run progresses we find the discrepancy increasing. The situation is somewhat the same as in Fig. 39; measured values are lower than expected. Note that the foot of the field line is at a high latitude. Propagation is northward from NPG. The same arguments involving northward propagation and the latitudinal cutoff which were discussed in relation to Fig. 39 could be advanced here.

In Fig. 43 the intensities of the "bursts" are approximately the same as the calculated (expected) values. The discrepancy arises from the absence of signals at the satellite during certain periods of time. A loss mechanism would seem to be involved. This burst phenomenon is discussed in detail in Section H and will not be considered further here.

In Fig. 44 the main discrepancy occurs near the beginning of the run where local time at the foot of the field line is approximately 1000 LMT. Daytime absorption rates were utilized in the calculations. From the beginning of the run until almost 1842 UT it is impossible to make the calculations fit the data even if one assumes that penetration of the daytime ionosphere occurred directly over NPG. If nighttime absorption rates are used in the calculations at the beginning of the run the discrepancy is reduced essentially to zero. It appears that the measurements between 1838 and 1842 UT are showing the transition of the ionosphere from nighttime to daytime conditions. Notice the small discrepancy between the measurements and the calculations after 1842 UT which is approximately 1100 LMT at the field line foot.

K. DISCUSSION AND CONCLUSIONS

The properties of whistler-mode propagation have been examined. Existing theory has been utilized to calculate intensities of whistler-mode signals expected in the magnetosphere. These calculations have been compared to the actual intensity of signals as measured by calibrated vlf receivers aboard two satellites. It is concluded that the average intensity of vlf whistler-mode signals in the magnetosphere may usually be predicted to an

accuracy of +10 db by the use of available models and existing theory. Most, if not all, discrepancies greater than 10 db may be resolved on the basis of related phenomena reported in the literature or by the new observations of OGO-II. This study strongly supports the validity of our present understanding of the major features of whistler-mode propagation which until now, has been based largely on theoretical development and experimental observations of naturally occurring phenomena.

Other important contributions have come from this study. These are discussed as new observations in Chapter VIII and include:

1. A Northern hemisphere latitudinal cutoff of vlf signals.
2. Strong enhancements of vlf signals near the antipodes of vlf transmitters.
3. A pronounced dip in the intensity of vlf signals over the magnetic equator.
4. A belt, or band, of intense noise at 18 kHz around both polar regions.

These new observations are described in as much detail as possible with the limited amount of available data. Various mechanisms which might lead to acceptable explanations are suggested.

L. SUGGESTIONS FOR FURTHER WORK

The greatest need for proper continuation of this research is additional data. On future satellites special emphasis should be given to obtaining:

1. Low altitude data from Northern hemisphere vlf stations during local summertime.
2. Data from Southern hemisphere vlf stations at both low and high altitudes during both summertime and wintertime.

These new data would complement the data of the present study, and might indicate whether our present interpretations are correct.

REFERENCES

- Allcock, G. McK., Geometrical optics convergence coefficient for whistler propagation, J. Res. NBS, 68D, 1225-27, 1964.
- Allcock, G. McK., The propagation of whistlers underneath the ionosphere, J. Geophys. Res., 71(9), 2279-83, May 1, 1966.
- Allcock, G. McK. and F. A. McNeill, The reception of whistler mode signals at a point remote from the transmitter's magnetic conjugate point, J. Geophys. Res., 71(9), 2285-94, May 1, 1966.
- Angerami, J. J., A whistler study of the distribution of thermal electrons in the magnetosphere, Tech. Rept. No. 3412-7, Radioscience Laboratory, Stanford Electronics Labs., Stanford University, Stanford, Calif., May 1966.
- Angerami, J. J. and D. L. Carpenter, Whistler studies of the plasmopause in the magnetosphere-2; electron density and total tube content near the knee in magnetospheric ionization, J. Geophys. Res., 71(3), 711-725, Feb. 1, 1966.
- Barber, N. F. and D. D. Crombie, VLF reflection from the ionosphere in the presence of a transverse magnetic field, J. Atmos. & Terr. Phys., 16, 37, 1959.
- Barrington, R. E. and J. S. Belrose, Preliminary results from the very-low frequency receiver aboard Canada's Alouette satellite, Nature, 198 (4881), 651-56, May 18, 1963.
- Barron, D. W., The waveguide mode theory of radio propagation when the ionosphere is not sharply bounded, Phil. Mag., 45, 1069, 1959.
- Bauer, S. J. and R. E. Bourdeau, Upper atmosphere temperatures derived from charged particle observations, J. Atmos. Sci., 19, 218-225, May 1962.
- Bell, T. F., Wave particle gyroresonance interactions in the earth's outer ionosphere, Tech. Rept., 3412-5, Radioscience Laboratory, Stanford Electronics Labs., Stanford University, Stanford, Calif., May 1964.
- Budden, K. G., Radio Waves in the Ionosphere, Cambridge University Press, Cambridge, England, 1961.
- Carpenter, D. L., New experimental evidence of the effect of magnetic storms on the magnetosphere, J. Geophys. Res., 67(1), 135-145, January 1962a.
- Carpenter, D. L., Electron-density variations in the magnetosphere deduced from whistler data, Tech. Rept. No. 11, Radioscience Laboratory, Stanford Electronics Labs., Stanford University, Stanford, Calif., March 1962b. (also published in J. Geophys. Res., 67(9), Aug. 1962).

- Carpenter, D. L. and N. Dunckel, A dispersion anomaly in whistlers received on Alouette I, J. Geophys. Res., 70(15), 3781-86, August 1, 1965.
- Carpenter, D. L., N. Dunckel and J. F. Walkup, A new very low frequency phenomenon: whistlers trapped below the protonosphere, J. Geophys. Res., 69(23), 5009-18, December 1, 1964.
- Carpenter, D. L. and R. L. Smith, Whistler measurements of electron density in the magnetosphere, Rev. Geophys., 2(3), 415-44, August 1964.
- Cartwright, D. G., Rocket observations of very low frequency radio noise at night, Planet. Space Sci., 12(1), 1964.
- Crary, J. H., The effect of the earth-ionosphere waveguide on whistlers, Tech. Rept. No. 9, Radioscience Laboratory, Stanford Electronics Labs., Stanford University, Stanford, Calif., July 17, 1961.
- Crombie, D. D., Difference between E-W and W-E propagation of vlf signals over long distances, J. Atmos. & Terr. Phys., 12, 110, 1958.
- Davies, K., Ionospheric Radio Propagation, National Bureau of Standards Monograph 80, U. S. Government Printing Office, Washington, D.C., April 1965.
- Delloue, J. Sur la direction d'arrivee et de la polarisation des atmospheriques siffeurs, Comp. Rend., 244(6), 797-99, 1957.
- Ficklin, B. P., M. E. Mills, L. E. Orsak, L. H. Rorden and R. H. Stehle, Description and operation of the instruments for the Stanford University/Stanford Research Institute Experiment (5002) to be flown on the POGO satellite, Tech. Memo No. 2, Stanford Research Institute, Menlo Park, Calif., March 1965.
- Gurnett, D. A., A satellite study of vlf hiss, Dept. of Physics and Astronomy Rept., University of Iowa, Iowa City, Iowa, 1966.
- Gurnett, D. A., S. D. Shawhan, N. M. Brice, and R. L. Smith, Ion cyclotron whistlers, J. Geophys. Res., 70(7), 1665-88, April 1, 1965.
- Gurnett, D. A. and B. J. O'Brien, High-latitude geophysical studies with satellite Injun 3, J. Geophys. Res., 69, 65, 1964.
- Guthart, H., Whistlers in a thermal magnetosphere, (Ph.D. dissertation) Stanford Research Institute, Menlo Park, Calif., October 1964.
- Haselgrove, J., Ray theory and a new method of ray tracing, Rept. of the Phys. Soc. Conf. on Physics of the Ionosphere, Cambridge, England, 355-364, Sept. 1954.

- Helliwell, R. A., Whistlers and Related Ionospheric Phenomena, Stanford University Press, Stanford, Calif., 1965.
- Helliwell, R. A. and E. Gehrels, Observations of magnetoionic duct propagation using man-made signals of very low frequency, Proc. IRE, 46(4), 785-87, 1958.
- Helliwell, R. A., J. Katsufakis, and G. B. Carpenter, Whistler-mode propagation studies using Navy vlf transmitters, Tech. Rept. No. 1, Radioscience Laboratory, Stanford Electronics Labs., Stanford University, Stanford, Calif., March 1962.
- Heritage, J. L., S. Weisbrod and J. E. Bickel, A study of signal versus distance data at vlf, VLF Symposium Record 4, 77, 1947.
- Hines, C. O., Heavy-ion effects in audio-frequency radio propagation, J. Atmos. & Terr. Phys., 11(1), 36-42, 1957.
- Hines, C. O., W. C. Hoffman, and H. Weil, Transverse whistler propagation, Rept. No. 2894-1-F, University of Michigan Research Institute, Ann Arbor, Michigan, 1959.
- Johler, J. R. and J. D. Harper, Reflection and transmission of radio waves at a continuously stratified plasma with arbitrary magnetic induction, J. Res. NBS, 66D(Radio Prop.), 81, 1962.
- Kimura, I., Effects of ions on whistler-mode ray tracing, Radio Science, 1(3)(new series), 269-284, March 1966.
- Kimura, I., R. L. Smith and N. M. Brice, An interpretation of transverse whistlers, J. Geophys. Res., 70(23), December 1965.
- Leiphart, J. P., R. W. Zeek, L. S. Bearce and E. Toth, Penetration of the Ionosphere by very-low-frequency radio signals--interim results of the LOFTI experiment, Proc. of IRE, 50(1), 6-17, 1962.
- Little, C. G. and H. Leinbach, Some measurements of high-latitude ionospheric absorption using extraterrestrial radio waves, Proc. of IRE, 46(1), 992-1018, Jan. 1958.
- Lomax, J. B., Measurement of vlf-transmission characteristics of the ionosphere with instrumented Nike-Cajun rockets, SRI Contract NOW 60-0405 (FEM), Final Report, Stanford Research Institute, Menlo Park, Calif., June 1961.
- Maeda, K. and I. Kimura, A theoretical investigation of the propagation path of the whistling atmospherics, Rept. Iono. Space Res., Japan, 19(3), 105-123, 1956.
- Maeda, K., T. Obayashi and I. Kimura, Rocket observation of the ionosphere by using the vlf doppler technique, Space Research V, 1071-79, North Holland Publ. Co., Amsterdam, 1965.

- Mlodnosky, R. F., and R. A. Helliwell, Graphic data on the earth's main magnetic field in space, J. Geophys. Res., 67(6), 2207-2214, 1962.
- Mlodnosky, R. F., R. A. Helliwell and L. H. Rorden, Daytime whistler-mode attenuation through the lower ionosphere at 15.5 kc as measured on Explorer VI during launch trajectory, Explorer VI, NASA SP-54, 1965.
- Omura, J. and T. Kailath, Some useful probability distributions, Tech. Rept. No. 7050-6, Stanford Electronics Labs., Stanford University, Stanford, Calif., Sept. 1965.
- Orsak, L. E., L. H. Rorden, G. B. Carpenter and B. P. Ficklin, VLF propagation and noise in the ionosphere observed by sounding rockets, Stanford Research Institute, Menlo Park, Calif., January 1965.
- Parks, G. S., Jr., G. H. Price, A. L. Whitson and H. W. Parker, Measurements of vlf wave front components over long paths, SRI Rept. Contract NObsr 85271(FBM), Stanford Research Institute, Menlo Park, Calif., March 1964.
- Parzen, E., Modern Probability Theory and Its Applications, John Wiley & Sons, New York, 1960
- Piggott, W. R., M. L. V. Pitteway and E. V. Thrane, The numerical calculation of wave-fields, reflexion coefficients and polarizations for long radio waves in the lower ionosphere. II. Phil. Trans. Roy. Soc., London, Series A 257(1079), 243-271, March 1965.
- Pitteway, M. L. V., The numerical calculation of wave-fields, reflexion coefficients and polarizations for long radio waves in the lower ionosphere. I. Phil. Trans. Roy. Soc., London, Series A 257(1079), 219-271, March 1965.
- Pitteway, M. L. V. and J. L. Jespersen, A numerical study of the excitation, internal reflection and limiting polarization of whistler waves in the lower ionosphere, J. Atmos. & Terr. Phys., 28(1), Jan. 1966.
- Poevlele, H., Strahlwege von radiowellen in der ionosphare, Sitz. Bayerischen Akad. Wiss. 1, 175-201, 1948.
- Ratcliffe, J. A., The Magneto-Ionic Theory and Its Application to the Ionosphere, Cambridge University Press, Cambridge, England, 1959.
- Rorden, L. H., R. A. Helliwell and R. L. Smith, An interpretation of LOFTI-I vlf observations, AGARDOGRAPH 74, Pergamon Press, New York, 75-81, 1964.
- Rorden, L. H., L. E. Orsak and B. P. Ficklin, Non-whistler-mode noise bursts observed on OGO-I, Paper presented at URSI Symp., April 18-21, 1966 at Washington, D.C, 1966a.

- Rorden, L. H., L. E. Orsak, B. P. Ficklin and R. H. Stehle, Instruments for the Stanford University/Stanford Research Institute vlf Experiment (4917) on the EOGO satellite, SRI Instrument Rept., Stanford Research Institute, Menlo Park, Calif., May 1966b.
- Smith, R. L., The use of nose whistlers in the study of the outer ionosphere, (Ph.D. dissertation) Tech. Rept. No. 6, Radioscience Laboratory, Stanford Electronics Labs., Stanford University, Stanford, Calif., July 11, 1960a.
- Smith, R. L., Guiding of whistlers in a homogeneous medium, J. of Res., NBS, 64D(5), September - October 1960b.
- Smith, R. L., Electron densities in the outer ionosphere deduced from nose whistlers, J. Geophys. Res., 66(8), 2578-79, August 1961a.
- Smith, R. L., Propagation characteristics of whistlers trapped in field-aligned columns of enhanced ionization, J. Geophys. Res., 66(11), 3699-3707, November 1961b.
- Smith, R. L., An explanation of subprotonospheric whistlers, J. Geophys. Res., 69(23), 5019-22, December 1, 1964.
- Smith, R. L., Non-ducted whistlers in the magnetosphere, Paper presented at URSI Symposium held in Washington, D.C., April 18-21, 1966.
- Smith, R. L. and N. Brice, Propagation in multicomponent plasmas, J. Geophys. Res., 69(23), 5029-40, December 1, 1964.
- Smith, R. L., R. A. Helliwell and I. W. Yabroff, A theory of trapping of whistlers in field-aligned columns of enhanced ionization, J. Geophys. Res., 65(3), 805-23, March 1960.
- Smith, R. L., I. Kimura, J. Vigneron and J. Katsufakis, Lower hybrid resonance noise and a new ionospheric duct, J. Geophys. Res., 71(7), 1925-27, April 1, 1966.
- Stix, T. H., The Theory of Plasma Waves, McGraw-Hill Book Company, New York, 1962.
- Storey, L. R. O., An investigation of whistling atmospherics, Phil. Trans. Roy. Soc. A, 246, 113-141, 1953.
- Van Zandt, T. E., B. Loftus and W. Calvert, Conjugate ducting in the top-side ionosphere observed by Explorer XX, Paper presented at URSI Symposium held in Washington, D.C., April 18-21, 1966.
- Wait, J. R., The mode theory of vlf ionospheric propagation for finite ground conductivity, Proc. IRE, 45, 760, 1957.
- Wait, J. R., Terrestrial propagation of vlf radio waves, J. Res. NBS, 64D (Radio Propagation), 153, 1960.

- Wait, J. R., Electromagnetic Waves in Stratified Media, Pergamon Press, New York, 1962.
- Wait, J. R. and A. Murphy, The geometrical optics of vlf sky wave propagation, Proc. IRE, 45, 754-760, 1957.
- Wait, J. R. and K. Spies, Influence on earth curvature and terrestrial magnetic field on vlf propagation, J. Geophys. Res., 65, 2325, 1960.
- Wait, J. R. and L. C. Walters, Reflection of electromagnetic waves from a lossy magnetoplasma, Radio Science, 68D(1), 95-101, 1964.
- Watt, D. A. and R. D. Croghan, Comparison of observed vlf attenuation rates and excitation factors with theory, Radio Science, 68D(1), 1-9, 1964.
- Yabroff, I., Computation of whistler ray paths, J. of Res. NBS, 65D(5), 485-505, September - October 1961.